Fluid-Structure Coupling Effects on the Dynamic Response of Pump-Turbine Guide Vanes

THÈSE N^{O} 5455 (2012)

PRÉSENTÉE LE 21 SEPTEMBRE 2012
À LA FACULTÉ DES SCIENCES ET TECHNIQUES DE L'INGÉNIEUR
LABORATOIRE DE MACHINES HYDRAULIQUES
PROGRAMME DOCTORAL EN MÉCANIQUE

ÉCOLE POLYTECHNIQUE FÉDÉRALE DE LAUSANNE

POUR L'OBTENTION DU GRADE DE DOCTEUR ÈS SCIENCES

PAR

Steven ROTH

acceptée sur proposition du jury:

Prof. J. Zhao, président du jury
Prof. F. Avellan, Dr M. Farhat, directeurs de thèse
Prof. E. Egusquiza, rapporteur
Prof. T. Gmür, rapporteur
Dr B. Huebner, rapporteur

ÉCOLE POLYTECHNIQUE
FÉDÉRALE DE LAUSANNE
Suisse
2012

A ma princesse, Jelena

If fate doesn't make you laugh,
then you don't get the joke.

Gregory David Roberts

Remerciements

On dit qu'un travail de thèse est avant tout une aventure personnelle. Or, en préambule de ce document, il m'importe de démentir cette affirmation en exprimant ma profonde gratitude à celles et ceux qui ont, de quelque façon que ce soit, contribué à l'accomplissement et la réussite de ma thèse. Face à l'immensité de l'océan, ces personnes ont su apporter, à temps, leur soutien moral, leurs connaissances techniques ou leur vaste savoir scientifique, afin que le navire sur lequel je me trouvais ne sombre pas et arrive à bon port.

En premier lieu, je ne pourrais manquer de remercier le Prof. François Avellan qui, en ses qualités de directeur de thèse, a su orchestrer le bon déroulement de cette belle aventure. Je lui suis reconnaissant de m'avoir proposé de réaliser une thèse de doctorat au sein de son laboratoire et de m'y avoir vivement encouragé. Il a su ensuite maintenir le cap de ce petit navire tantôt pris dans la "pétole", tantôt malmené par la tempête.

En second lieu, mes remerciements vont directement au Dr. Mohamed Farhat, chef de pont et co-directeur de thèse, qui a, généreusement, consacré une bonne partie de son précieux temps à illuminer la crête des vagues et à éviter les scélérates. Les longues discussions, néanmoins très intéressantes, tant à la cafétéria qu'à la table à cartes, m'ont été d'une grande aide.

Ce travail de recherche a été mené dans le cadre du projet Eureka Hydrodyna II dont les partenaires sont ALSTOM Hydro, ANDRITZ Hydro, VOITH Hydro et UPC-CDIF. Je remercie toutes les personnes impliquées dans ce projet qui ont su faire preuve d'intérêt durant les nombreuses réunions techniques et qui ont réussi à extraire le meilleur de moi-même tout au long de ces années de thèse. Mes remerciements s'adressent également à la Commission pour la Technologie et l'Innovation, CTI, et à Swisselectric Research qui ont également supporté le projet financièrement. Je remercie aussi les membres du jury, les Professeurs Gmür et Egusquiza ainsi que le Dr. Hübner, pour les questions intéressantes soulevées lors de la défense de thèse privée.

J'en viens maintenant aux équipiers sans lesquels les manoeuvres sur le pont ne se seraient, tout simplement, pas aussi bien déroulées. Vlad, dont la rigueur et la générosité n'ont cessé de me grandir, m'a tendu la main à plusieurs reprises même dans les déferlantes les plus impressionnantes. *El* Francisco a toujours été présent lors des manoeuvres les plus délicates, et y a gracieusement apporté ses connaissances techniques et scientifiques étendues ainsi que son sourire des plus rayonnants. J'ai eu aussi énormément de plaisir à travailler avec Maxime, qui a réussi à partager son grand savoir technique et pratique, ainsi qu'à garder son calme lorsqu'il entendait pour la énième fois : "Euh, tu peux changer la *neuf* avec la *dix*... stp...". Je garde encore le bon souvenir, parmi tant d'autres, d'un doux réveil à la lueur de l'aube méridienne, au son d'une guitare désaccordée et aussi sèche que moi! Priorité ou pas : "De l'eau !!!"

Je ne peux m'arrêter là dans le témoignage de ma reconnaissance pour toutes celles et ceux qui ont fait de ce beau voyage intellectuel un souvenir inoubliable. Je continue avec l'équipe du bureau d'étude. Je remercie ainsi Philippe F., Alain, Vincent, Pierre B. et Philippe C. qui ont toujours été disponibles au cours de cette longue traversée. Du côté du groupe "J'aime", je tiens à remercier tout particulièrement Georges avec qui les échanges sur le canal 16 ont été très sympathiques et enrichissants. Viennent ensuite Ran, Lillie, Davide, Ambrosio, Matteo et celui que j'aimerais particulièrement montrer du doigt, Sébastien B. Ma gratitude revient aussi à Henri-Pascal qui nous a laissé assez d'eau pour manoeuvrer correctement malgré la marée et le peu de place à quai.

Il me faut également remercier Pierre M. qui, dans son rôle de supérieur direct, a su maintenir la bonne humeur dans notre petite équipe. Ensuite, comment oublier l'équipe des mécaniciens qui, aux côtés de Maxime, a toujours été prête à mettre les mains dans le cambouis : Louis, Christian S., David, Jérôme, Mattias, Victor, Jean-Daniel et Raymond. Aussi, ma reconnaissance va directement à Isabelle qui a su démêler les noeuds administratifs les plus complexes tout au long du voyage. Finalement, je ne saurais oublier d'exprimer ma gratitude à Shadije pour son travail et sa gentille disponibilité durant les premières années de thèse.

Aussi, "au moindre coup de Trafalgar, c'est l'amitié qui prenait le quart". Une joyeuse équipe de fous furieux a peuplé les cales du navire tout au long de la traversée. Et ces aventures-là pourraient faire l'objet d'une thèse à elles-seules, dont la plupart des chapitres serait frappée par la censure. Tout comme la lune orchestre la marée, le va-et-vient des doctorants influence cycliquement l'ambiance au sein de cette belle équipe. J'ai regretté le départ de certains et me suis réjoui de l'arrivée d'autres... Je souhaite une longue et belle vie à cette équipe sans cesse renouvelée.

Un, deux, trois... quinze... c'est parti ! J'ai juste croisé Bob, Yes pur !, en prenant place à bord du bateau alors que lui en débarquait, mais on s'est souvent croisé en ville par la suite... Merci à toi pour tous ces bons moments et pour tes conseils scientifiques toujours avisés !

Merci aussi à toi Philippe A. pour cette belle amitié dont la charpente résiste à tout coup de vent ! Tu n'as cessé de m'encourager à parvenir sans trop de dommage à la fin de ma thèse. Que se soit la tête dans les enceintes du Mad, autour d'un bon petit plat ou lors de réunions *inter*minables, je garde également un excellent souvenir de nos fous rires.

Aussi, je ne peux oublier l'ami Ruchon qui a, un jour, osé me dépasser en windsurf au large d'Hermance... *Tcheu c'taguenet, i'pensait que j'pétouillais avec mon cassoton, ou bien...* Il a ensuite fallu qu'on se fasse un *surfin' road trip* au Portugal pour nouer définitivement notre amitié ! Bon vent à toi !

Comment oublier de saluer l'amitié qui me lie au Couple, avec un grand "C", du labo, j'ai nommé Séb et Cilecé ! Merci Cilecé de m'avoir mis dans le bain du couplage fluide-structure et de m'avoir convaincu de faire une thèse... J'ai aussi apprécié ta compagnie dans le meilleur bureau du LMH ! Séb, j'ai bien aimé cette douce rivalité entre *voileux* et *aileux* ! Merci à toi pour les nombreux bras de fer. La prochaine fois, je t'aurai !

Une passion commune a tissé nos liens d'amitié, Olivier B. Je suis heureux d'avoir pu compléter en ta compagnie les derniers miles manquants ! *Oh dear*, les fameux bords tirés au large de Guernesey resteront longtemps gravés dans ma mémoire !

Ensuite, viennent les moussaillons Pacot, Martino, Marc et Andres avec qui je partage une grande amitié depuis les études au Poly. Merci à toi, Paquito, d'avoir réussi à me ramener sain et sauf à la maison après cette partie de cache-cache à vélo... Je garde aussi un très bon souvenir de nos mois de colocation dans le Dix Vingt ! Martino, je me souviendrai encore longtemps de nos longues discussions dans lesquelles nous avons su *refaire* le monde à notre sauce, puisque *c'était mieux avant*, et oui... Marc, j'ai apprécié ton sympathique flegme hispano-fribourgeois qui défie même jusqu'à la gravité! Andres, tu m'as été d'un énorme soutien moral dans les moments les plus durs de la rédaction et je t'en remercie infiniment. J'ai beaucoup apprécié ton humilité et ta bonne humeur quotidienne qui font de toi un ami hors pair.

Parmi les personnes qui ont pris place à bord en cours de route, je ne veux pas oublier le petit Matthieu, qui a, malgré lui, réussi à me faire bien rire... Il a souvent été le seul à comprendre mon humour ainsi que le sujet de ma thèse, mais je peine encore à cerner son humour... et le sujet de sa thèse... Mais ça va venir, 120 secondes ne suffisent pas... Manquent encore, à la pelle : Christian L., Christian V., Arthur, Ebrahim et Arturo, à qui je souhaite un bon voyage. Et ceux qui ont débarqué plus tôt, à la louche : Ali, Amir, Marco, Martin et Stefan. Et finalement ceux qui n'étaient que de passage : Joao, Marcelo, Fatine, Felipe, Filippo, Florine et Philippe K. Merci tout spécialement à toi Danail d'avoir pris la peine d'éclairer mon chemin lorsque j'étais dans le doute.

Aussi, je ne pourrai omettre de saluer mes potes du bout du lac qui m'ont soutenu par leur amitié de longue date ! Fred, en particulier, a su être présent quand il le fallait le plus et me faire oublier, par nos nombreux délires, que je me trouvais dans une belle galère ! Merci aussi à mes amis de Lausanne qui ont toujours pris des nouvelles de l'avancement de mon travail et ont su me faire voir d'autres horizons.

Ensuite, je souhaite remercier toute ma famille, et particulièrement mes parents. Je leur suis infiniment reconnaissant de m'avoir donné l'éducation, la motivation et les moyens qui m'ont permis d'arriver là où je me trouve. Merci de m'avoir offert toutes ces années qui n'auraient tout simplement pas été aussi belles sans vous. Je ne peux oublier de remercier plus spécialement ma maman qui a eu le courage de lire ma thèse et d'en améliorer la qualité rédactionnelle.

Finalement, je ne pourrais conclure ces quelques lignes sans remercier de tout mon coeur ma belle princesse, Jelena. Le vent a fait converger nos chemins pour mon plus grand bonheur. L'amour que tu me portes m'a été d'un soutien sans égal durant ma thèse. Tu as réussi à me motiver jusqu'au bout, à me relever quand tout parraissait perdu et à me prendre par la main sur le chemin de ton coeur. Nous embarquons ensemble, pour le restant de nos jours, sur un petit bateau construit de nos propres mains. Et ce bateau est le plus beau qui soit.

Steven Roth

Résumé

L'Interaction Rotor-Stator, RSI, présent dans les pompes-turbines hydrauliques, donne naissance à une excitation périodique de leurs composants mécaniques. Cette interaction est provoquée par le passage des aubes de roue dans le sillage des aubes directrices, en mode turbine, ou en amont des aubes directrices, en mode pompe. Par conséquent, diverses parties structurelles de la machine, notamment les aubes directrices, sont soumises à des cycles de fatigue significatifs.

Le comportement dynamique des aubes directrices est influencé par l'écoulement du fluide. Les vibrations structurelles sont fortement affectées par les effets inertiels et dissipatifs apportés par le fluide, puisque la masse ajoutée et l'amortissement hydrodynamique sont souvent du même ordre de grandeur que leur pendant structurel. De plus, deux aubes directrices placées côte à côte s'influencent mutuellement par le biais du fluide environnant. Leurs fréquences propres ainsi que l'amplitude de leurs vibrations à des fréquences proches de la résonance peuvent, ainsi, être fortement modifiées.

Une mauvaise estimation du comportement dynamique des aubes directrices au stade de la conception peut entraîner des défaillances mécaniques prématurées, pendant la phase de mise en service de la machine, dues au RSI. Jusqu'à présent, les chercheurs ont étudié le phénomène du RSI, sans pour autant être parvenu à en établir une description analytique. Le concept de masse ajoutée a également fait l'objet de recherche, en particulier au niveau des aubes de roue. Cependant, relativement peu d'études sont dédiées au problème de l'amortissement hydrodynamique dans les machines hydrauliques. En outre, à la connaissance de l'auteur, la recherche ne s'est pas encore axée sur l'étude de l'influence des vibrations des aubes directrices sur les fluctuations de pression ni sur leur influence mutuelle.

Par conséquent, ce travail expérimental traite de la réponse des aubes directrices à l'excitation induite par le RSI. Les expériences sont menées à l'aide d'un modèle réduit de pompe-turbine ayant une faible vitesse spécifique et présentant $z_b = 9$ aubes de roue et $z_o = 20$ aubes directrices. La machine est stabilisée à son meilleur point de fonctionnement, à un angle d'ouverture de 18°. La grille d'aubes directrices consiste en un système mécanique complexe présentant de nombreux degrés de liberté. Le but de l'étude est de montrer que cette grille d'aube peut être vue comme un système mécanique du second ordre.

La réponse impulsionnelle des aubes directrices immergées est obtenue en utilisant une bougie d'allumage affleurant le flasque inférieur du canal inter-aubes directrices. Les expériences sont menées avec succès en eau calme, modèle à l'arrêt, ainsi qu'en fonctionnement.

En maintenant les conditions du meilleur point de fonctionnement constantes, la fréquence de rotation de la roue est ensuite balayée et les aubes directrices sont ainsi excitées par le RSI sur une large gamme de fréquence. La combinaison de z_b aubes de roue et de z_o aubes directrices fait apparaître de nombreux modes de pression diamétraux tournants. Les aubes directrices répondent jusqu'à la 5$^{\text{ème}}$ harmonique du RSI. Néanmoins, elles restent principalement excitées aux fréquences correspondant à la fondamentale du RSI $f = z_b n$ et à la seconde harmonique $f = 2z_b n$.

L'amplitude des fluctuations du déplacement et de l'angle de torsion des aubes directrices varie fortement en fonction de la fréquence de rotation de la roue. La fréquence du 1$^{\text{er}}$ mode propre de flexion et du 1$^{\text{er}}$ mode propre de torsion est contenue respectivement dans la gamme de fréquence de la 2$^{\text{nd}}$ harmonique et la 5$^{\text{ème}}$ harmonique du RSI. Les fluctuations de pression enregistrées proche des directrices vibrantes varient beaucoup et peuvent baisser jusqu'à 50% à la résonance. En conséquence, un transfert d'énergie entre la structure et l'écoulement a certainement lieu.

L'influence d'une aube directrice adjacente sur les vibrations d'une autre varie de manière significative selon qu'elle est placée du côté de l'intrados ou de l'extrados de cette dernière. Concernant les vibrations des aubes directrices en flexion, la force hydrodynamique exercée sur une aube directrice induite par les vibrations de l'aube directrice voisine positionnée du côté de son intrados est 10 fois supérieure à la force induite par l'aube directrice voisine positionnée du côté de son extrados. Quant aux vibrations en torsion, le couple hydrodynamique exercé sur une aube directrice induit par les vibrations de l'aube directrice voisine positionnée du côté de son intrados est 5 fois supérieur au couple induit par l'aube directrice voisine positionnée du côté de son extrados.

Le coefficient d'amortissement hydrodynamique et la masse ajoutée apportés par les vibrations des aubes directrices adjacentes sont identifiés et permettent de construire une matrice d'influence. Ces termes dépendent fortement de trois paramètres : l'amplitude relative de leurs vibrations, la vitesse absolue de l'écoulement et le déphasage entre leurs signaux de vibrations.

En considérant la périodicité de la grille d'aubes directrices, la matrice d'influence est construite de manière à prédire le comportement vibratoire de la grille d'aubes complète. Quatre et six modes propres différents sont respectivement traités pour le cas de la flexion et de la torsion. La partie réelle des valeurs propres de tous les modes de flexion reste positive sur toute la plage de fréquence de rotation de la roue, alors que celle relative au mode de torsion le plus facilement excité par le RSI devient négative au-dessus d'une certaine fréquence de rotation. Ainsi, ce mode est instable et on peut s'attendre à des dégats aux niveaux des directrices. Deux solutions sont finalement proposées pour limiter le risque de casse.

Mots-clés: Couplage fluide-structure, machines hydrauliques, pompe-turbine, Rotor-Stator Interaction, Grille d'aubes directrices

Abstract

Hydraulic pump-turbines are subject to a high periodic excitation due to the Rotor-Stator Interaction, RSI. Basically, the RSI is caused by the impeller blade passage in the wake of the guide vanes in generating mode, or upstream from the guide vanes in pumping mode. Therefore, the structural parts, notably the guide vanes, suffer from high cycle fatigue strength.

The dynamic behavior of the guide vanes is influenced by the surrounding flow. Additional inertia and dissipation strongly affect the structural vibrations; the added mass and the hydrodynamic damping being of the same order of magnitude as the structural mass and damping. In addition, should the entire guide vane cascade be considered, the neighboring guide vanes are influencing each other through the fluid medium. Their eigenfrequencies as well as the vibration amplitudes close to resonance may, thus, be strongly modified.

A poor assessment of their dynamic behavior during the design stage may lead to premature failures due to RSI in the early stage of commissioning. So far, researchers have studied the RSI phenomenon, but have not established an analytical description. They have also investigated the added mass, especially the one acting on vibrating runner blades. However, few studies are related to the hydrodynamic damping in hydraulic machines. Moreover, to the author's knowledge, researchers have not yet considered neither the influence of the guide vane vibrations on the pressure fluctuations arising from the RSI nor the coupling between the guide vanes.

Therefore, the present experimental work considers the response of the guide vanes in a pump-turbine reduced scale model to the RSI excitation. The pump-turbine is operated at the Best Efficiency operating Point, BEP, in turbine mode. The guide vane cascade consists of a complex mechanical system featuring many degrees of freedom. The study aims to show that the cascade may be viewed as a 2^{nd} order mechanical system.

The impulse response of immersed guide vanes is enabled with the use of a spark plug flush mounted in the bottom ring in a guide vane channel. This type of measurements is successfully undertaken in water, model at rest, and model in operation.

Keeping the operating conditions of the BEP constant, the impeller rotation frequency is then swept and the guide vanes are therefore excited by the RSI over a wide frequency range. The combination of z_b impeller blades with z_o guide vanes makes apparent many different rotating diametrical pressure modes. The guide vanes respond up to the RSI 5^{th} harmonic, but are mostly excited at the frequencies corresponding to the RSI fundamental $f = z_b n$ and the 2^{nd} harmonic $f = 2z_b n$.

The amplitude of the fluctuating bending displacement and torsion angle of the guide vanes is strongly varying across the impeller frequency range. The ranges of the 1st and the 5th RSI harmonic frequency contain the frequency of the 1st bending eigenmode and the 1st torsion eigenmode, respectively. The pressure fluctuations close to the vibrating guide vanes are strongly varying and may even decrease by 50% at resonance. Therefore, a transfer of energy between the vibrating structure and the flow pressure should occur.

The influence of an adjacent guide vane on the vibrations of a guide vane is found to vary significantly between its position on the pressure side and suction side of the latter. Regarding the guide vane bending vibrations, the hydrodynamic force acting on a guide vane induced by its neighboring guide vane on the pressure side is up to 10 times higher than the force induced by its suction side neighbor. As for the guide vane torsion vibrations, the hydrodynamic torque acting on a guide vane induced by its neighboring guide vane on the pressure side is up to 5 times higher than the force induced by its suction side neighbor.

The hydrodynamic damping coefficient and the added mass corresponding to the vibrations of the adjacent guide vanes are successfully identified and an influence matrix is built. These two terms are shown to depend strongly on the relative amplitude of their vibrations, the absolute flow velocity and the phase shift between their vibration signals.

Taking into account the periodicity condition, the influence matrix is built in order to predict the dynamics of the entire guide vane cascade. Four and six different eigenmodes are investigated for the case of bending and torsion motions, respectively. The eigenvalue real part of each bending eigenmode remains positive on the investigated impeller frequency range, that is the mechanical system is stable. On the other hand, the eigenvalue real part of the torsion eigenmode which is the most likely to be excited by the RSI becomes negative. This means that the mechanical system is unstable and premature failures of the guide vanes are expected. Finally, two different ways to prevent damage to the guide vanes excited at the RSI 5th harmonic frequency are proposed. On the one hand, it is shown that by increasing the structural damping constant by a factor 2, the mechanical system becomes stable. On the other hand, the modification of the shape of the cascade eigenmode is achieved by mistuning the cascade, such that its shape does no longer match the shape of the RSI pressure mode. This way, even if the mechanical system remains unstable, the risk of damaging the guide vanes is reduced.

Keywords: Fluid-structure coupling, Hydraulic Machines, Pump-Turbines, Rotor-Stator Interaction, Guide vane cascade, wicket gate cascade.

Contents

I Introduction 1

1 Problem overview 3
- 1.1 Thesis document organization 4

2 Hydraulic pump-turbines 5
- 2.1 Hydropower generation 5
- 2.2 Pumped-storage power plants 7
- 2.3 Pump-turbine technology 9
  - 2.3.1 Pump-turbine components 11
  - 2.3.2 Energy balance 11
- 2.4 Rotor-Stator Interaction phenomenon 13
  - 2.4.1 Physical principles 14

3 Fluid-structure coupling in the guide vane cascade 19
- 3.1 General definitions 19
- 3.2 Newton's law applied to the guide vanes 20
- 3.3 Hydrodynamic loading 20
- 3.4 Eigenmodes of the guide vanes 25

II Investigation methodology 27

4 Investigated pump-turbine 29
- 4.1 Pump-turbine characteristics 29

5 Test facility 37

6 Measuring apparatus 39
- 6.1 Impulse excitation system 39
  - 6.1.1 In air 39
  - 6.1.2 In water 39
- 6.2 Structural vibration measurement 40
- 6.3 Flow pressure measurement 43
- 6.4 Measuring chain 45

III Guide vane cascade dynamics 49

7 Rotating pressure modes in the stator due to the RSI 51

8 Impulse response 63
- 8.1 Guide vanes in place, dewatered model 63
  - 8.1.1 Eigenfrequencies 63
  - 8.1.2 Structural damping 66
- 8.2 Guide vanes in place, still water 68
  - 8.2.1 Eigenfrequencies 68
  - 8.2.2 Hydrodynamic damping 70
- 8.3 Guide vanes in place, model in operation 72
  - 8.3.1 Eigenfrequencies 74
  - 8.3.2 Hydrodynamic damping 75

9 Forced response of the guide vanes 79
- 9.1 Testing conditions 79
- 9.2 Pressure fluctuations and guide vane vibrations 81

10 Identification of the hydrodynamic parameters 97
- 10.1 Identification methodology 97
  - 10.1.1 Bending eigenmode 99
  - 10.1.2 Torsion eigenmode 101
- 10.2 Hydrodynamic parameters for the bending eigenmode 103
- 10.3 Hydrodynamic parameters for the torsion eigenmode 111

11 Eigenvalue problem 119
- 11.1 Bending eigenmode 119
- 11.2 Torsion eigenmode 121

12 The entire guide vane cascade 125
- 12.1 Bending eigenmode 125
- 12.2 Torsion eigenmode 127

IV Conclusions and Perspectives 133

13 Conclusions 135

14 Perspectives 137

Appendices 141

A Signal processing 141
- A.1 Random data spectral analysis 141

B Analytical identification of the guide vane dynamics 143
B.1 Deflection and rotation of a beam due to simple bending 143
B.2 Angular deflection of a beam due to simple torsion 144
B.3 Guide vane stiffness identification 145
B.3.1 Modified guide vanes 145
B.3.2 Usual guide vanes 146
B.4 Identification of the guide vane bending and torsion eigenfrequencies . . . 147
B.4.1 Modified guide vanes 147
B.4.2 Usual guide vanes 148
B.5 Identification of the guide vane mass and inertia 148
B.5.1 Modified guide vanes 148
B.5.2 Usual guide vanes 148

C Green functions for solving potential flow 151
C.1 Potential flow 151
C.2 Green functions 151
C.3 Application to the guide vane cascade 153

D Procedure for hydrodynamic parameter identification 157

E Rotating pressure modes due to the RSI - an acoustic approach 159

References 167

Curriculum Vitae 177

List of Publications 177

Notations

Latin

A	Surface area	[m^2]
B_o	Guide vane channel height	[m]
$\hat{B}$	Transfer function of the Butterworth filters	[-]
$\mathbf{B}_p$	Complex eigenvector	[m] or [rad]
$\mathbf{C}$	Absolute flow velocity	[m $\cdot$ s^{-1}]
$[C^s]$	Structural bending damping constant matrix	[kg $\cdot$ s^{-1}]
$\left[C^f\right]$	Hydrodynamic bending damping constant matrix	[kg $\cdot$ s^{-1}]
D	Diameter	[m]
D_h	Hydraulic diameter	[m]
$[D^s]$	Structural torsional damping constant matrix	[kg $\cdot$ m^2 $\cdot$ s^{-1}]
$\left[D^f\right]$	Hydrodynamic torsional damping constant matrix	[kg $\cdot$ m^2 $\cdot$ s^{-1}]
E	Pump-turbine specific energy	[J $\cdot$ kg^{-1}]
E	Young modulus	[GPa]
F_i	Total bending force acting on the i^{th} guide vane	[N]
$F_{i,j}^f$	Fluctuating bending force due to O_j vibrations acting on O_i	[N]
F_i'	Fluctuating bending force due to change of incidence angle of O_i	[N]
F_i^{RSI}	Fluctuating bending force due to the RSI acting on O_i	[N]
G	Shear modulus	[GPa]
$[G]$	2^{nd} matrix in the Newton's law using the Duncan transformation	diverse
$[H]$	1^{st} matrix in the Newton's law using the Duncan transformation	diverse
I_z	Moment of inertia in relation to the z-axis	[m^4]
I_p	Polar moment of inertia	[m^4]
$[\mathbf{I}]$	Identity matrix	[-]
$[I^s]$	Structural mass matrix	[kg]
$\left[I^f\right]$	Added mass matrix	[kg]
$[J^s]$	Structural inertia matrix	[kg $\cdot$ m^2]
$\left[J^f\right]$	Added inertia matrix	[kg $\cdot$ m^2]
$[K^s]$	Structural bending stiffness matrix	[kg $\cdot$ s^{-2}]

L	Guide vane chord length	[m]
$[L^s]$	Structural torsional stiffness matrix	[kg · m^2 · s^{-2}]
$\hat{L}_{ps}^{18n}$	Transfer function between pressure (pres. side) and the force due to the RSI	[m^2]
$\hat{L}_{ss}^{18n}$	Transfer function between pressure (suct. side) and the force due to the RSI	[m^2]
N	Impeller rotation frequency	[rpm]
O_i	Denomination of the i$^{\mathrm{th}}$ guide vane	
P	Pump-turbine power	[W]
Q	Pump-turbine volumetric discharge	[m^3 · s^{-1}]
R	Radius	[m]
R_3	Radius at a position between stay- and guide vanes	[m]
T_i	Total torsion torque acting on the i^{th} guide vane	[N · m]
$T_{i,j}^f$	Fluctuating torsion torque due to O_j vibrations acting on O_i	[N · m]
T_i'	Fluctuating torsion torque due to change of incidence angle of O_i	[N · m]
T_i^{RSI}	Fluctuating torsion torque due to the RSI acting on O_i	[N · m]
T	Measuring period	[s]
$\mathbf{U}$	Peripheral impeller velocity	[m · s^{-1}]
V	Fluid control volume	[m^3]
$\mathbf{W}$	Relative flow velocity	[m · s^{-1}]
W	Narrowest width of the guide vane channel	[m]
W_h	Hamming window function	[-]
Z	Elevation	[m]
c_0	Speed of sound	[m · s^{-1}]
$\mathbf{e}$	Unit vector	[-]
f	Frequency	[Hz]
f_0	Eigenfrequency	[Hz]
g	Gravitational acceleration	[m · s^{-2}]
g_i	Denomination of the i$^{\mathrm{th}}$ pressure sensor in the rotor-stator gap	
gH_X	Fluid specific energy at the section X	[J · kg^{-1}]
$gH_{r_{X \div Y}}$	Fluid specific energy losses between the sections X and Y	[J · kg^{-1}]
$h\left(t\right)$	Sinusoidal exponentially decreasing fitting curve	[-]
h^0	Y-intercept of the function $h\left(t\right)$	[-]
k_-	1^{st} nodal diameter number	[-]
k_+	2^{nd} nodal diameter number	[-]
l	length	[m]
m,m'	Integers for RSI harmonics	[-]
n	Impeller rotation frequency	[Hz]
n_-	1^{st} diametrical pressure mode rotating frequency	[Hz]

n_+	2^{nd} diametrical pressure mode rotating frequency	[Hz]
$\mathbf{n}$	Unit vector normal to a surface	[-]
p	Gauge pressure	[Pa]
p^a	Absolute pressure	[Pa]
p^{atm}	Atmospheric pressure	[Pa]
p_r	Rotating pressure field	[Pa]
$p_{r,m}$	m'^{th} component of the rotating pressure field	[Pa]
p_s	Stationary pressure field	[Pa]
$p_{s,m}$	m^{th} component of the stationary pressure field	[Pa]
s_i	Denomination of the i^{th} pressure sensor in the guide vane channel	
t	Time	[s]
$\mathbf{x}$	Cartesian coordinate	[m]
y	Guide vane bending displacement	[m]
z_b	Impeller blade number	[-]
z_o	Guide vane number	[-]
$\Im$	Imaginary part of a complex number	
$\Re$	Real part of a complex number	

Greek

α	Guide vane torsion rotation	[rad]
α_O	Guide vane opening angle	[°]
β_F	Beam extremity rotation due to a bending force F	[rad]
β_T	Beam extremity rotation due to a shear torque T	[rad]
$[\delta C]$	Matrix of the relative residuals assessing the Caughey condition	[-]
ϵ_X	Relative difference of the X quantity	[-]
ϵ'_{dp}	Relative error on the differential pressure measurements	[-]
ϵ'_Q	Relative error on the flow discharge measurements	[-]
ϵ_{F_i}	Absolute uncertainty for bending force measurements	[-]
ϵ_{T_i}	Absolute uncertainty for torsion torque measurements	[-]
$\epsilon_{p_{s_i}}$	Absolute uncertainty measurement of the pressure sensor s_i	[-]
ϕ	phase	[rad]
$\Delta\phi_k$	Phase shift relative to the RSI pressure mode k	[rad]
η	Total efficiency	[-]
η_e	Energetic efficiency	[-]
η_h	Volumetric efficiency	[-]
η_{rm}	Mechanical efficiency expressing the losses by disc friction	[-]
η_m	Mechanical efficiency expressing the losses in the bearings	[-]

λ	Damping coefficient	[s^{-1}]
μ	Mass per unit length	[kg $\cdot$ m^{-1}]
ν	Kinematik viscosity	[m^2 $\cdot$ s^{-1}]
θ	Angular position in the stator	[°]
θ_r	Angular position in the rotor	[°]
ρ	Fluid density	[kg $\cdot$ m^{-3}]
ω	Pulsation	[rad $\cdot$ s^{-1}]
$[\Delta]$	Matrix containing the eigenvalues of the matrix $[H^o]^{-1}[G^o]$	diverse
Φ	Flow velocity potential	[m^2 $\cdot$ s^{-1}]
Φ^f	Flow velocity potential due to guide vane vibrations	[m^2 $\cdot$ s^{-1}]
Φ^{RSI}	Flow velocity potential due to the RSI excitation	[m^2 $\cdot$ s^{-1}]
$\Gamma^2_{X,Y}$	Coherence function between two signals X and Y	[-]
Λ	Influence coefficient of the guide vane vibrations	[-]
Λ_y	Influence coefficient of the guide vane bending vibrations	[-]
Λ_α	Influence coefficient of the guide vane torsion vibrations	[-]
Θ	Green function	[-]
$\partial\Omega$	Fluid control volume boundary	[m^2]

Subscripts

1	Impeller high pressure side
$\bar{1}$	Impeller low pressure side
I	Pump-turbine installation high pressure side
$\bar{I}$	Pump-turbine installation low pressure side
A	Section of the water intake in the upper reservoir
$\bar{A}$	Section of water admission in the lower reservoir
B	Upper reservoir free surface
$\bar{B}$	Lower reservoir free surface
S	Relative to a source of sound
e	External streamline
ext	External quantity
int	Internal quantity
m	Meridional flow velocity component
max	Maximum quantity
ref	Reference quantity
t	Transferred quantity
tot	Total quantity
u	Peripheral flow velocity component
y	Relative to bending displacement
α	Relative to torsion rotation

Superscripts

S	Quantity relative to the structure
$R-R$	Obtained using the Rayleigh-Ritz method
exp	Quantity experimentally obtained
f	Quantity relative to the fluid
$\hat{}$	Spectral quantity
$\tilde{}$	RMS value
$\bar{}$	Stationary quantity
$'$	Fluctuating quantity
$\dot{}$	First time derivative
$\ddot{}$	Second time derivative
$\circ$	Indicates a matrix which is linked to a decoupled system of equations

Dimensionless Numbers

Re	Reynolds number	$Re = \dfrac{C_{max} \cdot D_h}{\nu}$ [-]
c_p	Pressure factor	$c_p = \dfrac{p}{\rho \cdot E}$ [-]
c_y	Displacement factor	$c_y = \dfrac{y}{\delta}$ [-]
c_α	Rotation factor	$c_\alpha = \dfrac{\alpha \cdot \frac{L}{2}}{\delta}$ [-]
$\varphi_{\bar{1}e}$	Discharge coefficient	$\varphi_{\bar{1}e} = \dfrac{Q}{\frac{\pi^2}{4} D_{\bar{1}e}^3 n}$ [-]
$\psi_{\bar{1}e}$	Energy coefficient	$\psi_{\bar{1}e} = \dfrac{E}{\frac{\pi^2}{4} D_{\bar{1}e}^2 n^2}$ [-]
κ	Reduced frequency	$\kappa = \dfrac{2\pi f \frac{L}{2}}{C_{ref}}$ [-]
ν	Specific speed	$\nu = \dfrac{\varphi_{\bar{1}e}^{0.5}}{\psi_{\bar{1}e}^{0.75}}$ [-]

Acronyms

BEP	Best Efficiency operating Point
DOF	Degree Of Freedom
EPFL	Ecole Polytechnique Fédérale de Lausanne
FFT	Fast Fourier Transform
FPS	Frame Per Second
LMH	Laboratoire de Machines Hydrauliques
OECD	Organization for Economic Co-operation and Development
RSI	Rotor-Stator Interaction

Part I

Introduction

Chapter 1

Problem overview

Hydraulic pump-turbines are subject to high periodic loading due to the Rotor-Stator Interaction, RSI. Basically, the RSI is caused by the impeller blade passage in the wake of the guide vanes in generating mode, or upstream from the guide vanes in pumping mode. Therefore, the structural parts, notably the guide vanes, suffer from high cycle fatigue strength.

The dynamic behavior of the guide vanes is influenced by the surrounding flow. Additional inertia and dissipation strongly affect the structural vibrations; the added mass and the hydrodynamic damping being of the same order of magnitude as the structural mass and damping. In addition, should the entire guide vane cascade be considered, the neighboring guide vanes are influencing each other through the fluid medium. Their eigenfrequencies as well as the vibration amplitudes close to resonance may, thus, be strongly modified.

A poor assessment of the guide vane dynamics during the design stage may lead to premature failures due to RSI in the early stage of commissioning. So far, researchers have studied the RSI phenomenon, but have not established an analytical description. They have also investigated the added mass, especially the one acting on vibrating runner blades. But, few studies are related to the hydrodynamic damping in hydraulic machines. Moreover, to the author's knowledge, researchers have not yet considered neither the influence of the guide vane vibrations on the pressure fluctuations arising from the RSI nor the coupling between the guide vanes.

Therefore, the present experimental work considers the response of the guide vanes in a pump-turbine reduced scale model to the RSI excitation. The pump-turbine is operated at the Best Efficiency operating Point, BEP, in turbine mode. The guide vane cascade consists of a complex mechanical system featuring many degrees of freedom. The study aims to show that the cascade may be viewed as a 2^{nd} order mechanical system. The fluid-structure coupling parameters are then identified and are shown to depend strongly on the flow velocity and the vibration phase and amplitude. From the measurements on two isolated guide vanes, the response of the entire guide vane cascade to the RSI excitation may be predicted. Finally, solutions are proposed to prevent damage to the guide vanes.

1.1 Thesis document organization

The thesis document is organized in four main parts:

Part I is the introduction of the present text. Firstly, the hydraulic pump-turbines are placed in the general context of hydropower to progressively introduce the RSI phenomenon. Then, the fluid-structure coupling in pump-turbine guide vane cascade is theoretically presented.

Part II describes the investigation methodology. The pump-turbine concerned in the study is detailed. Then, the test facilities are described, as well as the measuring apparatus.

Part III concerns the dynamics of the guide vane cascade. The study of the RSI pressure modes is firstly given. Then, the testing conditions for the investigation of the fluid-structure coupling in the cascade are presented. Next, the guide vanes vibrations as well as their influence on the pressure fluctuations are studied prior to the identification of the hydrodynamic parameters. The analysis of the eigenmodes problem is then investigated and, finally, the vibrations of the complete guide vanes cascade are analyzed.

Finally, a general discussion concludes the present text. Perspectives for the future are also provided.

Chapter 2

Hydraulic pump-turbines

2.1 Hydropower generation

The world electrical production is currently essentially based on fossil fuels; 67.1% of electricity generated in 2009 being shared between natural gas, oil and coal [43]. The distribution of electrical production is shown by energy source in Figure 2.1 for the years 1973 and 2009. The extraction and the excessive use of fossil fuels causes numerous damages. For instance, the greenhouse gas emission is said to cause the global warming, whose main consequence might be the rise of sea level which is forecasted to have severe environmental and social impacts [86].

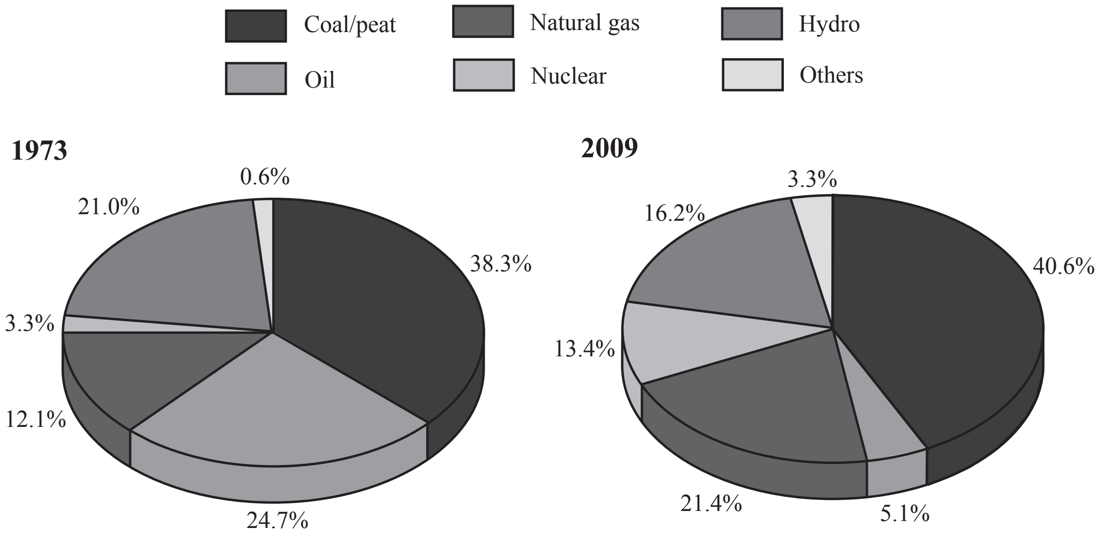

Figure 2.1: Distribution of electrical production by energy source for the years 1973 and 2009 [43].

Alternative sources of electricity generation are diverse. Nuclear fission and fusion constitute the alternative *non-renewable* sources. Solar, biomass, wind, hydropower, ocean thermal gradients, ocean tides and ocean waves are the available *renewable* sources. With the necessary current tendency to reduce the industrial impacts on the environment, these alternative sources, *renewable* and *non-renewable*, are likely to be more widely used in the future. In 2009, they are already sharing 8% more of the world electrical production than in 1973, while the electrical energy generation has rised from 6115 TWh to 20055 TWh [43].

With the growth of the world population and the global warming consequences, the water [1] and energy supply will constitute great challenges in the 21st century [76]. Moreover, water and energy present a mutual necessity [39] in the sense that the access to water needs energy and water is needed for energy production. In energy production, water is *indirectly* employed for cooling, wasting, extracting and conducting heat. But, water may also be *directly* used for electrical energy production, in so-called hydropower installations.

Nowadays, hydropower is being utilized in over 160 countries. The net installed capacity has reached 980 GW at the end of 2009. Hydropower largely contributes to the global energy mix by providing 17% of the world's estimated installed electrical capacity and 72% of the estimated renewable energy-sourced capacity at the end 2010 [44]. The International Hydropower Association, IHA, estimates that hydropower plants commissioning will grow at an average rate of 3% per year [44], whilst the electricity consumption is forecasted to grow at an average rate of 2.3% until 2035 [81].

The worldwide installed hydropower capacity and hydropower plants still under construction at beginning-2008 are shown by region in Figure 2.2 [87]. Europe has the greatest number of installed capacity, followed by Eastern Asia and Middle East which notably have the greatest number of hydropower plants under construction. In emerging economies, like in Asia and Latin America, hydropower is currently strongly developing. As an example, the Chinese government has set a 300 GW hydropower capacity target for 2020, and China currently has a sufficient number of projects under construction to meet the target. Pumped-storage plants are notably required among the many hydroelectric

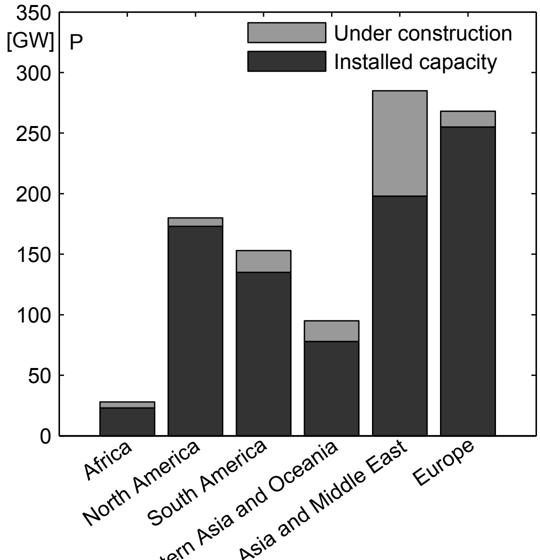

Figure 2.2: Worldwide installed and under construction hydropower capacity at beginning-2008 [87].

projects in China, in order to meet the future peak electricity demand [84]. In low income countries, as in Africa, the ”translating of [recognized substantial hydropower potential] into commissioned projects still encompasses many difficulties” [41]; 90% of Africa’s current hydropower plants being operational in only eight countries. In developing countries, energy supply security is currently one of the main issues to guarantee the growth of the economy [85]. A correct transfer of technology is the key component to meet the economic target by ensuring a technical independence. Finally, OECD economies in North America and Europe focus on the rehabilitation of existing plants [55], [15], [82], the development of new technologies [59], [65] and the construction of pumped-storage power plants, such as Germany’s Goldisthal pumped-storage scheme [14].

Switzerland has about 2% of the world installed hydropower capacity. Figure 2.3 shows the distribution of the electrical production in 2010. 56.5 % of electrical power is produced by run-of-river and storage hydropower plants, whereas production by nuclear power plants represents 38.1 %; the remaining 5.4 % being produced by conventional thermic turbines, wind, solar, etc.

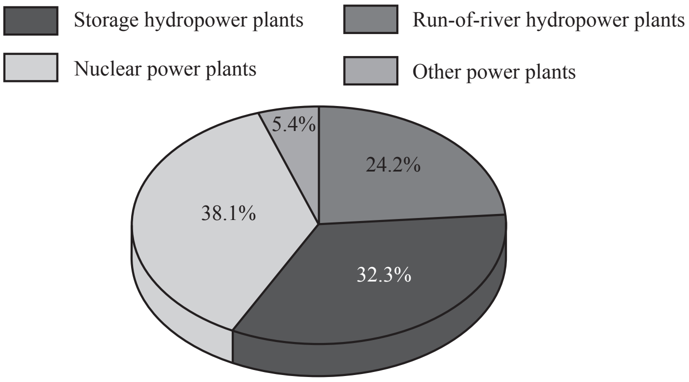

Figure 2.3: Electrical production distribution in 2010 in Switzerland [62].

2.2 Pumped-storage power plants

Electrical energy must be efficiently stored and rapidly made available. On the one hand, the demand is daily and seasonally varying and, technically, the production may not always be instantaneously adapted to this demand. Nuclear and thermal powerplants, for instance, generate stable electrical power and a great inertia is technically imposed in the way of operating [19]. On the other hand, the intermittent sources of energy, such as wind or solar must be balanced [83]. Therefore, storage sources fulfill the requirements to finally stabilize the electrical grid, [37] and [75].

The types of electrical storage are listed in Table 2.1. The diverse storage sources are plotted in Figure 2.4 representing the instantaneously available power P versus the stored energy E.

Among the available storage sources, the pumped-storage powerplants present a large storage capacity, an efficiency between 70% and 80% and low cost; the installation requiring nevertheless specifically adapted geographical sites. This technology takes also

Table 2.1: Comparison of storage technologies [75].

Technology	Advantages	Drawbacks	Power source	Energy source
Hydraulic pumped-storage	Large storage capacity Low costs	Specific locations Construction delay		Pertinent solution
Compressed air	Large storage capacity Low costs	Specific locations Need natural gas		Pertinent solution
Redox flow battery	Large storage capacity	Small energy density	Conceivable solution	Pertinent solution
NaS battery	Large energy and power density	High cost Operating security	Pertinent solution	Pertinent solution
Metal-Air battery	Large energy density	Hard recharge	-	Pertinent solution
Li-ion battery	Large energy and power density Good efficiency	High cost Special recharge cycle	Pertinent solution	Non-mature solution
Ni-Cd battery	Large energy and power density Efficiency		Pertinent solution	Conceivable solution
Pb-Acid battery	Low cost	Life span	Pertinent solution	Pertinent solution
Flywheel	High power	Small energy density	Pertinent solution	Pertinent solution
Magnetic storage SMES	High power	Small energy density High cost	Pertinent solution	
Super capacitance	Life span Good efficiency	Small energy density	Pertinent solution	Non-mature solution

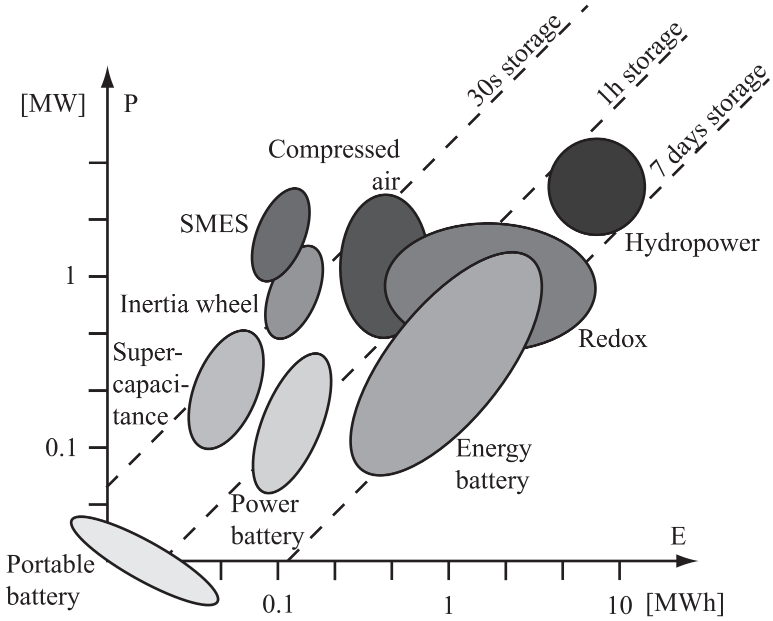

Figure 2.4: Utilization range of storage sources [75]: instantaneously available power P versus the stored energy E.

advantage of over 100 years old experience. Moreover, pumped-storage powerplants inject money into the economy, since electricity tends to be generated when its price is high and the water, to be pumped when the price is low.

In 2009, more than 127 GW of pumped-storage power plants were operating throughout the world [66]. A growth rate of 60% over the next four years was expected.

Thanks to its geographical location and its topology, Switzerland plays a key role in the European electrical network regulation. In Table 2.2, the exports and imports of electrical energy in 2010 and during winter 2009/2010 are given [62]. The balance between exports and imports is close to zero which illustrates the important position of Switzerland in the European electrical energy business. The revenues from electricity exports are 5064 millions Swiss francs (7.65 cts./kWh) and the expense for electricity imports are 3736 millions Swiss francs (5.60 cts./kWh).

Table 2.2: Electrical energy exports and imports of Switzerland in 2010 and 2009 [62].

Year 2010	[x 10^9 kWh]
Exports	66.3
Imports	66.8
Imports/exports ratio	1.01
Winter 2009 / 2010	[x 10^9 kWh]
Exports	27.3
Imports	32.4
Imports/exports ratio	1.19

The daily electricity production in Switzerland is illustrated in Figure 2.5 for four dates in 2010, whereas the daily electrical consumption is shown in Figure 2.6. The production is classified by types of power plants. Because of technological requirements, all powerplants except hydropower plants are generating a constant power all day long. Only hydropower may ensure the balance between production and consumption. In summer, when the electrical consumption is low, the extra energy is used to feed the storage basin; an important part being also exported at an economically profitable price.

After the Fukushima Daiichi nuclear power plant accident in Japan due to the earthquake and tsunami in March 2011, Switzerland decided, less than two months later, to abandon plans to build new nuclear reactors; the operation of the last one being suspended in 2034. This decision will lead to a turnaround of the electrical supply strategy by switching from a centralized to a decentralized and irregular electrical production [63]. The pumped-storage power plants precisely meet the requirements to ensure a safe and high quality supply of electricity. At least 3 huge pumped-storage plants are already planned to be commissioned up to 2015 increasing the hydropower capacity by 2 GW, [5] and [6].

2.3 Pump-turbine technology

The first pumped storage plants started commercial operation in Europe at the end of the 1920's [64]. These hydraulic stations consisted of units with a separate centrifugal pump and a separate turbine both coupled to their motor-generator. The pump of these tandem pump-turbines may be single- or double-suction, single- or multi-stage designs. The turbines are preferably Francis-type, but in case of very high head sites, Pelton

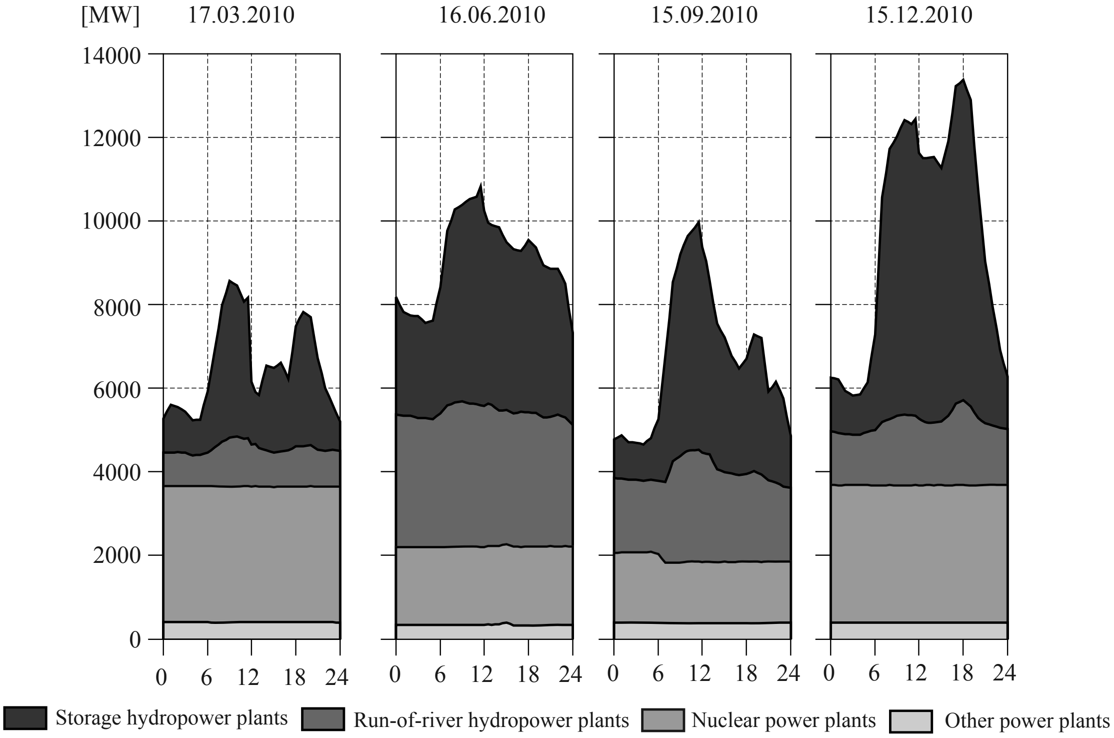

Figure 2.5: Daily electrical production of four days in 2010 in Switzerland [61].

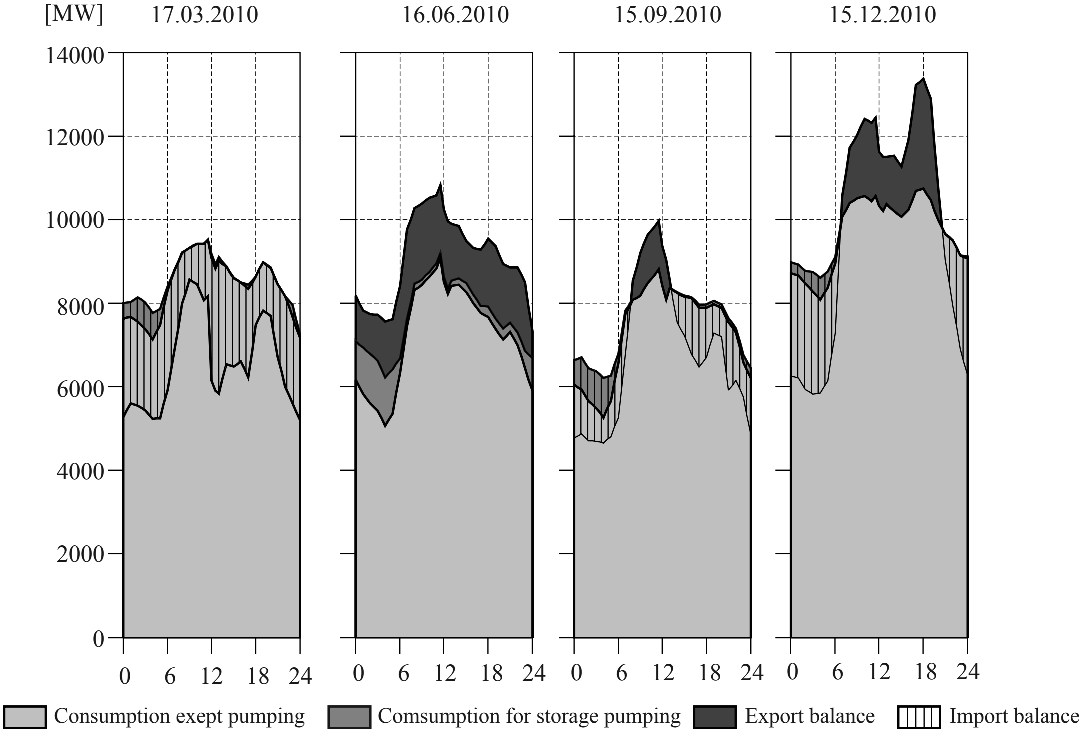

Figure 2.6: Daily electrical consumption of four days in 2010 in Switzerland [61].

turbines may be used [53]. Both the pump and the turbine are designed to be operated at the most favorable operating conditions, making them still competitive [6].

Owing to the high costs of separate machines and the improved pump design, reversible pump-turbines are often used. One impeller/runner, rotating in one direction for pumping and in the other direction for generating electricity, is coupled to the motor-generator. The machine may be Francis (radial), Deriaz (diagonal) or bulb (axial) type, whether it is used for application in high, medium or low head ranges, respectively [53]. Reversible pump-turbines may be single- or multi-stage designs [70].

However, due to the advance in research leading to a better design in pump mode and because of the presence of adjustable guide vanes enabling more flexible operating conditions, single-stage reversible Francis-type pump-turbines are nowadays mainly chosen [54]; the power regulation being, therefore, more efficient. Moreover, the pumped-storage plants currently tend to be located where a very high head is available in order to save the capital costs per unit of stored energy and to reduce the size of the reservoirs and the powerhouse [78]. Moreover, a pumped-storage plant does not produce energy, but rather “transfers the energy from times of low demand to peak demand periods”[60]. High rate of utilization induces frequent start and stop which reduces the reliability of the utilities in comparison with conventional generating hydraulic machines.

In addition, pumped-storage is currently a dominant ancillary services provider. More than a simple peak power supplier, a pumped-storage plant offers indeed services “to improve system reliability, such as frequency control, voltage regulation, and reserve operation”[79]. In the 21st century, to keep the pumped-storage competitive against other generating sources, focus must be put, in particular, on quicker mode changes, the reduction of capital costs, the improvement of part load efficiency and the extensive use of the adjustable speed technology.

2.3.1 Pump-turbine components

The Figure 2.7 shows the main components of a reversible Francis-type pump-turbine. In turbine mode, the spiral casing distributes the water flow on the whole circumference of the impeller. The stay vanes are used for structural stiffening as well as flow distribution. The guide vanes regulate the flow discharge. The impeller converts the hydraulic power into mechanical power. The draft tube recovers the residual kinetic energy at the turbine outlet. In pumping mode, the water flow reaches the impeller after passing through the draft tube. The stay- and guide vanes as well as the spiral casing play the role of the pump diffuser. This time, the impeller converts mechanical power into hydraulic power.

2.3.2 Energy balance

Technically, a reversible Francis-type pump-turbine is a reaction hydraulic machine [18] which is coupled to an electrical machine connected to the grid. It has the ability to convert hydraulic power into mechanical power or the inverse, depending on whether it is used in turbine mode to generate electrical power, or in pumping mode to store surplus electrical power. The global installation of a typical pumped-storage hydropower plant is shown in Figure 2.8. The pump-turbine is placed between an upper and a lower reservoir.

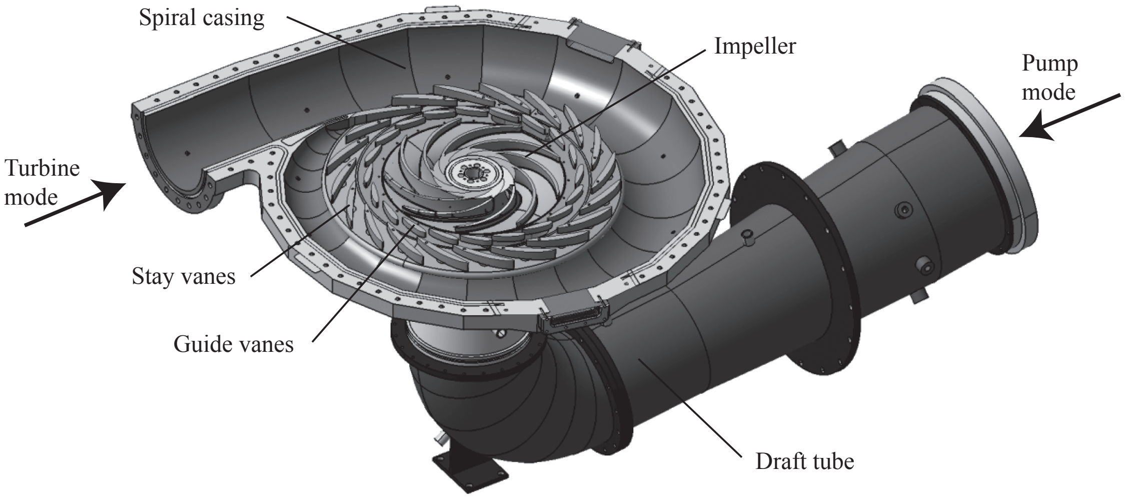

Figure 2.7: Pump-turbine main components.

The specific energy E of the pump-turbine is defined as:

$$\begin{aligned} E &= gH_I - gH_{\bar{I}} \\ &= gH_A - gH_{\bar{A}} \pm \left(gH_{r_{\bar{I}\div\bar{A}}} - gH_{r_{A\div I}} \right) \ , \end{aligned} \tag{2.1}$$

where the $-$ sign is used in generating mode and the $+$ sign in pumping mode; gH_X being the specific energy available at the fluid section X and $gH_{r_{X\div Y}}$, the specific energy losses from the fluid section X to Y.

The hydraulic power P_h corresponds to the power available between the sections I and $\bar{I}$ and is obtained as follows:

$$P_h = \rho Q E \ , \tag{2.2}$$

ρ and Q being the water density and flow discharge at the pump-turbine section I, respectively.

The Figure 2.9 shows the mechanical power balance in the impeller in both generating and pumping modes. In the same way as the hydraulic power, the transformed power P_t is defined as:

$$P_t = \rho Q_t E_t \ , \tag{2.3}$$

where Q_t and E_t are the transferred discharge and specific energy, respectively. The difference between P_t and P_h is the volumetric and friction losses between the sections I and 1 and the respective low pressure sections $\bar{I}$ and $\bar{1}$.

By definition, $Q > 0$ in generating mode and $Q < 0$ in pumping mode. According to eq. 2.3, the power sign follows the same sign convention. The power P supplied to or by the electrical machine, depending on whether one is generating or pumping, is given by:

$$P = \eta \cdot P_t = (\eta_e \cdot \eta_h \cdot \eta_{rm} \cdot \eta_m) \cdot P_t \ , \tag{2.4}$$

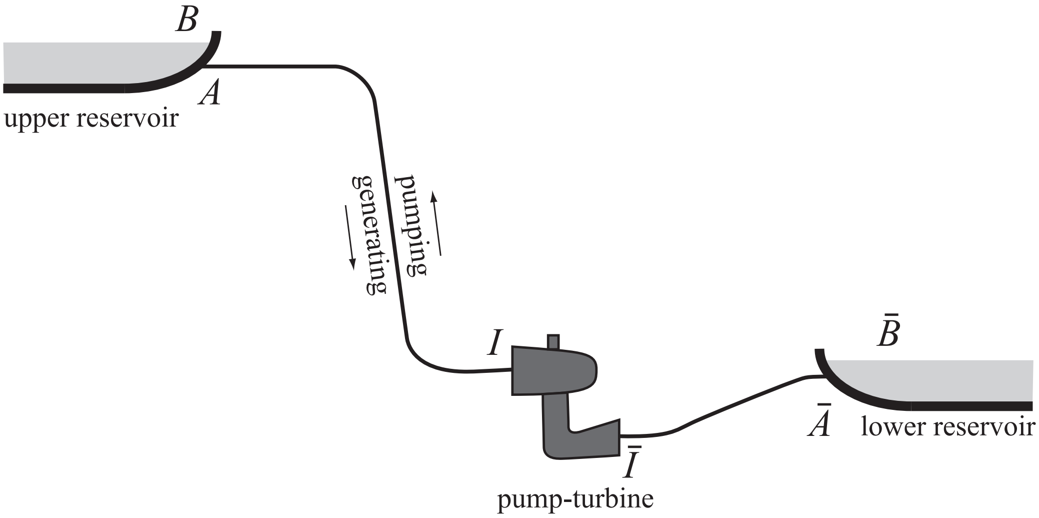

Figure 2.8: Global installation of a typical pumped-storage hydropower plant.

η being the total efficiency, η_e, the energetic efficiency, η_h, the volumetric efficiency, η_{rm}, the mechanical efficiency in the impeller expressing the losses by disc friction and η_m, the mechanical efficiency in the shaft expressing the power losses in the bearings.

Finally, the velocity triangles at the low and high pressure sides of the machine in generating mode, on the external stream line e, are drawn in Figure 2.10. The Euler equation expresses the transferred specific energy E_t as a function of the absolute flow velocity $\boldsymbol{C}$ and the peripheral impeller velocity $\boldsymbol{U}$ at the low and high pressure sides of the machine, as follows:

$$E_t = \boldsymbol{C}_{1e} \cdot \boldsymbol{U}_{1e} - \boldsymbol{C}_{\bar{1}e} \cdot \boldsymbol{U}_{\bar{1}e} \tag{2.5}$$

2.4 Rotor-Stator Interaction phenomenon

A pump-turbine operating under steady-state conditions is nevertheless subject to unsteady phenomena resulting from the interaction of the rotating with the stationary parts of the machine, the so-called Rotor-Stator Interaction, RSI. Although studies are dedicated to the prediction of this strong excitation, incidents may still occur. “The highest vibration levels in large pump turbines are, in general, originated in the RSI”[69]. For instance, Fisher et al. [33] and Coutu et al. [24] report relevant case studies of cracks appearing in hydraulic runners. The guide vanes may also be damaged. The complications due to the machine shutdown and guide vane replacements are highlighted by Ducheney [31], Henscheid [40] and Finnegan et al. [32].

In the present study, the RSI is the source of the guide vane vibrations. By addressing the physical principles of this phenomenon, one is interested to determine the excitation function of the mechanical system constituted by the guide vane cascade.

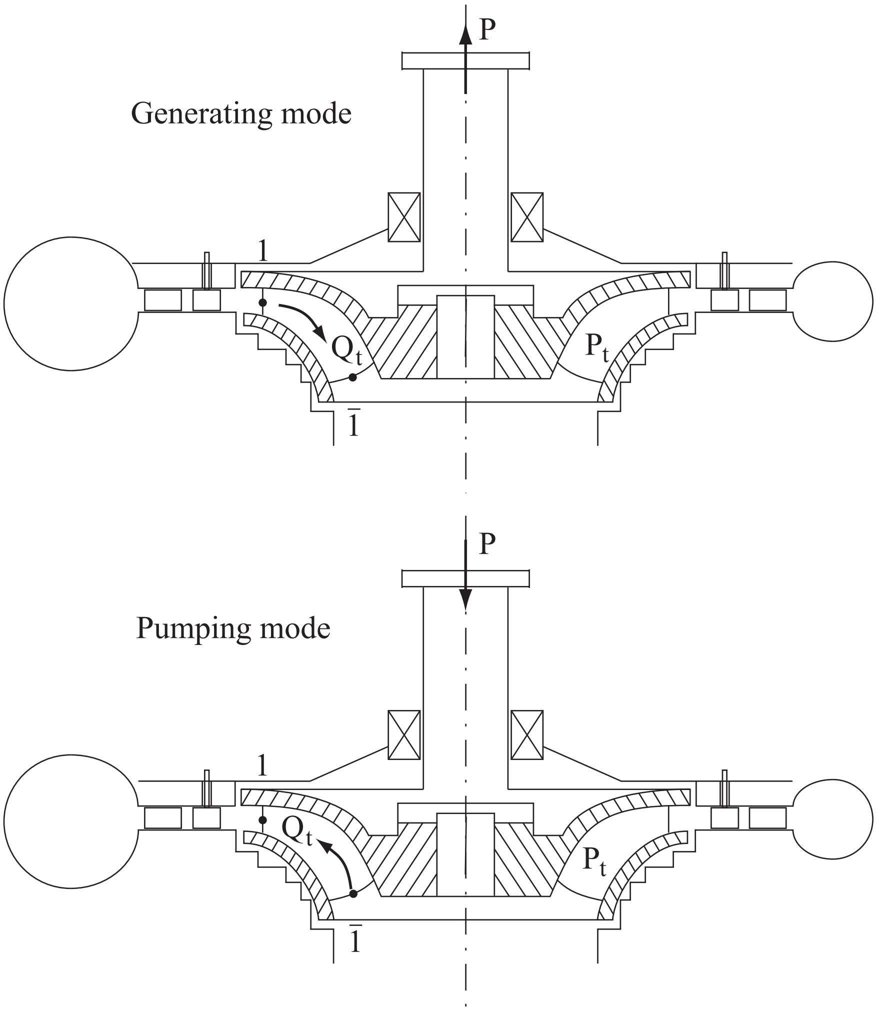

Figure 2.9: Mechanical power balance in the impeller in both generating and pumping modes.

2.4.1 Physical principles

Basically, two blade rows, one moving with respect to the other, are mutually interacting. The resulting phenomena may arise from different sources which are discussed below.

First, the *potential flow interaction* causes fluid pressure and flow velocity fluctuations both downstream and upstream from the rotor-stator clearance. In the following lines, we restrict our approach to the turbine mode, the corresponding approach in radial pump and axial compressor being discussed by Arndt et al. [2] and Kaji and Okazaki [46]. On the one hand, in a guide vane channel, the flow is perturbed by the impeller blade which actually obstructs the channel outlet periodically. Therefore, the associated flow velocity and fluid pressure fluctuations mainly contain the blade passing frequency $f = z_b n$, where z_b refers to the blade number and n to the impeller rotation frequency. Harmonics $f = m' z_b n$, where m' is an integer, are nonetheless also present because of the imperfectly sinusoidal fluctuations. Ruchonnet et al. [73] take into account this potential flow interaction in the hydroacoustic model of a pump-turbine. On the other hand, the flow downstream from

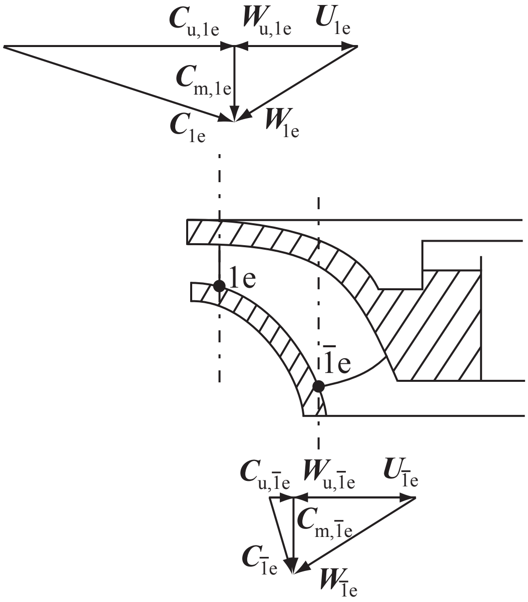

Figure 2.10: Velocity triangle at the low and high pressure sides of the machine.

the guide vanes is spatially perturbed due to the periodical flow velocity defects in the potential wake of the guide vanes [47]. The potential effects depend strongly on rotor-stator gap thickness. In axial gas turbines, Dring et al. [29] state that “the potential flow over a row of airfoils can cause unsteadiness in both the upstream and downstream rows if the axial gap between them is less than approximately the airfoil chord”.

Second, the fluid viscosity reinforces the flow velocity defect in the guide vane wake [48]. The resulting *potential and viscous wakes interaction* causes the relative flow velocity $\boldsymbol{W}_1$ at the impeller blade leading edge to fluctuate in time due to the periodic spatial variations of the absolute flow velocity $\boldsymbol{C}_1$, the impeller peripheral velocity $\boldsymbol{U}_1$ staying constant, see Figure 2.11. The frequency at which $\boldsymbol{W}_1$ fluctuates is $f = mz_o n$, m being an integer and z_o, the guide vanes number. The shape of the guide vanes wake, the opening angle and the rotor-stator gap thickness are responsible for the number of harmonics m present in the fluctuations. The fluctuations of $\boldsymbol{W}_1$, both in terms of magnitude and direction, induce oscillations of the pressure field around the impeller blades. As a result, the impeller blades are undergoing a fluctuating lift force. It is rather difficult to distinguish between potential wake and viscous wake effects, but Kemp and Sears [48] note that, “the unsteady forces arising from passage through viscous wakes are of about the same size as those due to [potential wakes]”. Arndt et al. [3] adds that, if the rotor-stator clearance is small, both wake and potential mechanisms initiate RSI.

Third, the possible vortex shedding, whose physics and generation process on an isolated hydrofoil is well described by Ausoni [4] and Zobeiri [91], at the guide vane trailing edge may play a role in the RSI as well. If flow conditions and guide vane geometry are favorable to vortex shedding, the impeller inflow velocity $\boldsymbol{W}_1$ may be influenced.

Finally, vibrating blades may have an effect on RSI. Collard and Cizmas [21] numer-

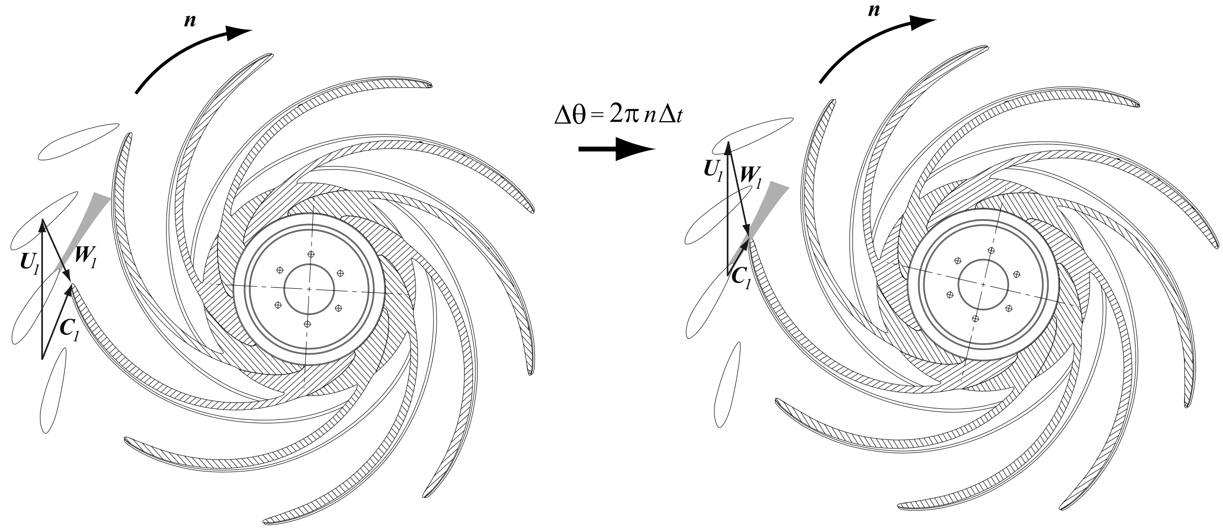

Figure 2.11: Influence of guide vane wake flow defect on the impeller inlet velocity triangle.

ically study the effects of vibrating rotor blades in an axial gas turbine. The efficiency is found to decrease by approximately 1.8% compared to the turbine with rigid blades. Giesing [35] proposes a general method for determining the unsteady incompressible flow around one or more vibrating bodies placed in small amplitude gust fields. Kahl [45] studied the effects of mistuning and coupling in a turbomachinery bladings. Beretta [11] proves that the effect of rotor blade vibrations may be linearly superposed to rotor blades gust response in an axial gas turbomachine. Rottmeier [72] highlight the dependence of the gust phase on the pressure field around rotor blades.

The physics resulting from all these root phenomena is very complex. Research is incidentally devoted to simplified numerical methods to take into account the RSI [20]. Moreover, these root phenomena produce other effects, such as guide vane vibrations [58], impeller vibrations [23], shaft vibrations [38] and spinning pressure modes in the stator. In pump-turbines, Blanc-Coquand and Lavigne [13] note that the fluctuating pressure field due to the RSI is much more complex in the rotor-stator clearance than away from this zone. Many rotating pressure modes are actually present close to the rotor-stator clearance, but only the most energetic pressure modes remain in the spiral casing.

To the author's knowledge, in the case of radial hydraulic machines, the RSI physics has never been analytically approached. Tanaka [77], Franke et al. [34] and Dubas [30] address the problem with elementary fluid flow principles and construct the RSI pressure mode shapes based on requirements to satisfy consistency and the fluid physics. The pressure consists of a modulation of the stator and rotor pressure fields which are firstly decomposed in Fourier series. This approach makes apparent the RSI spinning modes, but apparently fails to analytically predict the predominance of one spinning mode on another; the predominance being only qualitatively appreciated based on the fact that a mode with few diametrical nodes is more energetic. Nevertheless, numerous RSI studies are based on this simplified approach, [92] and [33]. In addition to the complexity of the root phenomena, the lack of data, [16] and [25], may be the reason for the absence of analytical approach to explain RSI physics. In the following lines, this approach to the

RSI is given.

The stationary $p_s\left(\theta\right)$ and rotating $p_r\left(\theta_r\right)$ pressure fields are decomposed in Fourier series as follows:

$$p_s\left(\theta\right) = \sum_{m=0}^{\infty} p_{s,m} cos\left(mz_o\theta + \phi_m\right) \tag{2.6}$$

$$p_r\left(\theta_r\right) = \sum_{m'=0}^{\infty} p_{r,m'} cos\left(m'z_b\theta_r + \phi_{m'}\right) \tag{2.7}$$

m and m' being integers, θ, the angular position in the stator, θ_r, the angular position in the rotor, $p_{s,m}$, the amplitude of the m^{th} component of the stationary pressure Fourier series and $p_{r,m'}$, the amplitude of the $m^{'th}$ component of the rotating pressure Fourier series.

The resulting pressure field $p\left(\theta\right)$ may be seen as a modulation which may be expressed as the product of the two pressure fields:

$$\begin{aligned} p\left(\theta\right) &= p_s\left(\theta\right) \cdot p_r\left(\theta_r\right) \\ &= \left(\sum_{m=0}^{\infty} p_{s,m} cos\left(mz_o\theta + \phi_m\right)\right) \cdot \left(\sum_{m'=0}^{\infty} p_{r,m'} cos\left(m'z_b\theta_r + \phi_{m'}\right)\right) \\ &= \sum_{m=0}^{\infty}\sum_{m'=0}^{\infty} p_{s,m} \cdot p_{r,m'} \cdot cos\left(mz_o\theta + \phi_m\right) \cdot cos\left(m'z_b\theta_r + \phi_{m'}\right) \end{aligned} \tag{2.8}$$

Knowing that the angular position in the rotor θ_r may be expressed as $\theta_r = \theta + n \cdot t$, n being the impeller frequency, and by using a well-known trigonometric identity, the total pressure field may be written as follows:

$$\begin{aligned} p\left(\theta, t\right) = \sum_{m=0}^{\infty}\sum_{m'=0}^{\infty} \frac{p_{s,m} \cdot p_{r,m'}}{2} &\cdot \left(cos\left(m'z_bnt - \left(m'z_b + mz_o\right) \cdot \theta + \phi_m + \phi_{m'}\right)\right. \\ &+ \left. cos\left(m'z_bnt - \left(m'z_b - mz_o\right) \cdot \theta - \phi_m + \phi_{m'}\right)\right) \end{aligned} \tag{2.9}$$

Finally, by introducing the numbers of diametrical nodes $k_+ = m'z_b + mz_o$ and $k_- = m'z_b - mz_o$, the total pressure field, consisting of the excitation function of the guide vane cascade mechanical system, is given as:

$$p\left(\theta, t\right) = \sum_{m=0}^{\infty}\sum_{m'=0}^{\infty} \frac{p_{s,m} \cdot p_{r,m'}}{2} \cdot \left(cos\left(m'z_bnt - k_+ \cdot \theta + \phi_m + \phi_{m'}\right)\right. \tag{2.10}$$

$$+ \left. cos\left(m'z_bnt - k_- \cdot \theta - \phi_m + \phi_{m'}\right)\right) \tag{2.11}$$

The combination of given integers m and m' makes apparent two rotating pressure modes featuring k_+ and k_- diametrical nodes. As mentioned above, this approach fails to predict which of these two modes predominates and, therefore, does not agree with the experiments in terms of relative amplitude. Nevertheless, it successfully predicts the number of diametrical nodes that would feature a pressure mode oscillating at a given frequency.

Another interesting approach to RSI has been developed by Blake [12], which succeeds in predicting the mode that predominates for a combination of given integers m and m'. Since it is based on the acoustic fluid theory, some assumptions are not in accordance with the potential flow theory. Even though the results may be controversial, the author has adapted the theory to the case of a radial hydraulic pump-turbine. The approach may be found in Appendix E.

Chapter 3

Fluid-structure coupling in the guide vane cascade

3.1 General definitions

Whenever a solid body is vibrating in a flow, one may observe many physical effects due to the coupling between the structural and the fluid motions. Naudascher [57] proposes an interesting general approach to flow-induced vibrations. He defines three basic elements:

- *Body oscillators*: either a rigid structure or structural part, that is elastically supported so that it can perform linear or angular movements, or a structure or structural part that is elastic in itself so that it can perform flexural movements.
- *Fluid oscillators*: a passive mass of fluid that can undergo oscillations usually governed either by fluid compressibility or by gravity.
- *Sources of excitation*: one may distinguish three types of sources:
    - *Extraneously induced excitation*: caused by fluctuations in flow velocities or pressures that are independent of any flow instability originating from the structure considered and independent of structural movements.
    - *Instability-induced excitation*: brought by a flow instability.
    - *Movement-induced excitation*: due to fluctuating forces that arise from movements of the vibrating body or fluid oscillator, the vibrations of the latter being thus self-excited.

According to this approach, in the case of the guide vane cascade, the z_o guide vanes consist of z_o rigid body oscillators. The flow compressibility and the gravity effect are neglected, so that there is no fluid oscillator. The guide vanes are extraneously excited by the Rotor-Stator Interaction. Moreover, the vibrations of the guide vanes consist of a movement-induced excitation.

3.2 Newton's law applied to the guide vanes

The Newton's law governing the bending displacement y_i of the guide vane O_i is expressed as follows [36]:

$$I^S \ddot{y}_i\left(t\right) + C^S \dot{y}_i\left(t\right) + K^S y_i\left(t\right) = F_i\left(t\right) \tag{3.1}$$

where I^S denotes the bending structural inertia, C^S the bending structural damping, K^S the bending structural stiffness and F_i the external force acting on the guide vane O_i.

The torsion angle α_i of the guide vane O_i is governed by the expression:

$$J^S \ddot{\alpha}_i\left(t\right) + D^S \dot{\alpha}_i\left(t\right) + L^S \alpha_i\left(t\right) = T_i\left(t\right) \tag{3.2}$$

where J^S denotes the torsion structural inertia, D^S the torsion structural damping, L^S the torsion structural stiffness and T_i the external torque acting on the guide vane O_i.

3.3 Hydrodynamic loading

The external bending force F_i acting on the guide vane O_i may be written as the sum of a mean hydrodynamic loading $\bar{F}_i$, a fluctuating contribution F_i' linearly dependent of the fluctuating angle of incidence α_i, for small displacement, a fluctuating contribution F_i^{RSI} from the Rotor-Stator Interaction and fluctuating contributions $F_{i,j}^f$ from the vibrations of the guide vane O_j, with $1 \leq j \leq z_o$:

$$F_i\left(t\right) = \bar{F}_i + F_i'\left(t\right) + F_i^{RSI}\left(t\right) + \sum_j^{z_o} F_{i,j}^f\left(t\right) \tag{3.3}$$

The fluctuating force contribution F_i' linearly dependent of the angle of incidence is zero when the flow velocity is zero.

The lift force F_i results from the pressure field and from wall shear stresses on the guide vane O_i surface as follows [8]:

$$F_i\left(t\right) = \int_{A_i} -\left(p(t)\left[\mathbf{I}\right] \cdot \mathbf{n}\right) \cdot \mathbf{e}_{i,2} dA_i + \int_{A_i} \left(\tau(t) \cdot \mathbf{n}\right) \cdot \mathbf{e}_{i,2} dA_i\ , \tag{3.4}$$

$p\left(t\right) = p^a\left(t\right) - p^{atm}$ being the gauge pressure obtained by subtracting the atmospheric pressure p^{atm} from the absolute pressure p^a, A_i the guide vane O_i surface, τ the shear stress tensor, $[\mathbf{I}]$ the identity matrix, $\mathbf{n}$ the vector normal to the guide vane surface and $\mathbf{e}_{i,2}$ the vector perpendicular to the chord profile, see Figure 3.1.

For high Reynolds number, the viscosity effects may be neglected. Moreover, by ignoring any turbulence effect that might occur, one obtains:

$$F_i\left(t\right) \approx \int_{A_i} -\left(p(t)\left[\mathbf{I}\right] \cdot \mathbf{n}\right) \cdot \mathbf{e}_{i,2} dA_i \tag{3.5}$$

By discretizing the guide vane surface in n area segments $A_{i,k}$

$$F_i\left(t\right) \approx \sum_{k=1}^{n} a_{i,k} \cdot p\left(\mathbf{x}_{i,k}, t\right) \tag{3.6}$$

where $a_{i,k} = \mathbf{n_{i,k}} \cdot \mathbf{e}_{i,2} \cdot A_{i,k}$.

Assuming a potential flow, the unsteady Bernoulli equation [74] between a position $\mathbf{x} = \mathbf{x}_{i,k}$ in the stator and the spiral casing inlet I, see Figure 2.8, where a steady flow is assumed, is written as:

$$p^a\left(\mathbf{x}_{i,k}, t\right) + \rho g Z\left(\mathbf{x}_{i,k}\right) + \rho \frac{\partial \Phi\left(\mathbf{x}_{i,k}, t\right)}{\partial t} + \frac{1}{2}\rho |\nabla \Phi\left(\mathbf{x}_{i,k}, t\right)|^2 = \rho \cdot gH_I + Cste \tag{3.7}$$

$p^a\left(\mathbf{x}_{i,k}, t\right)$ being the absolute pressure, $Z\left(\mathbf{x}_{i,k}\right)$, the elevation at the position $\mathbf{x}_{i,k}$, gH_I, the specific energy at the section I and $\Phi\left(\mathbf{x}_{i,k}, t\right)$, the velocity potential.

Taking into account the eqs. 2.1 and 3.7 and neglecting the losses in the spiral casing and those from the low pressure side of the impeller to the downstream reservoir, one may define the dimensionless pressure factor c_p as follows:

$$\begin{aligned} c_p &= \frac{p\left(\mathbf{x}_{i,k}, t\right)}{\rho \cdot E} \\ &= \frac{p^a\left(\mathbf{x}_{i,k}, t\right) - p^{atm}}{\rho \cdot E} \\ &= 1 - \frac{1}{E}\left(g\left(Z\left(\mathbf{x}_{i,k}\right) - Z_{\bar{B}}\right) + \frac{\partial \Phi\left(\mathbf{x}_{i,k}, t\right)}{\partial t} + \frac{1}{2}|\nabla \Phi\left(\mathbf{x}_{i,k}, t\right)|^2\right) \end{aligned} \tag{3.8}$$

$p\left(\mathbf{x}_{i,k}, t\right)$ being the gauge pressure.

Decomposing the pressure in a mean and fluctuating parts $p = \bar{p} + p'$ and the flow potential $\Phi = \bar{\Phi} + \Phi'$ and assuming small perturbations, the pressure factor may be expressed in a linearized form:

$$\begin{aligned} c_p &= 1 - \frac{1}{E}[g\left(Z\left(\mathbf{x}_{i,k}\right) - Z_{\bar{B}}\right) + \frac{\partial \Phi'\left(\mathbf{x}_{i,k}, t\right)}{\partial t} + \frac{1}{2}|\nabla \bar{\Phi}\left(\mathbf{x}_{i,k}\right)|^2 \\ &+ \nabla \bar{\Phi}\left(\mathbf{x}_{i,k}, t\right) \cdot \nabla \Phi'\left(\mathbf{x}_{i,k}, t\right)] \end{aligned} \tag{3.9}$$

The superposition principle applicable to the theory of potential flow allows us to write:

$$\Phi' = \Phi^{RSI} + \Phi^f \tag{3.10}$$

where Φ^{RSI} is the flow velocity potential perturbed field due to RSI and Φ^f, the perturbed field due to the vibrations of the guide vanes.

The pressure factor for the case with vibrating guide vanes placed in the cascade may be written as:

$$\begin{aligned} c_p &= \bar{c}_p + c_p^{RSI} + c_p^f \\ &= 1 - \frac{1}{E}[g\left(Z\left(\mathbf{x}_{i,k}\right) - Z_{\bar{B}}\right) + \frac{1}{2}|\nabla \bar{\Phi}\left(\mathbf{x}_{i,k}\right)|^2 \\ &+ \frac{\partial \Phi^{RSI}\left(\mathbf{x}_{i,k}, t\right)}{\partial t} + \nabla \bar{\Phi}\left(\mathbf{x}_{i,k}\right) \cdot \nabla \Phi^{RSI}\left(\mathbf{x}_{i,k}, t\right) \\ &+ \frac{\partial \Phi^f\left(\mathbf{x}_{i,k}, t\right)}{\partial t} + \nabla \bar{\Phi}\left(\mathbf{x}_{i,k}\right) \cdot \nabla \Phi^f\left(\mathbf{x}_{i,k}, t\right)] \end{aligned} \tag{3.11}$$

For the case without moving guide vanes, eq. 3.11 yields:

$$\begin{aligned}
\bar{c_p} + c_p^{RSI} &= \frac{\bar{p} + p^{RSI}\left(\mathbf{x}_{i,k}, t\right)}{\rho \cdot E} \\
&= 1 - \frac{1}{E}[g\left(Z\left(\mathbf{x}_{i,k}\right) - Z_{\bar{B}}\right) + \frac{1}{2}|\nabla\bar{\Phi}\left(\mathbf{x}_{i,k}\right)|^2 \\
&+ \frac{\partial\Phi^{RSI}\left(\mathbf{x}_{i,k}, t\right)}{\partial t} + \nabla\bar{\Phi}\left(\mathbf{x}_{i,k}\right) \cdot \nabla\Phi^{RSI}\left(\mathbf{x}_{i,k}, t\right)]
\end{aligned} \tag{3.12}$$

Replacing eq. 3.12 in eq. 3.11, one obtains:

$$\begin{aligned}
c_p &= \bar{c_p} + c_p^{RSI} - \frac{1}{E}\left(\frac{\partial\Phi^f\left(\mathbf{x}_{i,k}, t\right)}{\partial t} + \nabla\bar{\Phi}\left(\mathbf{x}_{i,k}\right) \cdot \nabla\Phi^f\left(\mathbf{x}_{i,k}, t\right)\right) \\
&= \bar{c_p} + c_p^{RSI} + c_p^f
\end{aligned} \tag{3.13}$$

The mass conservation principle for potential flow is expressed as:

$$\triangle\Phi = 0 \text{ , in } V \tag{3.14}$$

where V is the fluid control volume.

The superposition principle $\Phi = \bar{\Phi} + \Phi^{RSI} + \Phi^f$ and the linearity of the Laplace operator yields:

$$\triangle\Phi^f = 0 \tag{3.15}$$

For small displacements, this potential has to satisfy the following Neumann condition on the boundary made by the guide vane surface A_j, see Figure 3.1:

$$\frac{\partial\Phi^f\left(\mathbf{x}_{j,k}, t\right)}{\partial n} = \dot{y}_j\left(t\right)\mathbf{e}_{j,2} \cdot \mathbf{n}_{j,k} + \left(\dot{\alpha}_j\left(t\right)\mathbf{e}_{j,3} \times \mathbf{x}_{j,k}\right) \cdot \mathbf{n}_{j,k} \text{ , for } \mathbf{x}_{j,k} \in A_j \tag{3.16}$$

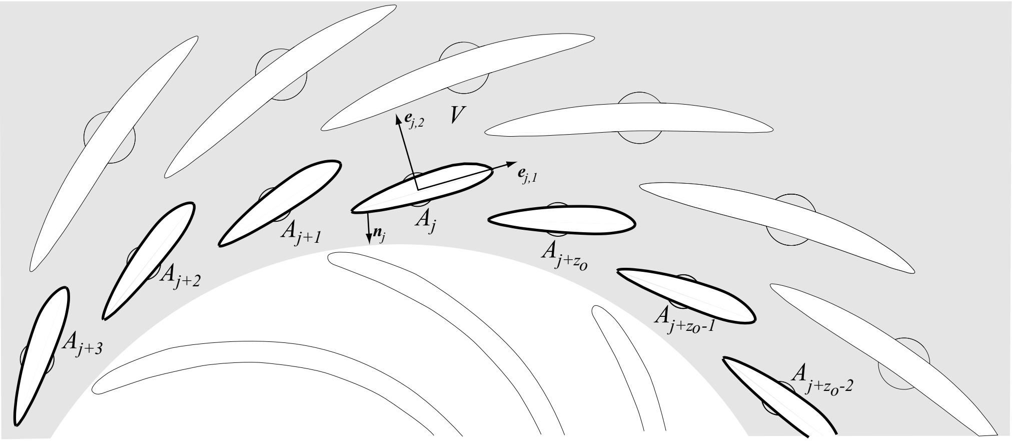

Figure 3.1: Fluid domain V and moving boundaries A_j.

As shown in eq. C.16 in Appendix C, the potential at any position $\mathbf{x}_{i,k}$ in the fluid volume V may be expressed as a function of the boundary condition:

$$\begin{aligned}
\Phi^f\left(\mathbf{x}_{i,k},t\right) &= \sum_j^{z_o} \Lambda_j\left(\mathbf{x}_{i,k}\right)\frac{\partial \Phi^f\left(\mathbf{x}_{j,k},t\right)}{\partial n} \\
&= \sum_j^{z_o} \Lambda_j^y\left(\mathbf{x}_{i,k}\right)\cdot \dot{y}_j\left(t\right) + \sum_j^{z_o} \Lambda_j^\alpha\left(\mathbf{x}_{i,k}\right)\cdot \dot{\alpha}_j\left(t\right) \qquad (3.17)
\end{aligned}$$

Replacing eq. 3.17 in eq. 3.13, one obtains:

$$\begin{aligned}
c_p\left(\mathbf{x}_{i,k},t\right) &= \bar{c}_p + c_p^{RSI} \\
&- \frac{1}{E}\sum_j^{z_o}(\Lambda_j^y\left(\mathbf{x}_{i,k}\right)\cdot \ddot{y}_j\left(t\right) + \Lambda_j^\alpha\left(\mathbf{x}_{i,k}\right)\cdot \ddot{\alpha}_j\left(t\right) \\
&+ \nabla\bar{\Phi}\left(\mathbf{x}_{i,k},t\right)\cdot\left(\nabla\Lambda_j^y\left(\mathbf{x}_{i,k}\right)\cdot \dot{y}_j\left(t\right) + \nabla\Lambda_j^\alpha\left(\mathbf{x}_{i,k}\right)\cdot \dot{\alpha}_j\left(t\right)\right)) \qquad (3.18)
\end{aligned}$$

From eqs. 3.3, 3.6 and 3.18, the force acting on the guide vane O_i may be expressed as:

$$\begin{aligned}
F_i\left(t\right) &= \bar{F}_i + F_i^{RSI}\left(t\right) \\
&- K_i^{f,\alpha}\cdot\alpha_i\left(t\right) \\
&- \sum_j^{z_o}\left(I_{i,j}^f\cdot\ddot{y}_j\left(t\right) + I_{i,j}^{f,\alpha}\cdot\ddot{\alpha}_j\left(t\right)\right) \\
&- \sum_j^{z_o}\left(C_{i,j}^f\cdot\dot{y}_j\left(t\right) + C_{i,j}^{f,\alpha}\cdot\dot{\alpha}_j\left(t\right)\right) \qquad (3.19)
\end{aligned}$$

$K_i^{f,\alpha}$ being the fluid torsion stiffness acting on the guide vane O_i; $I_{i,j}^{f,\alpha}$, the added mass on the guide vane O_i due to the torsion motion of the guide vane O_j; $I_{i,j}^f$, the added mass on the guide vane O_i due to the bending motion of the guide vane O_j; $C_{i,j}^{f,\alpha}$, the hydrodynamic damping constant on the guide vane O_i due to the torsion motion of the guide vane O_j and $C_{i,j}^f$, the hydrodynamic damping constant on the guide vane O_i due to the bending motion of the guide vane O_j.

For the torque, the same procedure may be followed and the hydrodynamic torque is expressed as:

$$\begin{aligned}
T_i\left(t\right) &= \bar{T}_i + T^{RSI}\left(t\right) \\
&- L_i^{f,\alpha}\cdot\alpha_i\left(t\right) \\
&- \sum_j^{z_o}\left(J_{i,j}^f\cdot\ddot{y}_j\left(t\right) + J_{i,j}^{f,\alpha}\cdot\ddot{\alpha}_j\left(t\right)\right) \\
&- \sum_j^{z_o}\left(D_{i,j}^f\cdot\dot{y}_j\left(t\right) + D_{i,j}^{f,\alpha}\cdot\dot{\alpha}_j\left(t\right)\right) \qquad (3.20)
\end{aligned}$$

where $L_i^{f,\alpha}$ is the fluid torsion stiffness acting on the guide vane O_i; $J_{i,j}^{f,\alpha}$ the added mass on the guide vane O_i due to the torsion motion of the guide vane O_j; $J_{i,j}^f$ the added mass on the guide vane O_i due to the bending motion of the guide vane O_j; $D^{f,\alpha}_{i,j}$ the hydrodynamic damping constant on the guide vane O_i due to the torsion motion of the guide vane O_j; $D^{f}_{i,j}$ the hydrodynamic damping constant on the guide vane O_i due to the bending motion of the guide vane O_j.

Using eqs. 3.1, 3.2, 3.19 and 3.20 together, the dynamics of the guide vane cascade is governed by the following set of equations:

$$[I]\,\ddot{\mathbf{y}} + [C]\,\dot{\mathbf{y}} + [K]\,\mathbf{y} = \mathbf{F} \tag{3.21}$$

with $\mathbf{y} = \left(y_1 \ ... \ y_{z_o} \ \alpha_1 \ ... \ \alpha_{z_o}\right)^T$, $\mathbf{F} = \left(\bar{F}_1 + F_1^{RSI} \ ... \ \bar{F}_{z_o} + F_{z_o}^{RSI} \ \bar{T}_1 + T_1^{RSI} \ ... \ \bar{T}_{z_o} + T_{z_o}^{RSI}\right)^T$, the matrix $[I]$, $[C]$ and $[K]$ being defined as follows:

$$[I] = \begin{bmatrix} I_1^S + I_{1,1}^f & I_{1,2}^f & \cdots & I_{1,z_o}^f & I_{1,1}^{f,\alpha} & I_{1,2}^{f,\alpha} & \cdots & I_{1,z_o}^{f,\alpha} \\ I_{2,1}^f & I_2^S + I_{2,2}^f & \cdots & I_{2,z_o}^f & I_{2,1}^{f,\alpha} & I_{2,2}^{f,\alpha} & \cdots & I_{2,z_o}^{f,\alpha} \\ \vdots & \vdots & \ddots & \vdots & \vdots & \vdots & \ddots & \vdots \\ I_{z_o,1}^f & I_{z_o,2}^f & \cdots & I_{z_o}^S + I_{z_o,z_o}^f & I_{z_o,1}^{f,\alpha} & I_{z_o,2}^{f,\alpha} & \cdots & I_{z_o,z_o}^{f,\alpha} \\ J_{1,1}^f & J_{1,2}^f & \cdots & J_{1,z_o}^f & J_1^S + J_{1,1}^{f,\alpha} & J_{1,2}^{f,\alpha} & \cdots & J_{1,z_o}^{f,\alpha} \\ J_{2,1}^f & J_{2,2}^f & \cdots & J_{2,z_o} & J_{2,1}^{f,\alpha} & J_2^S + J_{2,2}^{f,\alpha} & & J_{2,z_o}^{f,\alpha} \\ \vdots & \vdots & \ddots & \vdots & \vdots & \vdots & \ddots & \vdots \\ J_{z_o,1}^f & J_{z_o,2}^f & \cdots & J_{z_o,z_o}^f & J_{z_o,1}^{f,\alpha} & J_{z_o,2}^{f,\alpha} & \cdots & J_{z_o}^S + J_{z_o,z_o}^{f,\alpha} \end{bmatrix} \tag{3.22}$$

$$[C] = \begin{bmatrix} C_1^S + C_{1,1}^f & C_{1,2}^f & \cdots & C_{1,z_o}^f & C_{1,1}^{f,\alpha} & C_{1,2}^{f,\alpha} & \cdots & C_{1,z_o}^{f,\alpha} \\ C_{2,1}^f & C_2^S + C_{2,2}^f & \cdots & C_{2,z_o}^f & C_{2,1}^{f,\alpha} & C_{2,2}^{f,\alpha} & \cdots & C_{2,z_o}^{f,\alpha} \\ \vdots & \vdots & \ddots & \vdots & \vdots & \vdots & \ddots & \vdots \\ C_{z_o,1}^f & C_{z_o,2}^f & \cdots & C_{z_o}^S + C_{z_o,z_o}^f & C_{z_o,1}^{f,\alpha} & C_{z_o,2}^{f,\alpha} & \cdots & C_{z_o,z_o}^{f,\alpha} \\ D_{1,1}^f & D_{1,2}^f & \cdots & D_{1,z_o}^f & D_1^S + D_{1,1}^{f,\alpha} & D_{1,2}^{f,\alpha} & \cdots & D_{1,z_o}^{f,\alpha} \\ D_{2,1}^f & D_{2,2}^f & \cdots & D_{2,z_o}^f & D_{2,1}^{f,\alpha} & D_2^S + D_{2,2}^{f,\alpha} & & D_{2,z_o}^{f,\alpha} \\ \vdots & \vdots & \ddots & \vdots & \vdots & \vdots & \ddots & \vdots \\ D_{z_o,1}^f & D_{z_o,2}^f & \cdots & D_{z_o,z_o}^f & D_{z_o,1}^{f,\alpha} & D_{z_o,2}^{f,\alpha} & \cdots & D_{z_o}^S + D_{z_o,z_o}^{f,\alpha} \end{bmatrix} \tag{3.23}$$

$$[K] = \begin{bmatrix} K_1^S & 0 & \cdots & 0 & K_1^{f,\alpha} & \cdots & \cdots & 0 \\ 0 & K_2^S & \cdots & 0 & 0 & K_2^{f,\alpha} & \cdots & 0 \\ \vdots & \vdots & \ddots & \vdots & \vdots & \vdots & \ddots & \vdots \\ 0 & \cdots & \cdots & K_{z_o}^S & 0 & \cdots & \cdots & K_{z_o}^{f,\alpha} \\ 0 & \cdots & \cdots & 0 & L_1^S + L_1^{f,\alpha} & \cdots & \cdots & 0 \\ 0 & 0 & \cdots & 0 & 0 & L_2^S + L_2^{f,\alpha} & \cdots & 0 \\ \vdots & \vdots & \ddots & \vdots & \vdots & \vdots & \ddots & \vdots \\ 0 & \cdots & \cdots & 0 & 0 & \cdots & \cdots & L_{z_o}^S + L_{z_o}^f \end{bmatrix} \tag{3.24}$$

Münch et al. [56] found that a single hydrofoil immersed in a flow and exhibiting torsion motion may be seen as a 2^{nd} order mechanical system. The hydrodynamic loading is modeled as a combination of inertia, damping and stiffness effects. In eq. 3.21, these terms are modeled by the diagonal terms of the matrices $[I]$, $[C]$ and $[K]$.

The experimental investigation in the present document is devoted to the identification of the non-diagonal terms of the matrices. Therefore, it aims to show that the guide vane cascade behaves as a 2^{nd} order mechanical system. Moreover, as reported in [49], the non-diagonal terms depend on the vibration phase, the distance between the vibrating structure and the amplitude of the vibrations. In addition to these parameters, Basak and Raman [7] found that the Reynolds number has also an influence on the coupling between two neighboring vibrating structures. The present study intends to highlight the dependency of these parameters in the case of the guide vane cascade. Faced to the complexity of the entire cascade, the mechanical system is first reduced to a simple 2 DOF system by considering only two neighboring guide vanes. Then, we will show that this approach allows to analyze the dynamics of the entire cascade. Finally, solutions are proposed to prevent damage to the guide vanes.

3.4 Eigenmodes of the guide vanes

To conclude this introductive part, the theory of complex eigenmodes is concisely given. The free motion of the guide vane cascade is obtained by imposing $\mathbf{F} = \mathbf{0}$ in eq. 3.21:

$$[I]\,\ddot{\mathbf{y}} + [C]\,\dot{\mathbf{y}} + [K]\,\mathbf{y} = \mathbf{0} \tag{3.25}$$

The Caughey condition is necessary and sufficient for the mechanical system to feature $2z_o$ real modes. This condition is expressed:

$$[C]\,[I]^{-1}\,[K] = [K]\,[I]^{-1}\,[C] \tag{3.26}$$

If the Caughey condition is not satisfied, the modes are complex and the formulation of the problem may be established using the Duncan transformation [28]. Therefore, the eq. 3.25 may be written as follows:

$$[H]\,\dot{\mathbf{z}} + [G]\,\mathbf{z} = \mathbf{0} \tag{3.27}$$

with $\mathbf{z}^T = \left(\dot{\mathbf{y}}^T \; \mathbf{y}^T\right)$ and $\dot{\mathbf{z}}^T = \left(\ddot{\mathbf{y}}^T \; \dot{\mathbf{y}}^T\right)$. The matrices $[H]$ and $[G]$ are defined as:

$$[H] = \begin{bmatrix} [0] & [I] \\ [I] & [C] \end{bmatrix} \tag{3.28}$$

$$[G] = \begin{bmatrix} -\,[I] & [0] \\ [0] & [K] \end{bmatrix} \tag{3.29}$$

Applying the change of variables $\mathbf{z} = [B]\,\mathbf{q}$, the system of equations in eq. 3.27 may be decoupled:

$$[B]^T\,[H]\,[B]\,\dot{\mathbf{q}} + [B]^T\,[G]\,[B]\,\mathbf{q} = [H^o]\,\dot{\mathbf{q}} + [G^o]\,\mathbf{q} = \mathbf{0} \tag{3.30}$$

where $[B]$ is the change of base matrix and where $[H^o] = [B]^T [H] [B]$ and $[G^o] = [B]^T [G] [B]$ are diagonal matrices.

Multiplying by $[H^o]^{-1}$, the eq. yields to:

$$\dot{\mathbf{q}} + [H^o]^{-1} [G^o] \mathbf{q} = \dot{\mathbf{q}} + [\Delta] \mathbf{q} = \mathbf{0} \tag{3.31}$$

where $[\Delta]$ is the diagonal matrix containing the eigenvalues of the matrix $[H^o]^{-1} [G^o]$.

The system regroups $4z_o$ independent equations:

$$\dot{q}_p + \delta_p q = 0 \ , \ p = 1, 2, ...4z_o \tag{3.32}$$

The integration of eq. 3.32 gives the following solutions:

$$q_p = Q_p e^{\delta_p t} \tag{3.33}$$

In the z-coordinates, the solution may be written as follows:

$$\mathbf{z}_p = \mathbf{B}_p Q_p e^{-\delta_p t} \tag{3.34}$$

The complex eigenvalues δ_p are found by solving the characteristic equation:

$$|\, [H]^{-1} [G] - \delta_p [\mathbf{I}] \,| = \begin{vmatrix} [I]^{-1} [C] & [I]^{-1} [K] \\ -[\mathbf{I}] & [0] \end{vmatrix} = 0 \tag{3.35}$$

where $[\mathbf{I}]$ is the $2z_o \times 2z_o$ identity matrix.

The $4z_o$ eigenvalues δ_p are complex conjugated:

$$\begin{cases} \delta_p = \lambda_p + i\omega_{0,p} \\ \delta_p^* = \lambda_p - i\omega_{0,p} \end{cases} \tag{3.36}$$

where λ_p is the damping coefficient and $\omega_{0,p} = 2\pi f_{0,p}$, the eigenpulsation.

The $4z_o$ eigenvectors $\mathbf{B}_p$ associated to the eigenvalues may be obtained by solving:

$$\left[[H]^{-1} [G] - \delta_p [\mathbf{I}] \right] \mathbf{B}_p = \mathbf{0} \tag{3.37}$$

and may be written as follows:

$$\begin{cases} \mathbf{B}_p = \{\beta_{lp} e^{i\phi_{lp}}\} \ , \text{ for } l = 1, 2, ...(2 \cdot 2 \cdot z_o) \\ \mathbf{B}_p^* = \{\beta_{lp} e^{-i\phi_{lp}}\} \ , \text{ for } l = 1, 2, ...(2 \cdot 2 \cdot z_o) \end{cases} \tag{3.38}$$

Each eigenmode has not only different amplitude β_{lp} but also different phase ϕ_{lp}. The eigenshape must therefore be defined in the phase space. For dissipative motion with complex modes, the solution finally yields:

$$\mathbf{y} = \sum_{p}^{2 \cdot z_o} \beta_{ip} Y_p e^{-\lambda_p t} cos\left(\omega_p t - \psi_{ip} - \phi_p\right), \text{ for } i = 2z_o + 1, 2z_o + 2...4z_o \tag{3.39}$$

where ϕ_p and Y_p are defined by the initial conditions $y(0)$ and $\dot{y}(0)$.

Taking into account the periodicity condition of the guide vane cascade, the phase shift between two adjacent components of the eigenvector is expressed as:

$$\Delta\phi_p = \phi_{l+2,p} - \phi_{l,p} = \frac{2\pi}{z_o} \cdot p \tag{3.40}$$

Part II

Investigation methodology

Chapter 4

Investigated pump-turbine

4.1 Pump-turbine characteristics

The fluid-structure coupling in the guide vane cascade is investigated in the Hydrodyna pump-turbine reduced scale model, see Figure 4.1. This low specific speed $\nu = 0.17$, [42], pump-turbine features the characteristics listed in Table 4.1. The relative efficiency η/η_{max} hill chart in turbine mode for opening angles α_o ranging from 12° to 34° is given in Figure 4.2. In Figure 4.3, two cross section views of the pump-turbine are shown, on which the narrowest width of the guide vane channel W, the height of the distributor channel B_o, and the two diameters D_{1e} and $D_{\bar{1}e}$ are defined.

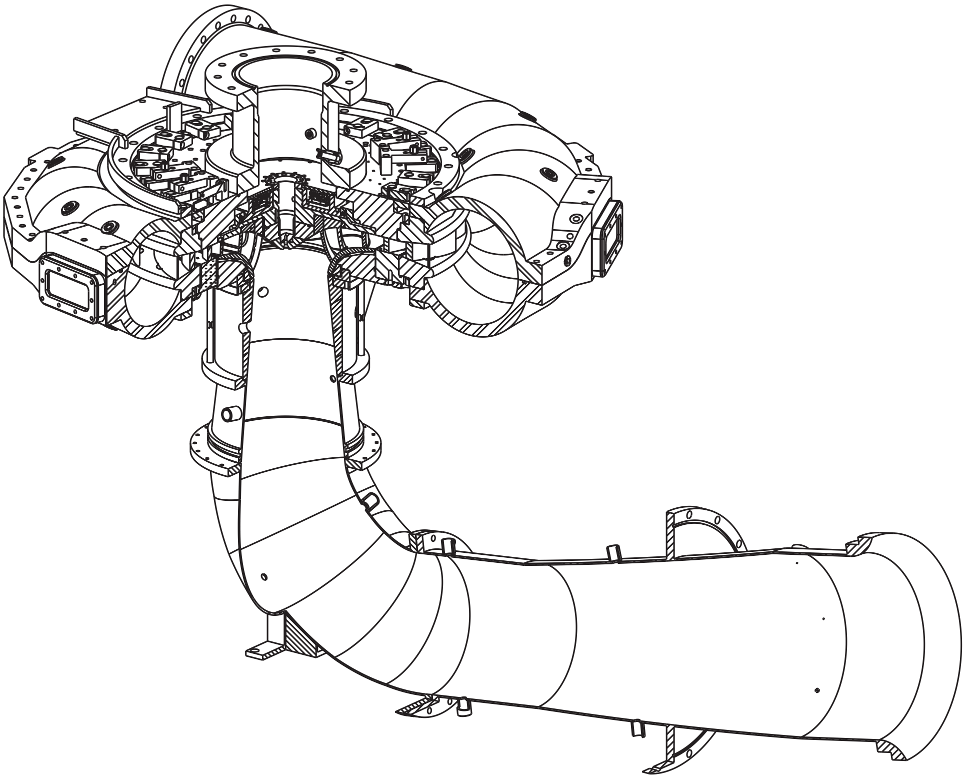

Figure 4.1: Hydrodyna pump-turbine reduced scale model.

Table 4.1: Characteristics of the Hydrodyna pump-turbine reduced scale model.

Characteristics	**Value**
Specific speed ν	0.17
Number of impeller blades z_b	9
Number of guide vanes z_o	20
Outer impeller diameter D_{1e}	527 mm
Impeller diameter at low pressure side $D_{\bar{1}e}$	250 mm
Height of the distributor channel B_o	36 mm
Narrowest width of guide vane channel W	25 mm

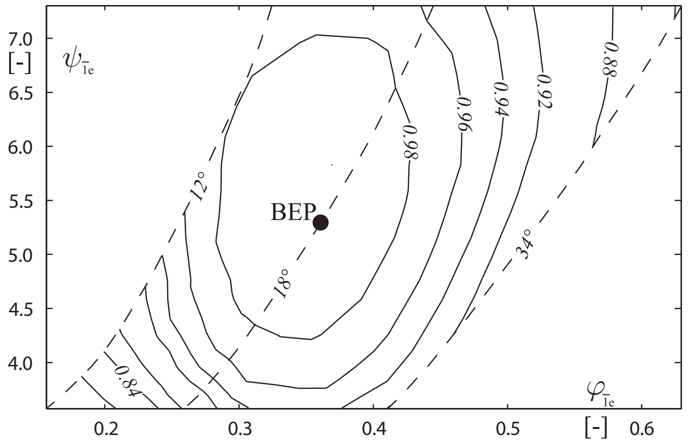

Figure 4.2: Relative efficiency η/η_{max} hill chart in generating mode for opening angles α_o ranging from 12° to 34°.

The Best Efficiency operating Point, BEP, is reached at 18° opening angle and corresponds to a discharge coefficient $\varphi_{\bar{1}e} = 0.36$ and an energy coefficient $\psi_{\bar{1}e} = 5.3$. These coefficients are defined in [42] as follows:

$$\varphi_{\bar{1}e} = \frac{Q}{\frac{\pi^2}{4} D_{\bar{1}e}^3 n} = 0.36 \tag{4.1}$$

$$\psi_{\bar{1}e} = \frac{E}{\frac{\pi^2}{4} D_{\bar{1}e}^2 n^2} = 5.3 \tag{4.2}$$

Q being the discharge and E the specific energy of the machine.

The specific speed ν is expressed from these two coefficients as follows:

$$\nu = \frac{\varphi^{0.5}}{\psi^{0.75}} = 0.17 \tag{4.3}$$

The guide vanes O_{10} and O_{11}, see Figure 4.3, are modified, their stems being more flexible than those of the usual guide vanes. The material is similar (CuSn12) for all the

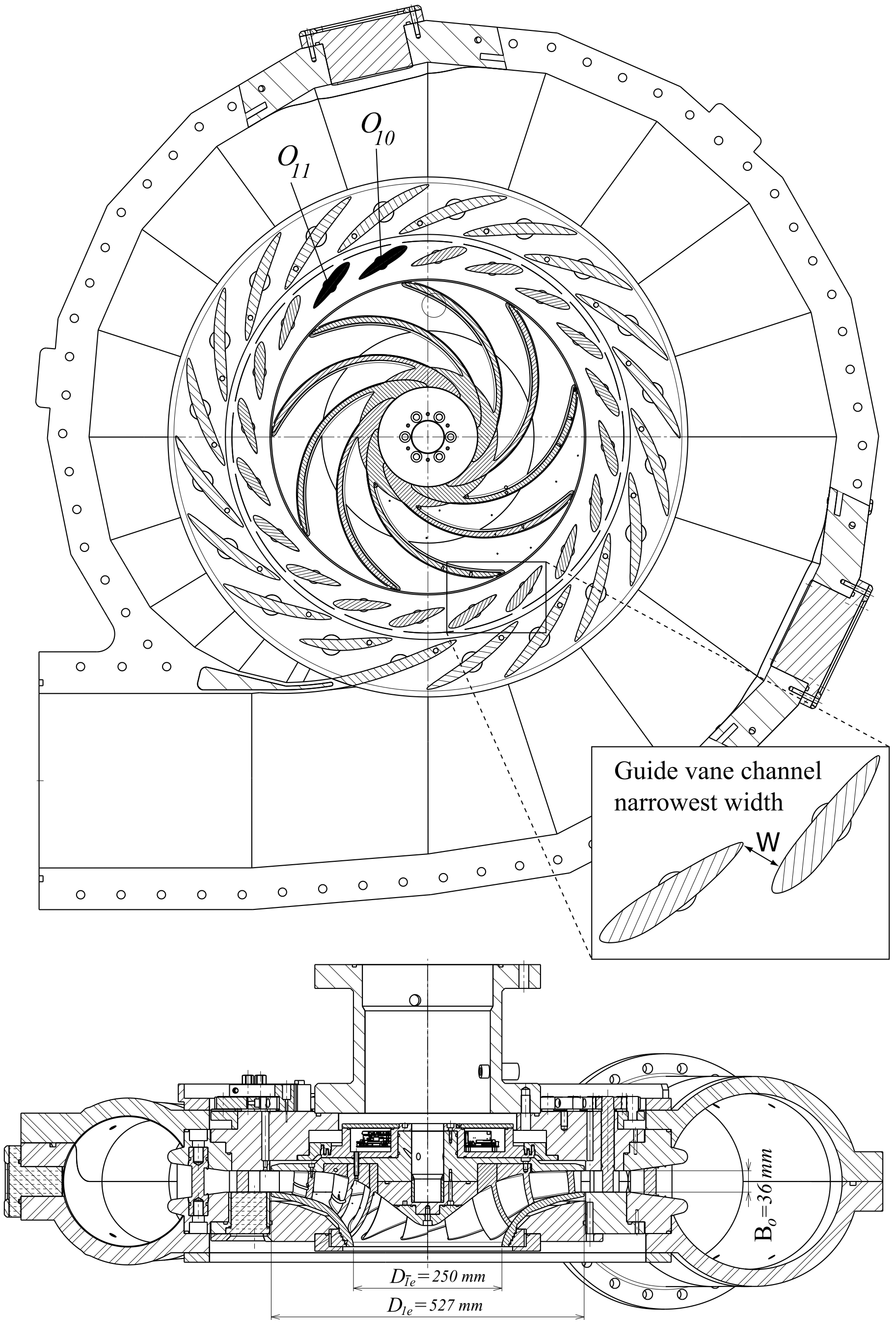

Figure 4.3: Sections of the Hydrodyna pump-turbine reduced scale model.

guide vanes. The assembly of the two types of guide vanes in the pump-turbine model is shown in Figure 4.4. The drawings of the modified guide vane featuring a flexible stem and the usual guide vane having a stiff stem are given in Figures 4.5 and 4.6, respectively. As may be observed, the span width of the modified guide vanes is 0.2 mm smaller. Therefore, we avoid any contact of the modified guide vanes with the upper or lower flange, and we ensure reliable measurement of bending and torsion motions. Moreover, the modified guide vanes are loosened from their lever and held in place with stiff stainless steel clamp, see Figure 4.7.

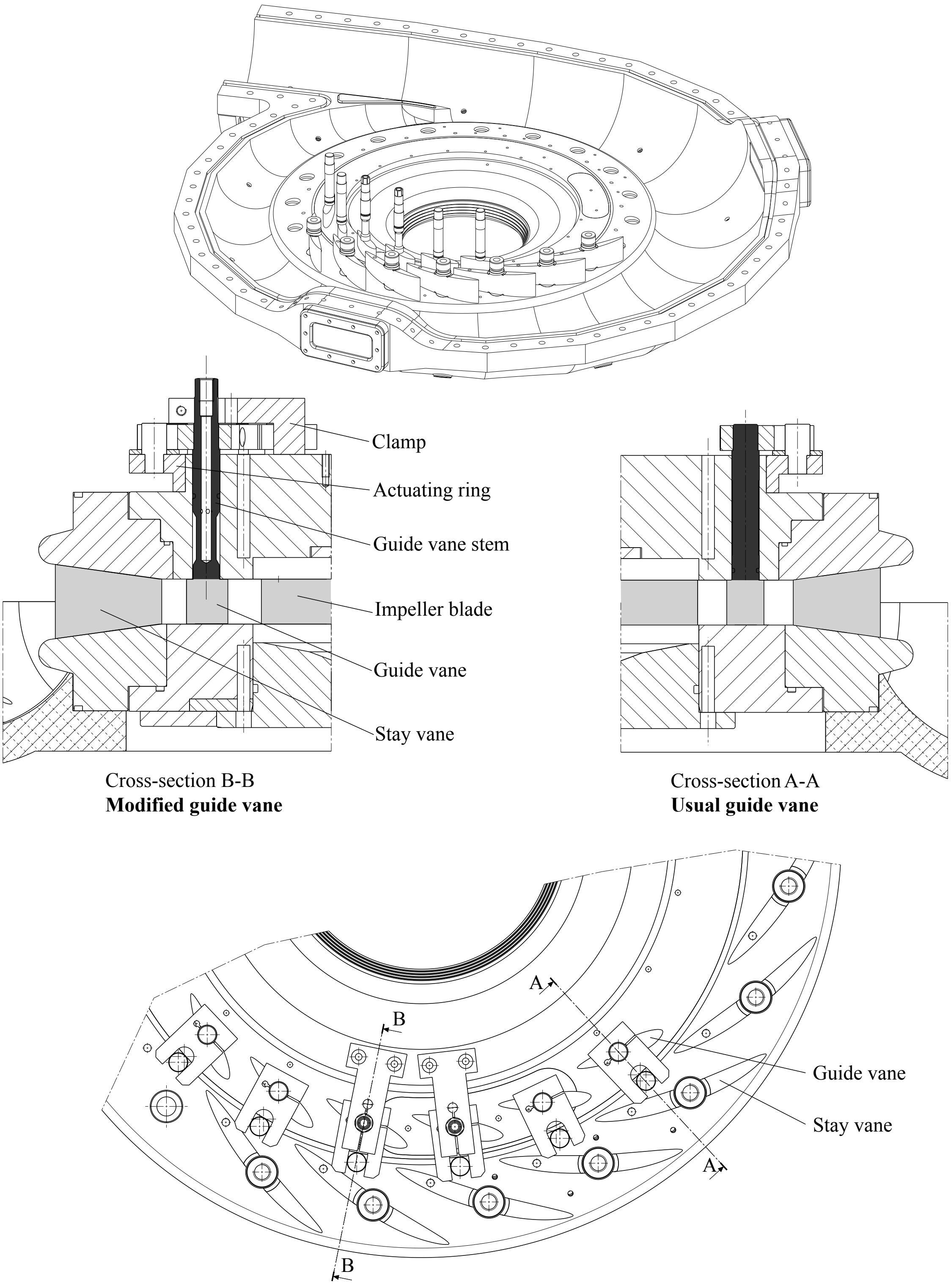
Clamp
Actuating ring
Guide vane stem
Impeller blade
Guide vane
Stay vane
Cross-section B-B
Modified guide vane
Cross-section A-A
Usual guide vane
A
A
B
B
Guide vane
Stay vane

Figure 4.4: Assembly of the two types of guide vanes in the pump-turbine model.

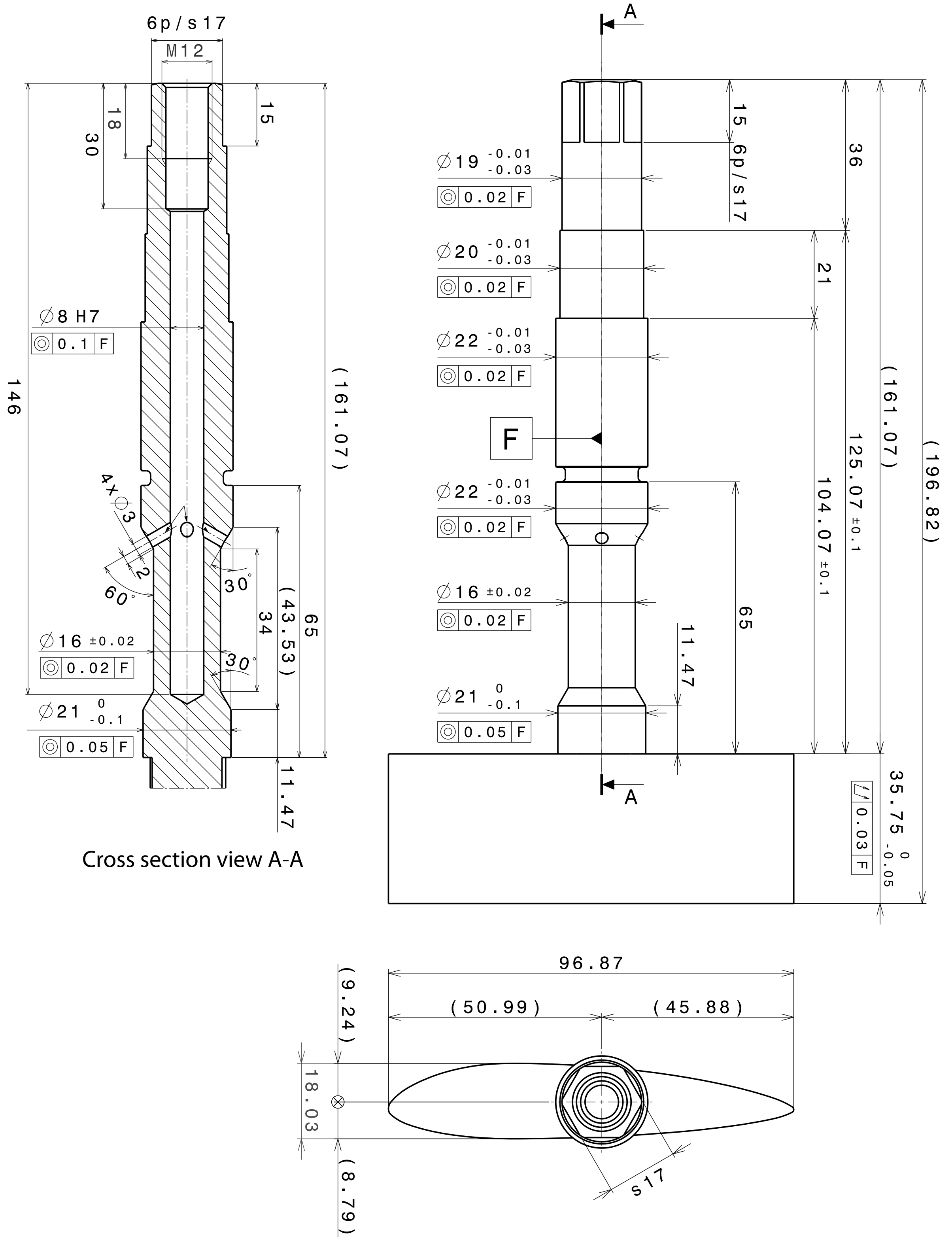
6p/s17
M12
18
30
15
146
∅8 H7
◎ 0.1 F
(161.07)
4x∅3
2
60°
30°
30°
34
(43.53)
65
∅16 ±0.02
◎ 0.02 F
∅21 0 -0.1
◎ 0.05 F
11.47
Cross section view A-A
A
15
6p/s17
36
∅19 -0.01 -0.03
◎ 0.02 F
∅20 -0.01 -0.03
◎ 0.02 F
21
∅22 -0.01 -0.03
◎ 0.02 F
F
(161.07)
125.07 ±0.1
104.07 ±0.1
(196.82)
∅22 -0.01 -0.03
◎ 0.02 F
∅16 ±0.02
◎ 0.02 F
65
11.47
∅21 0 -0.1
◎ 0.05 F
A
35.75 0 -0.05
⫽ 0.03 F
96.87
(50.99)
(45.88)
(9.24)
18.03
(8.79)
s17

Figure 4.5: Working drawing of the modified guide vane featuring a flexible stem.

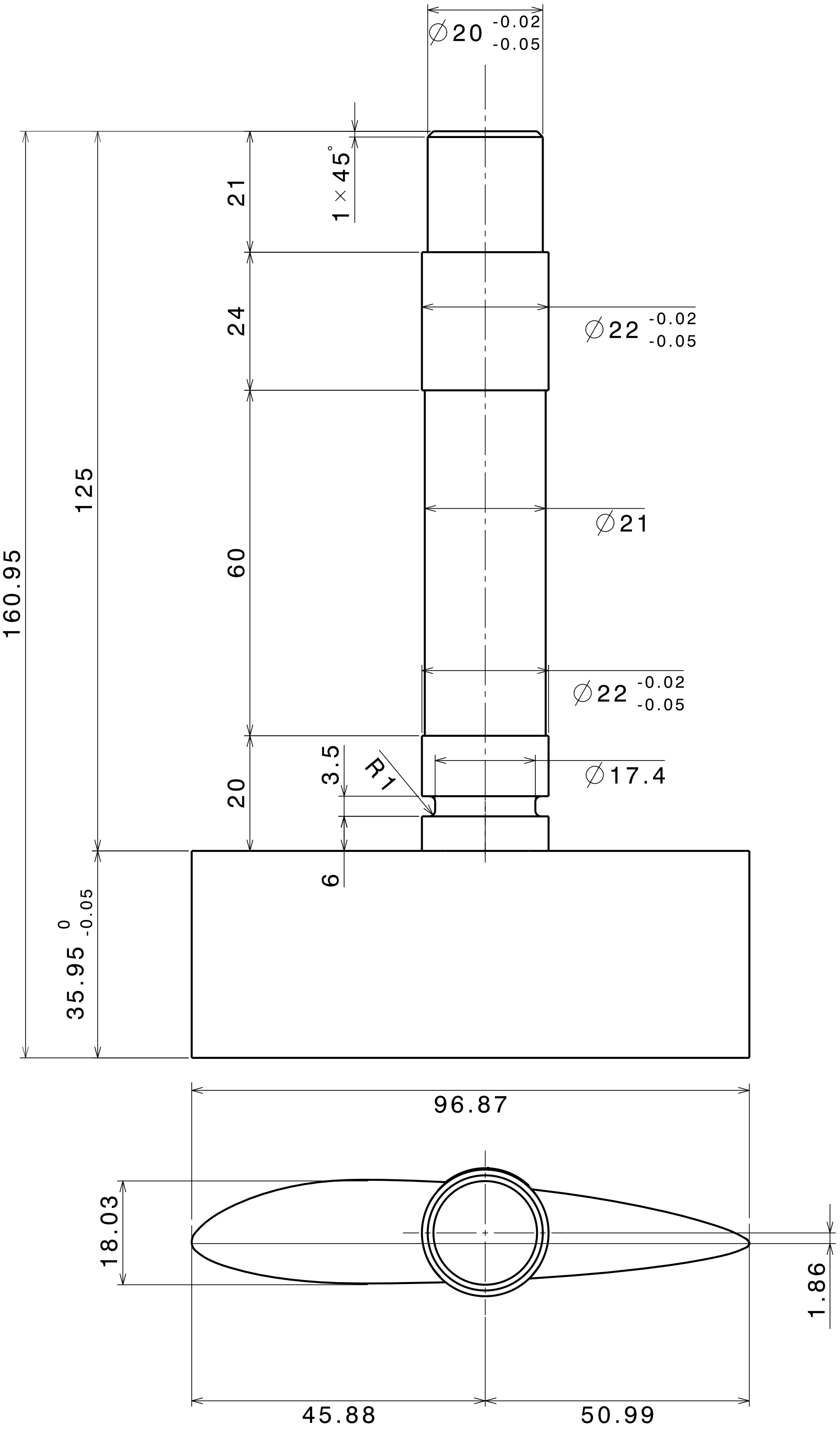
∅20 -0.02 -0.05
1 × 45°
21
24
60
20
125
160.95
∅22 -0.02 -0.05
∅21
∅22 -0.02 -0.05
3.5
R1
∅17.4
6
35.95 0 -0.05
96.87
18.03
1.86
45.88
50.99

Figure 4.6: Working drawing of the usual guide vane having a stiff stem.

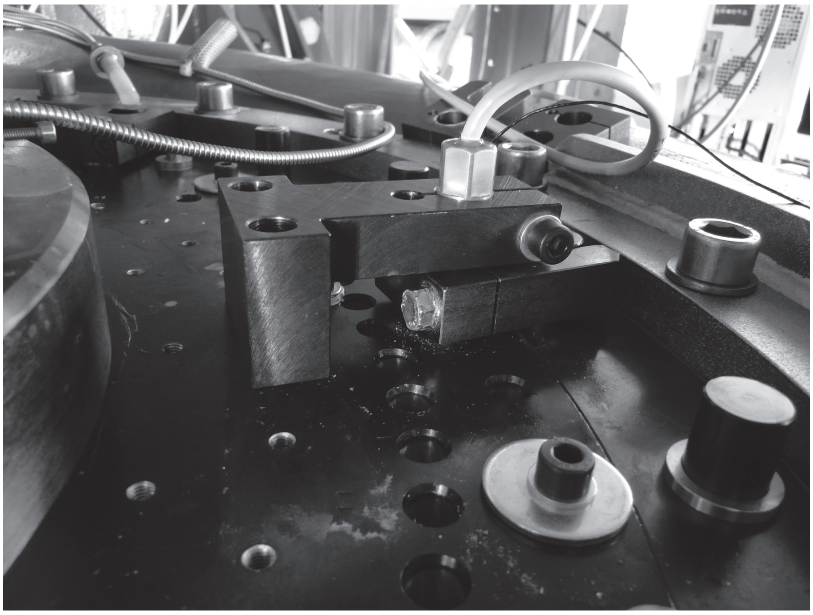

Figure 4.7: Clamping system to hold the modified guide vane in place.

Chapter 5

Test facility

The pump-turbine reduced scale model is placed in the EPFL PF2 test rig, see Figure 5.1, featuring a maximum specific energy $E = 1.25 \cdot 10^3$ J·kg^{-1}, a maximum discharge $Q = 1.4$ m^3·s^{-1}; the rotation speed being limited to $N = 2.5 \cdot 10^3$ rpm. The test rig fulfills the IEC standards 60193 [42] and reaches 0.2 % accuracy for the shaft torque, the discharge and the differential pressure measurements. The closed loop circuit is made up of one circulating pump, driven by a 1000 kW power electric motor, a valve controlling the head losses, an air vessel for controlling the Net Positive Suction Head, NPSH. The pump-turbine reduced scale model is coupled to a 300 kW electrical generator.

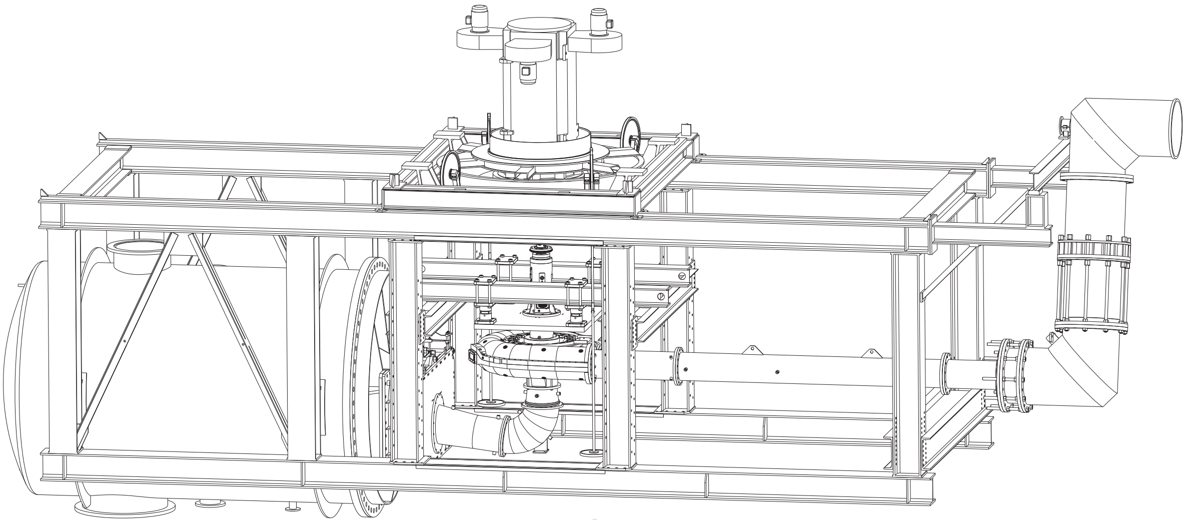

Figure 5.1: EPFL PF2 test rig.

The specific energy E is measured using ROSEMOUNT 3051SCD4A differential pressure sensors placed on the high and low pressure sides of the machine. They are calibrated from 0.1 up to 0.6 MPa by increasing and, then, decreasing the pressure value. The calibration curve is given on the left hand side in Figure 5.2. The relative error ϵ'_{dp} is less than 1 ‰ and is defined as follows:

$$\epsilon'_{dp} = \frac{p_{ref} - a_{dp} \cdot S_{dp}}{p_{ref}} \tag{5.1}$$

S_{dp} being the output voltage signal of the sensor and a_{dp} the calibration coefficient obtained with a linear regression on the measured values.

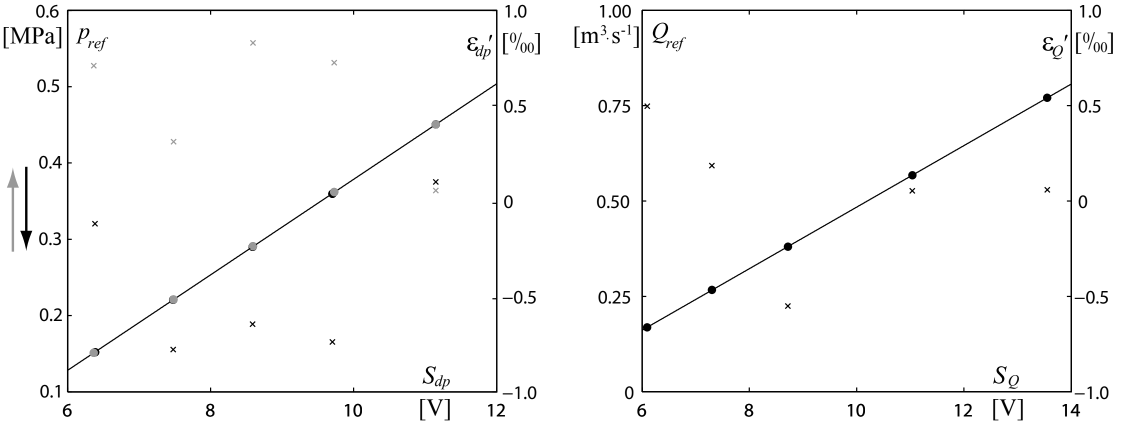

Figure 5.2: Calibration of the Rosemount differential pressure sensors for specific energy E measurement (left) and calibration of the electromagnetic flow meter (right)

The flow discharge is measured using an electromagnetic flow meter. It is calibrated up to 1 m^3·s^{-1}. The calibration curve is given on the right hand side in Figure 5.2. Again, the relative error ϵ_Q' is less than 1 ‰ and is defined as follows:

$$\epsilon_Q' = \frac{Q_{ref} - a_Q \cdot S_Q}{Q_{ref}} \tag{5.2}$$

S_Q being the output voltage signal of the flow meter and a_Q the calibration coefficient obtained with a linear regression on the measured values.

Finally, the impeller rotation speed N is measured with the help of a tachometer: the HEIDENHAIN ERA 180-1AK.1003-9000 counter provides 9000 impulses per impeller revolution to the HEIDENHAIN IBV 600 electronic converters.

Chapter 6

Measuring apparatus

6.1 Impulse excitation system

6.1.1 In air

To proceed to modal analyzes in air, an instrumented hammer Dytran 5850B is used. It has the role of giving an impulse excitation to the guide vanes. A wide range of frequency is thereby excited. The force sensitivity may be chosen among 1, 10 and 100 mV·lbf^{-1}(pound-force).

6.1.2 In water

To create an impulse excitation in water, a non-intrusive system is used, see [67]. A BOSCH Super W7DC spark plug, see Figure 6.1 is flush mounted on the wall of the bottom flange in a guide vane channel at the location SP, see Figure 6.2.

Figure 6.1: BOSCH Super W7DC spark plug used as a non-intrusive system to get the impulse excitation in water

The discharge of 1.55 μF capacitor under a 4.3 kV voltage supply in a very short time ($\Delta t < 25$ μm) generates a discharge energy of 14.3 J producing a rapid increase of the water temperature. The explosive growth of a vapor bubble produces a strong pressure wave traveling towards the hydrofoil at the speed of sound. The hydrofoil is, thereby, impulsively excited on a wide band frequency range. Several collapses and rebounds of the bubble occur, but the first pressure wave is the strongest.

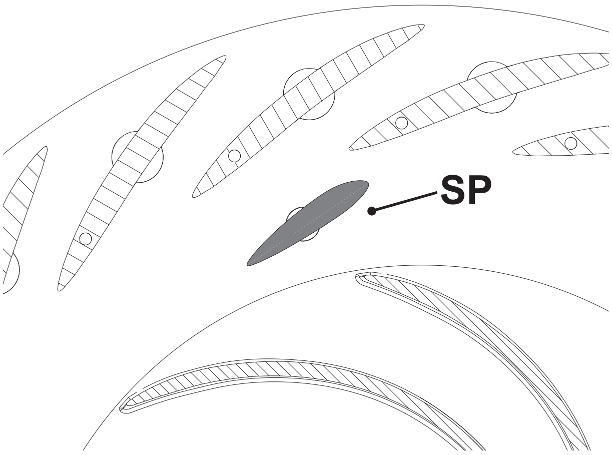

Figure 6.2: Spark plug location SP

The visualization of the spark generated bubble is obtained with an ultra high speed PHOTRON FASTCAM SA1.1 video system at 8'000 frames per second with a resolution of 832x608 pixels. The growing and then collapsing vapor bubble can be observed in Figure 6.3

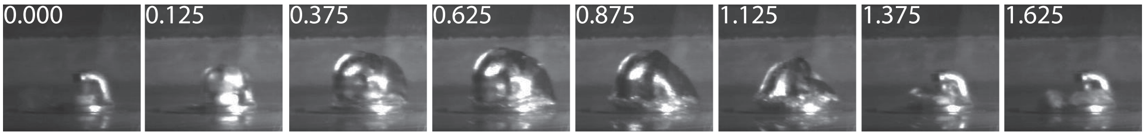

Figure 6.3: Spark generated bubble visualization at zero flow velocity (time in [ms])

6.2 Structural vibration measurement

The two guide vanes having a flexible stem are equipped with two full Wheatstone bridges of semi-conductor strain gages; one being sensitive to bending and the other to torsion motion, see Figure 6.4. A 5 V input voltage supplies each Wheatstone bridge. The properties of the strain gages Kyowa KSN-2-120-F3-11 are given in Table 6.1.

First, the guide vanes are statically calibrated by applying a reference bending force ranging from -150 N to 150 N, in the direction perpendicular to a line inclined by 2.3° from the guide vane chord. Then, the guide vanes are statically calibrated by applying a torsion torque ranging from -33 N·m to 33 N·m, on the guide vane stem. The direction of positive force and torque is shown in Figure 6.5.

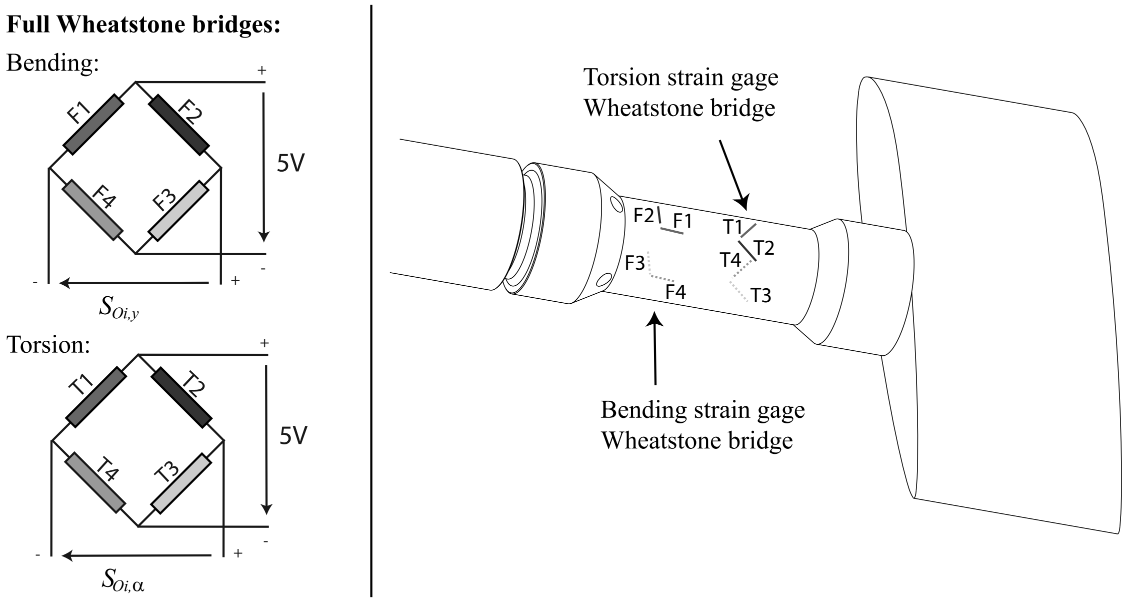
Full Wheatstone bridges:
Bending:
F1
F2
F3
F4
5V
+
-
$S_{Oi,y}$
Torsion:
T1
T2
T3
T4
5V
$S_{Oi,\alpha}$
Torsion strain gage Wheatstone bridge
Bending strain gage Wheatstone bridge

Figure 6.4: Strain gage Wheatstone bridges for torsion and bending monitoring.

Table 6.1: Characteristics of Kyowa KSN-2-120-F3-11 semi-conductor strain gages.

Gage length	Gage resistance	Gage factor	Max. allowable strain	Max. allowable current
2 mm	120 Ω	∼ 100	3000 μm	20 mA

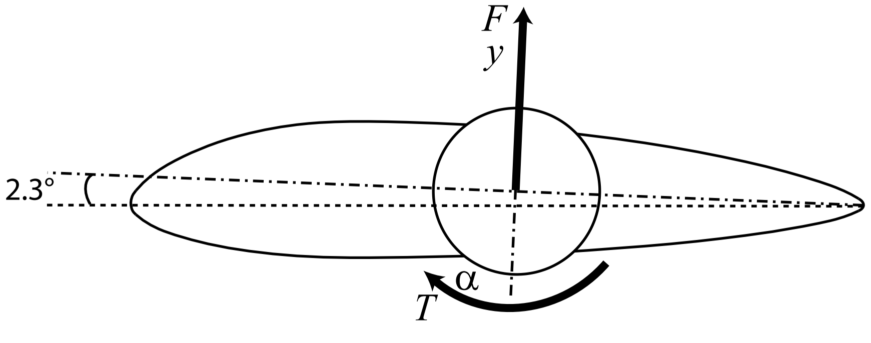

Figure 6.5: Direction of positive force and torque.

The force and torque calibration diagrams are drawn in Figure 6.6.

The calibration curves for the guide vanes O_{10} and O_{11} are given in Figures 6.7 and 6.8, for force and torque, respectively.

In these figures, the output voltage values of the two Wheatstone bridges, $S_{O_i,y}$ and $S_{O_i,\alpha}$, corresponding to the reference forces F_{ref} and torques T_{ref} applied to the guide vanes are plotted. The absolute measurement uncertainty, $\epsilon_{F_{ref}}$ and $\epsilon_{T_{ref}}$ are also given

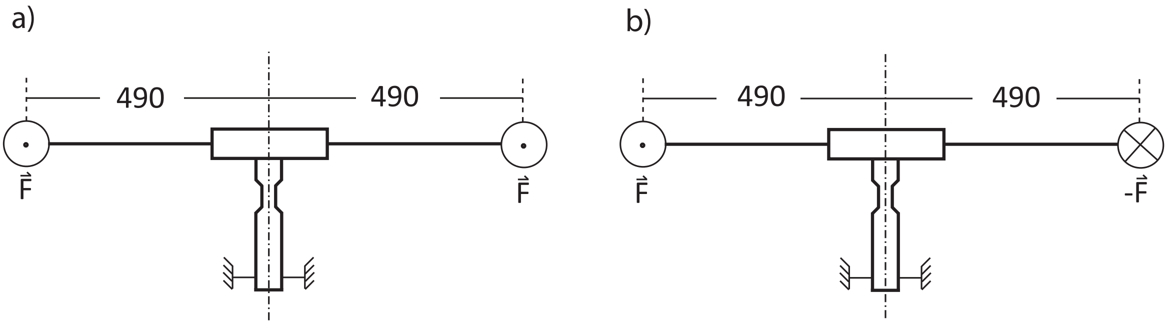

Figure 6.6: Force a) and Torque b) calibration diagrams (lever arm units: [mm]).

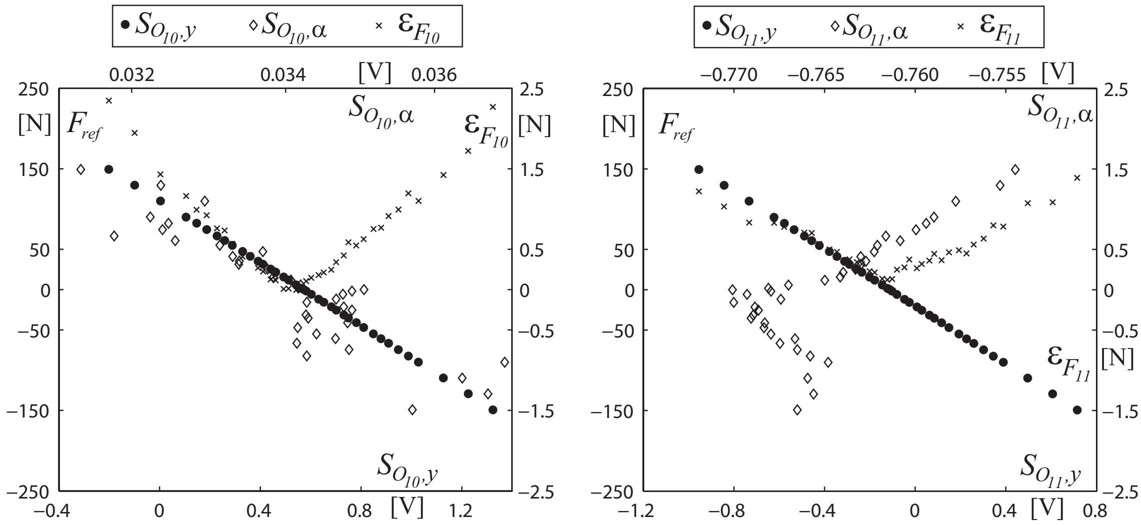

Figure 6.7: Bending force calibration for the guide vane O_{10} (left) and O_{11} (right).

and are expressed as follows:

$$\epsilon_{F_i} = F_{ref} - F_i \tag{6.1}$$

$$\epsilon_{T_i} = T_{ref} - T_i \tag{6.2}$$

with F_i and T_i being computed as follows:

$$\begin{pmatrix} F_i \\ T_i \end{pmatrix} = \begin{pmatrix} a_{O_i} & b_{O_i} \\ c_{O_i} & d_{O_i} \end{pmatrix} \begin{pmatrix} S_{O_i,y} \\ S_{O_i,\alpha} \end{pmatrix} \tag{6.3}$$

where the sensitivity coefficients a_{O_i}, b_{O_i}, c_{O_i} and d_{O_i} are obtained with a multivariate linear regression.

On the one hand, the output voltage signals $S_{O_{10},\alpha}$ and $S_{O_{11},\alpha}$ are 283 and 117 times less sensitive than $S_{O_{10},y}$ and $S_{O_{11},y}$, respectively, when applying a bending force. On the

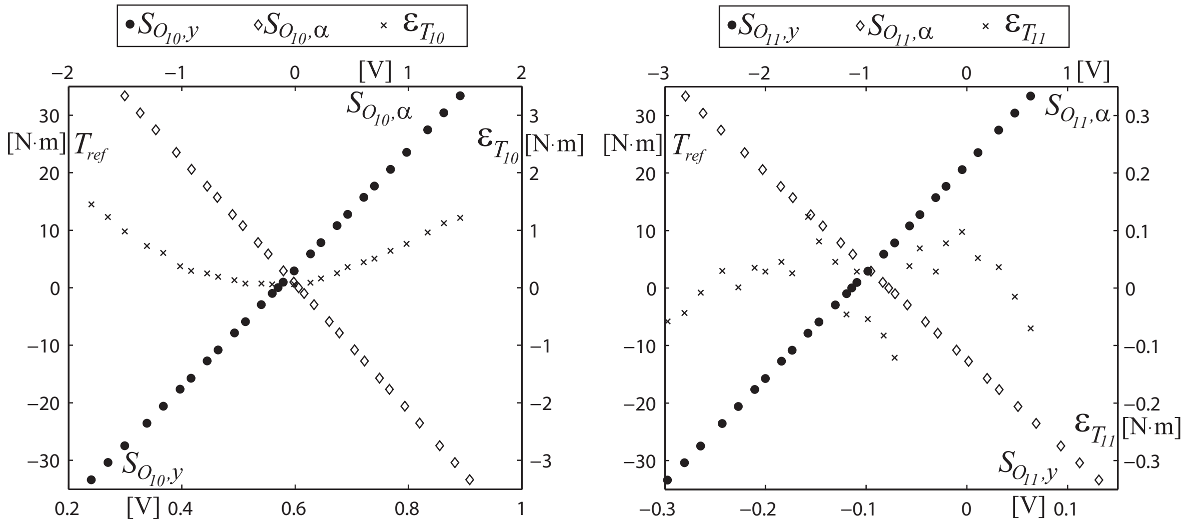

Figure 6.8: Bending force calibration for the guide vane O_{10} (left) and O_{11} (right).

other hand, the output voltage signals $S_{O_{10},y}$ and $S_{O_{11},y}$ are 4 and 11 times less sensitive than $S_{O_{10},\alpha}$ and $S_{O_{11},\alpha}$, respectively, when applying a torsion torque.

Using the expression $F_i = K^s \cdot y_i$ and $T_i = L^s \cdot \alpha_i$, K^s and L^s being the structural bending stiffness and torsion stiffness, respectively, the bending displacement and torsion angle may be linked to the Wheatstone bridge output signals:

$$\begin{pmatrix} y_i \\ \alpha_i \end{pmatrix} = \begin{pmatrix} \frac{a_{O_i}}{K^s} & \frac{b_{O_i}}{K^s} \\ \frac{c_{O_i}}{L^s} & \frac{d_{O_i}}{L^s} \end{pmatrix} \begin{pmatrix} S_{O_i,y} \\ S_{O_i,\alpha} \end{pmatrix} = \begin{pmatrix} a^*_{O_i} & b^*_{O_i} \\ c^*_{O_i} & d^*_{O_i} \end{pmatrix} \begin{pmatrix} S_{O_i,y} \\ S_{O_i,\alpha} \end{pmatrix} \tag{6.4}$$

where $a^*_{O_i} = \frac{a_{O_i}}{K^s}$, $b^*_{O_i} = \frac{b_{O_i}}{K^s}$, $c^*_{O_i} = \frac{c_{O_i}}{K^s}$ and $d^*_{O_i} = \frac{d_{O_i}}{K^s}$ are the sensitivity coefficients for bending displacement and torsion angle. These coefficients may be used for displacement and angle monitoring during dynamic tests, since the Wheatstone bridge output voltage is proportional to the structural strain, which is proportional to the bending deflection and torsion angle.

The characteristics of the guide vanes equipped with strain gages are given in Table 6.2.

6.3 Flow pressure measurement

To monitor the dynamic pressure in the pump-turbine stator, 22 miniature piezoresistive pressure sensors are used. A unit consists of a deformable membrane-like part on which a Wheatstone bridge made up of 4 semi-conducting thin layers placed in such a way that the effect of pressure stretches or compresses them. The overall unit has a diameter of 5.55 mm. The units are flush mounted on the wall of the head cover at different locations, see Figure 6.9. The pressure sensors g_i are located in the rotor-stator gap at the angular position corresponding to the guide vane O_i. The pressure sensors denoted by s_i are positioned in the guide vane channel on the pressure side of the guide vane O_i.

Table 6.2: Characteristics of the guide vanes O_{10} and O_{11} equipped with strain gages.

	O_{10}	O_{11}
Static force range	±150 N	±150 N
Static force abs. uncertainty	$0 \div 2.3$ N	$0 \div 1.4$ N
Static torque range	±33 N·m	±33 N·m
Static torque abs. uncertainty	$0 \div 1.5$ N·m	$-1.1 \div 1.1$ N·m
Sensitivity coefficient a_{O_i}	-195.5 N·V^{-1}	-178.7 N·V^{-1}
Sensitivity coefficient b_{O_i}	-41.7 N·V^{-1}	-15.7 N·V^{-1}
Sensitivity coefficient c_{O_i}	0.1 N·m·V^{-1}	-0.1 N·m·V^{-1}
Sensitivity coefficient d_{O_i}	-21.9 N·m·V^{-1}	-16.3 N·m·V^{-1}
Static displ. range	±0.117 mm	±0.117 mm
Static displ. abs. uncertainty	$0 \div 2 \cdot 10^{-3}$ mm	$0 \div 1 \cdot 10^{-3}$ mm
Static angle range	$\pm9.1 \cdot 10^{-3}$ rad	$\pm9.1 \cdot 10^{-3}$ rad
Static angle abs. uncertainty	$0 \div 0.4 \cdot 10^{-3}$ rad	$-0.3 \cdot 10^{-3} \div 0.3 \cdot 10^{-3}$ rad
Sensitivity coefficient $a^*_{O_i}$	-1.53·10^{-4} mm·V^{-1}	-1.4·10^{-4} mm·V^{-1}
Sensitivity coefficient $b^*_{O_i}$	-0.33·10^{-4} mm·V^{-1}	-0.12·10^{-4} mm·V^{-1}
Sensitivity coefficient $c^*_{O_i}$	0.28·10^{-4} rad·V^{-1}	-0.28·10^{-4} rad·V^{-1}
Sensitivity coefficient $d^*_{O_i}$	-60.66·10^{-4} rad·V^{-1}	-45.15·10^{-4} rad·V^{-1}
Bandwidth	< 25 kHz	< 25 kHz

The pressure sensors are statically calibrated up to 0.5 MPa absolute pressure. The same conditioning electronics as for measurement is used, in order to include the conditioning effects in the sensitivity coefficients. The sensors are placed in a vessel in which the pressure, measured with a high precision reference sensor, may be modified. Ten pressure values ranging from 0.1 to 0.5 MPa are tested by increasing and decreasing the pressure. The calibration sensitivity coefficients are identified using a linear regression. The absolute measurement uncertainty is defined as follows:

$$\epsilon_{p_{s_i}} = p_{ref} - a_{s_i} \cdot S_{s_i} \tag{6.5}$$

where a_{s_i} is the pressure sensor s_i sensitivity coefficient and S_{s_i} is the output voltage.

The calibration curve of the pressure sensor s_{10} is given, as an example, in Figure 6.10. The characteristics of the pressure sensors are given in Table 6.3.

Table 6.3: Characteristics of the pressure sensors.

	Value
Range	0.5 MPa
Abs. uncertainty	±0.5 kPa
Sensitivity	70 kPa·V^{-1}
Bandwidth	< 25 kHz

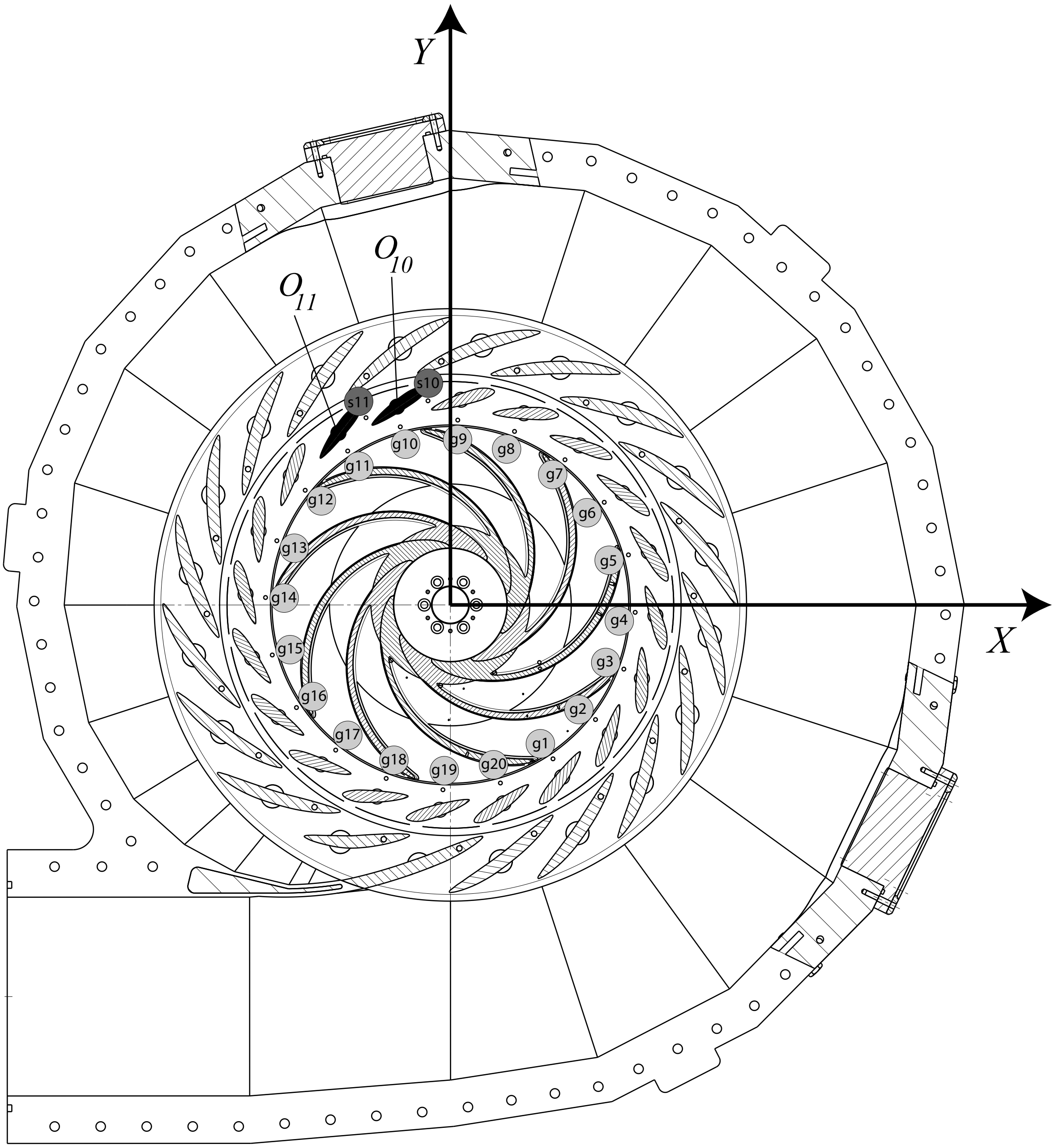

Figure 6.9: Locations of the flush mounted pressure sensors on the head cover.

6.4 Measuring chain

The measuring chain is shown in Figure 6.11. The discharge, the specific energy and the impeller rotation speed are measured using an electromagnetic flowmeter, differential pressure sensors and a tachometer, respectively. These measurands are simultaneously recorded using HBM MGC+ digitizers with 24 bits A/D resolution at 2'400 Hz sampling frequency over 20 s. The opening angle value is measured with an incremental coder and is directly connected to the command PC. The pump-turbine operating points data are transferred from the command to the storage PC. Then, the vibrations of the guide vane

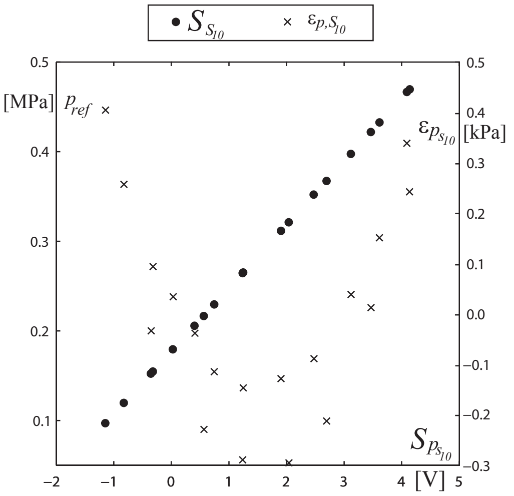

Figure 6.10: Pressure calibration curve of the sensor s_{10}.

and pressure fluctuation signals are simultaneously recorded using NI PXI digitizers with 24 bits A/D resolution at 5 kHz sampling frequency over 15.36 s, keeping the operating conditions of the pump-turbine constant.

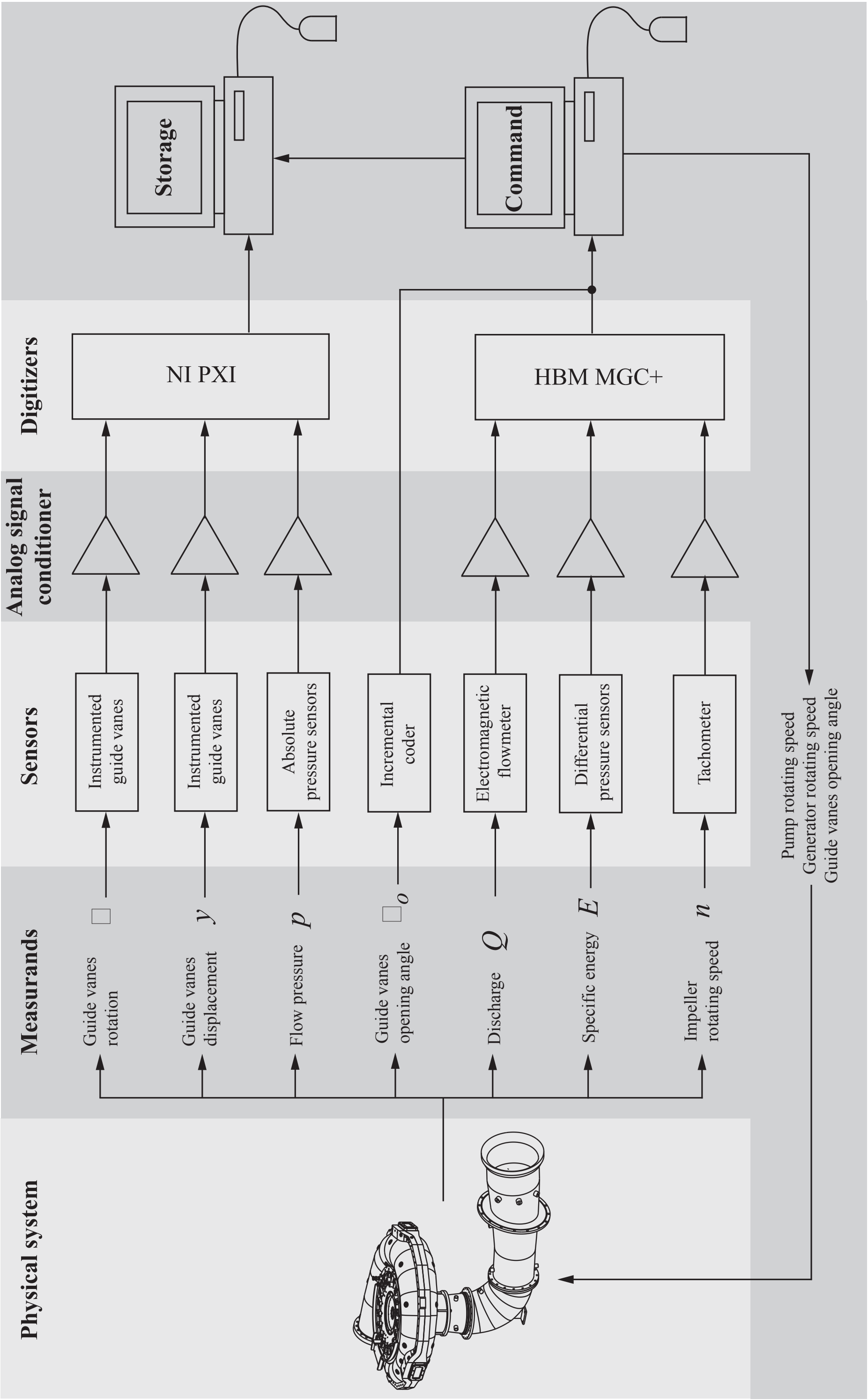
Physical system
Measurands
Sensors
Analog signal conditioner
Digitizers
Storage
Command
Guide vanes rotation
□
Guide vanes displacement
y
Flow pressure
p
Guide vanes opening angle
□o
Discharge
Q
Specific energy
E
Impeller rotating speed
n
Instrumented guide vanes
Instrumented guide vanes
Absolute pressure sensors
Incremental coder
Electromagnetic flowmeter
Differential pressure sensors
Tachometer
NI PXI
HBM MGC+
Pump rotating speed
Generator rotating speed
Guide vanes opening angle

Figure 6.11: Measuring chain for the experiments.

Part III

Guide vane cascade dynamics

Chapter 7

Rotating pressure modes in the stator due to the RSI

The interaction of $z_b = 9$ impeller blades with $z_o = 20$ guide vanes makes apparent an infinite number of pressure rotating modes as analytically shown in Appendix E; the properties of the first m and m' combinations being given in Table 7.1. For each combination, the number of diametrical nodes, k_- and k_+ are firstly given. The frequency f of the pressure fluctuations monitored in the stator is then indicated by the ratio f/n. The rotating frequency ratio, $n_-/n = \frac{f}{k_- n}$ and $n_+/n = \frac{f}{k_+ n}$ are also mentioned. The predominance of one mode on the other for a given combination of m and m' is evaluated as well, based on the acoustic wave propagation approach: the value of the Bessel functions, $J_-\left(\frac{m' z_b 2\pi n}{c_o} R_1\right)$ and $J_+\left(\frac{m' z_b 2\pi n}{c_o} R_1\right)$, appearing in eq. E.17 quantifies the predominance. Finally, the phase shift between two pressure signals monitored at two angular positions distant by $\Delta\theta = \frac{2\pi}{z_o}$, defined in eq. E.18, is also given.

In this table, the first five most predominant RSI modes are highlighted in gray. Moreover, according to the acoustic wave propagation approach, the main mode features $k = -2$ diametrical nodes, rotates at a frequency $n_- = 9n$ and, therefore, this mode, at a fixed location in the stator, exhibits a frequency $f = 18n$. Franke et al. [34] and Zobeiri [90] have notably studied this mode for the same configuration of impeller blade and guide vane numbers.

These authors have also analyzed the mode oscillating at $f = 9n$. It is nonetheless always confused with the mode featuring the same frequency but having $k_- = -11$ diametrical nodes. The acoustic wave propagation approach predicts the presence of $k_- = 9$ diametrical nodes for this pressure mode oscillating at $f = 9n$, which actually reflects the impeller blade passage. Nevertheless, this approach underestimates the effect of this mode. Close to the rotor-stator gap, as already mentioned in Appendix E, the convective effect predominates and, therefore, the impeller passage frequency $f = 9n$ is more significant that the prediction based on the acoustic wave propagation approach. This mode spins at the impeller rotation frequency $n_- = n$.

Three other RSI pressure modes oscillating in the stator at $f = 27n$, $f = 36n$ and $f = 45n$ are highlighted in Table 7.1. They feature $k_- = 7$, $k_- = -4$ and $k_- = 5$ and spin at $n_- = 3.86n$, $n_- = -9n$ and $n_- = 9n$, respectively. The shape of these five most predominant RSI rotating pressure modes is shown in Figure 7.1.

Table 7.1: RSI pressure mode in the stator corresponding to the first m and m' combinations, for a pump-turbine featuring $z_b = 9$ impeller blades and $z_o = 20$ guide vanes: Numbers of diametrical nodes $k-$ and k_+; dimensionless frequency f/n of the modes monitored in the stator; phase shift $\Delta\phi_k$ between two pressure signals monitored at two angular positions distant by $\Delta\theta = \frac{2\pi}{z_o}$; dimensionless rotating frequencies, n_-/n and n_+/n; Bessel function values, J_{k-} and J_{k+}, in the acoustic wave propagation approach.

m	m'	k_-	k_+	f/n	n_-/n	n_+/n	J_{k-}	J_{k+}	$\Delta\phi_k$
[-]	[-]	[-]	[-]	[-]	[-]	[-]	[-]	[-]	[rad]
0	1	9	9	9	1.00	1.00	$0.32 \cdot 10^{-22}$	$0.32 \cdot 10^{-22}$	2.83
0	2	18	18	18	1.00	1.00	$5.47 \cdot 10^{-45}$	$5.47 \cdot 10^{-45}$	-0.63
0	3	27	27	27	1.00	1.00	$1.08 \cdot 10^{-66}$	$1.08 \cdot 10^{-66}$	2.20
0	4	36	36	36	1.00	1.00	$2.27 \cdot 10^{-88}$	$2.27 \cdot 10^{-88}$	-1.26
0	5	45	45	45	1.00	1.00	$4.90 \cdot 10^{-110}$	$4.90 \cdot 10^{-110}$	1.57
1	1	-11	29	9	-0.82	0.31	$-4.99 \cdot 10^{-29}$	$3.01 \cdot 10^{-86}$	2.83
1	2	-2	38	18	-9.00	0.47	$3.44 \cdot 10^{-4}$	$1.62 \cdot 10^{-105}$	-0.63
1	3	7	47	27	3.86	0.57	$2.91 \cdot 10^{-14}$	$3.65 \cdot 10^{-126}$	2.20
1	4	16	56	36	2.25	0.64	$1.59 \cdot 10^{-34}$	$3.00 \cdot 10^{-147}$	-1.26
1	5	25	65	45	1.80	0.69	$1.72 \cdot 10^{-55}$	$1.56 \cdot 10^{-168}$	1.57
2	1	-31	49	9	-0.29	0.18	$-5.57 \cdot 10^{-93}$	$1.01 \cdot 10^{-155}$	2.83
2	2	-22	58	18	-0.82	0.31	$1.48 \cdot 10^{-56}$	$8.68 \cdot 10^{-171}$	-0.63
2	3	-13	67	27	-2.08	0.40	$-8.78 \cdot 10^{-29}$	$2.08 \cdot 10^{-189}$	2.20
2	4	-4	76	36	-9	0.47	$3.16 \cdot 10^{-7}$	$2.86 \cdot 10^{-209}$	-1.26
2	5	5	85	45	9	0.53	$1.01 \cdot 10^{-8}$	$1.00 \cdot 10^{-229}$	1.57

These rotating pressure modes are experimentally highlighted in the following lines. One focuses on the pressure fluctuations in the rotor-stator gap at the BEP, see Figure 4.2. The specific energy of the pump-turbine is set to $E = 435$ J·kg^{-1} and the impeller rotation speed at 16.3 Hz. The 20 guide vanes feature a stiff stem in order to get rid of any fluid-structure coupling.

The pressure fluctuations are monitored using the 20 pressure sensors located in the rotor-stator gap, namely g_i $(1 < i < 20)$, during 2.56 s. The sampling frequency is 51.2 kHz.

In Figure 7.2, the phase average of the pressure fluctuations monitored by the two adjacent pressure sensors, g_{10} and g_{11}, is plotted. The phase average is obtained over 42 impeller revolutions representing 2.56 s.

The two pressure signals are phase shifted by 3.5 rad. The frequencies $f = 9n$ and $f = 18n$ predominate in both signals.

The FFT is applied to signals which are 2^{14} samples long. A hamming window is used. The spectra are averaged over 8 records. In Figure 7.3, the waterfall diagram of the amplitude spectra of the pressure factor fluctuations is plotted against the angular position θ of the pressure sensors in the rotor-stator vaneless gap. Most of the spectral density energy is concentrated at the frequencies $f = mz_bn$ revealing the RSI modes.

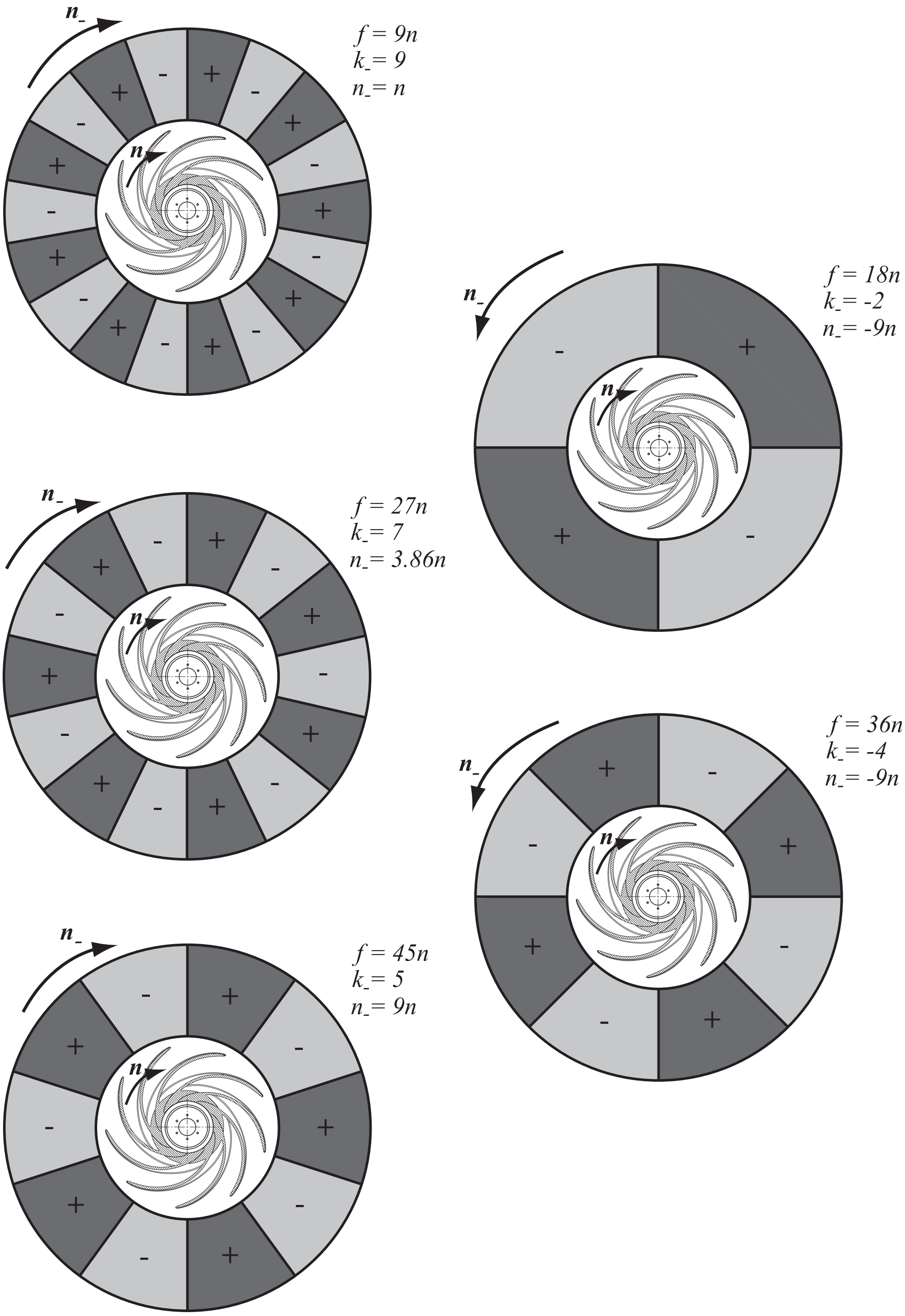
n_
f = 9n
k_= 9
n_= n
n
f = 18n
k_= -2
n_= -9n
n_
n
f = 27n
k_= 7
n_= 3.86n
n_
n
f = 36n
k_= -4
n_= -9n
n_
n
f = 45n
k_= 5
n_= 9n
n_
n

Figure 7.1: Shape of the five most predominant RSI rotating pressure modes for the case of $z_b = 9$ impeller blades and $z_o = 20$ guide vanes.

Nevertheless, the pressure fluctuations are predominant at the frequencies corresponding to the fundamental $f = 9n$ and the second harmonic $f = 18n$ of the RSI.

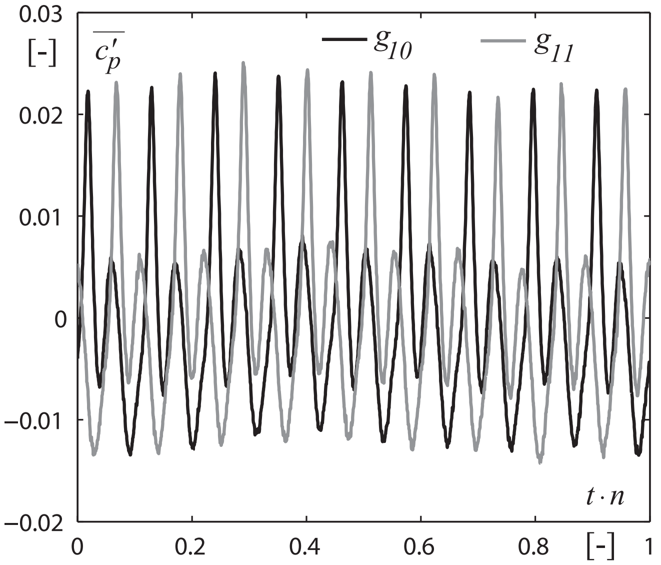

Figure 7.2: Phase average of the pressure factor fluctuations monitored by the sensors g_{10} and g_{11} over 42 impeller revolutions.

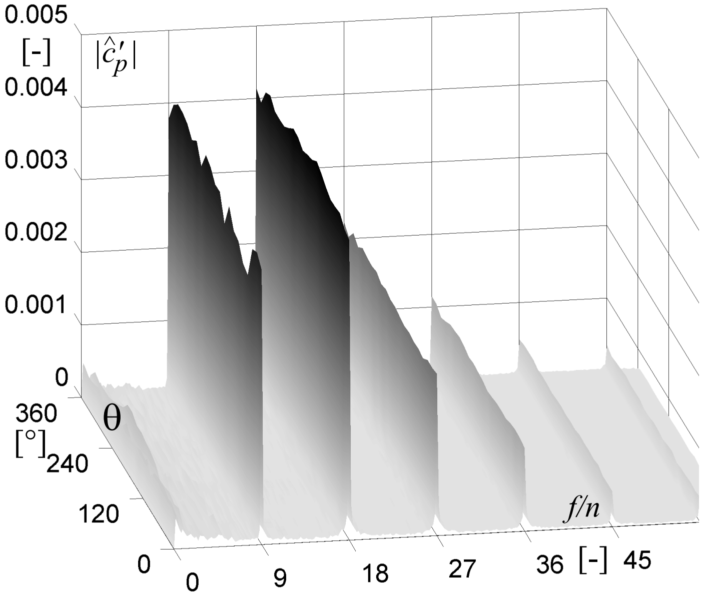

Figure 7.3: Waterfall diagram of the amplitude spectra of the pressure factor fluctuations against the angular position θ of the pressure sensors in the rotor-stator vaneless gap, namely g_i $(1 < i < 20)$.

In Figure 7.4, the spectra amplitude value of pressure fluctuations $|\hat{c}_p'|$ at the frequencies $f = mz_b n$ corresponding to the RSI fundamental and the harmonics are represented against the angular position θ in the rotor-stator gap. The standard deviation indicating the variation from the mean value is represented by intervals.

The low standard deviations highlight the reliability of the measurements. The pressure fluctuations amplitude at the RSI 2^{nd} harmonic is slightly higher than the one at the fundamental. At the 5^{th} harmonic $f = 45n$, the pressure fluctuations amplitude is more than 8 times inferior to the amplitude at the 2^{nd} harmonic frequency $f = 18n$.

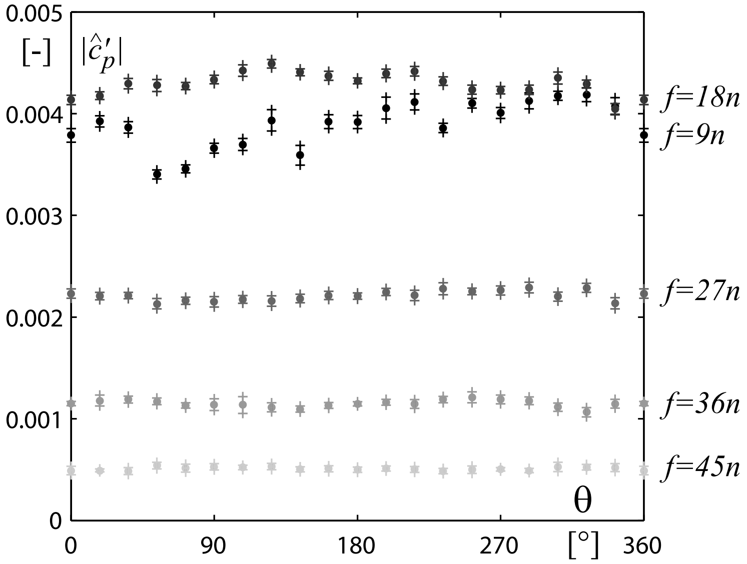

Figure 7.4: Values of the amplitude spectra of the pressure factor fluctuations $|\hat{c}'_p|$ at the frequencies $f = mz_b n$ corresponding to the RSI fundamental and the first four harmonics, against the angular position θ in the rotor-stator gap.

In Figure 7.5, the pressure fluctuations are radially represented at 20 equidistant angular positions in the rotor-stator gap during a period corresponding to $\frac{1}{9}$ of the impeller rotation period $\frac{1}{n}$. The frame rate is set to $FPS = 10 \cdot 9n$. The pressure fluctuation factor is normalized so as to get a qualitative visualization of the circumferential pressure evolution.

The circumferential evolution of the pressure fluctuations is rather disorganized, but one may nevertheless distinguish a pressure mode rotating at $f = 9n$ in the opposite direction to the impeller rotation.

In a similar way, in Figures 7.6 to 7.10, the pressure fluctuations at the RSI fundamental, 2^{nd}, 3^{rd}, 4^{th} and 5^{th}, harmonics are represented, respectively. The magnitude and phase of each of these RSI modes are extracted from the Hamming windowed FFT and the corresponding "filtered" time signals are reconstructed. The values are monitored at 20 equidistant angular positions in the rotor-stator gap during a period corresponding to $\frac{1}{2}$, $\frac{1}{18}$, $\frac{1}{9}$, $\frac{1}{18}$ and $\frac{1}{18}$ of the impeller rotation period $\frac{1}{n}$, respectively. The frame rate is chosen in order to fulfill the Shannon-Nyquist theorem and it is set to $FPS = 10 \cdot 2n$, $FPS = 10 \cdot 18n$, $FPS = 10 \cdot 9n$, $FPS = 10 \cdot 18n$, $FPS = 10 \cdot 18n$, respectively. As for the pressure fluctuations raw signal, in Figure 7.5, these filtered signals are normalized so as to get a qualitative visualization of the circumferential pressure evolution.

As predicted at the beginning of the section, the circumferential evolution of the pressure fluctuations at the RSI fundamental $f = 9n$ exhibits a 9-nodal diameter mode

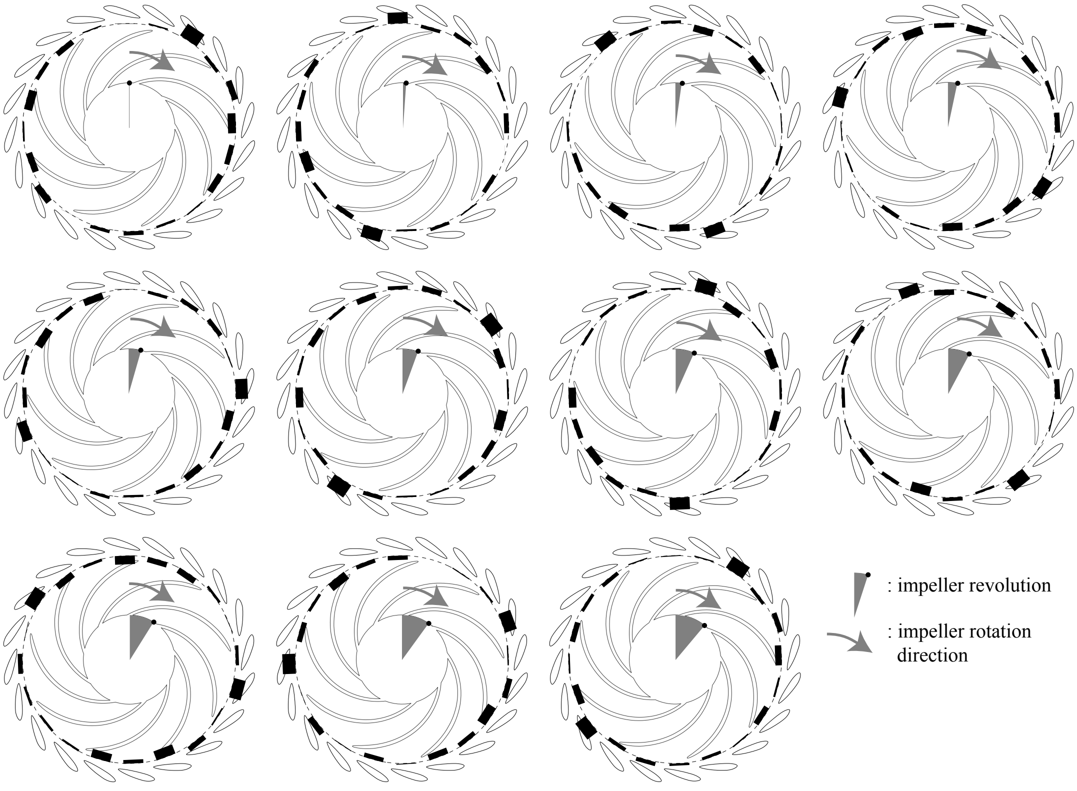

Figure 7.5: Qualitative circumferential evolution of the pressure fluctuations in the rotor-stator gap during $\frac{1}{9n}$ s at a frame rate $FPS = 10 \cdot 9n$.

rotating at the same frequency as the impeller $n_{-} = n$, see Figure 7.6. As already mentioned above, in the literature, some authors mention the presence of a 11-nodal diameter mode at this frequency. It is certainly a confusion, since the 9-nodal diameter mode clearly predominates in this study. Moreover, the combination of z_b impeller blades with z_o guide vanes induces a spatial modulation which might erroneously be confused with a 2-nodal diameter mode. Finally, the small number of monitoring points compared to the number of diametrical nodes may make erroneously believe that the mode is rotating in the opposite direction to the impeller.

At the RSI 2^{nd} harmonic, the circumferential shape of the pressure mode is a 2-nodal diameter mode rotating at $n_{-} = 9n$ in the opposite direction to the impeller, see Figure 7.7, as forecasted by the theory. This mode may already be observed in the pressure fluctuations circumferential evolution without filtering, see Figure 7.5.

At the RSI 3^{rd} harmonic, the circumferential shape of the pressure mode is a 7-nodal diameter mode rotating at a rotating frequency slightly inferior to $n_{-} = 4n$, as predicted, see Figure 7.8.

At the RSI 4^{th} harmonic, the pressure mode features 4-nodal diameters and rotates at $n_{-} = -9n$ in the opposite direction to the impeller, see Figure 7.9.

At the RSI 5^{th} harmonic frequency, the circumferential shape of the pressure mode features 5-nodal diameters rotating at the frequency $n_{-} = 9n$ in the same direction as the

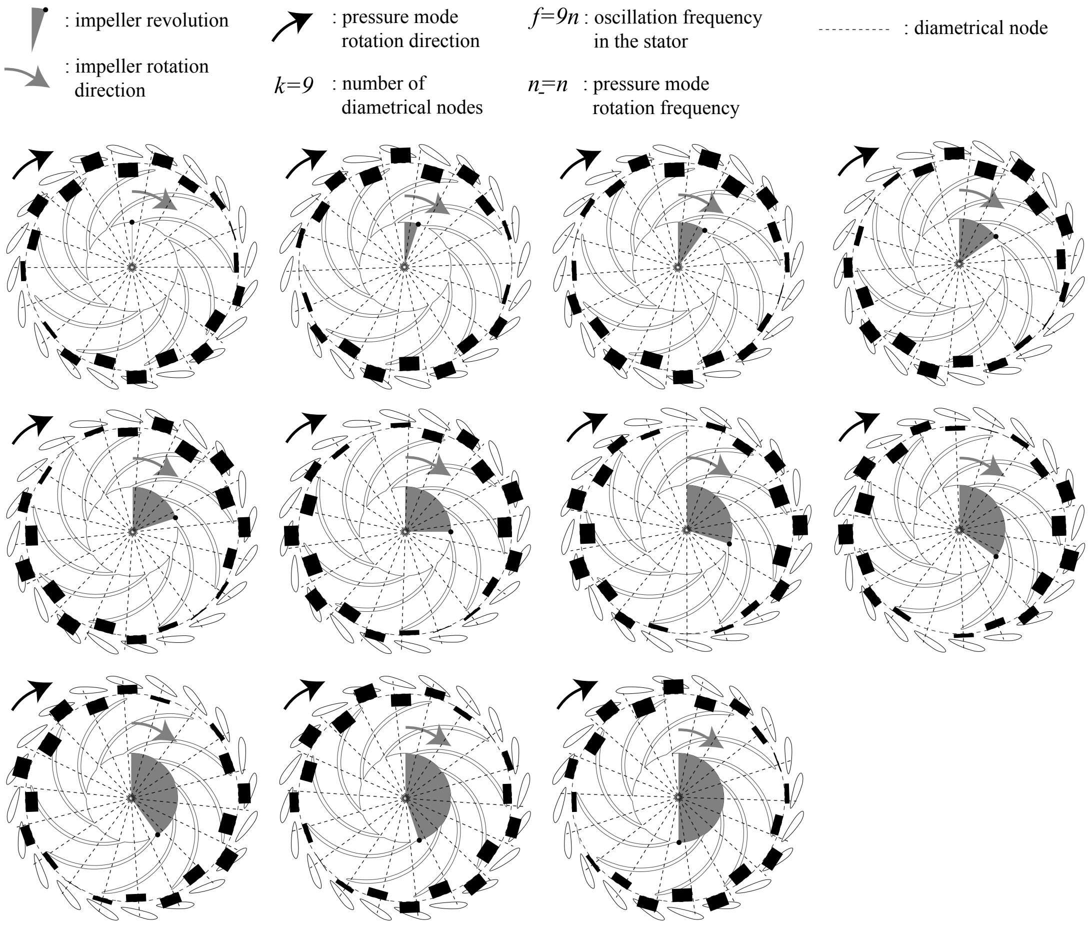
: impeller revolution
: impeller rotation direction
: pressure mode rotation direction
$k=9$: number of diametrical nodes
$f=9n$: oscillation frequency in the stator
$n_-=n$: pressure mode rotation frequency
: diametrical node

Figure 7.6: Qualitative circumferential evolution of the pressure fluctuations at the RSI fundamental $f = 9n$ in the rotor-stator gap, during $\frac{1}{2}$ of impeller revolution at a frame rate $FPS = 10 \cdot 2n$.

impeller, see Figure 7.10.

Finally, this study of the rotating pressure modes due to RSI successfully agrees with the theoretical prediction in terms of frequency. At each f/n ratio, the pressure mode featuring k_- nodal diameters predominates, whereas the mode with k_+ nodal diameters is not energetic enough to be observed.

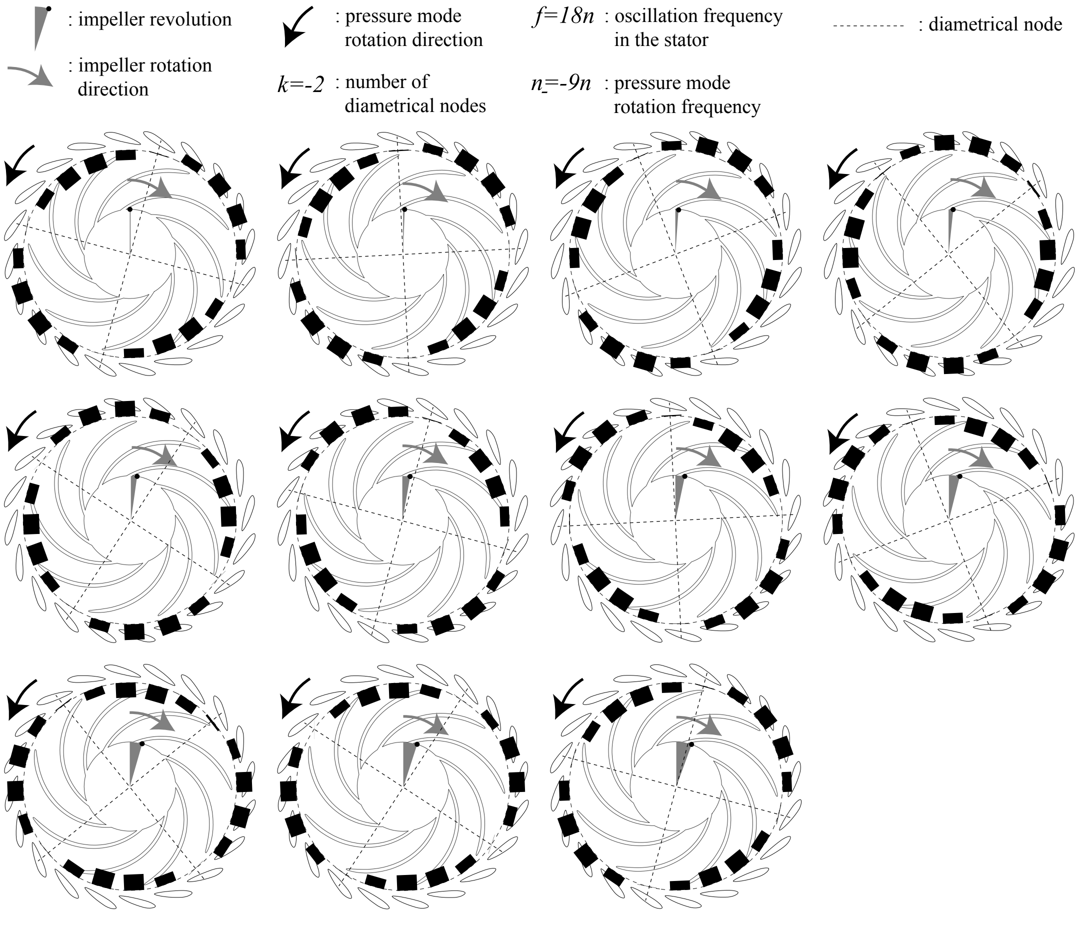
: impeller revolution
: impeller rotation direction
: pressure mode rotation direction
k=-2 : number of diametrical nodes
f=18n : oscillation frequency in the stator
n_=-9n : pressure mode rotation frequency
: diametrical node

Figure 7.7: Qualitative circumferential evolution of the pressure fluctuations at the RSI 2^{nd} harmonic $f = 18n$ in the rotor-stator gap, during $\frac{1}{18}$ of impeller revolution at a frame rate $FPS = 10 \cdot 18n$.

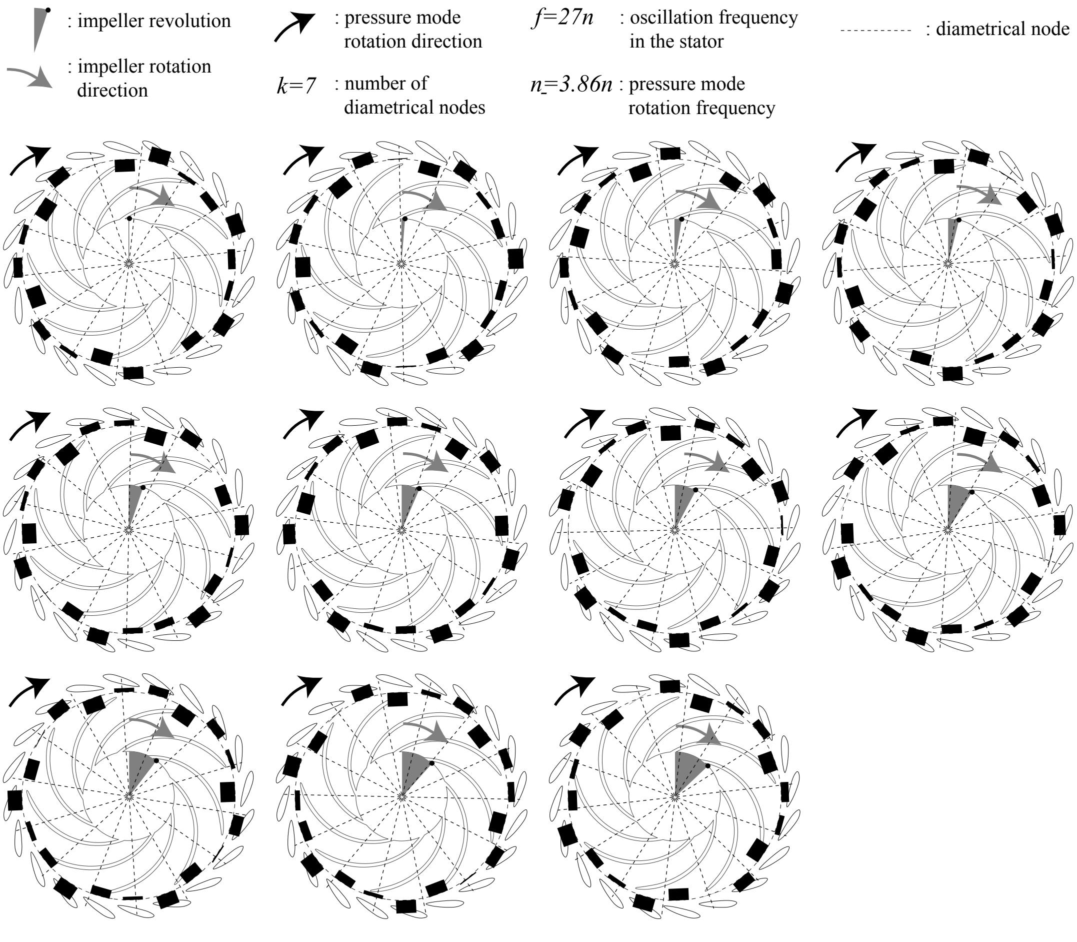
: impeller revolution
: impeller rotation direction
: pressure mode rotation direction
k=7 : number of diametrical nodes
f=27n : oscillation frequency in the stator
n_=3.86n : pressure mode rotation frequency
: diametrical node

Figure 7.8: Qualitative circumferential evolution of the pressure fluctuations at the RSI 3^{rd} harmonic $f = 27n$ in the rotor-stator gap, during $\frac{1}{2\cdot 3.86}$ of impeller revolution at a frame rate $FPS = 10 \cdot (2 \cdot 3.86n)$.

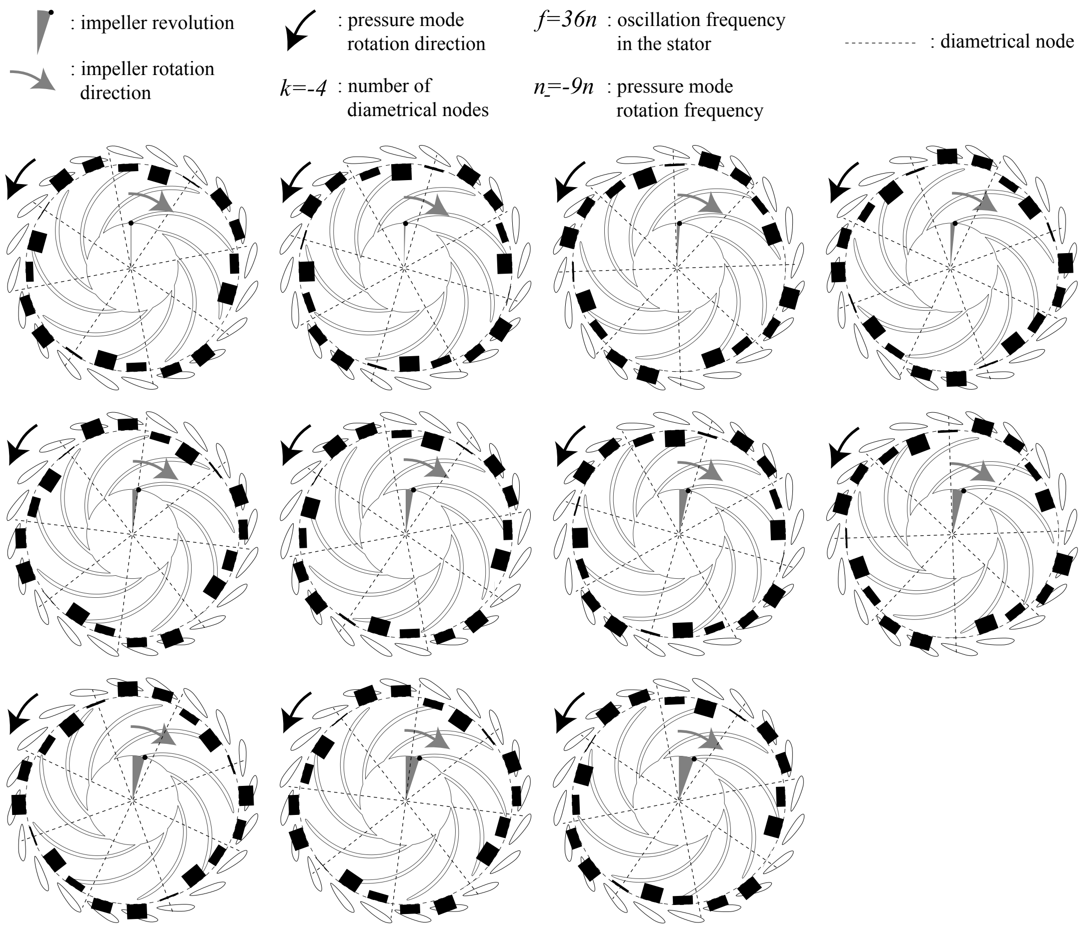
: impeller revolution
: impeller rotation direction
: pressure mode rotation direction
k=-4 : number of diametrical nodes
f=36n : oscillation frequency in the stator
n_=-9n : pressure mode rotation frequency
: diametrical node

Figure 7.9: Qualitative circumferential evolution of the pressure fluctuations at the RSI 4^{th} harmonic $f = 36n$ in the rotor-stator gap, during $\frac{1}{18}$ of impeller revolution at a frame rate $FPS = 10 \cdot 18n$.

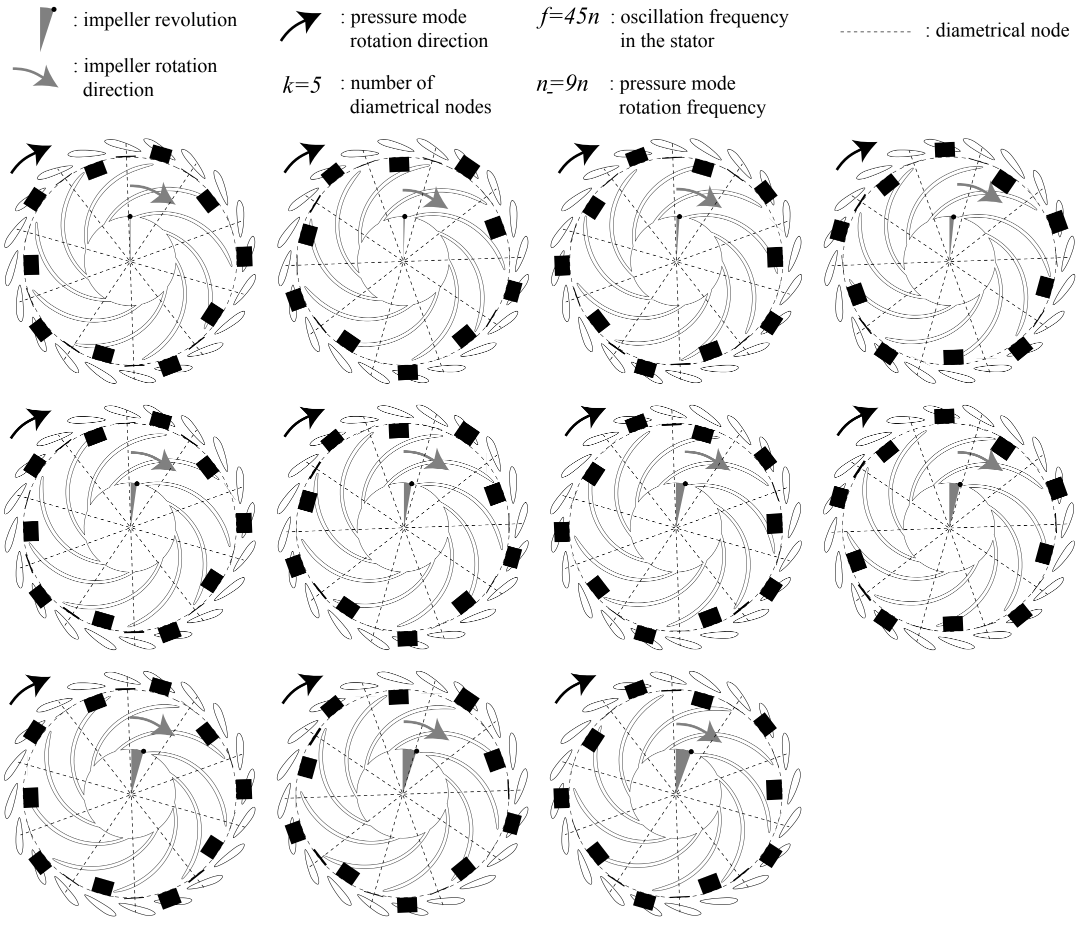
: impeller revolution
: impeller rotation direction
: pressure mode rotation direction
k=5 : number of diametrical nodes
f=45n : oscillation frequency in the stator
n_=9n : pressure mode rotation frequency
: diametrical node

Figure 7.10: Qualitative circumferential evolution of the pressure fluctuations at the RSI 5^{th} harmonic $f = 45n$ in the rotor-stator gap, during $\frac{1}{18}$ of impeller revolution at a frame rate $FPS = 10 \cdot 18n$.

Chapter 8

Impulse response

The results reported in this chapter are related to the impulse response in air, in water, model at rest, and model in operation. They are all the more relevant since the study of the guide vane cascade forced response, see Chapter 9, is based on them.

The modal analysis in air aims to detect the eigenmodes of the guide vanes and to compare them to the theoretical eigenmodes. The eigenfrequencies, the eigenshape and the structural damping related to the mode are studied.

The modal analysis in water, model at rest, intends to detect the eigenmodes of the guide vanes immersed in still water and, therefore, to identify the added mass as well as the hydrodynamic damping.

The impulse response of the guide vanes placed in the operating machine highlight the interaction between the vibrating guide vanes. It is the necessary preliminary approach to the guide vanes forced response study reported in the Chapter 9.

8.1 Guide vanes in place, dewatered model

The guide vanes are mounted in the pump-turbine model and clamped. The draft tube, the lower flange and the impeller are removed in order to have access to the guide vanes. They are hit with the help of an instrumented hammer, see Section 6.1.1, at the trailing edge in the direction perpendicular to the chord. This aims to excite, at least, the first bending and the first torsion eigenmodes. The sampling frequency is 30 kHz. The FFT is used to find the eigenfrequencies. The FFT is applied to 2^{14}-sample-long signals, which represents 0.546 s. The frequency resolution is therefore 1.83 Hz. 16 impacts are done which allow the spectra to be averaged.

To study the impulse response of the guide vanes, the bending displacement y and the torsion angle α are normalized with their maximum absolute value, $|y|_{max}$ and $|\alpha|_{max}$, respectively. This scaled values do not deteriorate the identification of neither the damping coefficients nor the eigenfrequencies.

8.1.1 Eigenfrequencies

In Figure 8.1, the first 0.25 s of typical normalized bending displacement and torsion angle impulse response signals of the two guide vanes, O_{10} and O_{11}, are plotted.

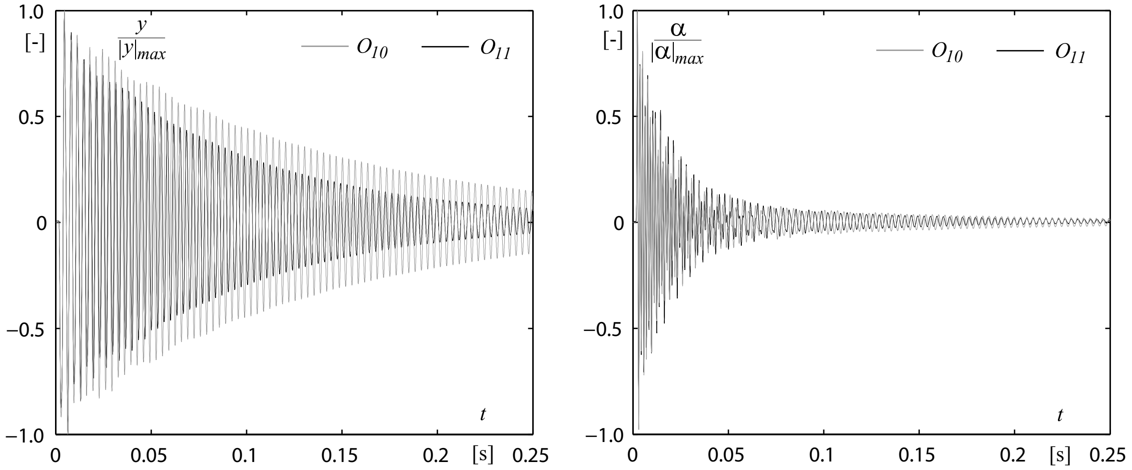

Figure 8.1: Impulse response in air: time signal of normalized bending displacement (left) and torsion angle (right).

In Figure 8.1, one may observe that the torsion signal is damped more than the bending signal. A single frequency predominates in the bending signal, whereas the torsion signal contains more frequencies.

In Figure 8.2, the amplitude spectra of the normalized bending displacement and torsion angle of the two guide vanes, O_{10} and O_{11}, are plotted.

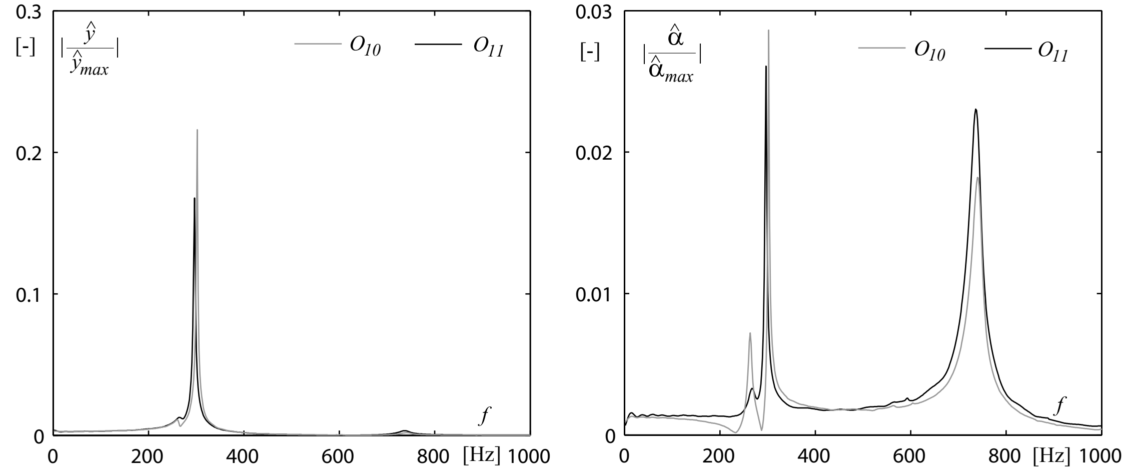

Figure 8.2: Impulse response in air: amplitude spectra of the guide vane O_{10} and O_{11} normalized bending displacement (left) and of the normalized torsion angle (right).

In Appendix B.4.1, the first bending and the first torsion eigenfrequencies are analytically estimated using the Rayleigh-Ritz method, R-R. The 1st bending eigenfrequency is found to be $f_{0,y}^{R-R} = 306$ Hz and the 1st torsion eigenfrequency is estimated at $f_{0,\alpha}^{R-R} = 645$ Hz. Two main frequencies, around 300 Hz and 740 Hz, are present in the bending and torsion signals, see Figure 8.2. In the following lines, it is shown that these two frequencies correspond to those of the eigenmodes analytically estimated.

Both analytical and experimental eigenfrequencies are reported in Table 8.1. The inertia, I^S and J^S, related to the first bending mode and to the first torsion mode, respectively, are also given. They are deduced from the stiffness constant, K^S and L^S , analytically determined in Appendix B.3 as follows:

$$I^S = \frac{K^S}{(2\pi f_{0,y})^2} \tag{8.1}$$

$$J^S = \frac{L^S}{(2\pi f_{0,\alpha})^2} \tag{8.2}$$

The relative difference between experimental and analytical frequencies, $\epsilon_{f^S_{0,y}}$ and $\epsilon_{f^S_{0,\alpha}}$, and mass/inertia, ϵ_{I^S} and ϵ_{J^S}, are also given in Table 8.1.

Table 8.1: First bending and first torsion eigenfrequencies of the guide vane O_{10} and O_{11} placed in air, $f^S_{0,y}$ and $f^S_{0,\alpha}$; relative difference $\epsilon_{f^S_{0,y}}$ and $\epsilon_{f^S_{0,\alpha}}$ from the theoretical eigenfrequencies; corresponding structural mass/inertia, I^S and J^S; and relative difference from theoretical values, ϵ_{I^S} and ϵ_{J^S}.

	O_{10}	**O_{11}**	**Analytical**
$f^S_{0,y}$	302 Hz	297 Hz	306 Hz
$\epsilon_{f^S_{0,y}}$	-1.3 %	-2.9 %	-
I^S	0.33 kg	0.34 kg	0.32 kg
ϵ_{I^S}	3.1 %	6.3 %	-
$f^S_{0,\alpha}$	740 Hz	736 Hz	645 Hz
$\epsilon_{f^S_{0,\alpha}}$	14.7 %	14.1 %	-
J^S	$1.75 \cdot 10^{-4}$ kg · m^2	$1.77 \cdot 10^{-4}$ kg · m^2	$2.31 \cdot 10^{-4}$ kg · m^2
ϵ_{J^S}	-24.2 %	-23.3 %	-

The $\epsilon_{f^S_{0,y}}$ absolute value is less than 3% for both guide vanes and, therefore it may easily be concluded that the 302 Hz and 297 Hz frequencies correspond to the first bending eigenfrequency of the guide vanes O_{10} and O_{11}, respectively.

The $\epsilon_{f^S_{0,\alpha}}$ values are comprised between 14% and 15%. Nevertheless, one may state that the 740 Hz and 736 Hz frequencies are those of the first torsion eigenmode of the guide vanes O_{10} and O_{11}, respectively, for three main reasons. First, no other frequency predominates in the corresponding frequency range. Second, the torsion signal is much more responsive at this frequency than the bending signal. Finally, the identification of the analytical torsion eigenfrequency is based on the balance between the deformation and the kinetic energies, see Appendix B.4.1. For simplicity reason, these energies are determined for a pure torsion motion. In the real case, the eccentricity of the hydrofoil center of gravity from the stem neutral axis should make the deformation energy slightly higher and, at the same time, should increase the theoretical value of the torsion eigenfrequency.

Concerning the impulse response spectra plotted in Figure 8.2, the amplitude of the peaks must be put into perspective. One should keep in mind that the Fourier transform is applied to an exponentially decreasing oscillating signal. The bending mode is much more energetic than the torsion mode; the former being even present in the torsion signal. The torsion mode is much more damped and, therefore, only the bending one remains on a vast range of the torsion signal length, making its amplitude high in the averaged spectra. Finally, on both angle and displacement spectra, a smaller peak appears at $f = 264$ Hz and $f = 270$ Hz for the guide vane O_{10} and O_{11}, respectively. We suppose the presence of the frequency of the bending eigenmode in the direction perpendicular to the y-direction. The torsion strain gage bridge is indeed more sensitive to this motion type. The peak hardly appears in the bending displacement signal; the bending strain gage bridge being theoretically not sensitive to this type of motion.

8.1.2 Structural damping

The structural damping of the two guide vanes, O_{10} and O_{10}, is identified from the impulse response signals. Because the time signal contains many frequencies, it is first filtered. A Butterworth band-pass filter centered on the corresponding eigenfrequency is used. The characteristics of the filters are given in Table 8.2.

Table 8.2: Characteristics of the Butterworth band-pass filters.

Mode	**Filter order**	**Cut-off frequencies**
Bending	3	[250 Hz;350 Hz]
Torsion	3	[690 Hz;790 Hz]

The frequency response magnitude and phase of the Butterworth filters for the cases of bending and torsion modes are plotted in Figure 8.3. It may be observed that the filters may alter the time signals in terms of phase if the cut-off frequencies are not equally positioned on both sides of the concerned frequency. Nevertheless, in terms of amplitude, the signals are not modified so long as the cut-off frequencies are sufficiently far from each other and, therefore, the filter has no repercussion on the damping identification accuracy.

Then, by applying the Hilbert transform [68], the envelope of the filtered signal is obtained. Finally, an exponential fitting of the envelope is applied for estimating the damping value. The fitting curve $h\left(t\right)$ is expressed as:

$$h\left(t\right) = h^0 \cdot e^{-\lambda \cdot t} \tag{8.3}$$

where h^0 is the fitting curve y-intercept and λ, the damping coefficient.

In Figure 8.4, the identification procedure of structural damping of the bending mode and of the torsion mode is illustrated for the case of the guide vane O_{10}. The original signal, the filtered signal, the envelope and the fitting curve are plotted.

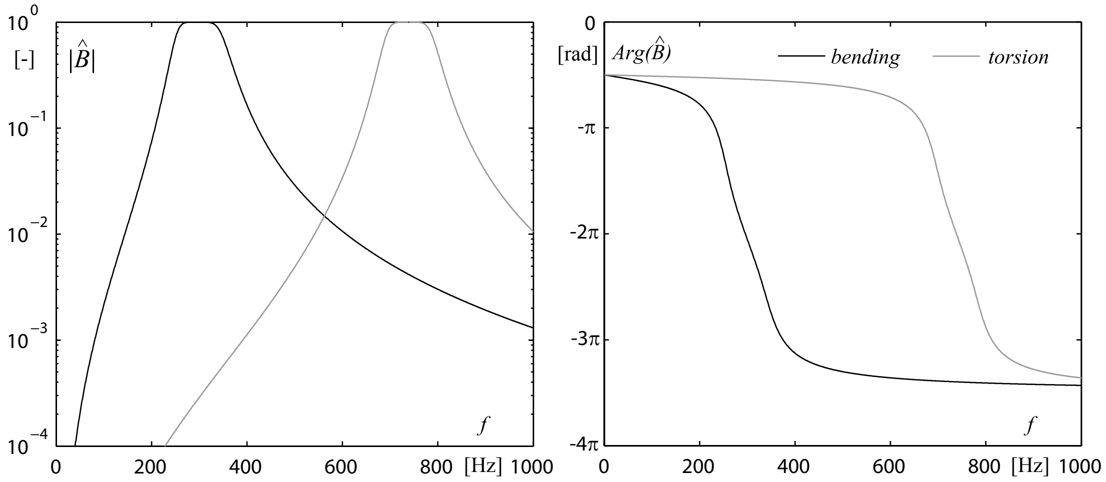

Figure 8.3: Butterworth filter frequency response magnitude and phase for the bending and the torsion modes.

The damping constants, C^S and D^S and damping factors, η_y^S and η_α^S are defined as functions of the damping coefficients as follows:

$$C^S = 2I^S\lambda_y^S \tag{8.4}$$

$$\eta_y^S = \frac{\lambda_y^S}{2\pi f_{0,y}^S} \tag{8.5}$$

$$D^S = 2J^S\lambda_\alpha^S \tag{8.6}$$

$$\eta_\alpha^S = \frac{\lambda_\alpha^S}{2\pi f_{0,\alpha}^S} \tag{8.7}$$

$$\tag{8.8}$$

The damping values are averaged over 16 records. The mean values of the damping constants and factors are listed in Table 8.3. The standard deviations are also indicated.

Table 8.3: Structural damping constants and factors of the guide vanes O_{10} and O_{11}.

	$\mathbf{O_{10}}$	$\mathbf{O_{11}}$
damping factor η_y^S	(0.40 ± 0.01) %	(0.51 ± 0.05) %
damping constant C^S	$(5.00 \pm 0.12)\ \mathrm{kg \cdot s^{-1}}$	$(6.57 \pm 0.44)\ \mathrm{kg \cdot s^{-1}}$
damping factor η_α^S	(1.50 ± 0.07) %	(1.46 ± 0.09) %
damping constant D^S	$(0.024 \pm 0.001)\ \mathrm{kg \cdot m^2 \cdot s^{-1}}$	$(0.024 \pm 0.002)\ \mathrm{kg \cdot m^2 \cdot s^{-1}}$

The two guide vanes O_{10} and O_{11} feature relatively similar damping constant values. The damping of the guide vane O_{11} bending mode is nevertheless 30% higher than the guide vane O_{10}, whereas the damping of the guide vane O_{11} torsion mode is 3% lower

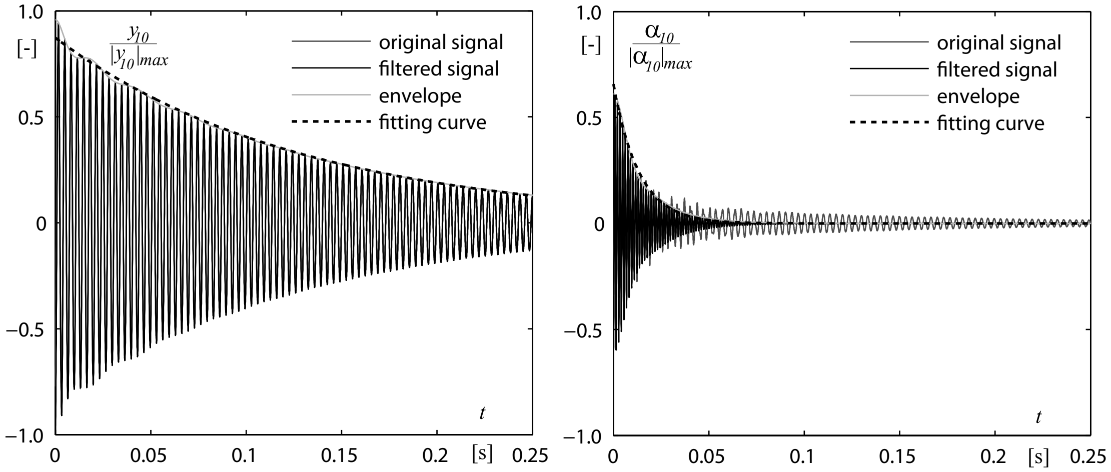

Figure 8.4: Identification procedure of structural damping of the bending mode (left) and of the torsion mode (right) for the case of the guide vane O_{10} in air.

than the guide vane O_{10}. The low standard deviation values indicate fair measurements and reliable damping results.

8.2 Guide vanes in place, still water

The guide vanes are excited with the help of an immersed spark plug, flush mounted in the lower flange in a guide vane channel, producing a strong shock wave, see Section 6.1.2. The guide vanes are mounted in the model and clamped. To avoid any influence of the neighboring guide vanes, these are completely removed from the model. The signals are recorded at 20 kHz. The Fast Fourier Transforms are applied to 2^{14}-sample-long signals, which correspond to 0.819 s, leading to 1.22 Hz frequency resolution. The spectra are averaged over 8 records for the two guide vanes.

8.2.1 Eigenfrequencies

In Figure 8.5, the first 0.25 s of typical normalized bending displacement and torsion angle signals, for the two guide vanes, O_{10} and O_{11}, placed in water, model at rest, are plotted. The bending and torsion signals are damped more than in air. Moreover, the guide vane O_{10} presents a higher damping than the guide vane O_{11}. One may also remark the lower frequency of the vibrations, at least in the bending displacement signal.

In Figure 8.6, the amplitude spectra of the normalized bending displacement and of the normalized torsion angle are plotted. In the torsion angle amplitude spectra, the amplitude at the bending eigenfrequency is lower than the one observed in the corresponding amplitude spectra in air, because of the higher damping of the vibrations in water, model at rest, and because of the added mass.

The Table 8.4 lists the eigenfrequencies of the guide vanes O_{10} and O_{11} placed in still water, the added mass/inertia for the bending and torsion modes and the ratio of added

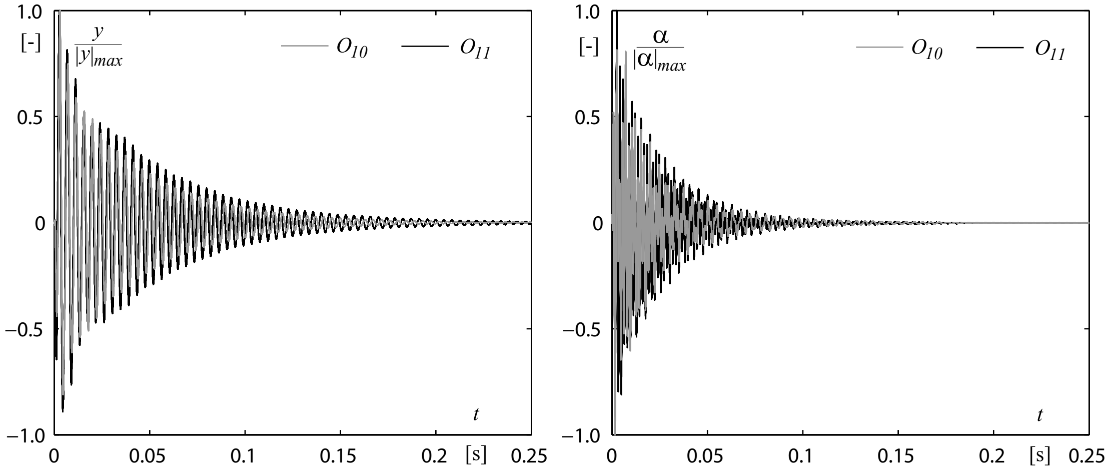

Figure 8.5: Impulse response in water, model at rest: time signal of normalized bending displacement (left) and torsion angle (right).

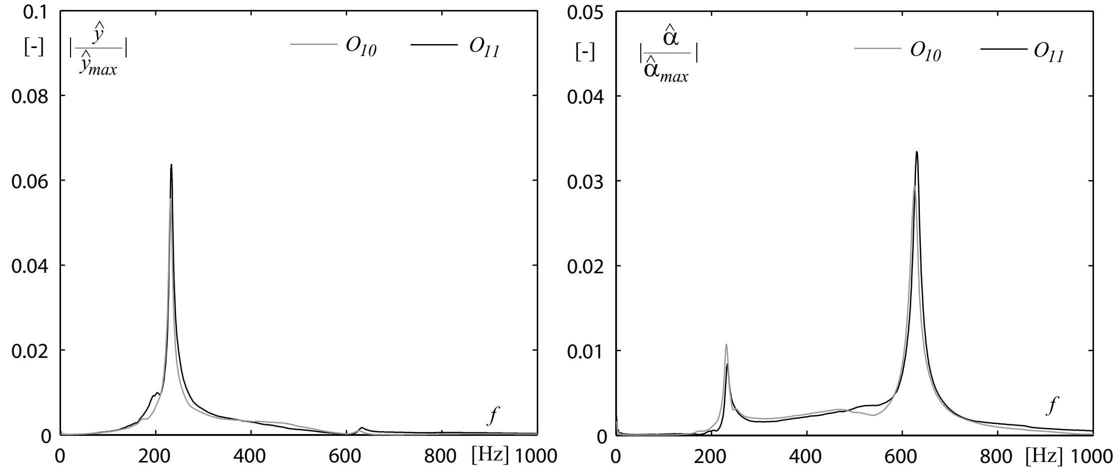

Figure 8.6: Impulse response in still water: magnitude of amplitude spectra of the guide vane O_{10} and O_{11} normalized bending displacement (left) and of the normalized torsion angle (right).

to structural mass/inertia. The fluid mass motion induced by the vibrations of the guide vanes reduces the value of the eigenfrequencies. The added mass/inertia, I^f and J^f, is deduced from the structural inertia, I^S and J^S, and from the eigenfrequencies in air and in water, model at rest. The eigenfrequencies in air may be estimated as follows:

$$f_{0,y}^S = \frac{1}{2\pi}\sqrt{\frac{K^S}{I^S}} \tag{8.9}$$

$$f_{0,\alpha}^S = \frac{1}{2\pi}\sqrt{\frac{L^S}{J^S}} \tag{8.10}$$

Table 8.4: Guide vanes first bending and first torsion eigenfrequencies in water, model at rest, $f^f_{0,y}$ and $f^f_{0,\alpha}$, added mass/inertia, I^f and J^f, for the bending and torsion modes, respectively, and ratio of structural inertia to added mass/inertia.

	O_{10}	**O_{11}**
$f^f_{0,y}$	231 Hz	233 Hz
I^f	0.23 kg	0.21 kg
I^f/I^S	69.7 %	61.8 %
$f^f_{0,\alpha}$	626 Hz	630 Hz
$J^{f,\alpha}$	$6.95 \cdot 10^{-5}$ kg · m²	$6.45 \cdot 10^{-5}$ kg · m²
$J^{f,\alpha}/J^S$	39.7 %	36.4 %

and the eigenfrequencies in water, model at rest, are expressed as:

$$f^f_{0,y} = \frac{1}{2\pi}\sqrt{\frac{K^S + K^f}{I^S + I^f}} \tag{8.11}$$

$$f^f_{0,\alpha} = \frac{1}{2\pi}\sqrt{\frac{L^S + L^f}{J^S + J^f}} \tag{8.12}$$

The fluid stiffness in still water is zero, see Section 3.3, and using eqs. 8.9 to 8.12, one obtains the expression for the added mass I^f and the added inertia $J^{f,\alpha}$:

$$I^f = I^S \cdot \left(\left(\frac{f^S_{0,y}}{f^f_{0,y}}\right)^2 - 1\right) \tag{8.13}$$

$$J^{f,\alpha} = J^S \cdot \left(\left(\frac{f^S_{0,\alpha}}{f^f_{0,\alpha}}\right)^2 - 1\right) \tag{8.14}$$

For the bending and the torsion modes, the added mass and the added inertia are significant and, thus, strongly affect the eigenfrequencies. The influence is nevertheless higher for the bending mode than for the torsion mode. For the bending mode, the added mass represents 69.7% and 61.8% of the structural mass for the guide vanes O_{10} and O_{11}, respectively. For the torsion mode, the added inertia represents 39.7% and 36.4% of the structural inertia for the guide vanes O_{10} and O_{11}, respectively.

8.2.2 Hydrodynamic damping

The damping of the two guide vanes, O_{10} and O_{11} placed in still water, is identified from the impulse response signals, as in the case in air. Because the time signal contains many frequencies, it is first filtered. A Butterworth band-pass filter centered on the corresponding eigenfrequency is applied. The characteristics of the filters are given in Table 8.5.

The frequency response magnitude and phase of the Butterworth filters for the cases of bending and torsion modes are plotted in Figure 8.7. As in the case in air, the time signals

Table 8.5: Characteristics of the Butterworth band-pass filters.

Mode	Filter order	Cut-off frequencies
Bending	3	[180 Hz;280 Hz]
Torsion	3	[580 Hz;680 Hz]

may be modified in terms of phase if the cut-off frequencies are not positioned equally on both sides of the concerned frequency. No alteration in terms of amplitude should occur so long as the cut-off frequencies are sufficiently far from each other. Therefore, the filters have no repercussion on the damping identification accuracy.

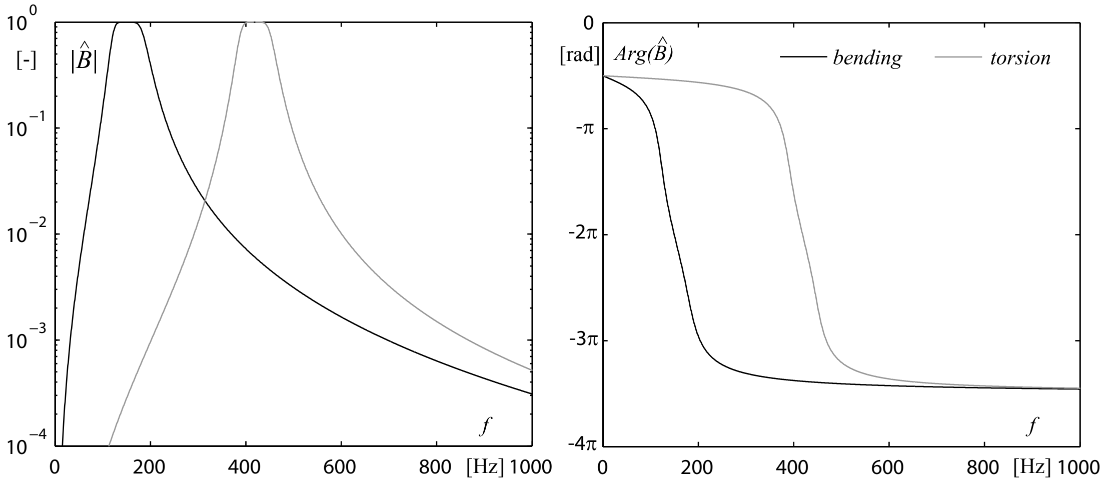

Figure 8.7: Butterworth filter frequency response magnitude and phase for the bending and torsion modes in still water.

Then, the similar procedure as in air is followed for estimating the damping of the guide vane in water, model at rest.

In Figure 8.8, the bending and torsion eigenmodes damping identification procedure is illustrated for the case in water, model at rest. The original signal, the filtered signal, the envelope and the fitting curve are plotted for the guide vane O_{10}.

The damping values are averaged over 8 records for the two guide vanes. The damping constant and factor mean values are listed in Table 8.6. The standard deviations are also indicated. The hydrodynamic damping constants, C^f and $D^{f,\alpha}$, are determined by subtracting the structural damping constants, C^S and D^S, from the total damping constants, $C = 2I\lambda_y$ and $D = 2J\lambda_\alpha$, by assuming the linearity of damping with the frequency. Therefore, the hydrodynamic damping may directly be expressed as function of the inertia terms, the total damping coefficients, λ_y and λ_α and the structural damping constants, C^S and D^S, as follows:

$$C^f = C - C^S = 2I\lambda_y - C^S = 2\left(I^S + I^f\right)\cdot\lambda_y - C^S \tag{8.15}$$

$$D^{f,\alpha} = D - D^S = 2J\lambda_\alpha - D^S = 2\left(J^S + J^f\right)\cdot\lambda_\alpha - D^S \tag{8.16}$$

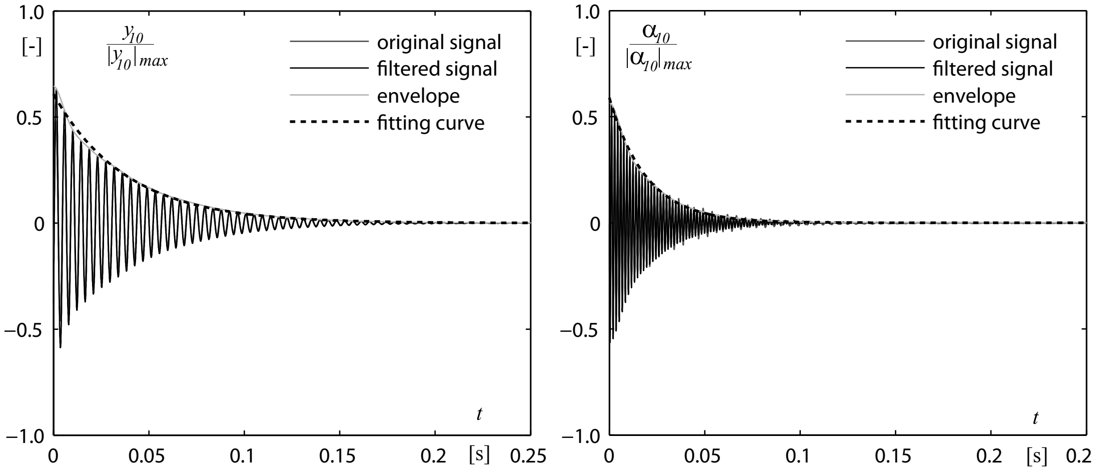

Figure 8.8: Damping identification procedure of the bending mode (left) and the torsion mode (right) for the case of the guide vane O_{10} placed in still water.

Table 8.6: Damping constant and factor values for the guide vanes O_{10} and O_{11} in still water.

	$\mathbf{O_{10}}$	$\mathbf{O_{11}}$
total damping factor η_y	(1.79 ± 0.03) %	(1.67 ± 0.22) %
total damping constant C	(29.2 ± 0.4) $\mathrm{kg \cdot s^{-1}}$	(26.8 ± 3.6) $\mathrm{kg \cdot s^{-1}}$
hydro. damp. const. C^f	(24.2 ± 0.5) $\mathrm{kg \cdot s^{-1}}$	(20.2 ± 4.0) $\mathrm{kg \cdot s^{-1}}$
total damping factor η_α	(1.31 ± 0.23) %	(1.15 ± 0.06) %
total damping constant D	(0.025 ± 0.004) $\mathrm{kg \cdot m^2 \cdot s^{-1}}$	(0.022 ± 0.001) $\mathrm{kg \cdot m^2 \cdot s^{-1}}$
hydro. damp. const. $D^{f,\alpha}$	(0.001 ± 0.005) $\mathrm{kg \cdot m^2 \cdot s^{-1}}$	(-0.002 ± 0.003) $\mathrm{kg \cdot m^2 \cdot s^{-1}}$

In Table 8.6, it may be observed that the damping factor of the bending motion is higher than the one of the torsion motion, whereas it was the inverse in air. The two guide vanes feature relatively similar damping values. The low standard deviation indicates reliable results. On the one hand, for the torsion mode, the hydrodynamic damping constant value is found to be negligible, which agree with the potential flow approach. At zero mean flow velocity, only the fluid inertia terms remain in eq. 3.20; the dissipative terms vanishing. On the other hand, for the bending mode, the hydrodynamic damping constant value is 4.8 and 3.0 times higher than the structural damping constant value for the guide vanes O_{10} and O_{11}, respectively. In the absence of mean flow velocity, the energy dissipation is certainly due to the viscosity of the fluid.

8.3 Guide vanes in place, model in operation

Should the pump-turbine be operating, one encounters many difficulties in the eigenfrequencies and damping identification. On the one hand, the RSI and the turbulent noise perturb the simple impulse response of the guide vanes. The RSI is well known and the operating conditions have been chosen in order not to have neither the RSI fundamental frequency nor the harmonics close to the guide vanes eigenfrequencies. Therefore, keeping the machine operating at the BEP at 18° opening angle, the specific energy is set to $E = 98$ J·kg^{-1} and the rotation frequency to $n = 7.4$ Hz. The discharge is thus $Q = 0.108$ m^3·s^{-1}. The flow turbulence noise must be dealt with. One will see in the following sections that it is still present in the filtered signals. On the other hand, the excitation procedure which consists of the rapid growth of a vapor bubble produced by an immersed spark plug, providing a strong shock wave in the fluid, see Section 6.1.2, is limited by the operating head. Above the specific energy value $E = 98$ J·kg^{-1}, the static pressure in the stator is too high for the shock wave to be energetic enough in order to excite the guide vanes. Sometimes, the vapor bubble is not even formed. The signals are recorded at 20 kHz. The Fast Fourier Transforms are applied to 2^{14}-sample-long signals, which correspond to 0.819 s, leading to 1.22 Hz frequency resolution. The spectra are averaged over 8 records for the two guide vanes.

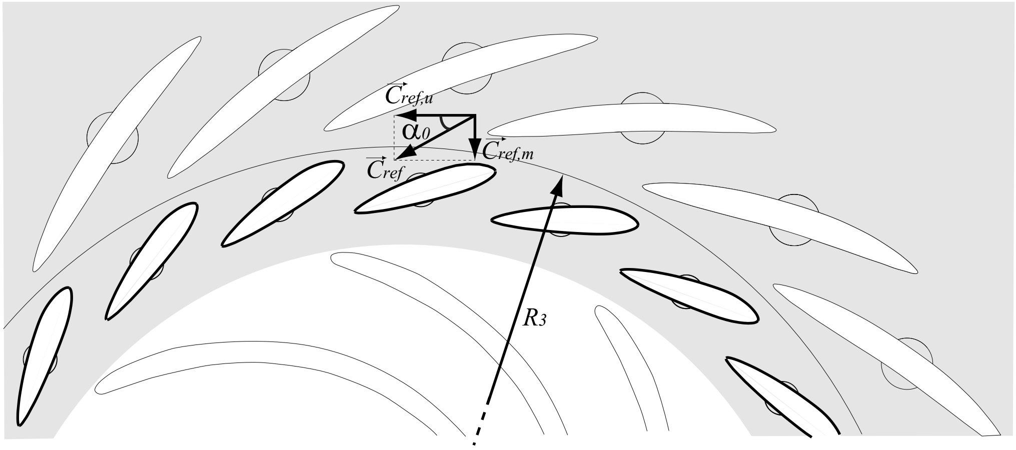

Figure 8.9: Definition of the reference flow velocity C_{ref} at the radius R_3.

The reduced frequency, comparing the oscillating period $\frac{1}{f}$ with the advection time $\frac{L}{C_{ref}}$, is defined as follows [56]:

$$\kappa = \frac{2\pi f L/2}{C_{ref}} = \frac{\pi f L}{C_{ref}} \tag{8.17}$$

where L is the chord length and C_{ref}, a reference flow velocity defined as follows, see Figure 8.9:

$$\begin{aligned} C_{ref} &= \frac{C_{ref,m}}{sin\left(\alpha_o\right)} = \frac{Q}{A \cdot sin\left(\alpha_o\right)} = \frac{Q}{2\pi R_3 \mathrm{B}_o sin\left(\alpha_o\right)} \\ &= \frac{0.108}{2\pi \cdot 0.325 \cdot 0.036 \cdot sin\left(18°\right)} = 4.8\mathrm{m} \cdot \mathrm{s}^{-1} \end{aligned} \tag{8.18}$$

A being the surface crossed by the flow and B_o, the guide vane channel width.

The reduced frequency takes the values $\kappa_y = 15$ and $\kappa_\alpha = 41$ for the bending and the torsion modes, respectively, which show the relevance of the unsteady effects.

8.3.1 Eigenfrequencies

In Figure 8.10, the first 0.25 s of typical normalized bending displacement and torsion angle signals, for the two guide vanes, O_{10} and O_{11}, placed in the operating machine, are plotted. One may distinguish the response to a permanent excitation in the bending displacement time signals after the impulse response is damped. The guide vane O_{10} is damped less rapidly than O_{11}; the response of the former to the permanent excitation featuring an even higher amplitude. In the torsion angle time signals, the permanent excitation is negligible compared to the impulse response.

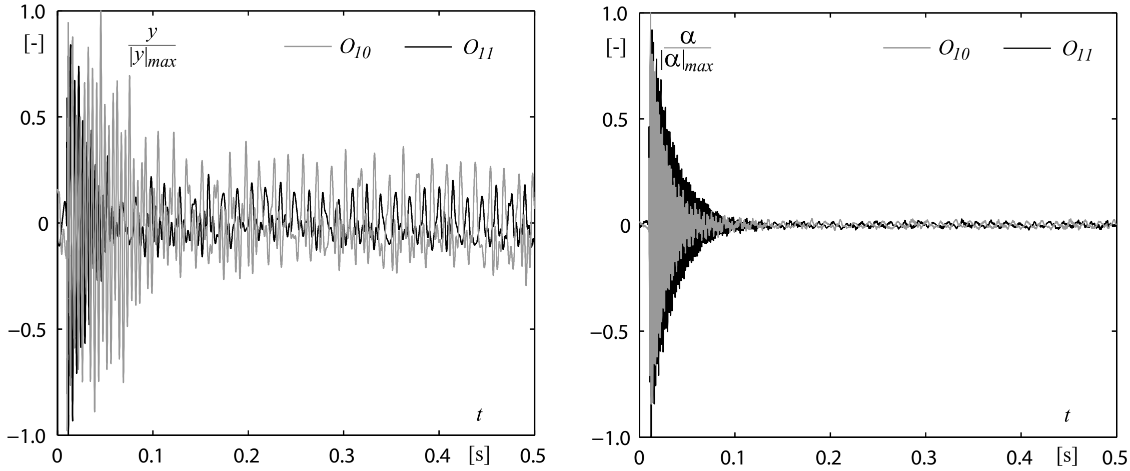

Figure 8.10: Guide vane impulse response, model in operation: time signal of normalized bending displacement (left) and torsion angle (right).

In Figure 8.11, the averaged amplitude spectra of the normalized bending displacement and of the normalized torsion angle are plotted. The permanent excitation observed in the time signals is clearly observed at 67 Hz, 134 Hz and 200 Hz with peaks representing the response to the fundamental, the 2^{nd} and the 3^{rd} harmonics of the RSI, respectively. In the torsion angle amplitude spectra, the peaks at the two eigenfrequencies are much higher than the one related to the RSI fundamental. That is, the guide vanes are excited by the RSI more in terms of bending than in terms of torsion.

The Table 8.7 lists the guide vanes O_{10} and O_{11} eigenfrequencies in the model in operation, the added mass/inertia for the bending and torsion modes and the ratio of added to structural mass/inertia. The added mass and inertia are found using eqs. 8.13 and 8.14.

The eigenfrequencies are slightly higher when operating the machine than those in water, model at rest. The bending eigenfrequency of the guide vane O_{10} is 1.3% higher than the value in still water, whereas the torsion eigenfrequency is 2.4 % higher. In the bending eigenfrequencies range, the guide vane O_{11} responds to two frequencies: 226 Hz and 236 Hz, see Figure 8.11. The guide vane O_{11} torsion eigenfrequency is 1.9 % higher than in still water. According to Conca et al. [22] and Brennen [17], the added mass and inertia should not vary between the cases in water, model at rest, and model in operation. These terms should actually be independent of the flow velocity. Therefore, the added

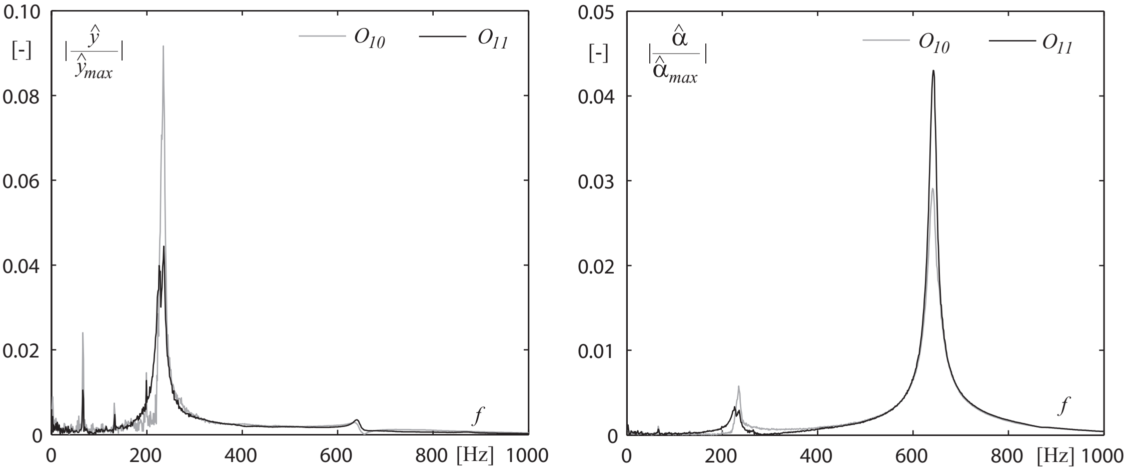

Figure 8.11: Guide vanes impulse response, model in operation: amplitude spectra of the guide vane O_{10} normalized bending displacement (left) and of the normalized torsion angle (right).

Table 8.7: Guide vanes first bending and first torsion eigenfrequencies in the model in operation, $f_{0,y}$ and $f_{0,\alpha}$, added mass/inertia, I^f and J^f, for the bending and torsion modes, respectively, and ratio of added to structural mass/inertia.

	$\mathbf{O_{10}}$	$\mathbf{O_{11}}$
$f^f_{0,y}$	234 Hz	226/236 Hz
I^f	0.22 kg	0.25/0.20 kg
I^f/I^S	66.7 %	73.5 %/58.8 %
$f^f_{0,\alpha}$	641 Hz	642 Hz
$J^{f,\alpha}$	$5.82 \cdot 10^{-5}$ kg · m^2	$5.56 \cdot 10^{-5}$ kg · m^2
$J^{f,\alpha}/J^S$	33.2 %	31.4 %

mass and inertia observed here must be brought by the vibrations of the neighboring guide vanes. The Chapter 9 is incidentally devoted to the identification of the contributions of the neighboring vibrating guide vane.

8.3.2 Hydrodynamic damping

The damping of the two guide vanes, O_{10} and O_{11} placed in the model in operation, is identified from the impulse response signals. As already mentioned, because the time signal contains many frequencies, it must first be filtered. Aiming to filter the maximum of flow turbulence noise, the very narrow frequency bandwidth is chosen for the bending mode. The characteristics of the filters are given in Table 8.8.

The same procedure mentioned in the preceding sections is used to identify the damping values.

In Figures 8.12 and 8.13, the damping identification procedure of the bending and

Table 8.8: characteristics of the band-pass filters in the case of the machine being operated.

Mode	Filter type	Cut-off frequencies
Bending	Butterworth (3^{rd} order)	[213 Hz;253 Hz]
Torsion	Butterworth (3^{rd} order)	[580 Hz;680 Hz]

torsion eigenmodes is illustrated for the guide vanes O_{10} and O_{11}, respectively. The original signal, the filtered signal, the envelope and the fitting cure are plotted.

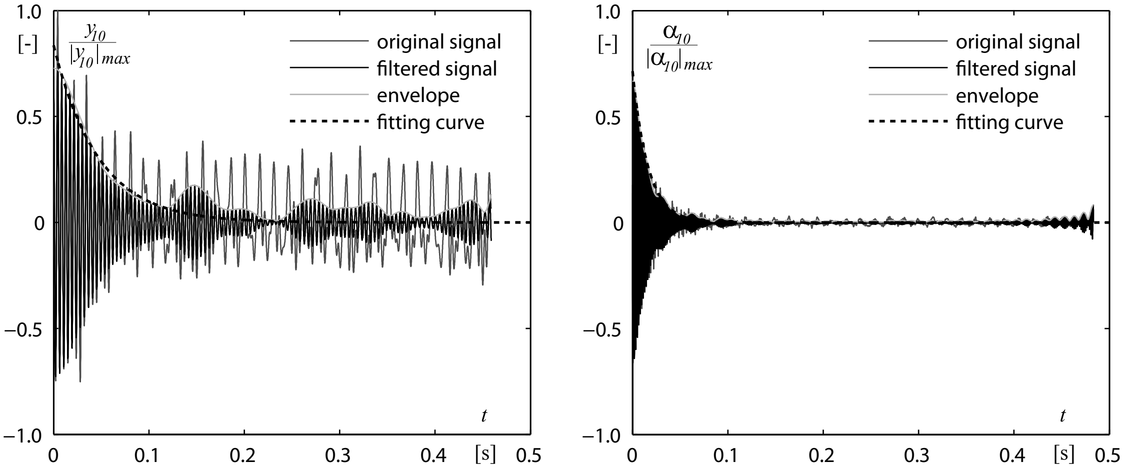

Figure 8.12: Guide vane O_{10} damping identification procedure, model in operation.

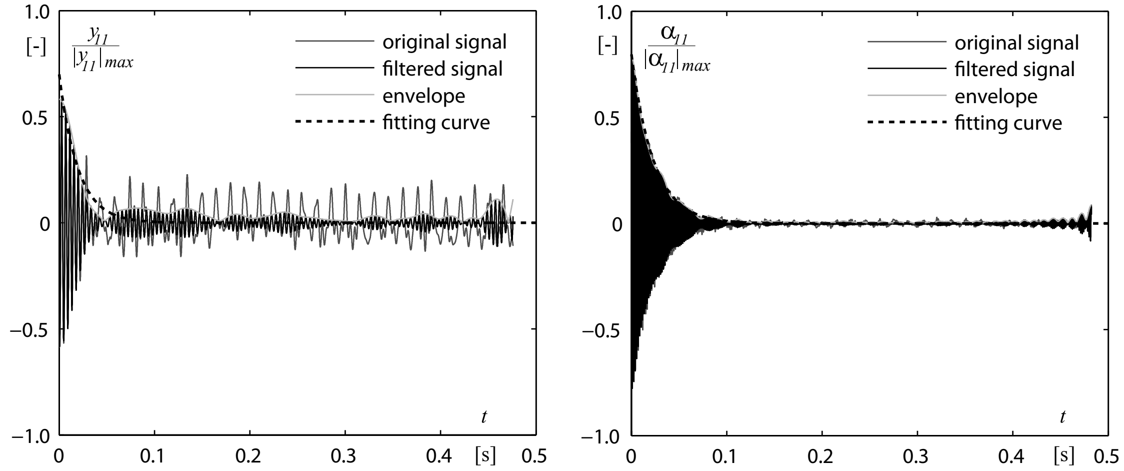

Figure 8.13: Guide vane O_{11} damping identification procedure, model in operation.

The damping coefficient values is averaged over 8 records for the guide vanes O_{11} and O_{10}. The damping constants and factors mean values are listed in Table 8.9. The standard deviation is also indicated.

Table 8.9: Damping constant and factor values for the guide vanes O_{10} and O_{11} in the machine being operated.

	$\mathbf{O_{10}}$	$\mathbf{O_{11}}$
total damping factor η_y	(1.6 ± 0.2) %	(3.0 ± 0.2) %
total damping constant C	(25.1 ± 3.1) kg $\cdot$ s^{-1}	(49.4 ± 3.7) kg $\cdot$ s^{-1}
hydro. damp. const. C^f	(20.1 ± 3.2) kg $\cdot$ s^{-1}	(42.8 ± 4.1) kg $\cdot$ s^{-1}
total damping factor η_α	(1.5 ± 0.0) %	(1.0 ± 0.0) %
total damping constant D	(0.030 ± 0.001) kg $\cdot$ m^2 $\cdot$ s^{-1}	(0.020 ± 0.000) kg $\cdot$ m^2 $\cdot$ s^{-1}
hydro. damp. const. $D^{f,\alpha}$	(0.006 ± 0.002) kg $\cdot$ m^2 $\cdot$ s^{-1}	(-0.004 ± 0.002) kg $\cdot$ m^2 $\cdot$ s^{-1}

As may be qualitatively seen in Figures 8.12 and 8.13, the filtered bending signal still contains turbulent noise. The hydrodynamic damping values are therefore underestimated.

As a conclusion, one may expect a similar behavior of the two guide vanes between the case in still water and the case in the machine in operation. But the results prove that the guide vanes respond differently in the pump-turbine in operation. At these reduced frequency values, $\kappa_y = 15$ and $\kappa_\alpha = 41$, the dissipation due to the fluid advection should be close to zero and the total dissipation should be similar to the one measured in water, model at rest, [71]. On the one hand, it may be observed that the guide vane O_{10} features a lower hydrodynamic bending damping constant $C^f = 20.1 \pm 3.2$ kg $\cdot$ s^{-1} than in still water $C^f = 24.2 \pm 0.5$ kg $\cdot$ s^{-1} and, on the other hand, it may be seen that the guide vane O_{11} presents a much higher hydrodynamic bending damping constant $C^f = 42.8 \pm 4.1$ kg $\cdot$ s^{-1} than in still water $C^f = 20.2 \pm 4.0$ kg $\cdot$ s^{-1}, see Table 8.9. By all evidence, the guide vanes are mutually interacting. With the study of the guide vane forced response reported in the next chapters, we will quantify the added mass and inertia as well as the hydrodynamic damping brought by the vibrations of the neighboring guide vanes.

Chapter 9

Forced response of the guide vanes

This chapter is devoted to the study of the forced response of the two modified guide vanes, O_{10} and O_{11}, to the excitation due to RSI. The testing conditions are first given. Then, the pressure vibrations of the guide vanes are analyzed in detail as well as the pressure fluctuations in the proximity of the vibrating guide vanes.

9.1 Testing conditions

The forced response of the guide vanes and the flow pressure in the rotor-stator vaneless gap are monitored over a wide frequency range by varying the frequency f of the main RSI modes. The pump-turbine is operated at the Best Efficiency Point, BEP, see Figure 4.2, in turbine mode, corresponding to $\alpha_0 = 18°$ guide vane opening angle, a discharge coefficient $\varphi_{\bar{1}e} = 0.36$ and an energy coefficient $\psi_{\bar{1}e} = 5.3$, defined in eq. 4.2. The impeller rotating frequency varies from $N_{min} = 700$ rpm ($n_{min} = 11.7$ Hz) to $N_{max} = 910$ rpm ($n_{max} = 15.2$ Hz). The specific energy E and discharge Q are adjusted to keep the pump-turbine model at the BEP operating conditions. On the one hand, the frequency $f = 18n$ of the RSI mode with $k = -2$ diametrical nodes ranges from 210 Hz to 273 Hz and contains, thereby, the 1^{st} bending eigenfrequency of the guide vanes O_{10} and O_{11} in water, model at rest, 231 and 233 Hz, see Table 8.4. On the other hand, the frequency $f = 45n$ of the RSI mode with $k = 5$ diametrical nodes ranges from 525 to 683 Hz and contains, consequently, the 1^{st} torsion eigenfrequency of the guide vanes, 626 and 630 Hz. The impeller rotating speed and frequency as well as the corresponding RSI frequencies are summarized in Table 9.1.

Table 9.1: Minimum and maximum impeller rotating frequencies as well as the corresponding RSI frequencies for the investigated frequency range sweep.

	Impeller frequency		**RSI frequencies**				
	N	n	9n	18n	27n	36n	45n
minimum	700 rpm	11.7 Hz	105 Hz	210 Hz	315 Hz	420 Hz	525 Hz
maximum	910 rpm	15.2 Hz	137 Hz	273 Hz	410 Hz	546 Hz	683 Hz

In Figure 9.1, the experimentally measured values of the specific energy E_{exp} and the discharge Q_{exp} that maintain the operating conditions at the BEP are plotted against the impeller rotational frequency n. E_{exp} ranges from 223 $\mathrm{J\cdot kg^{-1}}$ to 372 $\mathrm{J\cdot kg^{-1}}$ and Q_{exp}, from 0.162 $\mathrm{m^3\cdot s^{-1}}$ to 0.211 $\mathrm{m^3\cdot s^{-1}}$. In addition, the figure gives the values of the specific energy E and discharge Q, if the expected value of $\varphi_{\bar{\mathrm{I}}e}$ and $\psi_{\bar{\mathrm{I}}e}$ have been reached. These values are obtained as follows:

$$E = \frac{\pi^2}{2} \cdot D_{\bar{I}e}^2 \cdot \psi_{\bar{I}e} \cdot n^2 \tag{9.1}$$

$$Q = \frac{\pi^2}{4} \cdot D_{\bar{I}e}^3 \cdot \varphi_{\bar{I}e} \cdot n \tag{9.2}$$

The relative differences $\epsilon_{\varphi_{\bar{\mathrm{I}}e}}$ and $\epsilon_{\psi_{\bar{\mathrm{I}}e}}$ are defined as:

$$\epsilon_{\varphi_{\bar{\mathrm{I}}e}} = \frac{\varphi_{\bar{\mathrm{I}}e} - \varphi_{\bar{\mathrm{I}}e,exp}}{\varphi_{\bar{\mathrm{I}}e}} \tag{9.3}$$

$$\epsilon_{\psi_{\bar{\mathrm{I}}e}} = \frac{\psi_{\bar{\mathrm{I}}e} - \psi_{\bar{\mathrm{I}}e,exp}}{\psi_{\bar{\mathrm{I}}e}} \tag{9.4}$$

with $\varphi_{\bar{\mathrm{I}}e,exp} = \frac{Q_{exp}}{\frac{\pi^2}{4} D_{\bar{\mathrm{I}}e}^3 n}$ and $\psi_{\bar{\mathrm{I}}e,exp} = \frac{E_{exp}}{\frac{\pi^2}{4} D_{\bar{\mathrm{I}}e}^2 n^2}$

With the relative differences $\epsilon_{\varphi_{\bar{\mathrm{I}}e}}$ and $\epsilon_{\psi_{\bar{\mathrm{I}}e}}$, the offset between the experimental and expected values of the coefficients, which is less than 1% for all investigated impeller rotational frequencies n, is also illustrated in Figure 9.1.

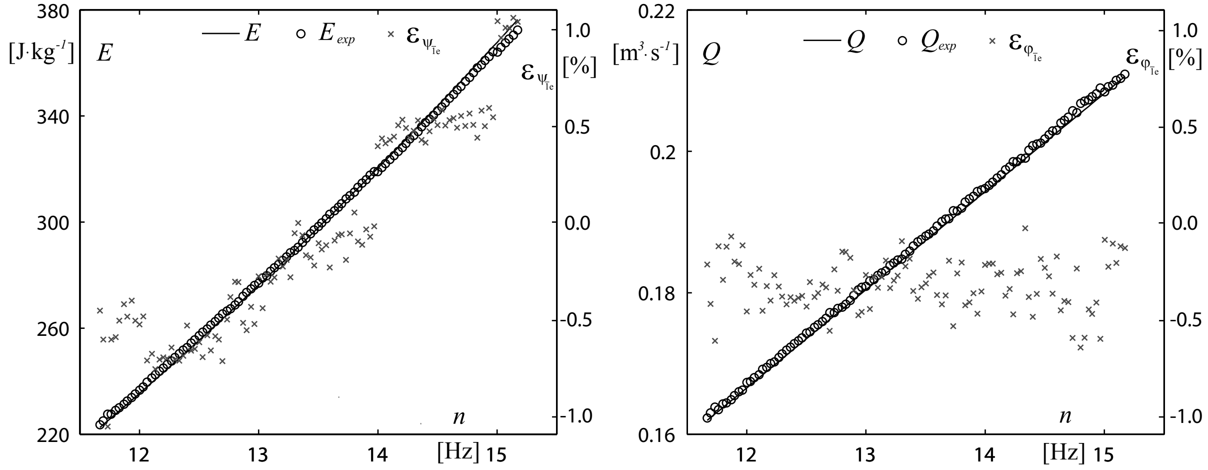

Figure 9.1: Experimental and expected values of specific energy, E_{exp} and E, and discharge, Q_{exp} and Q, versus impeller rotational frequency n to ensure BEP operating conditions.

The Reynolds number Re related to the flow in the guide vane channel is defined as follows:

$$Re = \frac{C_{max} \cdot D_h}{\nu} = \frac{Q \cdot D_h}{z_o \cdot (\mathrm{W} \cdot \mathrm{B}_o) \cdot \nu} \tag{9.5}$$

where C_{max} is the maximum absolute flow velocity in the guide vane channel, W, the narrowest width of the guide vane channel, B_o, the channel height, ν, the kinematic viscosity and D_h, the hydraulic diameter, [74], defined as:

$$D_h = \frac{2 \cdot \mathrm{W} \cdot \mathrm{B}_o}{\mathrm{W} + \mathrm{B}_o} \tag{9.6}$$

The Reynolds number is comprised between $2.7 \cdot 10^5$ and $3.5 \cdot 10^5$. The high Reynolds number indicates the dominance of the inertial effects on the viscous effects. Moreover, at BEP, the turbulence effects may be neglected and, therefore, the potential flow approach given in Section 3.3 is appropriate.

Finally, the reduced frequency defined in eq. 8.17 takes the constant values κ_y=9.3 and κ_α=23.1 over the entire frequency range corresponding to the RSI 2^{nd} harmonic and over the frequency range related to the RSI 5^{th} harmonic, respectively. In other words, this means that the unsteady effects are important.

9.2 Pressure fluctuations and guide vane vibrations

The value of the guide vane O_i bending displacement y_i is made dimensionless by introducing the bending displacement factor:

$$c_{y_i} = \frac{y_i}{\mathrm{W}} \tag{9.7}$$

W being the narrowest width of the guide vane channel defined in Figure 4.3.

The torsion angle factor of the guide vane O_i is defined as follows:

$$c_{\alpha_i} = \frac{\alpha_i \cdot \frac{L}{2}}{\mathrm{W}} \tag{9.8}$$

L being the guide vane chord length.

The RMS-values of the displacement and angle factors, $\tilde{c}_{y_i}$ and $\tilde{c}_{\alpha_i}$, of the guide vanes O_{10} and O_{11} are plotted on a logarithmic scale against the impeller rotating frequency n in Figure 9.2.

The guide vane O_{10} experiences a maximum RMS-value $\tilde{c}_{y_{10}}$ at $n = 12.9$ Hz. At this impeller frequency, the RSI 2^{nd} harmonic value is close to the 1^{st} bending eigenfrequency, 231 Hz, in water, model at rest, see Section 8.2.1. As for the guide vane O_{11}, its maximum RMS-value $\tilde{c}_{y_{11}}$ is reached at $n = 12.5$ Hz. The corresponding RSI 2^{nd} harmonic is 225 Hz. Therefore, this guide vane does not preferably respond at the 1^{st} bending eigenfrequency in water, model at rest, but at a 3% lower frequency.

The RMS-value of guide vane O_{11} torsion angle $\tilde{c}_{\alpha_{11}}$ presents two maxima at $n =$ 12.7 Hz and $n = 14.6$ Hz. The first maximum is linked to the bending mode excited by the RSI 2^{nd} harmonic. The second maximum is reached at an impeller frequency whose corresponding RSI 5^{th} harmonic is 660 Hz, being close to the 1^{st} torsion eigenmode frequency in water, model at rest, 626 Hz. The RMS-value of the guide vane O_{10} torsion $\tilde{c}_{\alpha_{10}}$ presents a maximum at $n = 13.0$ Hz and a minimum at $n = 14.6$ Hz. The first

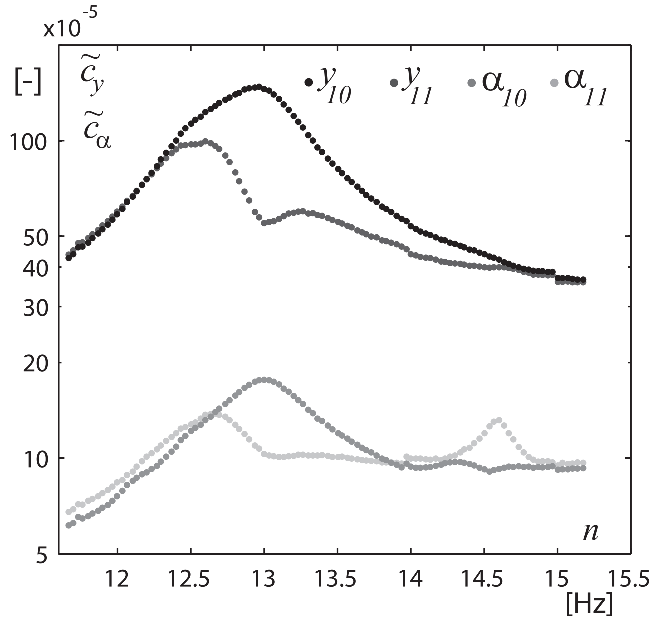

Figure 9.2: Displacement and angle factors RMS-values against the impeller frequency.

maximum is linked to the bending mode excited by the RSI 2^{nd} harmonic. The minimum may be caused by the guide vane resonance close to its 1^{st} torsion eigenmode frequency.

The RMS-values of the pressure factor, $\tilde{c}_p$, monitored with the sensors s_{10}, s_{11}, g_{10}, g_{11} and g_{15} are plotted against the impeller rotating frequency n in Figure 9.3.

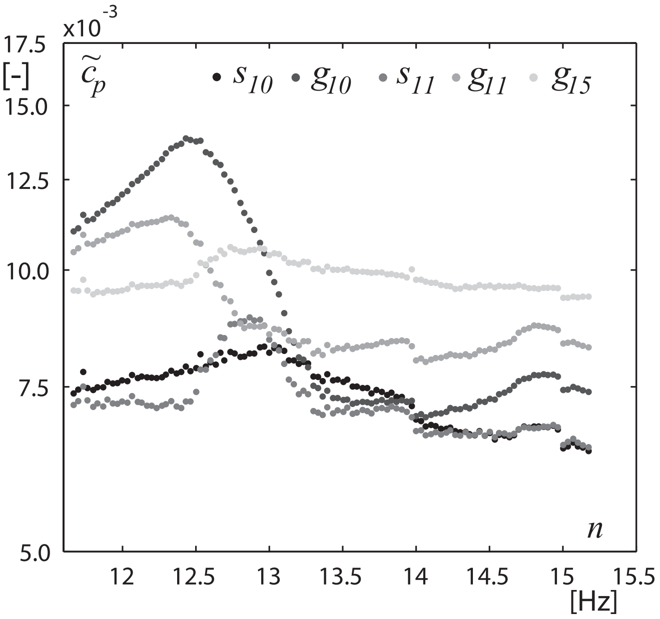

Figure 9.3: Pressure factor RMS-values against the impeller frequency.

The pressure sensor g_{15} experiences a fairly constant RMS-value around $\tilde{c}_p = 0.010$. The pressure factor fluctuations at this angular position are therefore not influenced by the impeller frequency sweep, while the pressure factor fluctuations monitored by the sensors g_{10} and g_{11}, located close to the flexible guide vanes O_{10} and O_{11}, respectively, are strongly influenced. After a maximum reached at $n = 12.5$ Hz, these RMS-values decrease. The relative difference between the maximum and the minimum RMS-values for the pressure sensors g_{10} and g_{11} is 50% and 30%, respectively. Thereby, a transfer of energy occurs locally from the flow to the vibrating guide vanes, O_{10} and O_{11}.

The pressure sensors, s_{10} and s_{11}, placed in the guide vane channel are also subject to the influence of the vibrations, since their RMS-values vary according to the impeller frequency. The pressure factor fluctuations monitored by these sensors feature a higher amplitude close to the resonance of the guide vanes. The increase of the fluctuations is nevertheless higher for the sensor s_{11} positioned between the two vibrating guide vanes.

The waterfall diagrams of the power spectral density of the pressure factor monitored by the pressure sensors g_{10}, g_{11}, g_{15}, s_{10} and s_{11} are plotted in Figures 9.4, 9.5 and 9.6, respectively, against the impeller frequency n. The frequency is normalized with the impeller frequency n to highlight the RSI fundamental frequency and its harmonics with the multiples of the impeller blade number $\frac{f}{n} = mz_b$. The power spectral densities are averaged over 8 blocks of 0.32 s, windowed with a Hamming function, each overlapping by 50%.

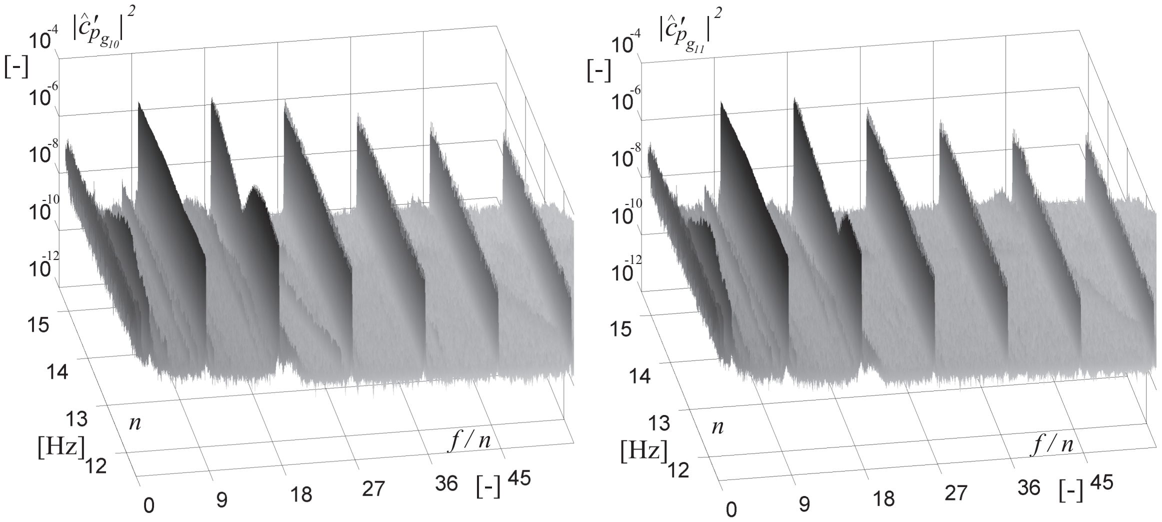

Figure 9.4: Waterfall diagrams of power spectral density of the pressure fluctuation factor monitored by the pressure sensors g_{10} (left) and g_{11} (right) against the impeller frequency n.

Most of the spectral energy is concentrated at the frequencies $f = mz_b n$ revealing the RSI modes. Moreover, the two main RSI modes oscillating at $f = 9n$ and $f = 18n$, present, as expected, a larger amplitude than the modes oscillating at higher $f/n = mz_b$ ratios. The amplitude of the pressure fluctuations at $f/n = 18$ and $f/n = 45$ for the pressure sensors s_{10}, s_{11}, g_{10} and g_{11} greatly varies depending on the impeller frequency n. Nevertheless, the variations of the pressure fluctuation amplitude at $f/n = 45$ are very small for the sensors g_{10} and g_{11}. In Figures 9.4 and 9.6, the concerned pressure

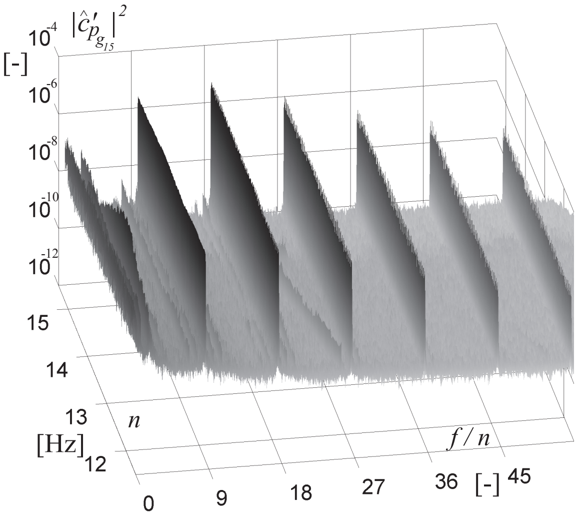

Figure 9.5: Waterfall diagrams of power spectral density of the pressure fluctuation factor monitored by the pressure sensors g_{15}, against the impeller frequency n.

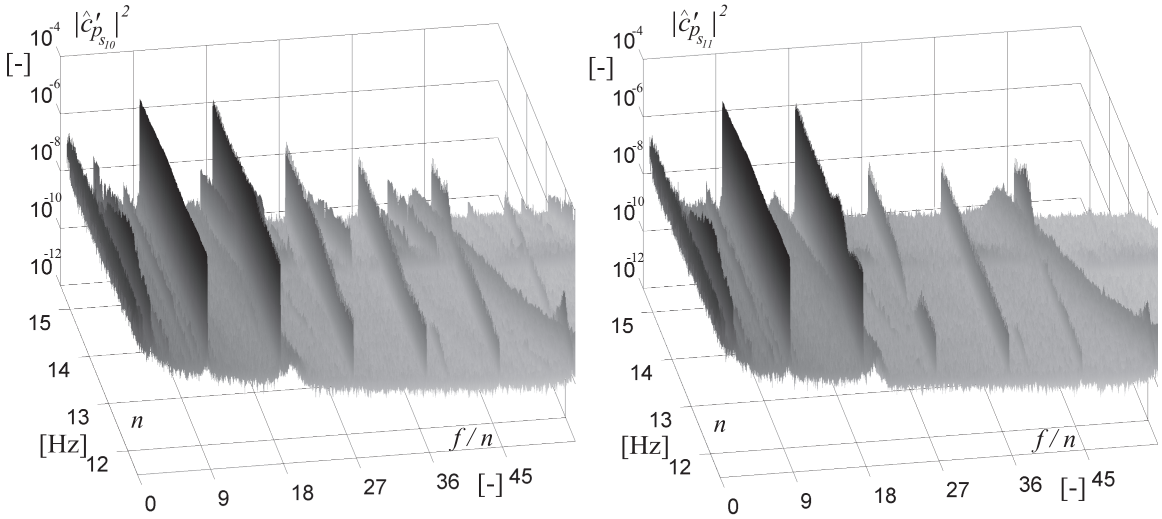

Figure 9.6: Waterfall diagrams of power spectral density of the pressure fluctuation factor monitored by the pressure sensors s_{10} (left) and s_{11} (right) against the impeller frequency n.

sensors monitor a higher amplitude at two fixed frequencies for all the impeller frequencies investigated. These frequencies correspond to the guide vane eigenfrequencies. Therefore, the guide vanes reaching resonance are strongly modifying the pressure fluctuations, when the eigenfrequencies corresponds to either the 2^{nd} or the 5^{th} RSI harmonics.

The waterfall diagrams of the power spectral density of the displacement factor fluctuations for the guide vanes O_{10} and O_{11} are plotted in Figure 9.7, against the impeller frequency n.

The waterfall diagrams of the power spectral density of the fluctuating angle factor

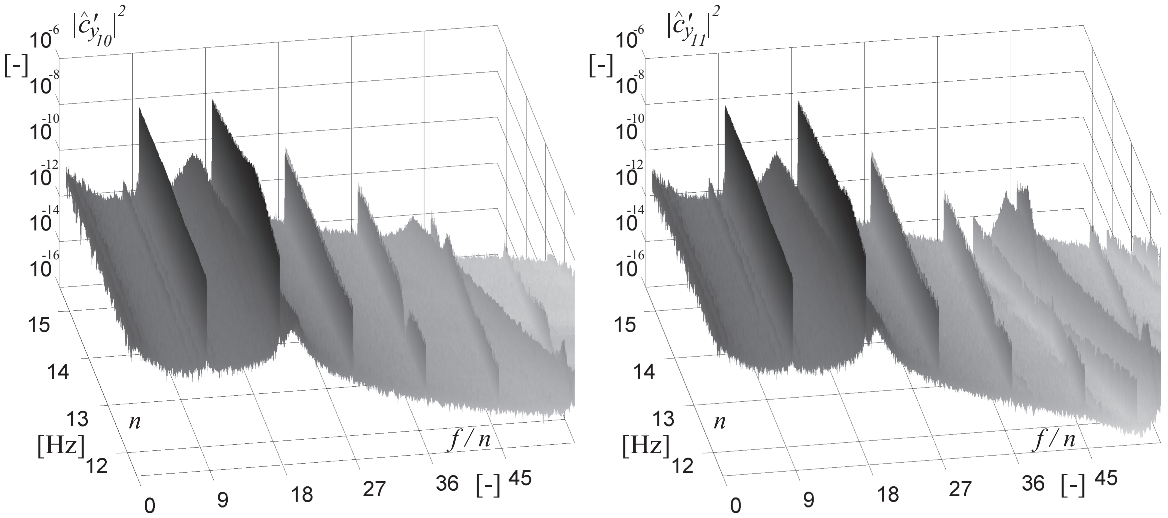

Figure 9.7: Waterfall diagrams of the power spectral density of the guide vanes O_{10} and O_{11} displacement factor fluctuations, against the impeller frequency n.

for the guide vanes O_{10} and O_{11} are plotted in Figure 9.8, against the impeller frequency n.

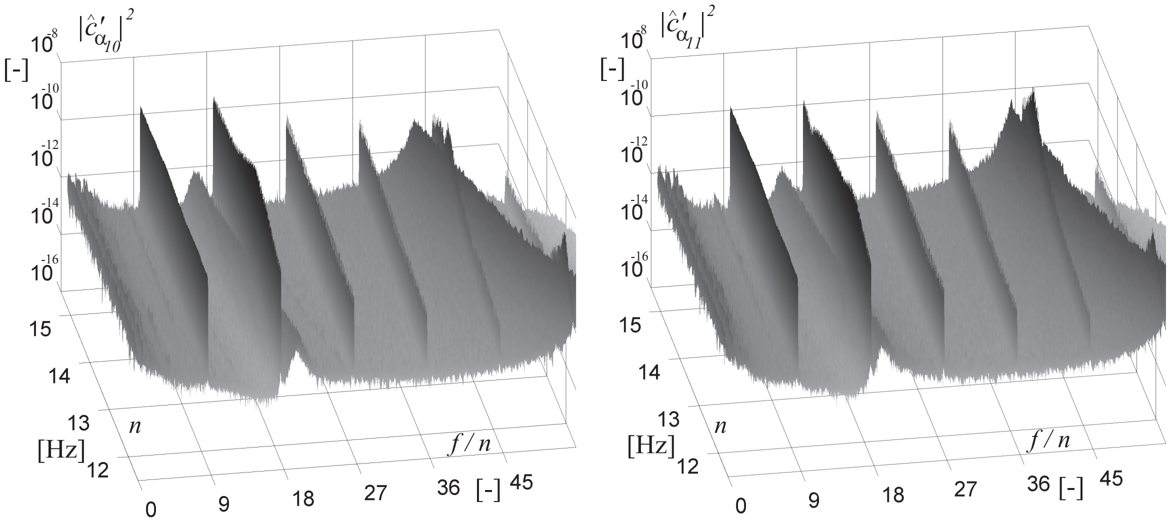

Figure 9.8: Waterfall diagrams of the power spectral density amplitude of the guide vanes O_{10} and O_{11} angle factor fluctuations, against the impeller frequency n.

Due to RSI excitation, most of the spectral energy is concentrated at RSI modes frequencies $f = mz_b n$. The response of the guide vanes to the two main RSI modes, $f = 9n$ and $f = 18n$, is nevertheless the highest. On the one hand, the 1^{st} bending eigenmode is clearly observed in Figure 9.7, its frequency crossing the RSI 2^{nd} harmonic frequency at $n = 12.9$ Hz. When the RSI 2^{nd} harmonic frequency approaches the eigenmode frequency, the response of the guide vanes greatly varies. The response of the guide vanes to the RSI 2^{nd} harmonic depends, thus, on the impeller frequency n, because of their 1^{st} bending eigenmode. On the other hand, the 1^{st} torsion eigenmode may clearly be identified in Figure 9.8. The eigenmode frequency crosses the RSI 5^{th} harmonic frequency and the response of the guide vanes is severely perturbed.

One may state that the two eigenmodes appear in both the bending displacement and the torsion angle waterfall diagrams. Nevertheless, the bending eigenmode predominates in the displacement waterfall diagrams, whereas the torsion eigenmode predominates in the torsion angle waterfall diagrams.

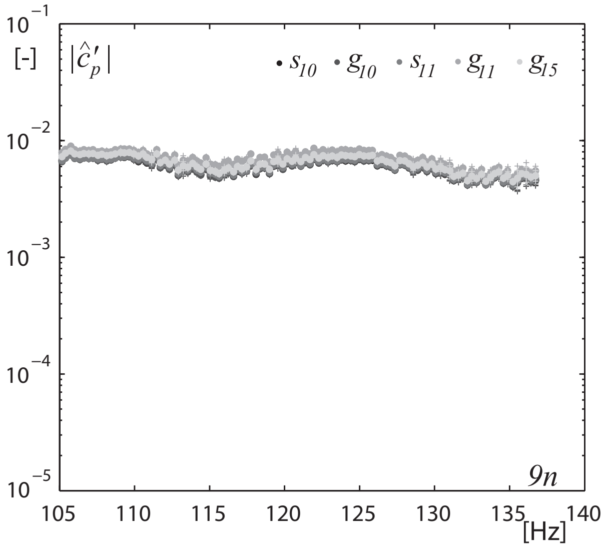

Figure 9.9: Averaged Fourier transform magnitude of pressure factor fluctuations, monitored by the pressure sensors g_{10}, s_{10}, g_{11}, s_{11}, g_{15}, at the RSI fundamental frequency $f = 9n$, for the investigated impeller frequency range.

The magnitude of the averaged Fourier transform of the pressure factor fluctuations monitored by the pressure sensors s_{10}, s_{11}, g_{10}, g_{11} and g_{15} at the RSI fundamental and the 2^{nd} to 5^{th} harmonic frequencies is plotted against the corresponding harmonic frequency in Figure 9.9 to 9.13, respectively, for the investigated impeller frequency range.

The magnitude of the pressure factor fluctuations monitored by each of the five sensors does not vary with the impeller frequency at the RSI fundamental, see Figure 9.9. It stays constant around $|\hat{c}'_p| = 0.007$ for the whole investigated impeller frequency range.

The magnitude of the pressure factor fluctuations $|\hat{c}'_{p_{g_{15}}}|$, monitored close to stiff guide vanes, at the RSI 2^{nd} harmonic frequency remains constant around $3.8 \cdot 10^{-3}$ for the investigated impeller frequency range, whereas the others present variations, see Figure 9.10. The magnitude of the pressure factor fluctuations monitored by the sensor $|\hat{c}'_{p_{g_{11}}}|$ features a maximum to minimum ratio of 5, while the ratio reaches 12 for the pressure sensor $|\hat{c}'_{p_{g_{10}}}|$. Concerning the pressure sensors positioned in the guide vane channels, the magnitude of the pressure factor fluctuations monitored by the sensor $|\hat{c}'_{p_{s_{11}}}|$ features a maximum to minimum ratio of 4.5, while the ratio reaches 1.5 for the pressure sensor $|\hat{c}'_{p_{s_{10}}}|$. The pressure sensors monitor very different pressure fluctuation along the investigated frequency range.

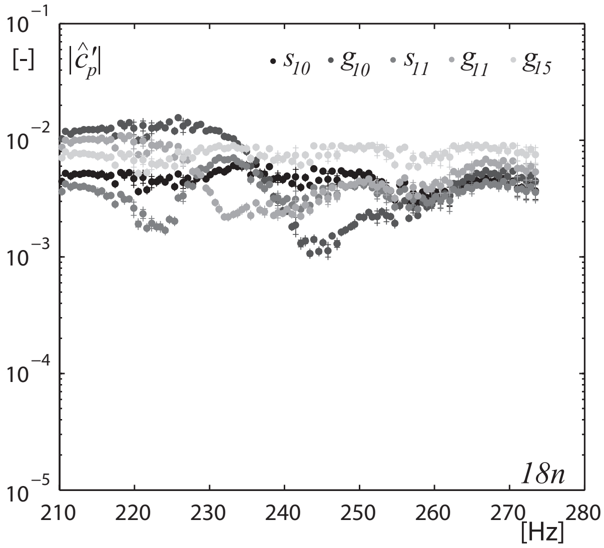

Figure 9.10: Averaged Fourier transform magnitude of pressure factor fluctuations, monitored by the pressure sensors g_{10}, s_{10}, g_{11}, s_{11}, g_{15}, at the RSI 2^{nd} harmonic frequency $f = 18n$, for the investigated impeller frequency range.

At the frequency corresponding to the RSI 3^{rd} harmonic, the three pressure sensors positioned in the rotor-stator gap do not vary according to the investigated impeller frequency, see Figure 9.11. Moreover, the pressure sensor s_{11} monitors lower fluctuations at the frequencies $f = 27n$ ranging from 338 to 380 Hz, whereas the pressure sensor s_{10} seems not to be subject to the vibrations of the guide vanes, its value staying constant along the impeller frequency range investigated. A surplus of energy is dissipated in a unknown manner in the flow at the position of the sensor s_{11}. Since no variation of the vibrations is monitored at the RSI 3^{rd} harmonic frequency, see Figure 9.16, one knows that this decrease of pressure fluctuations does not have any influence on the vibrating motion of the guide vanes.

At the frequencies $f = 36n$ corresponding to the RSI 4^{th} harmonic, the pressure fluctuations do not undergo any variation along the whole impeller frequency range, see Figure 9.12. The pressure sensors in the rotor-stator gap monitor fluctuations 10 times stronger than the pressure sensors in the guide vane channel.

The magnitude of the pressure factor fluctuations recorded at the frequencies $f = 45n$ corresponding to the RSI 5^{th} harmonic in the rotor-stator gap does not vary according to the investigated impeller frequency n, see Figure 9.13. Nevertheless, the pressure sensors in the guide vane channel monitor variations for frequencies ranging from 625 to 683 Hz. The magnitude of the pressure fluctuations factor monitored by the sensor $|\tilde{c}'_{p_{s_{11}}}|$ features a maximum to minimum ratio of 12, while the ratio reaches 4.5 for the pressure sensor $|\tilde{c}'_{p_{s_{10}}}|$.

The magnitude of the averaged Fourier transform of the fluctuating displacement and torsion angle factor, for the guide vanes O_{10} and O_{11} at the RSI fundamental and the 2^{nd} to 5^{th} harmonic frequencies is plotted against the corresponding frequencies on the left hand side of Figure 9.14 to 9.18, respectively, for the investigated impeller frequency range.

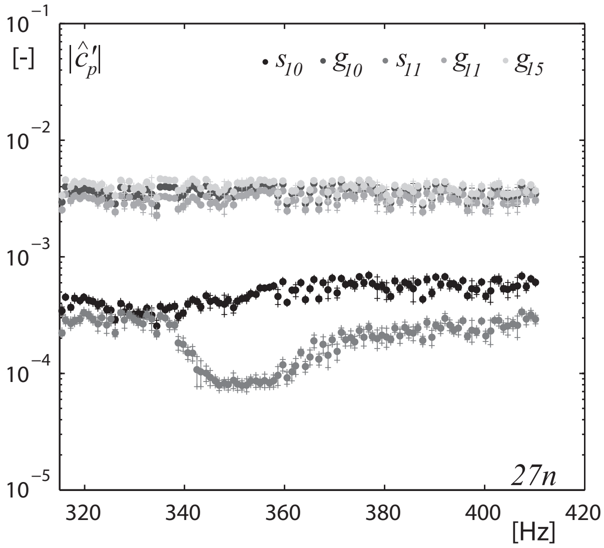

Figure 9.11: Averaged Fourier transform magnitude of pressure factor fluctuations, monitored by the pressure sensors g_{10}, s_{10}, g_{11}, s_{11}, g_{15}, at the RSI 3^{rd} harmonic frequency $f = 27n$, for the investigated impeller frequency range.

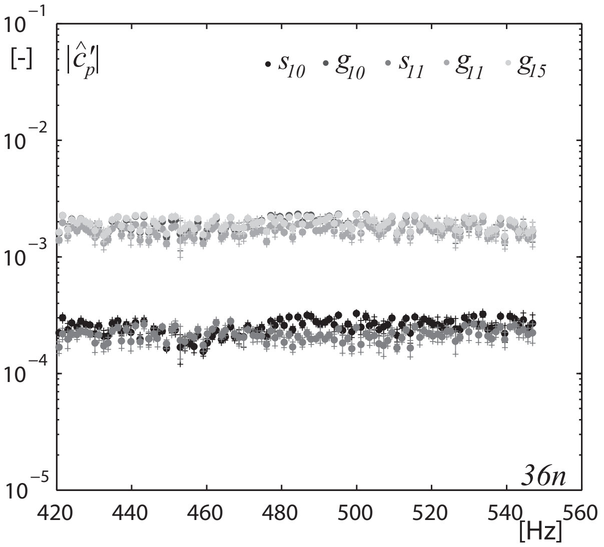

Figure 9.12: Averaged Fourier transform magnitude of pressure factor fluctuations, monitored by the pressure sensors g_{10}, s_{10}, g_{11}, s_{11}, g_{15}, at the RSI 4^{th} harmonic frequency $f = 36n$, for the investigated impeller frequency range.

The phase shifts between the vibrating motions of the two guide vanes $\Delta\phi_{y_{10},y_{11}}(f) = \phi_{y_{10}}(f) - \phi_{y_{11}}(f)$ and $\Delta\phi_{\alpha_{10},\alpha_{11}}(f) = \phi_{\alpha_{10}}(f) - \phi_{\alpha_{11}}(f)$ at the corresponding frequencies $f = mz_bn$ are given on the right hand side of the five figures.

For small amplitudes, the torsion angle factor definition, see eq. 9.8, may be seen as

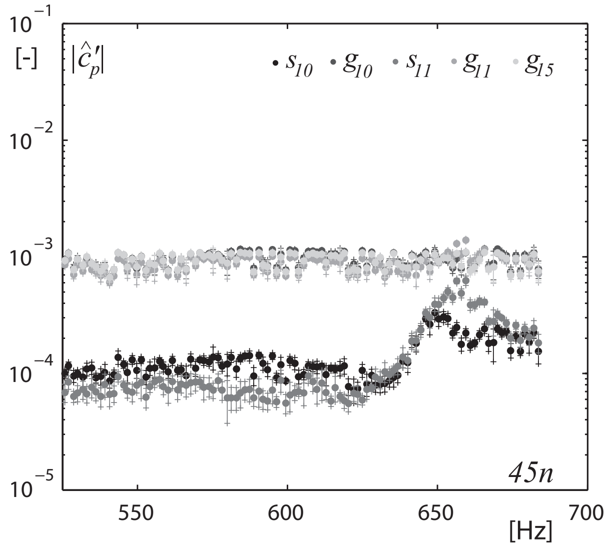

Figure 9.13: Averaged Fourier transform magnitude of pressure factor fluctuations, monitored by the pressure sensors g_{10}, s_{10}, g_{11}, s_{11}, g_{15}, at the RSI 5^{th} harmonic frequency $f = 45n$, for the investigated impeller frequency range.

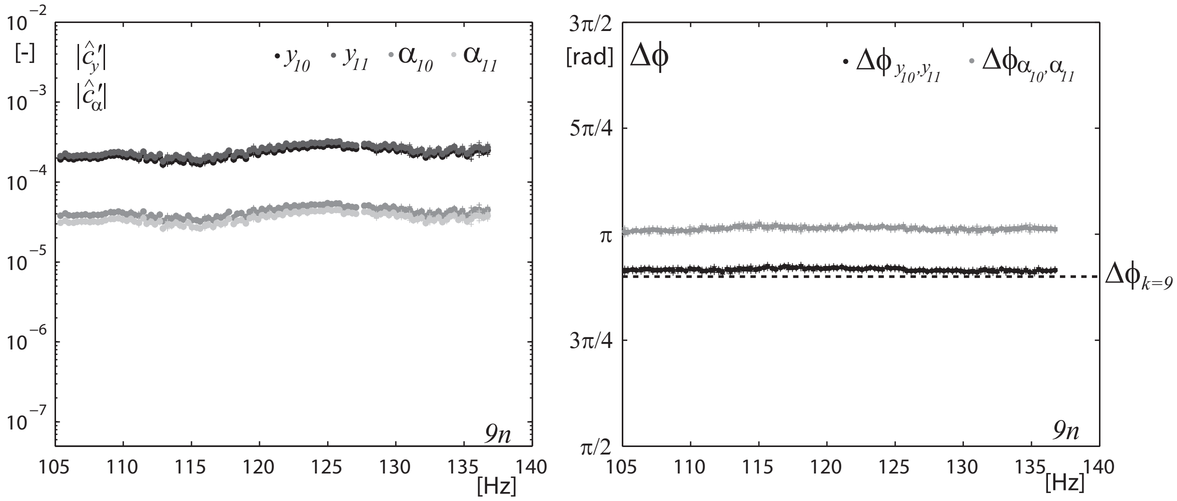

Figure 9.14: Averaged Fourier transform magnitude of displacement and torsion angle factors (left) and phase shift between the displacement signals and between the angle signals (right) at the RSI fundamental frequency, $f = 9n$, for guide vanes O_{10} and O_{11}, for the investigated impeller frequency range.

a displacement factor of the guide vane leading- or trailing edge as follows:

$$c_{\alpha_i} = \frac{\left(\alpha_i \cdot \frac{L}{2}\right)}{\delta} \approx \frac{y_i^{tip}}{\delta} \tag{9.9}$$

where y_i^{tip} is the local displacement of the guide vane leading- or trailing edge in the direction perpendicular to the chord. In this way, the two factors, c_{y_i} and c_{α_i}, may easily be compared with each other.

At the RSI fundamental frequencies, see Figure 9.14, the bending displacement factor is found to be 4 times higher than the torsion angle factor. The phase shift between the displacements and the torsion angle of the two guide vanes remains constant at $\Delta\phi_{y_{10},y_{11}} = 2.90$ rad and $\Delta\phi_{A_{10},A_{11}} = 3.16$ rad. Theoretically, as given in Table 7.1, the phase shift between the pressure signals monitored at the angular position of two adjacent guide vanes is $\Delta\phi_{k=9} = 2.83$ rad. The relative differences are 2% and 10% for the displacement and the torsion angle, respectively. One may state that the vibrating motion of the guide vanes is clearly forced by the pressure fluctuations arising from the RSI. Since guide vane resonances are far away from the exciting frequency, the phase shift between the motions is close to the pressure phase shift.

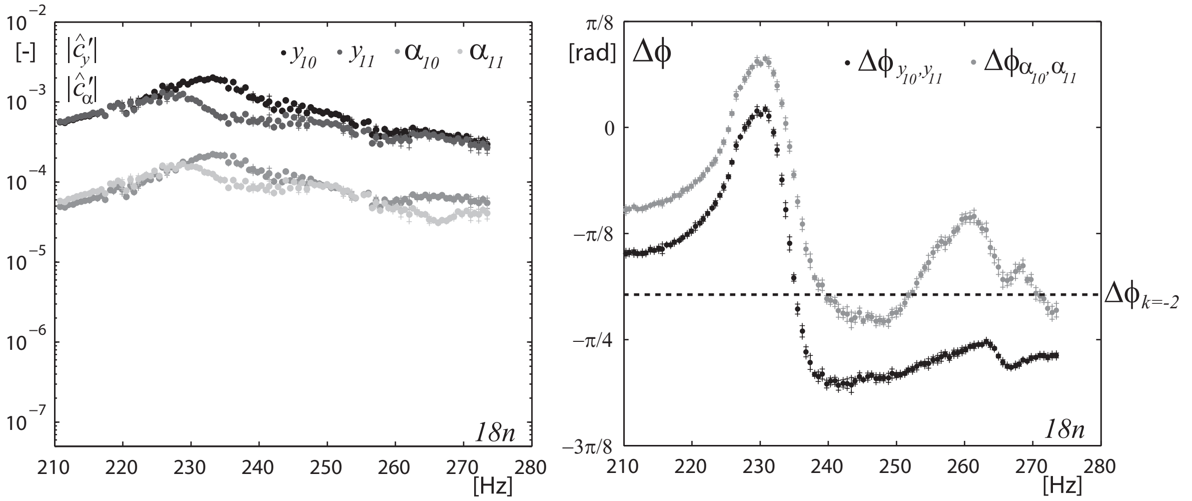

Figure 9.15: Averaged Fourier transform magnitude of displacement and torsion angle factors (left) and phase shift between the displacement signals and between the torsion angle signals (right) at the RSI 2^{nd} harmonic, $f = 18n$, for guide vanes O_{10} and O_{11}, for the investigated impeller frequency range.

At the RSI 2^{nd} harmonic frequencies, see Figure 9.15, the bending displacement factor of the guide vane O_{10} and O_{11} even exceeds 10 times the torsion angle factor. The eigenfrequency of the guide vanes found when placed in water, model at rest, is included in the frequency range constituted by the RSI 2^{nd} harmonic during the impeller frequency sweep. Nevertheless, as already pointed out with the RMS-values observation, the guide vanes O_{10} and O_{11} do not preferably respond at the same frequency, see Figure 9.15, as would be presumed by the modal analyzes in water, model at rest. Moreover, when the guide vane O_{10} is at resonance, the amplitude of the vibrations of the guide vane O_{11} clearly seem to be attenuated. The phase shift between the pressure monitored at the location of the guide vanes O_{10} and O_{11} imposed by the RSI mode at $f = 18n$ is $\Delta\phi_{k=-2} = -0.63$ rad. Therefore, $\Delta\phi_{y_{10},y_{11}}$ and $\Delta\phi_{\alpha_{10},\alpha_{11}}$ are close to this value at $f = 18n_{min}$: $\Delta\phi_{y_{10},y_{11}}(18n_{min}) = -0.47$ rad ($\epsilon_{\Delta\phi} = 25\%$) and $\Delta\phi_{\alpha_{10},\alpha_{11}}(18n_{min}) = -0.30$ rad ($\epsilon_{\Delta\phi} = 52\%$). The high value of the relative differences $\epsilon_{\Delta\phi}$ is due to the proximity of the bending eigenmode. When increasing the impeller rotating frequency, the phase shifts are strongly modified across structural resonance. The maximum phase shift value is reached at 230 Hz.

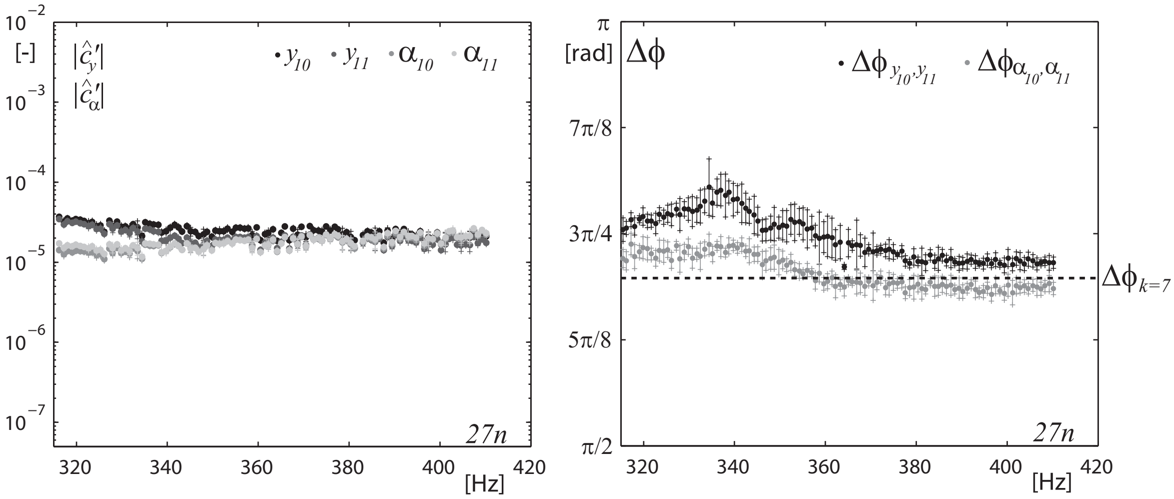

Figure 9.16: Averaged Fourier transform magnitude of displacement and torsion angle factors (left) and phase shift between the displacement signals and between the torsion angle signals (right) at the RSI 3^{rd} harmonic, $f = 27n$, for guide vanes O_{10} and O_{11}, for the investigated impeller frequency range.

At the RSI 3^{rd} harmonic frequencies, see Figure 9.16, the bending displacement factor of the guide vanes O_{10} and O_{11} is of the same order of magnitude as the torsion angle factor, see Figure 9.16. Nevertheless, through the frequency range, one may observe that the displacement factor increases, whereas the torsion angle factor decreases, by a factor 1.5. The reason is that, by increasing the impeller frequency, the RSI 3^{rd} harmonic frequency moves away from the 1^{st} bending eigenfrequency, 230 Hz, decreasing the bending displacement, whereas it comes closer to the 1^{st} torsion eigenfrequency, 630 Hz, increasing the torsion angle. As to the phase shift between the displacement and torsion motions, it is close to the phase shift imposed by the RSI: $\Delta\phi_{k=7} = 2.20$ rad.

At the RSI 4^{th} harmonic frequencies, see Figure 9.17, the torsion angle factor value triples by increasing the excitation frequency from $36n_{min}$ to $36n_{max}$, whereas the displacement factor presents a relatively constant amplitude throughout the frequency range, see Figure 9.17. Nevertheless, between 450 and 460 Hz, one may observe a local decrease of the displacement factors. One presumes the influence of the 1^{st} higher harmonic of the 1^{st} bending eigenfrequency. It is interesting to see an attenuation of the vibrations at this eigenfrequency harmonic, whereas the vibrations are severely amplified at the proximity of the bending eigenfrequency, see Figure 9.15. The phase shift between the torsion motions remains constant at $\Delta\phi_{k=-4} = -1.26$ rad, whereas the phase shift between the bending motions greatly varies due to the influence of the 1^{st} higher harmonic of the 1^{st} bending eigenfrequency already mentioned above.

Finally, at the RSI 5^{th} harmonic frequencies, see Figure 9.18, the maximum value of the torsion angle factor of the guide vanes O_{10} and O_{11} is 50 times higher than the respective displacement factor value because of the proximity of the 1^{st} torsion eigenfrequency. The

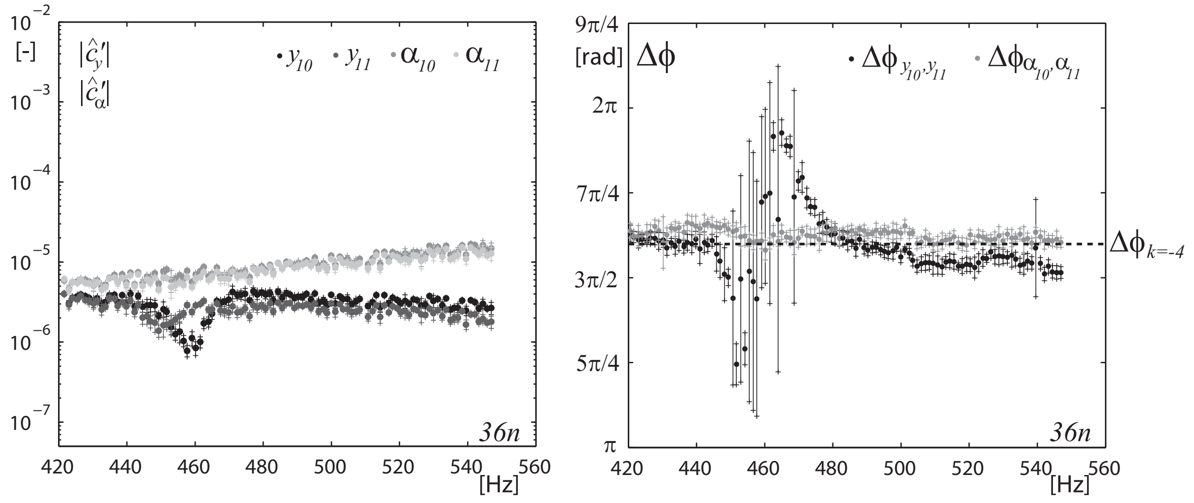

Figure 9.17: Averaged Fourier transform magnitude of displacement and torsion angle factors (left) and phase shift between the displacements and between the torsion angle signals (right) at the RSI 4^{th} harmonic, $f = 36n$, for guide vanes O_{10} and O_{11}, for the investigated impeller frequency range.

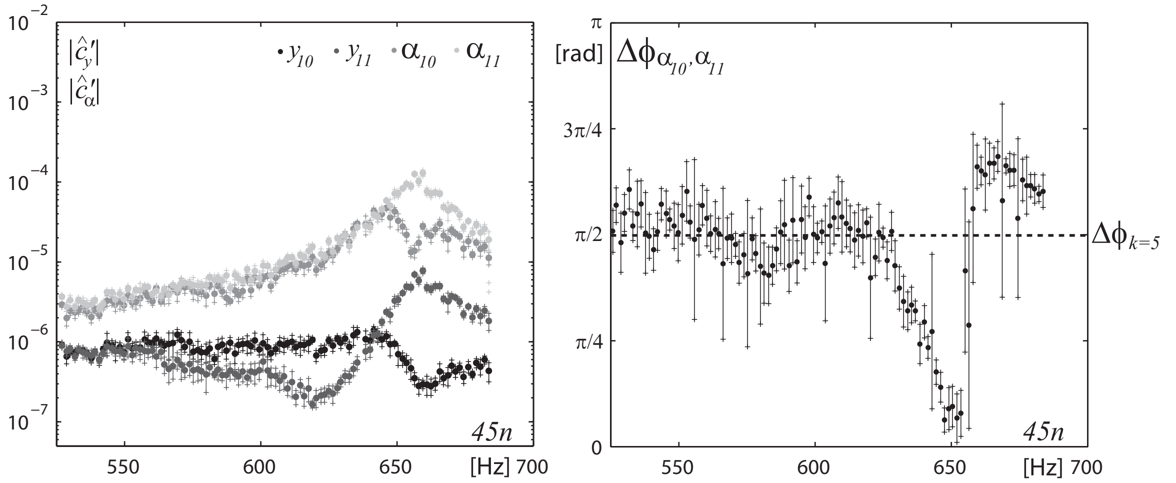

Figure 9.18: Averaged Fourier transform magnitude of displacement and torsion angle factors (left) and phase shift between the displacement signals and between the torsion angle signals (right) at the RSI 5^{th} harmonic, $f = 45n$, for guide vanes O_{10} and O_{11}, for the investigated impeller frequency range.

guide vane O_{11} responds preferably at 657 Hz, whereas the amplitude of the guide vane O_{10} vibrations at this frequency is strongly attenuated. The latter responds preferably at 646 Hz and 666 Hz. The amplitude of the guide vane O_{11} vibrations at the frequency $f = 45n$ is amplified by a factor 42 in the impeller frequency range investigated, whereas the factor is 17 for the guide vane O_{10}. The phase shift values between the torsion motions present a relatively high standard deviation. Nonetheless, one may observe that, away from resonance, the phase shift is close to $\Delta\phi_{k=5} = 1.57$ rad. Throughout the resonance, the phase shift greatly varies to get closer to zero near $45n = 650$ Hz. At 657 Hz, the phase shift is 2 rad and, at higher frequencies, the phase shift returns to 1.57 rad. The phase shift between the bending displacement is not possible to get in a reliable manner, because of the too low displacement values at these frequencies.

The waterfall diagrams of the coherence functions between the pressure factor fluctuations and vibrations of the guide vanes against the normalized frequency f/n are presented for the whole range of impeller frequencies n in Figures 9.19 to 9.23. The coherence functions are averaged over 8 blocks of 0.32 s, each overlapping by 50%.

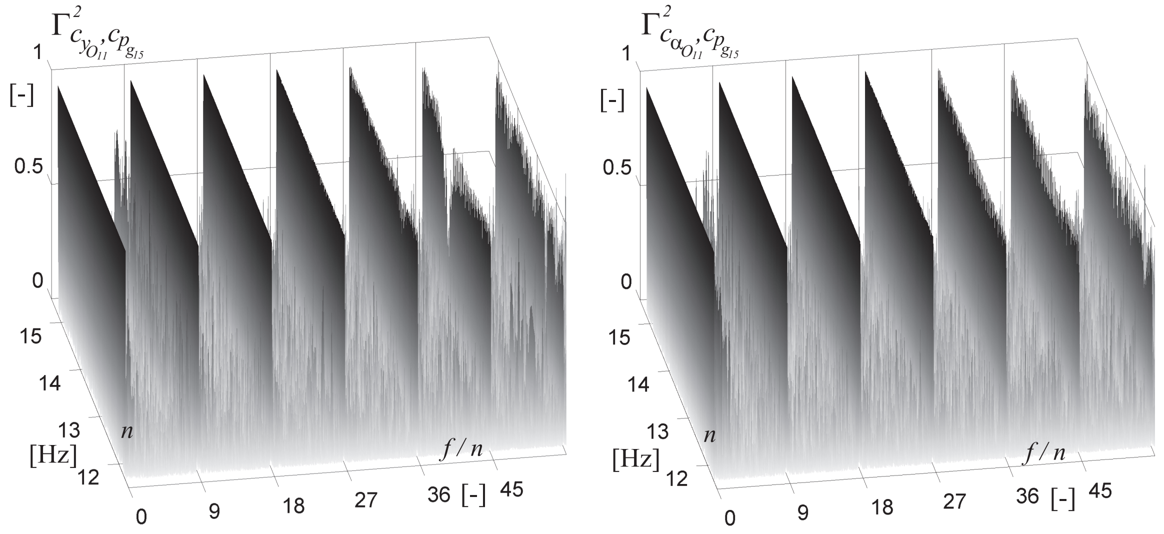

Figure 9.19: Waterfall diagrams of the coherence functions between the pressure factor monitored by the sensor g_{15} and the guide vane O_{11} displacement factor (left) and between the pressure factor monitored by the sensor g_{15} and the guide vane O_{11} torsion angle factor (right) against the impeller frequency n.

In these figures, the RSI modes clearly appear, while the correlation is poor in between. The coherence functions value tends to 1 at RSI modes frequencies $f = mz_bn$, for $1 \leq m \leq 3$. Because of the low response of the strain gages and the pressure sensors to higher RSI harmonics, the coherence functions do not exactly reach 1 at these frequencies. At the 4^{th} harmonic, the value of the coherence functions is the worst when the harmonic value comes closer to twice the value of the bending eigenfrequency. In Figure 9.17, one has already mentioned an influence of the 1^{st} higher harmonic of this guide vane eigenmode. At the 5^{th} harmonic, the coherence functions take low values when the harmonic frequency comes closer to the torsion eigenfrequencies.

Therefore, linear relations between these pressure, displacement and torsion angle factors might be built at RSI modes frequencies. Nevertheless, the accuracy of these linear relations will be higher for the harmonic up to the third one. The following chapter is devoted to the identification of the hydrodynamic parameters, namely the added mass and the hydrodynamic damping brought by the vibrations of the neighboring guide vanes. These parameters are deduced from influence matrices which is nothing else but a linear relations between a force and a displacement.

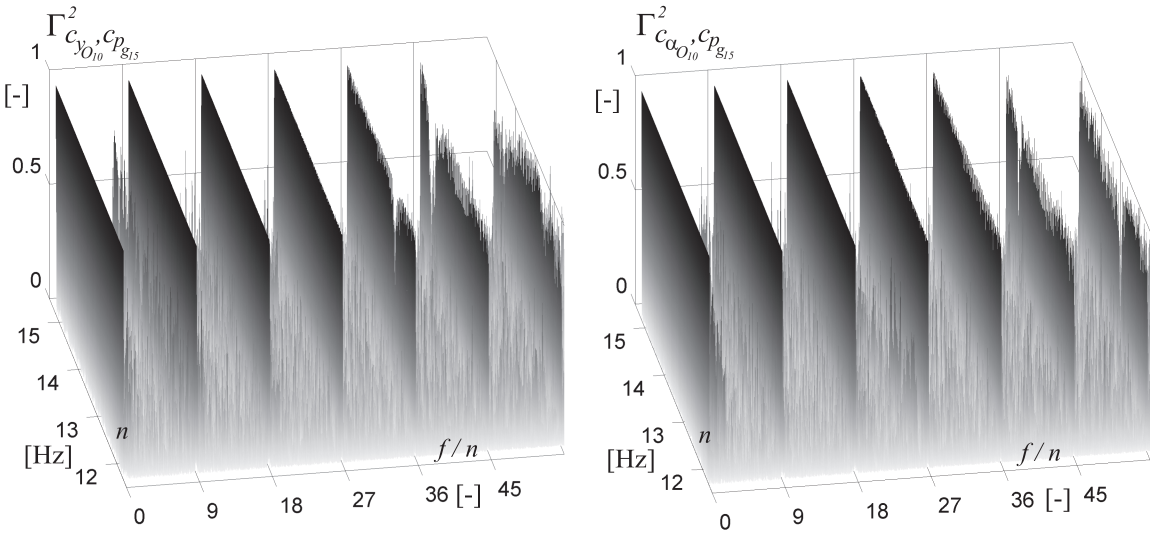

Figure 9.20: Waterfall diagrams of the coherence functions between the pressure factor monitored by the sensor g_{15} and the guide vane O_{10} displacement factor (left) and between the pressure factor monitored by the sensor g_{15} and the guide vane O_{10} torsion angle factor (right) against the impeller frequency n.

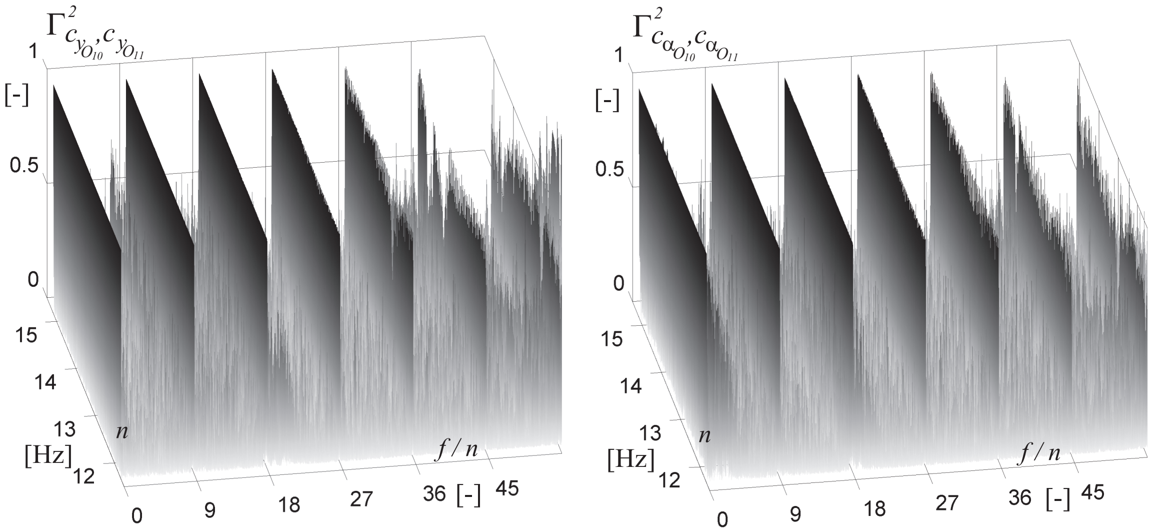

Figure 9.21: Waterfall diagrams of the coherence functions between the displacement factors of the guide vane O_{10} and O_{11} (left) and between the torsion angle factors of the guide vane O_{10} and O_{11} (right) against the impeller frequency n.

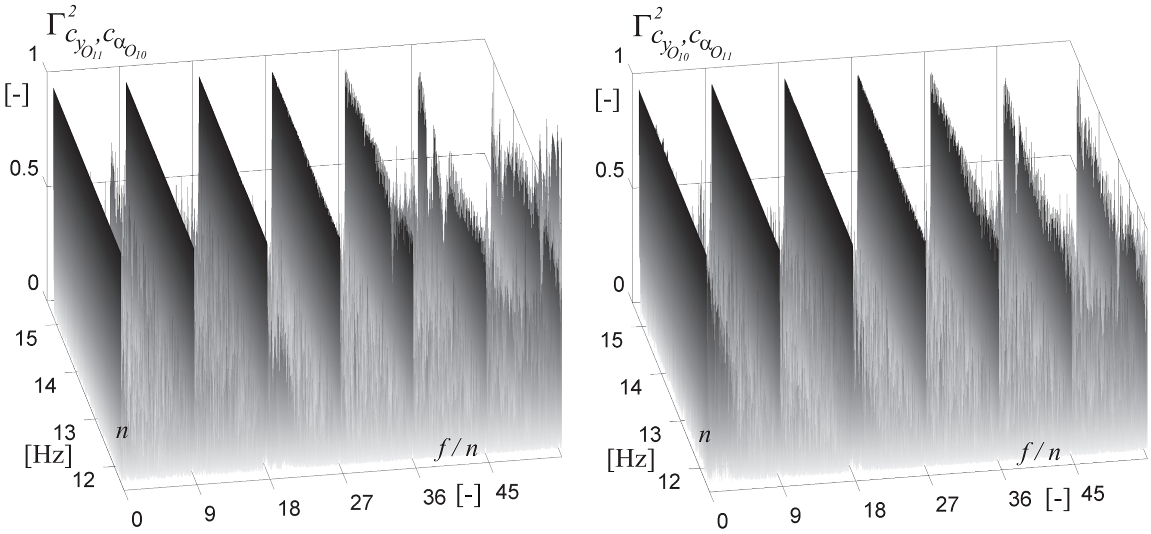

Figure 9.22: Waterfall diagrams of the coherence functions between the displacement factor of the guide vane O_{11} and the torsion angle factor of the guide vane O_{10} (left) and between the displacement factor of the guide vane O_{10} and the torsion angle factor of the guide vane O_{11} (right) against the impeller frequency n.

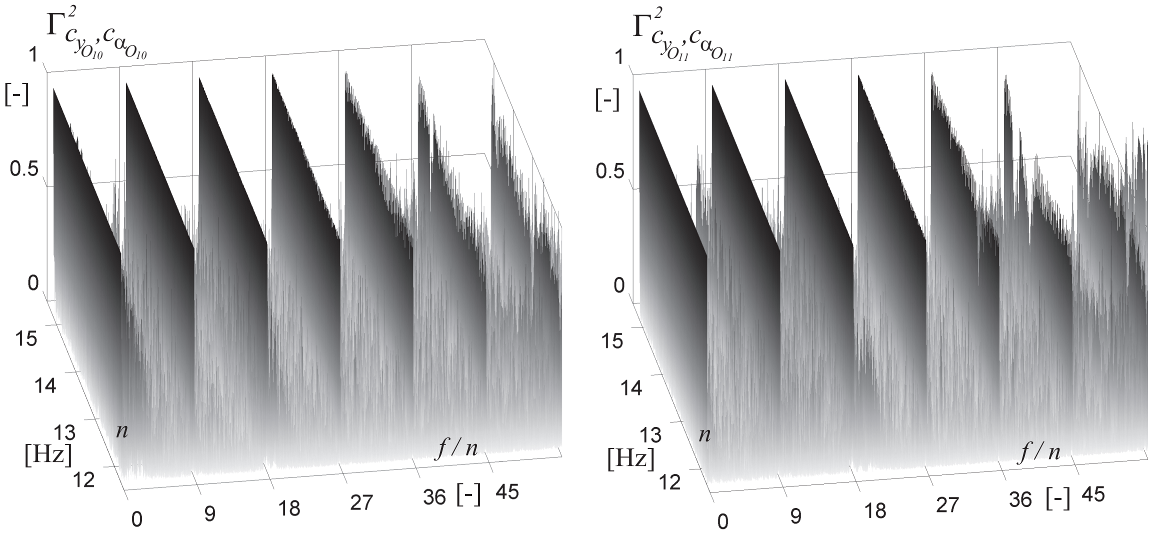

Figure 9.23: Waterfall diagrams of the coherence functions between the displacement factor of the guide vane O_{10} and the torsion angle factor of the guide vane O_{10} (left) and between the displacement factor of the guide vane O_{11} and the torsion angle factor of the guide vane O_{11} (right) against the impeller frequency n.

Chapter 10

Identification of the hydrodynamic parameters

After having analyzed the dynamics of the guide vanes and the pressure fluctuations at the frequency of the RSI modes in Chapter 9, the aim of the present chapter is to identify the hydrodynamic parameters to determine the unknown components of the matrices $\left[I^f\right]$, $\left[C^f\right]$ and $\left[K^f\right]$ in eq. 3.21. The methodology is exposed prior to the analysis of the bending and torsion modes. In Appendix D, the procedure used to identify the hydrodynamic parameters is summarized.

10.1 Identification methodology

Among the guide vanes placed in the cascade, two have a flexible stem, whereas the others have a stiff one. In Appendix B.3.2, it is shown that the bending and torsion stiffness of the usual guide vanes is 2.30 and 2.15 times higher than the corresponding stiffness of the modified guide vanes O_{10} and O_{11}, respectively. The bending and torsion eigenfrequencies are shown in Appendix B.4.2 to be 1.34 and 1.47 times higher than the corresponding eigenfrequencies of the modified guide vanes O_{10} and O_{11}, respectively. Therefore, the vibrating displacement of the usual guide vanes is negligible, and consequently, the displacement/angle vector $\mathbf{y}$ in eq. 3.21 established in Section 3.3 may be simplified as follows:

$$\mathbf{y} = \left(y_{10} \;\; y_{11} \;\; \alpha_{10} \;\; \alpha_{11}\right)^T \tag{10.1}$$

In a similar manner, the force/torque vector $\mathbf{F}$ yields:

$$\mathbf{F} = \left(F_{10} \;\; F_{11} \;\; T_{10} \;\; T_{11}\right)^T \tag{10.2}$$

Therefore, the consideration of a 4 Degrees of Freedom mechanical system permits the system of equations given in eq. 3.21 to be reduced to only four equations.

Based on the approach used in Section 3.3, one decomposes the restricted system of equations as follows:

$$\begin{cases} \left[I^S\right]\ddot{\mathbf{y}}\left(t\right) + \left[C^S\right]\dot{\mathbf{y}}\left(t\right) + \left[K^S\right]\mathbf{y}\left(t\right) = \mathbf{F}\left(t\right) \\ \mathbf{F}\left(t\right) = \bar{\mathbf{F}} + \mathbf{F}^{RSI}\left(t\right) - \left(\left[I^f\right]\ddot{\mathbf{y}}\left(t\right) + \left[C^f\right]\dot{\mathbf{y}}\left(t\right) + \left[K^f\right]\mathbf{y}\left(t\right)\right) \end{cases} \tag{10.3}$$

In the spectral domain, the eq. 10.3 yields:

$$\begin{cases} \left(-\omega^2\left[I^S\right]+\left[K^S\right]+i\omega\left[C^S\right]\right)\hat{\mathbf{y}}(\omega)=\hat{\mathbf{F}}(\omega) \\ \hat{\mathbf{F}}(\omega)=\hat{\mathbf{F}}^{RSI}(\omega)-\left(-\omega^2\left[I^f\right]+i\omega\left[C^f\right]+\left[K^f\right]\right)\hat{\mathbf{y}}(\omega) \end{cases} \tag{10.4}$$

The structural stiffness matrix $[K^s]$ is known from the analytical estimation given in Appendix B.3 and is expressed as:

$$[K^s]=\begin{bmatrix} 1.28\cdot10^6\ \mathrm{kg}\cdot\mathrm{s}^{-2} & 0 & 0 & 0 \\ 0 & 1.28\cdot10^6\ \mathrm{kg}\cdot\mathrm{s}^{-2} & 0 & 0 \\ 0 & 0 & 3610\ \mathrm{kg}\cdot\mathrm{m}^2\cdot\mathrm{s}^{-2} & 0 \\ 0 & 0 & 0 & 3610\ \mathrm{kg}\cdot\mathrm{m}^2\cdot\mathrm{s}^{-2} \end{bmatrix} \tag{10.5}$$

From Table 8.1, the structural mass/inertia matrix may be filled up:

$$[I^s]=\begin{bmatrix} 0.33\ \mathrm{kg} & 0 & 0 & 0 \\ 0 & 0.34\ \mathrm{kg} & 0 & 0 \\ 0 & 0 & 1.75\cdot10^{-4}\ \mathrm{kg}\cdot\mathrm{m}^2 & 0 \\ 0 & 0 & 0 & 1.77\cdot10^{-4}\ \mathrm{kg}\cdot\mathrm{m}^2 \end{bmatrix} \tag{10.6}$$

From Table 8.3, the structural damping matrix may be built:

$$[C^s]=\begin{bmatrix} 5.00\ \mathrm{kg}\cdot\mathrm{s}^{-1} & 0 & 0 & 0 \\ 0 & 6.57\ \mathrm{kg}\cdot\mathrm{s}^{-1} & 0 & 0 \\ 0 & 0 & 0.024\ \mathrm{kg}\cdot\mathrm{m}^2\cdot\mathrm{s}^{-1} & 0 \\ 0 & 0 & 0 & 0.024\ \mathrm{kg}\cdot\mathrm{m}^2\cdot\mathrm{s}^{-1} \end{bmatrix} \tag{10.7}$$

By substituting these matrices in the first equation of 10.4 and since we know the displacement/angle vector $\hat{\mathbf{y}}$ from the forced response measurements, one may obtain the total dynamic force/torque vector $\hat{\mathbf{F}}$ applied to the guide vanes O_{10} and O_{11}. The Fourier transform is applied to eight 2^{14}-sample-long signals $\mathbf{y}(t)$ overlapping by 50%, each of the eight sequences being windowed with a Hamming function. The Fourier transforms are not averaged to keep phase information.

At this stage of the identification procedure, the force/torque vector $\hat{\mathbf{F}}$ may be placed in the second equation of eq. 10.4 to identify the unknown components of the matrices $\left[I^f\right]$, $\left[C^f\right]$, $\left[K^f\right]$.

The fluid mass and inertia matrix in eq. 10.4 is expressed as:

$$\left[I^f\right]=\begin{bmatrix} \boxed{I^f_{10,10}} & I^f_{10,11} & I^{f,\alpha}_{10,10} & I^{f,\alpha}_{10,11} \\ I^f_{11,10} & \boxed{I^f_{11,11}} & I^{f,\alpha}_{11,10} & I^{f,\alpha}_{11,11} \\ J^f_{10,10} & J^f_{10,11} & \boxed{J^{f,\alpha}_{10,10}} & J^{f,\alpha}_{10,11} \\ J^f_{11,10} & J^f_{11,11} & J^{f,\alpha}_{11,10} & \boxed{J^{f,\alpha}_{11,11}} \end{bmatrix} \tag{10.8}$$

where the boxed components are known from Table 8.4 given in Section 8.2.1.

The hydrodynamic damping matrix in eq. 10.4 may be written as:

$$\left[C^f\right] = \begin{bmatrix} \boxed{C^f_{10,10}} & C^f_{10,11} & C^{f,\alpha}_{10,10} & C^{f,\alpha}_{10,11} \\ C^f_{11,10} & \boxed{C^f_{11,11}} & C^{f,\alpha}_{11,10} & C^{f,\alpha}_{11,11} \\ D^f_{10,10} & D^f_{10,11} & \boxed{D^{f,\alpha}_{10,10}} & D^{f,\alpha}_{10,11} \\ D^f_{11,10} & D^f_{11,11} & D^{f,\alpha}_{11,10} & \boxed{D^{f,\alpha}_{11,11}} \end{bmatrix} \tag{10.9}$$

where the boxed components are known from Table 8.6 given in Section 8.2.2.

The fluid stiffness matrix in eq. 10.4 is expressed as follows:

$$\left[K^f\right] = \begin{bmatrix} K^f_{10,10} & 0 & K^{f,\alpha}_{10,10} & 0 \\ 0 & K^f_{11,11} & 0 & K^{f,\alpha}_{11,11} \\ L^f_{10,10} & 0 & L^{f,\alpha}_{10,10} & 0 \\ 0 & L^f_{11,11} & 0 & L^{f,\alpha}_{11,11} \end{bmatrix} \tag{10.10}$$

We finally obtain four equations with 36 unknowns which consists of the non-diagonal terms of the matrices $\left[I^f\right]$ and $\left[C^f\right]$, the non-zero elements of the matrix $\left[K^f\right]$ and the fluctuating force and torque due to RSI, $\hat{\mathbf{F}}^{RSI}$. In the two following sections, the methodology for dealing with this underdetermined system of equations, and to finally identify the missing components of the matrices $\left[I^f\right]$, $\left[C^f\right]$, $\left[K^f\right]$, is consecutively given for the 1^{st} bending and torsion eigenmodes.

10.1.1 Bending eigenmode

As may be observed in Figure 9.15, the bending displacement factor at the RSI 2^{nd} harmonic frequency is 10 times higher than the torsion angle factor at the same frequency. In other words, as shown in eq. 9.9, this mean that the bending displacement is 10 times higher than the leading/trailing edge displacement due to torsion. Therefore, one may neglect the influence of the torsion at this RSI harmonic frequency and the vector $\hat{\mathbf{y}}$ is reduced to:

$$\hat{\mathbf{y}}\left(\omega\right) = \left(\hat{y}_{10}\left(\omega\right) \quad \hat{y}_{11}\left(\omega\right)\right)^T \text{ , for } \omega = 2\pi \cdot 18n. \tag{10.11}$$

At the frequencies of the RSI fundamental and the other harmonics, the displacement factor does not exceed the torsion angle factor in such a way to reduce the vector $\hat{\mathbf{y}}$ to this simple formulation. Therefore, one may only focus on the identification of the hydrodynamic parameters for the vibrating behavior at the RSI 2^{nd} harmonic frequency $f = 18n$.

The eq. 10.4 is reduced to a system of 2 equations:

$$\begin{cases} \left(-\omega^2\left[I^S\right] + \left[K^S\right] + i\omega\left[C^S\right]\right)\left(\hat{y}_{10}\left(\omega\right) \quad \hat{y}_{11}\left(\omega\right)\right)^T = \left(\hat{F}_{10}\left(\omega\right) \quad \hat{F}_{11}\left(\omega\right)\right)^T \\ \left(\hat{F}_{10}\left(\omega\right) \quad \hat{F}_{11}\left(\omega\right)\right)^T = \hat{\mathbf{F}}^{RSI}\left(\omega\right) - \left[\hat{H}^f\right]\left(\hat{y}_{10}\left(\omega\right) \quad \hat{y}_{11}\left(\omega\right)\right)^T \end{cases} \tag{10.12}$$

where the influence matrix $\left[H^f\right]$ is expressed as follows:

$$\begin{aligned}\left[\hat{H}^f\right] &= \begin{bmatrix}\hat{H}^f_{10,10} & \hat{H}^f_{10,11}\\ \hat{H}^f_{11,10} & \hat{H}^f_{11,11}\end{bmatrix}\\ &= \begin{bmatrix}-\omega^2 I^f_{10,10}+i\omega C^f_{10,10}+K^f_{10,10} & -\omega^2 I^f_{10,11}+i\omega C^f_{10,11}\\ -\omega^2 I^f_{11,10}+i\omega C^f_{11,10} & -\omega^2 I^f_{11,11}+i\omega C^f_{11,11}+K^f_{11,11}\end{bmatrix}\end{aligned} \tag{10.13}$$

For high ω, the stiffness terms, $K^f_{10,10}$ and $K^f_{11,11}$, being negligible in comparison to the inertia terms, disappear. Münch et al. [56] show that when $\omega \to \infty$, $\frac{K^f}{I^f\omega^2} \approx 10^{-3} \ll 1$. As a consequence, only the 2 non-diagonal components of the influence matrix $\left[\hat{H}^f\right]$ and the fluctuating force due to RSI, $\hat{\mathbf{F}}^{RSI}$, remain unknown.

To approximate the force contributions due to the RSI excitation, $\hat{\mathbf{F}}^{RSI}$, two assumptions are successively made. First, it is assumed that the guide vane O_{11} bending displacement amplitude, $|\hat{y}_{11}|$, is not high enough to induce any influence on the guide vane O_{10} at the RSI 1^{st} harmonic frequency corresponding to the lowest impeller frequency of the investigated range $f_{min} = 18n_{min}$. Therefore, the force spectral value acting on O_{10} due to the RSI at $f_{min} = 18n_{min}$ may be written from the 2^{nd} equation of Eq. (10.23):

$$\hat{F}^{RSI}_{10}\left(f_{min}\right) = \hat{F}_{10}\left(f_{min}\right) + \left(-\left(\omega_{min}\right)^2 I^f_{10,10} + i\left(\omega_{min}\right) C^f_{10,10}\right)\cdot \hat{y}_{10}\left(f_{min}\right) \tag{10.14}$$

with $\omega_{min} = 2\pi 18 n_{min}$.

The value of the force due to the RSI acting on the guide vane O_{11} at this frequency is assumed to be phase shifted by $\Delta\phi_{k=-2}$, given in Table 7.1, as follows:

$$\hat{F}^{RSI}_{11}\left(f_{min}\right) = \hat{F}^{RSI}_{10}\left(f_{min}\right)\cdot e^{-i\Delta\phi_{k=-2}} \tag{10.15}$$

The force due to the RSI excitation may be linearly linked to the pressure monitored in the guide vane channel on its pressure side as follows:

$$\begin{cases}\hat{F}^{RSI}_{10}\left(f=18n\right) = \hat{L}_{s,10}\cdot \hat{p}^{RSI}_{s_{10}}\left(f=18n\right)\\ \hat{F}^{RSI}_{11}\left(f=18n\right) = \hat{L}_{s,11}\cdot \hat{p}^{RSI}_{s_{11}}\left(f=18n\right)\end{cases} \tag{10.16}$$

where $\hat{L}_{s,10}$ and $\hat{L}_{s,11}$ are complex numbers which are supposed to be constant on the whole impeller frequency range. To determine the force due to the RSI excitation in the whole impeller frequency range, these constants as well as the pressure contribution from the RSI must be known and the following procedure is followed. At the location of the pressure sensors s_{10} and s_{11}, the guide vane vibrations influence the measurement and the contribution due to RSI may not be isolated. Therefore, the only pressure sensor which is not influenced by the guide vane vibrations is the sensor g_{15}. During measurements where all the guide vanes of the cascade feature stiff stem, avoiding in this way the contribution from the guide vane vibrations, the pressure monitored by the sensor g_{15} is supposed to be linearly linked to the pressure monitored by the sensor s_{10} and s_{11} with the complex constants $L_{sg,10}$ and $L_{sg,11}$, respectively.

In the case with the two modified guide vanes, the forces due to the RSI may then be known from the pressure monitored by the sensor g_{15} as follows:

$$\begin{cases} \hat{F}_{10}^{RSI}\left(f=18n\right) = \frac{\hat{L}_{s,10}}{\hat{L}_{sg,10}} \cdot \hat{p}_{g_{15}}\left(f=18n\right) = \hat{L}_{10} \cdot \hat{p}_{g_{15}}\left(f=18n\right) \\ \hat{F}_{11}^{RSI}\left(f=18n\right) = \frac{\hat{L}_{s,11}}{\hat{L}_{sg,11}} \cdot \hat{p}_{g_{15}}\left(f=18n\right) = \hat{L}_{11} \cdot \hat{p}_{g_{15}}\left(f=18n\right) \end{cases} \tag{10.17}$$

Finally, the complex numbers $\hat{L}_{10}$ and $\hat{L}_{11}$ are derived from the system of equations in Eq. (10.17) at the frequency $f = f_{min}$, at which the forces due to the RSI, $\hat{F}_{10}^{RSI}\left(f_{min}\right)$ and $\hat{F}_{11}^{RSI}\left(f_{min}\right)$ are already known from Eqs. (10.14) and (10.15). Assuming that the complex numbers remain constant in the whole impeller frequency range, the forces due to the RSI excitation at all these frequencies may be obtained using Eq. (10.17).

The hydrodynamic parameters, namely the added mass terms, $I_{10,11}^{f}$ and $I_{11,10}^{f}$ and the hydrodynamic damping terms, $C_{10,11}^{f}$ and $C_{11,10}^{f}$, may then be obtained from eq. 10.13 as follows:

$$I_{10,11}^{f}\left(f=18n\right) = -\frac{\Re\left(\hat{H}_{10,11}^{f}\right)}{\omega_{18n}^{2}} \tag{10.18}$$

$$I_{11,10}^{f}\left(f=18n\right) = -\frac{\Re\left(\hat{H}_{11,10}^{f}\right)}{\omega_{18n}^{2}} \tag{10.19}$$

$$C_{10,11}^{f}\left(f=18n\right) = \frac{\Im\left(\hat{H}_{10,11}^{f}\right)}{\omega_{18n}} \tag{10.20}$$

$$C_{11,10}^{f}\left(f=18n\right) = \frac{\Im\left(\hat{H}_{11,10}^{f}\right)}{\omega_{18n}} \tag{10.21}$$

10.1.2 Torsion eigenmode

As may be seen in Figure 9.18, the torsion angle factor at the RSI 5^{th} harmonic frequency is 50 times higher than the bending displacement factor at the same frequency. As already mentioned, this means that the displacement at the leading/trailing edge due to torsion angle is 50 times higher than the bending displacement. Therefore, one may neglect the bending displacement and the vector $\hat{\mathbf{y}}$ is reduced to:

$$\hat{\mathbf{y}}\left(\omega\right) = \left(\hat{\alpha}_{10}\left(\omega\right) \quad \hat{\alpha}_{11}\left(\omega\right)\right)^{T} \text{ , for } \omega = 2\pi \cdot 45n. \tag{10.22}$$

¡¡ At the frequencies of the RSI fundamental and the other harmonics, the torsion angle

factor does not exceed the displacement factor in such a way to reduce the vector $\hat{\mathbf{y}}$ to this simple formulation. Therefore, one may only focus on the identification of the hydrodynamic parameters for the vibrating behavior at the RSI 5^{th} harmonic frequency $f = 45n$.

The eq. 10.4 is reduced to a 2 DOF system of equations:

$$\begin{cases} \left(-\omega^2\left[I^S\right]+\left[K^S\right]+i\omega\left[C^S\right]\right)\left(\hat{\alpha}_{10}\left(\omega\right)\quad\hat{\alpha}_{11}\left(\omega\right)\right)^T=\left(\hat{T}_{10}\left(\omega\right)\quad\hat{T}_{11}\left(\omega\right)\right)^T \\ \left(\hat{T}_{10}\left(\omega\right)\quad\hat{T}_{11}\left(\omega\right)\right)^T=\hat{\mathbf{T}}_i^{RSI}\left(\omega\right)-\left[\hat{G}^f\right]\left(\hat{\alpha}_{10}\left(\omega\right)\quad\hat{\alpha}_{11}\left(\omega\right)\right)^T \end{cases} \tag{10.23}$$

$\left[\hat{G}^f\right]$ being an influence matrix expressed as follows:

$$\begin{aligned} \left[\hat{G}^f\right] &= \begin{bmatrix} \hat{G}^f_{10,10} & \hat{G}^f_{10,11} \\ \hat{G}^f_{11,10} & \hat{G}^f_{11,11} \end{bmatrix} \\ &= \begin{bmatrix} -\omega^2 J^{f,\alpha}_{10,10}+i\omega D^{f,\alpha}_{10,10}+L^{f,\alpha}_{10,10} & -\omega^2 J^{f,\alpha}_{10,11}+i\omega D^{f,\alpha}_{10,11} \\ -\omega^2 J^{f,\alpha}_{11,10}+i\omega D^{f,\alpha}_{11,10} & -\omega^2 J^{f,\alpha}_{11,11}+i\omega D^{f,\alpha}_{11,11}+L^{f,\alpha}_{11,11} \end{bmatrix} \end{aligned} \tag{10.24}$$

As mentioned in Section 10.1.1, for high ω, the stiffness terms $L^{f,\alpha}_{10,10}$ and $L^{f,\alpha}_{11,11}$ are neglected compared to the inertia terms. As a consequence, only the 2 non-diagonal components of the influence matrix $\left[\hat{G}^f\right]$ and the fluctuating torque due to RSI, $\hat{\mathbf{T}}_i^{RSI}$, remain unknown.

To approximate the torque contribution due to the RSI, $\hat{\mathbf{T}}^{RSI}$, one firstly assumes the guide vane O_{11} torsion angle $\hat{\alpha}_{11}$ being not high enough to induce any influence on the guide vane O_{10} at the RSI 5^{th} harmonic frequency corresponding to the lowest impeller frequency of the investigated range $f_{min}=45n_{min}$. Therefore, the torque acting on O_{10} due to the RSI at $f_{min}=45n_{min}$ may be written from the 2^{nd} equation of eq. 10.23:

$$\hat{T}^{RSI}_{10}\left(f_{min}\right)=\hat{T}_{10}\left(f_{min}\right)+\left(-\left(\omega_{min}\right)^2 J^{f,\alpha}_{10,10}+i\left(\omega_{min}\right)D^{f,\alpha}_{10,10}\right)\cdot\hat{\alpha}_{10}\left(f_{min}\right) \tag{10.25}$$

with $\omega_{min}=2\pi 45 n_{min}$.

The torque value acting on the guide vane O_{11} at this frequency is assumed to be phase shifted by $\Delta\phi_{k=5}$ given in Table 7.1 as follows:

$$\hat{T}^{RSI}_{11}\left(f_{min}\right)=\hat{T}^{RSI}_{10}\left(f_{min}\right)\cdot e^{-i\Delta\phi_{k=5}} \tag{10.26}$$

The same procedure as for the bending case is followed to determine the torque due to the RSI excitation in the whole impeller frequency range. Once this torque contribution known, the non-diagonal components of the influence matrix $\left[\hat{G}^f\right]$ may be obtained from eq. 10.23:

$$\hat{G}^f_{10,11}=\frac{\left(\hat{T}_{10}-\hat{T}^{RSI}_{10}\right)}{\hat{\alpha}_{11}} \tag{10.27}$$

$$\hat{G}^f_{11,10}=\frac{\left(\hat{T}_{11}-\hat{T}^{RSI}_{11}\right)}{\hat{\alpha}_{10}} \tag{10.28}$$

The hydrodynamic parameters, namely the added inertia terms, $J^{f,\alpha}_{10,11}$ and $J^{f,\alpha}_{11,10}$, and the hydrodynamic damping terms, $D^{f,\alpha}_{10,11}$ and $D^{f,\alpha}_{11,10}$, may then be obtained from eq. 10.25 as follows:

$$J^{f,\alpha}_{10,11}\left(f=45n\right)=-\frac{\Re\left(\hat{G}^{f}_{10,11}\right)}{\omega^{2}_{45n}} \tag{10.29}$$

$$J^{f,\alpha}_{11,10}\left(f=45n\right)=-\frac{\Re\left(\hat{G}^{f}_{11,10}\right)}{\omega^{2}_{45n}} \tag{10.30}$$

$$D^{f,\alpha}_{10,11}\left(f=45n\right)=\frac{\Im\left(\hat{G}^{f}_{10,11}\right)}{\omega_{45n}} \tag{10.31}$$

$$D^{f,\alpha}_{11,10}\left(f=45n\right)=\frac{\Im\left(\hat{G}^{f}_{11,10}\right)}{\omega_{45n}} \tag{10.32}$$

10.2 Hydrodynamic parameters for the bending eigenmode

The added mass on the guide vane O_{10} by the vibrations of the guide vane O_{11}, $I^{f}_{10,11}$; the added mass on the guide vane O_{11} by the vibrations of the guide vane O_{10}, $I^{f}_{11,10}$; the added masses $I^{f}_{10,10}$ and $I^{f}_{11,11}$; each being normalized by the corresponding structural mass I^{S}_{10} or I^{S}_{11}, are plotted in Figure 10.1 against the RSI 2^{nd} harmonic frequency $f = 18n$ for the whole impeller frequency range investigated. The standard deviations are also indicated by intervals.

The added mass on the guide vane O_{11} by the vibrations of the guide vane O_{10}, $I^{f}_{10,11}$, varies according to the excitation frequency $f = 18n$. It represents between 8.2% and 21.5% of the structural mass of the guide vane O_{10}, I^{S}_{10}. The added mass on the guide vane O_{10} by the vibrations of the guide vane O_{11}, $I^{f}_{11,10}$, is lower than $I^{f}_{10,11}$ and fluctuates between -4.4% and 5.0% of the structural mass of the guide vane O_{11}, I^{S}_{11}. As mentioned in Section 8.2.1, the added mass $I^{f}_{10,10}$ and $I^{f}_{11,11}$ represent 69.7% and 61.8% of the structural mass of the guide vane O_{10} and O_{11}, respectively.

The hydrodynamic damping constant acting on the guide vane O_{10} due to the vibrations of the guide vane O_{11}, $C^{f}_{10,11}$, the hydrodynamic damping constant acting on the guide vane O_{11} due to the vibrations of the guide vane O_{10}, $C^{f}_{11,10}$, the hydrodynamic damping constant $C^{f}_{10,10}$ and $C^{f}_{11,11}$, each being normalized by the corresponding structural damping constant C^{S}_{10} or C^{S}_{11}, are plotted in Figure 10.2 against the RSI 2^{nd} harmonic frequency $f = 18n$ for the whole impeller frequency range investigated. The standard deviations are also indicated by intervals.

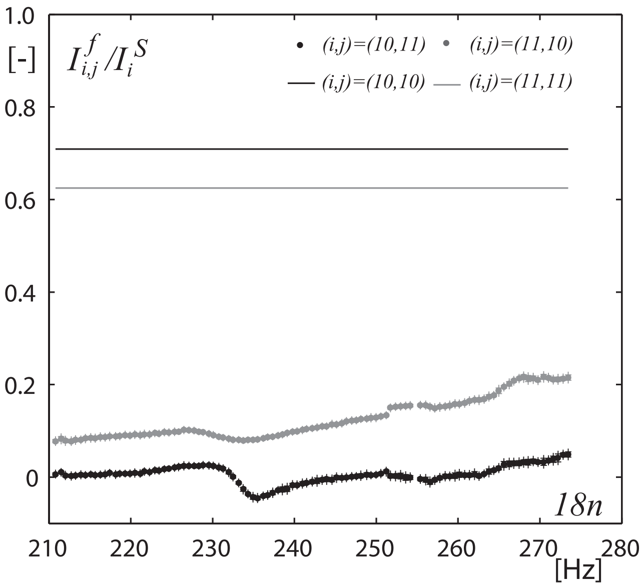

Figure 10.1: Added mass on the guide vane O_{10} by the vibrations of the guide vane O_{11}, $I^f_{10,11}$; added mass on the guide vane O_{11} by the vibrations of the guide vane O_{10}, $I^f_{11,10}$; added masses $I^f_{10,10}$ and $I^f_{11,11}$; each being normalized by the corresponding structural mass I^S_{10} or I^S_{11}, at the RSI 2^{nd} harmonic frequency $f = 18n$ for the whole impeller frequency range investigated.

We may observe high variations of the hydrodynamic damping due to the vibrations of the neighboring guide vanes throughout the investigated impeller frequency range. The hydrodynamic damping constant $C^f_{10,11}$ is from 0 up to 11.7 times higher than the structural damping constant C^S_{10} and the hydrodynamic damping constant $C^f_{11,10}$ represents between 0 and 461% of the structural damping constant C^S_{11}. As already mentioned, the damping constants $C^f_{10,10}$ and $C^f_{11,11}$ are assumed constant throughout the investigated impeller frequency range and correspond to 510% of C^S_{10} and 330% of C^S_{11}, respectively.

The amplitude of the total force $|\hat{F}_{10}|$ acting on the guide vane O_{10}; the contribution from the RSI, $|\hat{F}^{RSI}_{10}|$; the contribution from O_{10} vibrations, $|\hat{F}^f_{10,10}|$; and the contribution from O_{11} vibrations, $|\hat{F}^f_{10,11}|$; at the frequency corresponding to the RSI 2^{nd} harmonic frequency are normalized by $\hat{F}^{RSI}_{10}$ and plotted in Figure 10.3. The standard deviations are also indicated by intervals.

The amplitude of the total force acting on the guide vane O_{11}, $|\hat{F}_{11}|$; the contribution from the RSI, $|\hat{F}^{RSI}_{11}|$; the contribution from O_{11} vibrations, $|\hat{F}^f_{11,11}|$; and the contribution from O_{10} vibrations, $|\hat{F}^f_{11,10}|$; at the frequency corresponding to the RSI 2^{nd} harmonic frequency are normalized by $\hat{F}^{RSI}_{11}$ and plotted in Figure 10.4. The standard deviations are also indicated by intervals.

On the one hand, it may be seen that the force acting on the guide vane O_{10} due to the guide vane O_{11} vibrations is between 14 and 100 times lower than the force due to the guide vane O_{10} vibrations. On the other hand, the force acting on the guide vane O_{11} due to the guide vane O_{10} vibrations is between 2 and 10 times lower than the force due

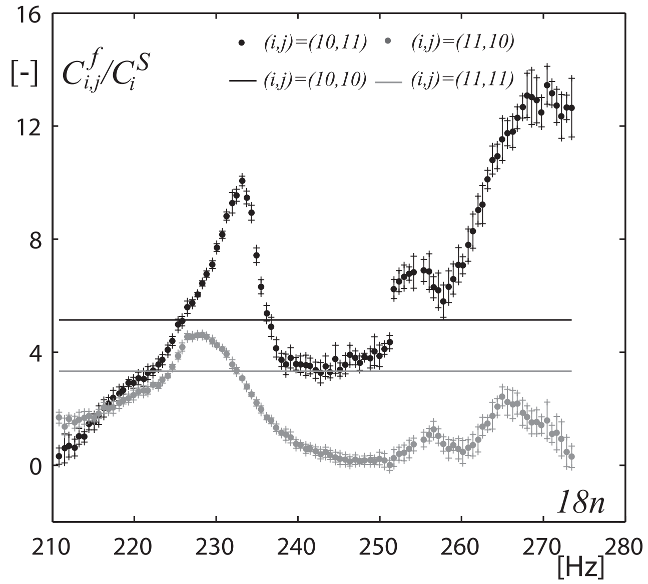

Figure 10.2: Hydrodynamic damping constant acting on the guide vane O_{10} due to the vibrations of the guide vane O_{11}, $C^f_{10,11}$; hydrodynamic damping constant acting on the guide vane O_{11} due to the vibrations of the guide vane O_{10}, $C^f_{11,10}$; hydrodynamic damping constants $C^f_{10,10}$ and $C^f_{11,11}$; each being normalized by the corresponding structural damping constant C^S_{10} or C^S_{11}, at the RSI 2^{nd} harmonic frequency $f = 18n$ for the whole impeller frequency range investigated.

to the guide vane O_{11} vibrations. The force amplitude $|\hat{F}^f_{11,10}|$ is between 2 and 10 times higher than the force amplitude $|\hat{F}^f_{10,11}|$ and, consequently, the assumption leading to the eq. 10.14 is verified. Finally, whereas the amplitude of the force due to the adjacent guide vane vibrations remain inferior to the amplitude of the force due to RSI, the amplitude of the force acting on a guide vane due to its vibrations may exceed the amplitude of the force due to the RSI by a factor 7 at resonance.

In Figure 10.5, the phase shift at the RSI 2^{nd} harmonic frequency $f = 18n$ between the displacement of the guide vanes O_{10} and O_{11} and the external force due to the RSI acting on the guide vane O_{10} and O_{11}, respectively, is plotted against the corresponding frequency. The standard deviations are also indicated by intervals.

One may see that, throughout the guide vane resonance, the phase shift at the RSI 2^{nd} harmonic frequency $f = 18n$ between the displacement and the external force due to the RSI greatly varies. Theoretically, a resonance modifies the phase shift by $-\pi$. Here, the resonance already occurs at a lower frequency than $f_{min} = 18n_{min}$ and, therefore, on the investigated impeller rotating frequency range, the phase shift varies by -2.8 rad and -2.4 rad for the guide vanes O_{10} and O_{11}, respectively. Moreover, between $18n = 230$ Hz and $18n = 240$ Hz, the phase shift between the displacement of the guide vane O_{11} and the external force due to the RSI locally varies due to the influence of the vibrations of the guide vane O_{10}.

In Figure 10.6, the ratio of the Fourier transform magnitude of the guide vane O_{10}

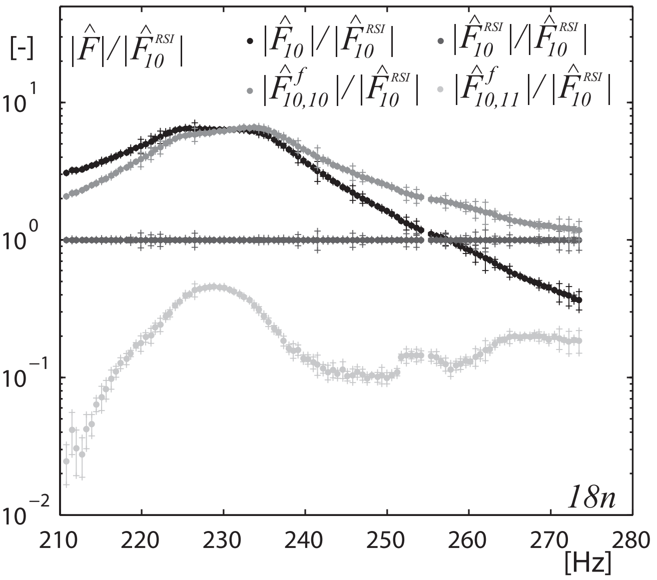

Figure 10.3: Fourier transform magnitude of normalized total force $|\hat{F}_{10}|/|\hat{F}_{10}^{RSI}|$ acting on the guide vane O_{10} at the 2^{nd} harmonic frequency and each of its contributions: the normalized contribution from RSI, $|\hat{F}_{10}^{RSI}|/|\hat{F}_{10}^{RSI}|$; the normalized contribution of the own vibrations, $|\hat{F}_{10,10}^{f}|$; and the normalized contribution from the vibrations of the guide vane O_{11}, $|\hat{F}_{10,11}^{f}|$.

bending displacement to the Fourier transform magnitude of the guide vane O_{11} bending displacement is plotted at the RSI 2^{nd} harmonic frequency $f = 18n$, for the investigated impeller frequency range. At resonance, the guide vane O_{10} vibrates with an amplitude 3 times higher than the guide vane O_{11}, whereas far from resonance, the ratio is 1.

As mentioned in Section 3.3, regarding the Figures 9.15 and 10.6, one may assume that at least three parameters are able to play a role in the added mass terms, $I_{10,11}^{f}$ and $I_{11,10}^{f}$, and in the hydrodynamic damping terms, $C_{10,11}^{f}$ and $C_{11,10}^{f}$: the phase shift between the displacement of the guide vanes O_{10} and O_{11}, $\Delta\phi_{y_{10},y_{11}}$, the relative amplitude of the vibrations, $\frac{|\hat{y}_{10}|}{|\hat{y}_{11}|}$, and the reference flow velocity C_{ref}. The added mass and hydrodynamic terms are approached by the following expressions:

$$I_{10,11}^{*f} = \left(0.5\ \mathrm{kg\cdot s\cdot m^{-1}}\cdot C_{ref} + 1.4\ \mathrm{kg}\cdot\frac{|\hat{y}_{10}|}{|\hat{y}_{11}|}\cdot sin\left(\Delta\phi_{y_{10},y_{11}} - 0.5\right) - 2.1\ \mathrm{kg}\right)\cdot 10^{-2} \tag{10.33}$$

$$I_{11,10}^{*f} = \left(2.75\ \mathrm{kg\cdot s\cdot m^{-1}}\cdot C_{ref} + 3.25\ \mathrm{kg}\cdot\frac{|\hat{y}_{11}|}{|\hat{y}_{10}|}\cdot sin\left(\Delta\phi_{y_{10},y_{11}} + 1.7\right) - 20\ \mathrm{kg}\right)\cdot 10^{-2} \tag{10.34}$$

$$C_{10,11}^{*f} = 25\ \mathrm{kg\cdot m^{-1}}\cdot C_{ref} + 22\ \mathrm{kg\cdot s^{-1}}\cdot\frac{|\hat{y}_{10}|}{|\hat{y}_{11}|}\cdot sin\left(\Delta\phi_{y_{10},y_{11}} + 1\right) - 185\ \mathrm{kg\cdot s^{-1}} \tag{10.35}$$

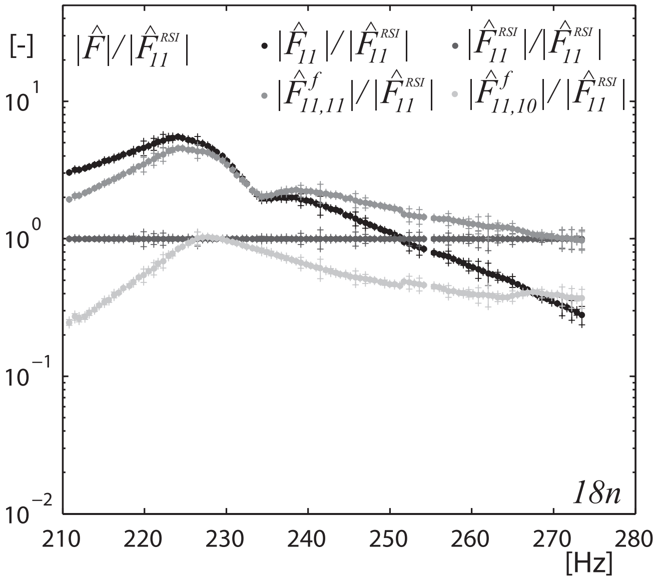

Figure 10.4: Fourier transform magnitude of normalized total force $|\hat{F}_{11}|/|F_{11}^{RSI}|$ acting on the guide vane O_{11} at the 2^{nd} harmonic frequency and each of its contributions: the normalized contribution from RSI, $|\hat{F}_{11}^{RSI}|/|\hat{F}_{11}^{RSI}|$; the normalized contribution of the own vibrations, $|\hat{F}_{11,11}^{f}|$; and the normalized contribution from the vibrations of the guide vane O_{10}, $|\hat{F}_{11,10}^{f}|$.

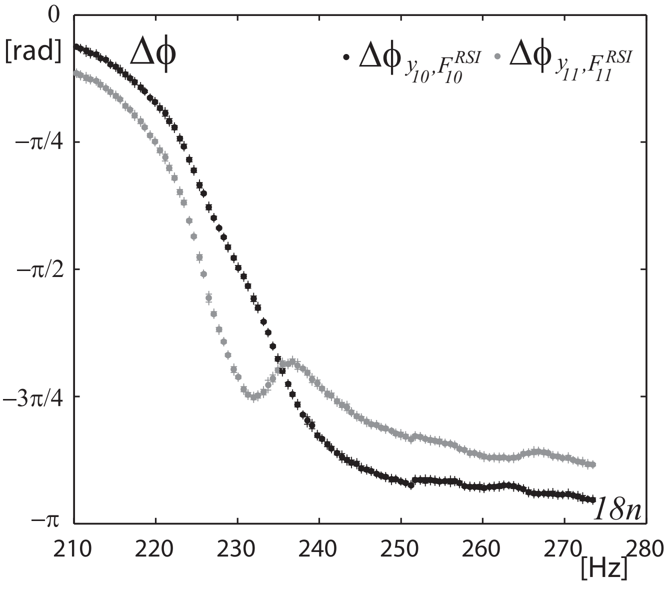

Figure 10.5: Phase shift between the displacement and the force at the RSI 2^{nd} harmonic frequency $f = 18n$.

$$C_{11,10}^{*f} = 5\ \mathrm{kg} \cdot \mathrm{m}^{-1} \cdot C_{ref} + 50\ \mathrm{kg} \cdot \mathrm{s}^{-1} \cdot \frac{|\hat{y}_{11}|}{|\hat{y}_{10}|} \cdot sin\,(\Delta\phi_{y_{10},y_{11}} + 0.4) - 21\ \mathrm{kg} \cdot \mathrm{s}^{-1} \quad (10.36)$$

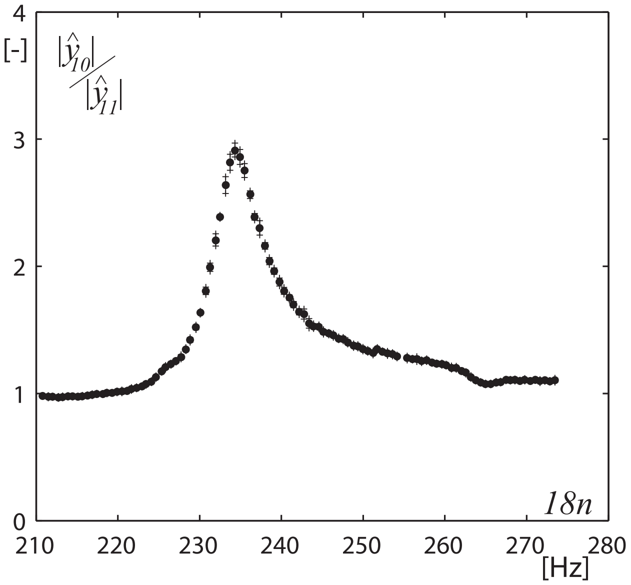

Figure 10.6: Ratio of the Fourier transform magnitude of the guide vane O_{10} bending displacement to the Fourier transform magnitude of the guide vane O_{11} bending displacement at the RSI 2^{nd} harmonic frequency $f = 18n$, for the investigated impeller frequency range.

The eqs. 10.33 to 10.36 are assumed to be valid for the investigated ranges, namely $-0.7 \leq \Delta\phi_{y_{10},y_{11}} \leq 0.3$ and $1 \leq \frac{|\hat{y}_{10}|}{|\hat{y}_{11}|} \leq 3$.

In Figure 10.7, the measured values, $I^{f}_{11,10}$, of the added mass on the guide vane O_{11} due to the vibrations of the guide vane O_{10} at the frequency $f = 18n$, are compared with the approximated values $I^{*f}_{11,10}$. Both are normalized with the structural mass I^{S}_{11} and plotted against the corresponding frequency $f = 18n$. The standard deviations are also indicated by intervals.

In Figure 10.8, the measured values, $I^{f}_{10,11}$, of the added mass on the guide vane O_{10} due to the vibrations of the guide vane O_{11} at the frequency $f = 18n$, are compared to the approximated values $I^{*f}_{10,11}$. Both are normalized with the structural mass I^{S}_{10} and plotted against the corresponding frequency. The standard deviations are also indicated by intervals.

In Figure 10.9, the measured values, $C^{f}_{11,10}$, of the hydrodynamic damping constant acting on the guide vane O_{11} due to the vibrations of the guide vane O_{10} at the frequency $f = 18n$, are compared to the approximated values $C^{*f}_{11,10}$. Both are normalized with the structural damping constant C^{S}_{11} and plotted against the corresponding frequency. The standard deviations are also indicated by intervals.

In Figure 10.10, the measured values, $C^{f}_{10,11}$, of the hydrodynamic damping constant acting on the guide vane O_{10} due to the vibrations of the guide vane O_{11} at the frequency $f = 18n$, are compared to the approximated values $C^{*f}_{10,11}$. Both are normalized with the structural damping constant C^{S}_{10} and plotted against the corresponding frequency. The standard deviations are also indicated by intervals.

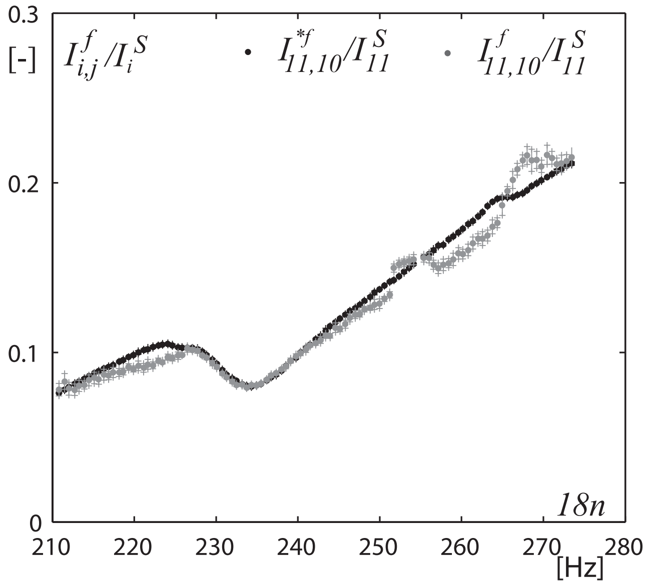

Figure 10.7: Measured values, $I^f_{11,10}$, and approximated values, $I^{*f}_{11,10}$, of the added mass on the guide vane O_{11} due to the vibrations of the guide vane O_{10} at the RSI 2^{nd} harmonic $f = 18n$, normalized with the structural mass I^S_{11}, against the corresponding frequency.

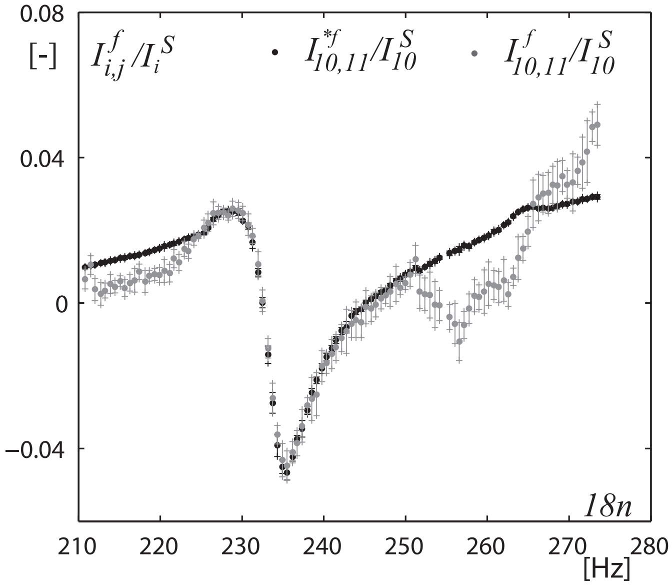

Figure 10.8: Measured values, $I^f_{10,11}$, and approximated values, $I^{*f}_{10,11}$, of the added mass on the guide vane O_{10} due to the vibrations of the guide vane O_{11} at the RSI 2^{nd} harmonic $f = 18n$, normalized with the structural mass J^S_{10}, against the corresponding frequency.

The approximated added mass and the hydrodynamic damping constants fit the measured values adequately. For the bending case, the guide vane cascade is therefore shown to behave as a 2^{nd} order mechanical system whose parameters are dependent of the flow

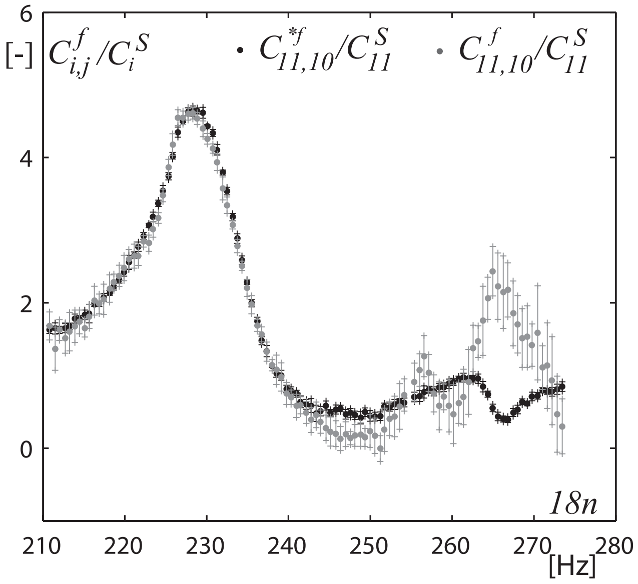

Figure 10.9: Measured values, $C^f_{11,10}$, and approximated values, $C^{*f}_{11,10}$, of the hydrodynamic damping constant acting on the guide vane O_{11} due to the vibrations of the guide vane O_{10} at the RSI 2^{nd} harmonic $f = 18n$, normalized with the structural damping constant C^S_{11}, against the corresponding frequency.

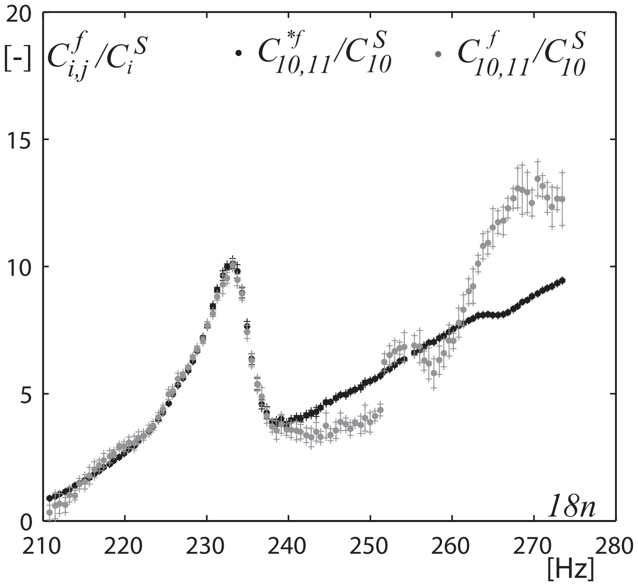

Figure 10.10: Measured values, $C^f_{10,11}$, and approximated values, $C^{*f}_{10,11}$, of the hydrodynamic damping constant acting on the guide vane O_{10} due to the vibrations of the guide vane O_{11} at the RSI 2^{nd} harmonic $f = 18n$, normalized with the structural damping constant C^S_{10}, against the corresponding frequency.

velocity, the vibration phase shift between two adjacent guide vanes and the relative amplitude of their vibrations.

10.3 Hydrodynamic parameters for the torsion eigenmode

The added inertia on the guide vane O_{10} by the vibrations of the guide vane O_{11}, $J^{f,\alpha}_{10,11}$; the added inertia on the guide vane O_{11} by the vibrations of the guide vane O_{10}, $J^{f,\alpha}_{11,10}$; the added inertia $J^{f,\alpha}_{10,10}$ and $J^{f,\alpha}_{11,11}$, each being normalized by the corresponding structural inertia J^{S}_{10} or J^{S}_{11}; are plotted in Figure 10.11 against the RSI 5^{th} harmonic frequency $f = 45n$ for the whole impeller frequency range investigated. The standard deviations are also indicated by intervals.

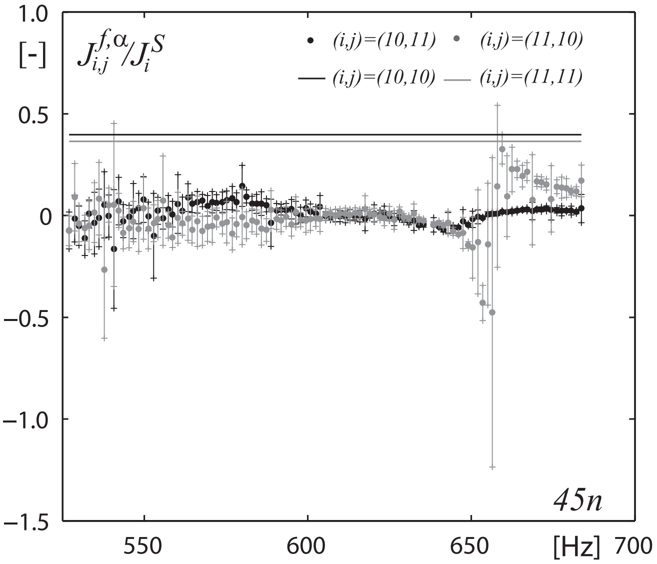

Figure 10.11: Added inertia on the guide vane O_{10} by the vibrations of the guide vane O_{11}, $J^{f,\alpha}_{10,11}$; added inertia on the guide vane O_{11} by the vibrations of the guide vane O_{10}, $J^{f,\alpha}_{11,10}$; added inertia $J^{f,\alpha}_{10,10}$ and $J^{f,\alpha}_{11,11}$; each being normalized by the corresponding structural inertia J^{S}_{10} or J^{S}_{11}, at the RSI 5^{th} harmonic frequency $f = 45n$ for the whole impeller frequency range investigated.

The added inertia on the guide vane O_{11} by the vibrations of the guide vane O_{10}, $J^{f,\alpha}_{10,11}$, varies slightly according to the excitation frequency $f = 45n$. It represents between -5% and 5% of the structural mass of the guide vane O_{10}, J^{S}_{10}. The added inertia on the guide vane O_{10} by the vibrations of the guide vane O_{11}, $J^{f,\alpha}_{11,10}$, varies more than $J^{f,\alpha}_{10,11}$ and fluctuates between -45% and 30% of the structural mass of the guide vane O_{11}, J^{S}_{11}. As mentioned in Section 8.2.1, the added mass $J^{f,\alpha}_{10,10}$ and $J^{f,\alpha}_{11,11}$ represent 39.7% and 36.4% of the structural mass of the guide vane O_{10} and O_{11}, respectively.

The hydrodynamic damping constant acting on the guide vane O_{10} due to the vibrations of the guide vane O_{11}, $D^{f,\alpha}_{10,11}$; the hydrodynamic damping constant acting on the guide vane O_{11} due to the vibrations of the guide vane O_{10}, $D^{f,\alpha}_{11,10}$; the hydrodynamic damping constant $D^{f,\alpha}_{10,10}$ and $D^{f,\alpha}_{11,11}$; each being normalized by the corresponding structural damping constant D^{S}_{10} or D^{S}_{11}, are plotted in Figure 10.12 against the RSI 5^{th} harmonic frequency $f = 45n$ for the whole impeller frequency range investigated. The standard deviations are also indicated by intervals.

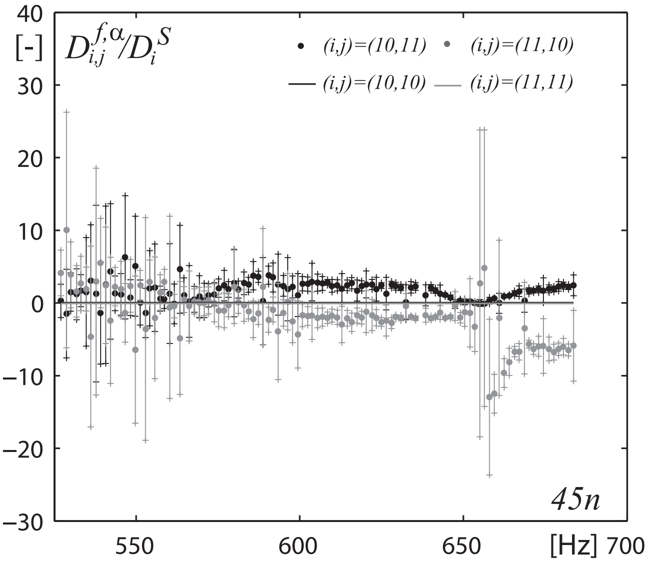

Figure 10.12: Hydrodynamic damping constant acting on the guide vane O_{10} due to the vibrations of the guide vane O_{11}, $D^{f,\alpha}_{10,11}$; hydrodynamic damping constant acting on the guide vane O_{11} due to the vibrations of the guide vane O_{10}, $D^{f,\alpha}_{11,10}$; hydrodynamic damping constants $D^{f,\alpha}_{10,10}$ and $D^{f,\alpha}_{11,11}$; each being normalized by the corresponding structural damping constant D^{S}_{10} or D^{S}_{11}, at the RSI 5^{th} harmonic frequency $f = 45n$ for the whole impeller frequency range investigated.

We may observe variations of the hydrodynamic damping due to the vibrations of the neighboring guide vanes throughout the investigated impeller frequency range. The hydrodynamic damping constant $D^{f,\alpha}_{10,11}$ is from 0 up to 2 times higher than the structural damping constant D^{S}_{10} and the hydrodynamic damping constant $D^{f,\alpha}_{11,10}$ represents between 0 and -12% of the structural damping constant C^{S}_{11}. As already mentioned, the damping constants $D^{f,\alpha}_{10,10}$ and $D^{f,\alpha}_{11,11}$ are assumed constant throughout the investigated impeller frequency range and correspond to 4% of D^{S}_{10} and 8% of D^{S}_{11}, respectively.

The amplitude of the total torque $|\hat{T}_{10}|$ acting on the guide vane O_{10}; the contribution from the RSI, $|\hat{T}^{RSI}_{10}|$; the contribution from O_{10} vibrations, $|\hat{T}^{f}_{10,10}|$; and the contribution from O_{11} vibrations, $|\hat{T}^{f}_{10,11}|$; at the frequency corresponding to the RSI 5^{th} harmonic frequency are normalized by $\hat{T}^{RSI}_{10}$ and plotted in Figure 10.13. The standard deviations are also indicated by intervals.

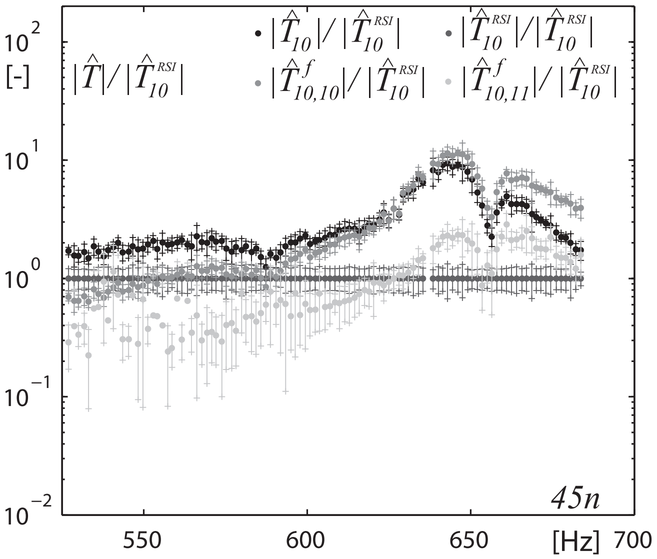

Figure 10.13: Fourier transform magnitude of normalized total torque $|\hat{T}_{10}|/|\hat{T}_{10}^{RSI}|$ acting on the guide vane O_{10} at the 5^{th} harmonic frequency and each of its contributions: the normalized contribution from RSI, $|\hat{T}_{10}^{RSI}|/|\hat{T}_{10}^{RSI}|$; the normalized contribution of the own vibrations, $|\hat{T}_{10,10}^{f}|$; and the normalized contribution from the vibrations of the guide vane O_{11}, $|\hat{T}_{10,11}^{f}|$.

The amplitude of the total torque $|\hat{T}_{11}|$ acting on the guide vane O_{11}; the contribution from the RSI, $|\hat{T}_{11}^{RSI}|$; the contribution from O_{11} vibrations, $|\hat{T}_{11,11}^{f}|$; and the contribution from O_{10} vibrations, $|\hat{T}_{11,10}^{f}|$; at the frequency corresponding to the RSI 5^{th} harmonic frequency are normalized by $\hat{T}_{11}^{RSI}$ and plotted in Figure 10.14. The standard deviations are also indicated by intervals.

It may be seen that the torque acting on the guide vane O_{10} due to the guide vane O_{11} vibrations is 5 times lower than the torque due to the guide vane O_{10} vibrations. Similarly, the torque acting on the guide vane O_{11} due to the guide vane O_{10} vibrations is 5 times lower than the torque due to the guide vane O_{11} vibrations. The torque amplitude $|\hat{T}_{11,10}^{f}|$ is 5 times higher than the torque amplitude $|\hat{T}_{10,11}^{f}|$ and, consequently, the assumption leading to eq. 10.25 is verified. Finally, the amplitude of the torque due to the adjacent guide vane vibrations may exceed the amplitude of the torque due to RSI by a factor 10 at resonance.

In Figure 10.15, the phase shift at the RSI 5^{th} harmonic frequency $f = 45n$ between the torsion angle of the guide vanes O_{10} and O_{11} and the external torque due to the RSI acting on the guide vane O_{10} and O_{11}, respectively, is plotted against the corresponding frequency. The standard deviations are also indicated by intervals.

The phase shift between the torsion angle and the external torque varies by $-\pi$ throughout the resonance, namely from 625 Hz to 683 Hz. Between $45n = 650$ Hz and $45n = 660$ Hz, the phase shift between the torsion angle of the guide vane O_{10} and the external torque due to the RSI locally varies due to the influence of the vibrations of

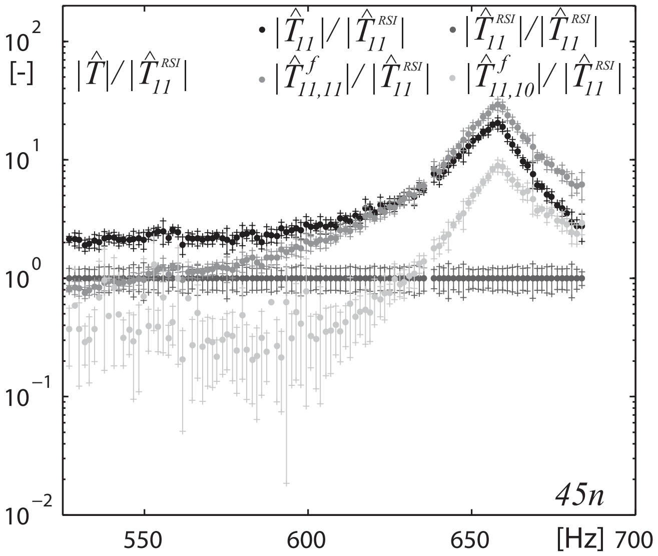

Figure 10.14: Fourier transform magnitude of normalized total torque $|\hat{T}_{11}|/|\hat{T}_{11}^{RSI}|$ acting on the guide vane O_{11} at the 5^{th} harmonic frequency and each of its contributions: the normalized contribution from RSI, $|\hat{T}_{11}^{RSI}|/|\hat{T}_{11}^{RSI}|$; the normalized contribution of the own vibrations, $|\hat{T}_{11,11}^{f}|$; and the normalized contribution from the vibrations of the guide vane O_{10}, $|\hat{T}_{11,10}^{f}|$.

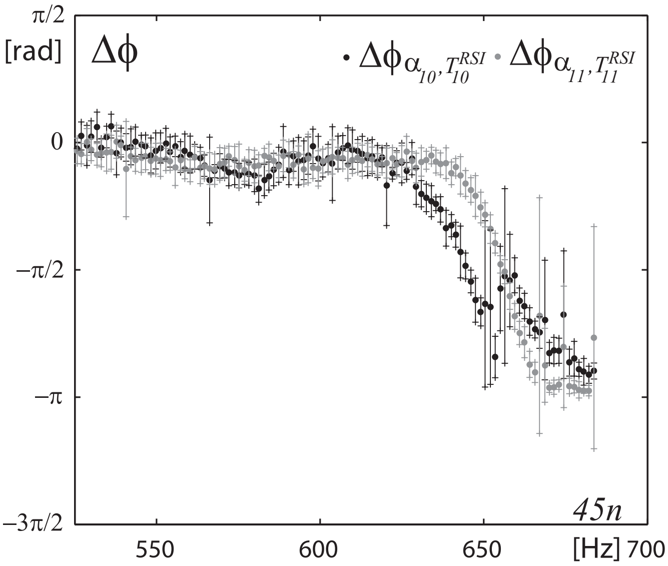

Figure 10.15: Phase shift between the torsion angle and the torque at the RSI 5^{th} harmonic frequency $f = 45n$.

the guide vane O_{11}.

In Figure 10.16, the ratio of the Fourier transform magnitude of the guide vane O_{10} torsion angle to the Fourier transform magnitude of the guide vane O_{11} torsion angle at the RSI 5^{th} harmonic frequency $f = 45n$, for the investigated impeller frequency range. At resonance, the guide vane O_{10} vibrates with an amplitude 9 times lower than the guide vane O_{11}, whereas, far from resonance, the ratio tends to 1.

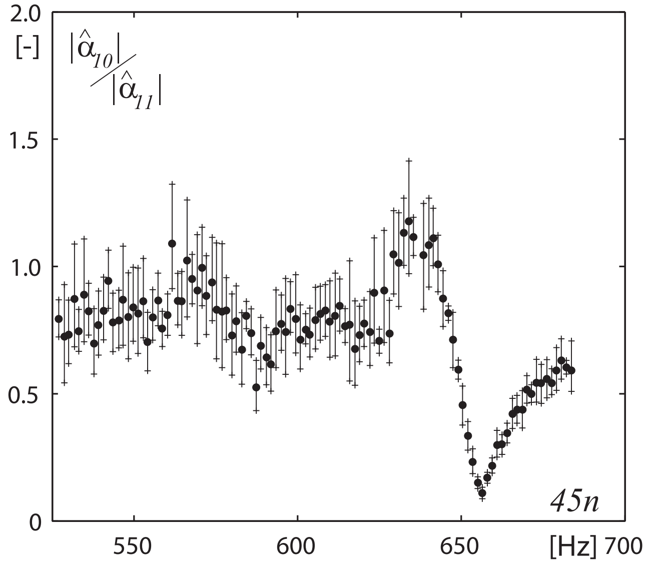

Figure 10.16: Ratio of the Fourier transform magnitude of the guide vane O_{10} torsion angle to the Fourier transform magnitude of the guide vane O_{11} torsion angle at the RSI 5^{th} harmonic frequency $f = 45n$, for the investigated impeller frequency range.

As for the bending motion case, three parameters are able to play a role in the added inertia, $J^{f,\alpha}_{10,11}$ and $J^{f,\alpha}_{11,10}$, and in the hydrodynamic damping, $D^{f,\alpha}_{10,11}$ and $D^{f,\alpha}_{11,10}$: the phase shift between the torsion angle of the guide vanes O_{10} and O_{11}, $\Delta\phi_{\alpha_{10},\alpha_{11}}$, the relative amplitude of the vibrations, $\frac{|\hat{\alpha}_{10}|}{|\hat{\alpha}_{11}|}$, and the reference flow velocity C_{ref}. These terms are approached by the following expressions:

$$J^{*f}_{10,11} = \left(1.5\ \mathrm{kg}\cdot\mathrm{m}^2\cdot\frac{|\hat{\alpha}_{10}|}{|\hat{\alpha}_{11}|}\cdot sin\left(\Delta\phi_{y_{10},y_{11}}-1.5\right)+0.10\ \mathrm{kg}\cdot\mathrm{m}^2\right)\cdot 10^{-5} \tag{10.37}$$

$$J^{*f}_{11,10} = \left(1\ \mathrm{kg}\cdot\mathrm{m}\cdot\mathrm{s}\cdot C_{ref}+1.5\ \mathrm{kg}\cdot\mathrm{m}^2\cdot\frac{|\hat{\alpha}_{11}|}{|\hat{\alpha}_{10}|}\cdot sin\left(\Delta\phi_{y_{10},y_{11}}-1.0\right)-9\ \mathrm{kg}\cdot\mathrm{m}^2\right)\cdot 10^{-5} \tag{10.38}$$

$$D^{*f}_{10,11} = 0.03\ \mathrm{kg}\cdot\mathrm{m}\cdot C_{ref}+0.08\ \mathrm{kg}\cdot\mathrm{m}^2\cdot\mathrm{s}^{-1}\cdot\frac{|\hat{\alpha}_{10}|}{|\hat{\alpha}_{11}|}\cdot sin\left(\Delta\phi_{y_{10},y_{11}}\right)-0.27\ \mathrm{kg}\cdot\mathrm{m}^2\cdot\mathrm{s}^{-1} \tag{10.39}$$

$$D^{*f}_{11,10} = -0.06\ \mathrm{kg}\cdot\mathrm{m}\cdot C_{ref}+0.08\ \mathrm{kg}\cdot\mathrm{m}^2\cdot\mathrm{s}^{-1}\cdot\frac{|\hat{\alpha}_{11}|}{|\hat{\alpha}_{10}|}\cdot sin\left(\Delta\phi_{y_{10},y_{11}}-3.1\right)+0.54\ \mathrm{kg}\cdot\mathrm{m}^2\cdot\mathrm{s}^{-1} \tag{10.40}$$

In Figure 10.17, the measured values, $J^{f,\alpha}_{11,10}$, of the added mass on the guide vane O_{11} due to the vibrations of the guide vane O_{10} at the frequency $f = 45n$, are compared to the approximated values $J^{*f,\alpha}_{11,10}$. Both are normalized with the structural inertia J^S_{11} and plotted against the corresponding frequency. The standard deviations are also indicated by intervals.

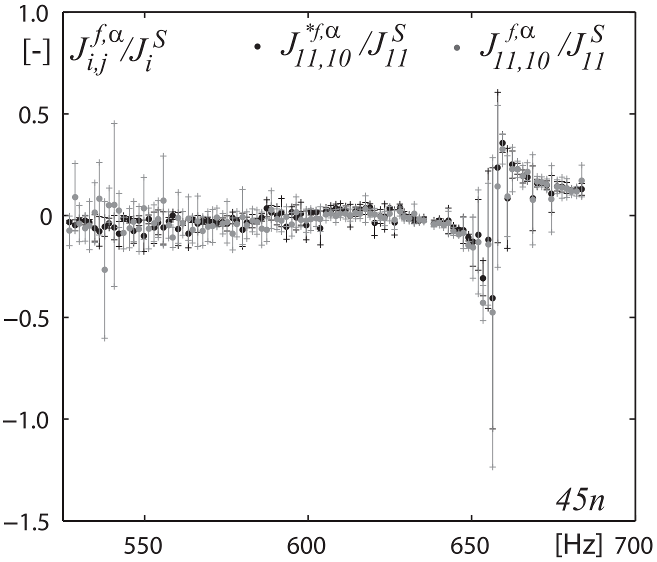

Figure 10.17: Measured values, $J^f_{11,10}$, and approximated values, $J^{*f}_{11,10}$, of the added inertia on the guide vane O_{11} due to the vibrations of the guide vane O_{10} at the RSI 5^{th} harmonic $f = 45n$, normalized with the structural inertia J^S_{11}, against the corresponding frequency.

In Figure 10.18, the measured values, $J^{f,\alpha}_{10,11}$, of the added mass on the guide vane O_{10} due to the vibrations of the guide vane O_{11} at the frequency $f = 45n$, are compared to the approximated values $J^{*f,\alpha}_{10,11}$. Both are normalized with the structural inertia J^S_{10} and plotted against the corresponding frequency. The standard deviations are also indicated by intervals.

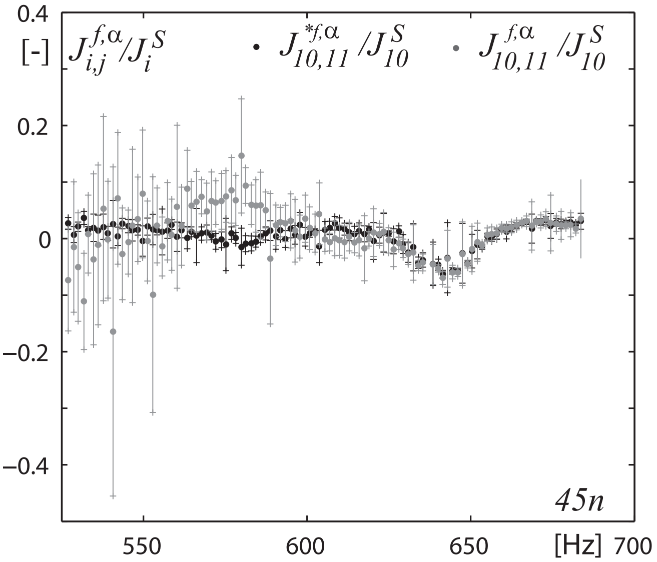

Figure 10.18: Measured values, $J^f_{10,11}$, and approximated values, $J^{*f}_{10,11}$, of the added inertia on the guide vane O_{10} due to the vibrations of the guide vane O_{11} at the RSI 5^{th} harmonic $f = 45n$, normalized with the structural inertia J^S_{10}, against the corresponding frequency.

In Figure 10.19, the measured values, $D^{f,\alpha}_{11,10}$, of the hydrodynamic damping constant acting on the guide vane O_{11} due to the vibrations of the guide vane O_{10} at the frequency $f = 45n$, are compared to the approximated values $D^{*f,\alpha}_{11,10}$. Both are normalized with the structural inertia D^S_{11} and plotted against the corresponding frequency. The standard deviations are also indicated by intervals.

In Figure 10.20, the measured values, $D^{f,\alpha}_{10,11}$, of the hydrodynamic damping constant acting on the guide vane O_{10} due to the vibrations of the guide vane O_{11} at the frequency $f = 45n$, are compared to the approximated values $D^{*f,\alpha}_{10,11}$. Both are normalized with the structural inertia D^S_{10} and plotted against the corresponding frequency. The standard deviations are also indicated by intervals.

The approximated added inertia and the hydrodynamic damping constants fit the measured values adequately. For the torsion case, the guide vane cascade is therefore shown to behave as a 2^{nd} order mechanical system whose parameters are dependent of the flow velocity, the vibration phase shift between two adjacent guide vanes and the relative amplitude of their vibrations.

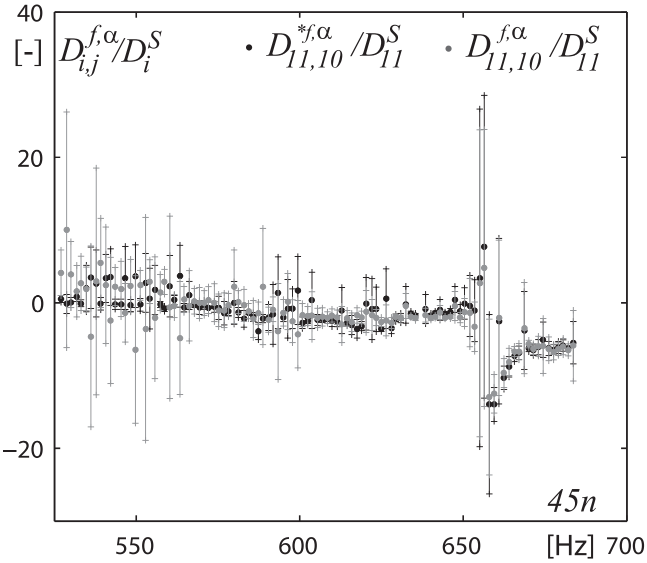

Figure 10.19: Measured values, $D^f_{11,10}$, and approximated values, $D^{*f}_{11,10}$, of the hydrodynamic damping constant acting on the guide vane O_{11} due to the vibrations of the guide vane O_{10} at the RSI 5^{th} harmonic $f = 45n$, normalized with the structural damping constant D^S_{11}, against the corresponding frequency.

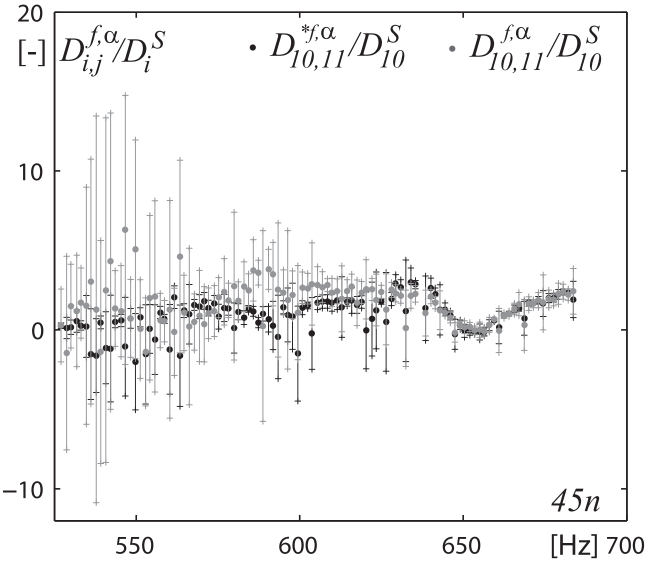

Figure 10.20: Measured values, $D^f_{10,11}$, and approximated values, $D^{*f}_{10,11}$, of the hydrodynamic damping constant acting on the guide vane O_{10} due to the vibrations of the guide vane O_{11} at the RSI 5^{th} harmonic $f = 45n$, normalized with the structural damping constant D^S_{10}, against the corresponding frequency.

Chapter 11

Eigenvalue problem

The aim of this chapter is to consider the eigenvalue problem linked to the bending motion and the torsion motion. The associated eigenvalues being complex, the eigenvectors are complex as well and defined in the phase space. The eigenfrequencies determined in this chapter are compared with the frequencies at which the guide vanes respond preferably in the tests.

11.1 Bending eigenmode

In this section, the bending eigenmode is considered. The relative residual $[\delta C]$, measuring the satisfaction of the Caughey condition, given in eq. 3.26, is defined as follows:

$$\delta C_{i,j} = \frac{\left[[C]\,[I]^{-1}\,[K] - [K]\,[I]^{-1}\,[C] \right]_{i,j}}{\left[[C]\,[I]^{-1}\,[K] \right]_{i,j}} \tag{11.1}$$

The Caughey condition is satisfied if $[\delta C] = 0$. The four elements of the relative residual $[\delta C]$ matrix at the RSI 2^{nd} harmonic frequency are given in Figure 11.1. The standard deviations are indicated by intervals.

In Figure 11.1, it may clearly be observed that the Caughey condition is not satisfied. The two diagonal terms of the $[\delta C]$ matrix present a value of 10% around the bending eigenfrequency value. At higher frequencies, the matrix components $\delta C_{10,10}$ and $\delta C_{11,11}$ are rising up to -0.4 and 0.3, respectively. One has to mention the small values of the standard deviation, except for frequencies where the denominator in eq. 11.1 is close to zero and for frequencies close to $f = 18 n_{max}$.

Since the Caughey condition is not satisfied, the eigenfrequencies of the mechanical system are found by following the procedure given in Section 3.4. The eigenfrequencies of the 2 DOF mechanical system are plotted in Figure 11.2 against the excitation frequency corresponding to the RSI 2^{nd} harmonic frequency $f = 18n$, for the investigated impeller frequency range.

In Figure 11.2, one may see that the eigenfrequencies vary depending on the impeller rotation frequency. As the mechanical system has two DOF, two eigenfrequencies exist for each impeller rotating frequency. Nevertheless, the resonance of the guide vanes is reached when the linear curve $f_{0,y,i}$ crosses one or the other eigenfrequency curves. As

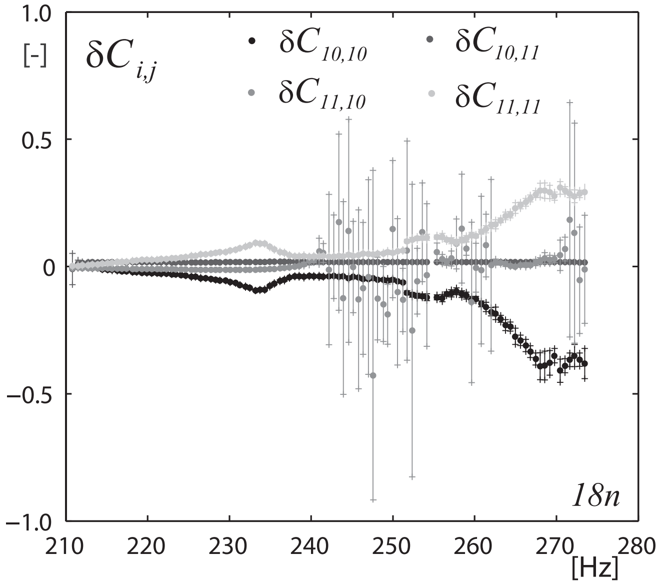

Figure 11.1: Component of the relative residual matrix $[\delta C]$ measuring the satisfaction of the Caughey condition for the case of bending motion, against the RSI 2^{nd} harmonic excitation frequency $f = 18n$.

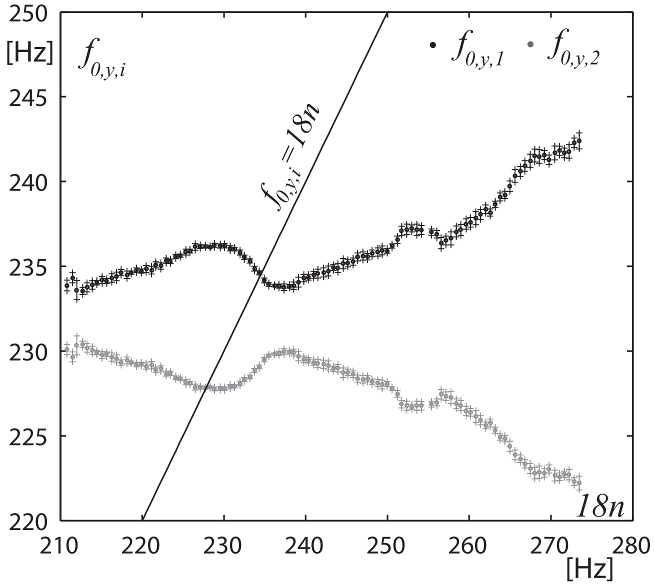

Figure 11.2: Eigenfrequencies of the 2 DOF system, against the RSI 2^{nd} harmonic excitation frequency $f = 18n$.

may be observed in the figure, in the present case, resonance occurs at 228 and 234 Hz, which corroborate the results, see Figure 9.15: the guide vane O_{10} reaches resonance at 234 Hz, whereas the amplitude of the vibrations of the guide vane O_{11} at this frequency is attenuated. The latter responds preferably at 228 Hz.

The eigenfrequencies of the corresponding conservative mechanical system are obtained imposing $[C] = 0$ in eq. 3.25. They are plotted in Figure 11.2 against the excitation frequency corresponding to the RSI 2^{nd} harmonic frequency $f = 18n$. Comparing Figure 11.3 with Figure 11.2, one may see that the eigenfrequencies are not very shifted due to the dissipation effect.

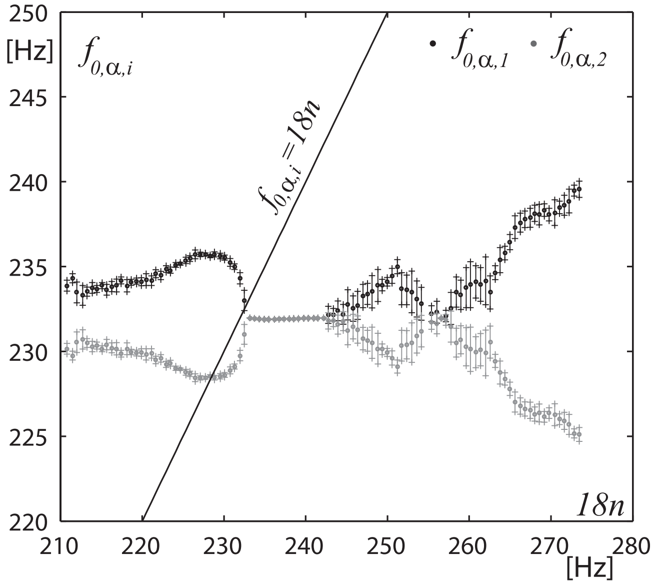

Figure 11.3: Eigenfrequencies of the corresponding 2 DOF's conservative system, against the RSI 2^{nd} harmonic excitation frequency $f = 18n$.

11.2 Torsion eigenmode

In this section, one focuses on the torsion eigenmode. The four elements of the relative residual $[\delta C]$ matrix, defined in eq. 11.1, at the RSI 5^{th} harmonic frequency are given in Figure 11.4

As may be observed the Caughey condition is not satisfied. At low frequencies, the large standard deviation values are due to the low torsion angle measured values. Above 630 Hz, the diagonal components of the relative residual $[\delta D^{\alpha}]$ matrix diverge from the zero value and rise up to -0.6. Therefore, the procedure explained in Section 3.4 must be followed to identify the eigenfrequencies.

The eigenfrequencies of the mechanical system are plotted in Figure 11.5 against the excitation frequency corresponding to the RSI 5^{th} harmonic frequency $f = 45n$.

At low frequencies, the standard deviation values are great because of the low torsion angle measured values. The linear curve $f_{0,\alpha,i} = 45n$ crosses the eigenfrequency curves around 610 Hz and 655 Hz. In Figure 9.15, the torsion angle factor fluctuations of the guide vane O_{11} are amplified at 655 Hz, whereas the torsion angle factor fluctuations of the guide vane O_{10} are attenuated. The guide vanes have reached resonance. Nevertheless,

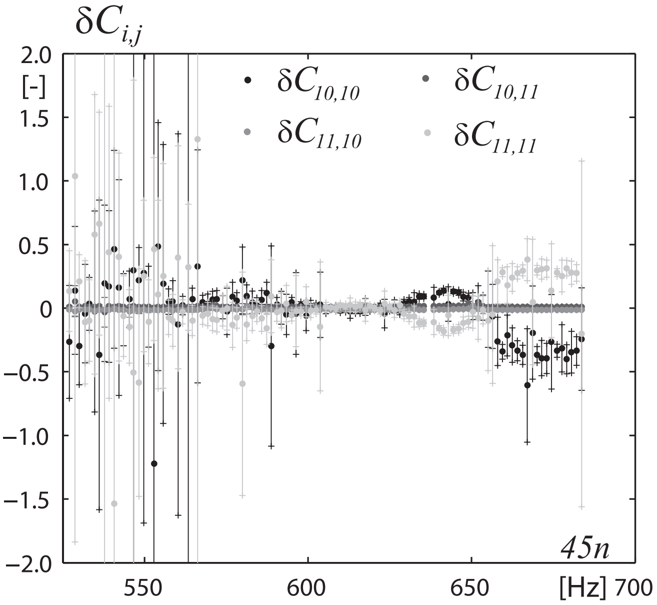

Figure 11.4: Component of the relative residual matrix $[\delta D]$ measuring the satisfaction of the Caughey condition for the case of torsion motion, against the RSI 5^{th} harmonic excitation frequency $f = 45n$.

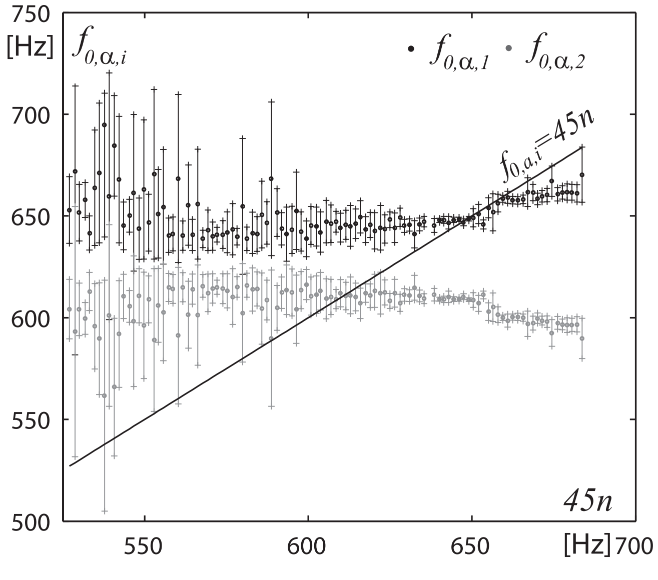

Figure 11.5: Eigenfrequencies of the 2 DOFs system against the RSI 5^{th} harmonic excitation frequency $f = 45n$.

the torsion angle factor fluctuations of the two guide vanes do not show any resonance at 610 Hz.

The eigenfrequencies of the corresponding conservative mechanical system are plotted in Figure 11.6 against the excitation frequency corresponding to the RSI 5^{th} harmonic frequency $f = 45n$. According to Figure 11.6, the resonance of the corresponding conservative mechanical system should be reached between 625 and 650 Hz. The shift of the eigenfrequencies due to dissipation is greater for the torsion than for the bending mode.

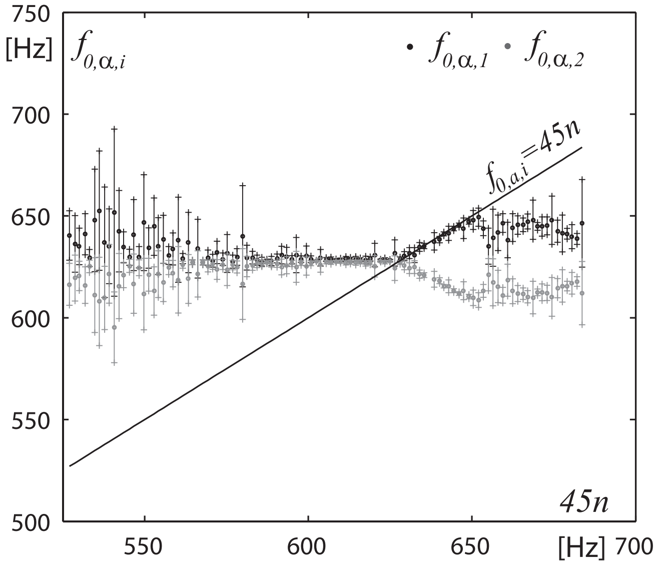

Figure 11.6: Eigenfrequencies of the corresponding conservative 2 DOFs system against the RSI 5^{th} harmonic excitation frequency $f = 45n$.

Chapter 12

The entire guide vane cascade

This chapter aims to predict the behavior of the entire cascade if all the $z_o = 20$ guide vanes feature a flexible stem, from the measurements on two instrumented guide vanes in the case where the others present a stiff stem. The structural inertia/mass, damping and stiffness of each guide vane are supposed to be identical.

12.1 Bending eigenmode

The $z_o \times z_o$ influence matrix $\left[\hat{H}^f\right]$ is constructed with the hydrodynamic parameters obtained from the measurements. Each guide vane present similar stiffness, damping and mass terms. Therefore, a guide vane influences itself and its neighbors similarly to another one. Moreover, based on the results obtained in Appendix C.3, one assumes that only the guide vanes placed adjacently influence each other; the influence matrix $\left[\hat{H}^f\right]$ being thus tri-diagonal. Therefore, one has:

$$\left[\hat{H}^f\right] \begin{cases} \hat{H}^f_{i,j} = \hat{H}^f_{10,10} \text{ , if } i = j \\ \hat{H}^f_{i,j} = \hat{H}^f_{10,11} \text{ , if } j = i+1 \\ \hat{H}^f_{i,j} = \hat{H}^f_{11,10} \text{ , if } j = i-1 \end{cases} \tag{12.1}$$

The $z_o = 20$ eigenvectors are identified following the procedure exposed in Section 3.4. We restrict the investigation to the p values $(0 \leq p \leq 3)$ corresponding to the measured phase shifts, since the eqs. 10.33 to 10.36 are valid in the investigated range of the phase shift between two adjacent guide vanes. The relative amplitude $\frac{\hat{y}_{10}}{\hat{y}_{11}}$ is 1. In Figure 12.1, the real part of the first four displacement eigenvectors $\mathbf{B}_p$ for $0 \leq p \leq 3$ are normalized with their maximum value and plotted.

According to eq. 3.40, each p value features a particular phase shift $\Delta\phi = \frac{2\pi}{z_o} \cdot p$ between two adjacent guide vanes of the cascade. Assuming a permanent response, one may compute the resulting displacement as follows:

$$\hat{\mathbf{y}}\left(18n\right) = \left[-\omega^2_{18n}\left[I\right] + \left[K\right] + \imath \cdot \omega_{18n}\left[C\right]\right]^{-1} \hat{\mathbf{F}}^{RSI}\left(18n\right) \tag{12.2}$$

In Figure 12.2, the eigenfrequency and the eigenvalue real part of the bending eigenmodes $0 \leq p \leq 3$ at the RSI 2^{nd} harmonic frequency $f = 18n$ are plotted against the corresponding frequency.

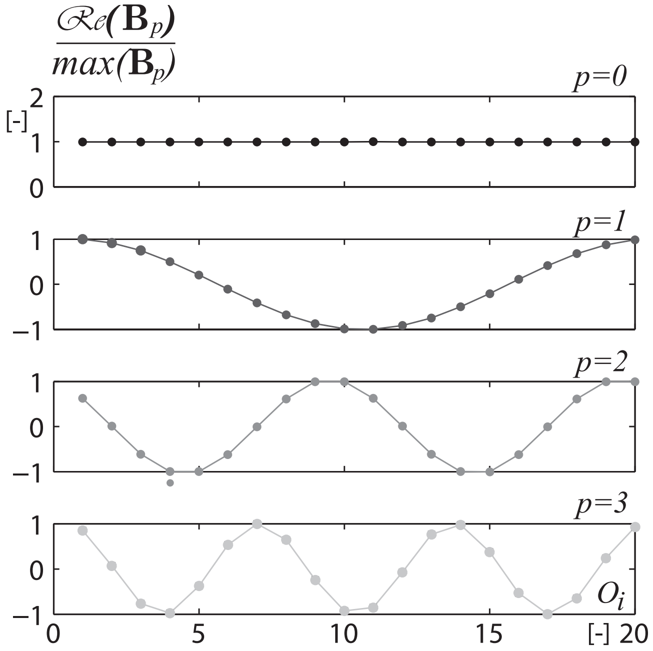

Figure 12.1: Real part of the first four displacement eigenvectors $\mathbf{B}_p$ for $0 \leq p \leq 3$ normalized with their maximum value.

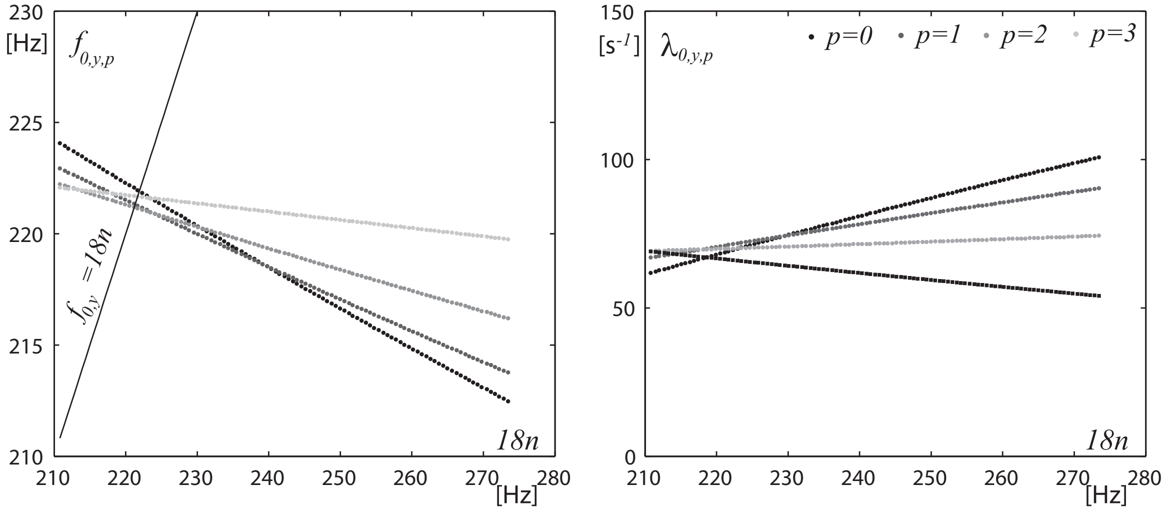

Figure 12.2: Eigenfrequency (left) and eigenvalue real part (right) of the bending modes $0 \leq p \leq 3$, against the RSI 2^{nd} harmonic excitation frequency $f = 18n$.

The frequency at which the guide vanes respond preferably varies from 221 Hz to 222 Hz according to the different eigenmodes, which is between 2% and 3% lower than the frequency at which the guide vanes respond preferably in the tests made with two adjacent flexible guide vanes. The real eigenvalue of each eigenmode is positive, that is the mechanical system is stable. Since the RSI pressure mode at this frequency features a phase shift $\Delta\phi_{p=2} = \frac{2\pi}{20} \cdot 2$, all the evidence suggests that the eigenmode $p = 2$ is most likely.

In Figure 12.3, the amplitude of the displacement factor of a guide vane in the cascade at the RSI 2^{nd} harmonic frequency $f = 18n$ is plotted for the mode $p = 2$. It may be observed that when considering the entire guide vane flexible, the vibration amplitude is twice lower than when considering only two flexible guide vanes, the others being stiff.

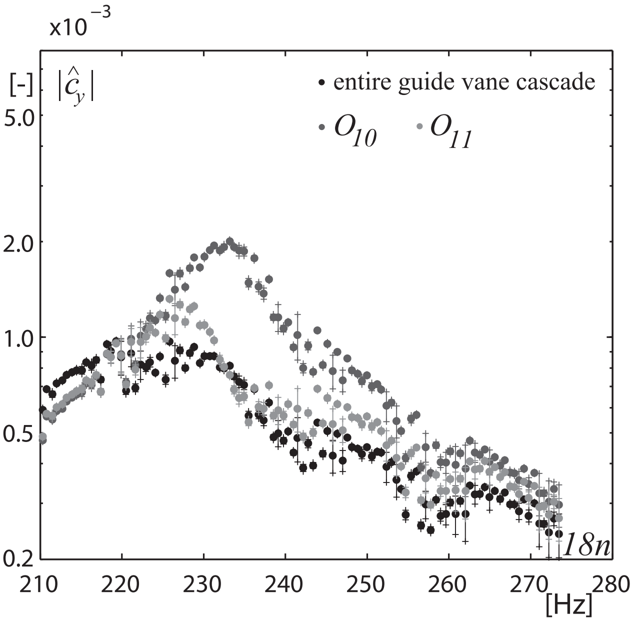

Figure 12.3: Measured values of displacement factor amplitude of the guide vanes O_{10} and O_{11} during the measurements and predicted values of displacement factor amplitude of a guide vane in the cascade if each one features a flexible stem and identical structural mass, damping and stiffness, at the RSI 2^{nd} harmonic frequency $f = 18n$, for the mode $p = 2$.

12.2 Torsion eigenmode

In a similar manner as for the bending mode, the $z_o \times z_o$ influence matrix $\left[\hat{G}^f\right]$ is constructed assuming that each guide vane influences itself and its adjacent neighbors similarly to another one. Moreover, based on the results obtained in Appendix C.3, one assumes that only the guide vanes placed adjacently are influencing each other; the influence matrix $\left[\hat{G}^f\right]$ being thus tri-diagonal. Therefore, one has:

$$\left[G^f\right] \begin{cases} \hat{G}^f_{i,j} = \hat{G}^f_{10,10} \text{ , if } i = j \\ \hat{G}^f_{i,j} = \hat{G}^f_{10,11} \text{ , if } j = i + 1 \\ \hat{G}^f_{i,j} = \hat{G}^f_{11,10} \text{ , if } j = i - 1 \end{cases} \tag{12.3}$$

The $z_o = 20$ torsion angle eigenvectors are identified following the procedure exposed in Section 3.4. As for the case of the bending eigenmodes, one restricts the investigation to the p values corresponding to the measured phase shifts, since the eqs. 10.37 to 10.40 are valid in the investigated range of the phase shift between two adjacent guide vanes. The relative amplitude $\frac{\hat{y}_{10}}{\hat{y}_{11}}$ is 1. In Figure 12.4, the real part of the first six torsion angle eigenvectors for $0 \leq p \leq 5$ are normalized with their maximum value are plotted.

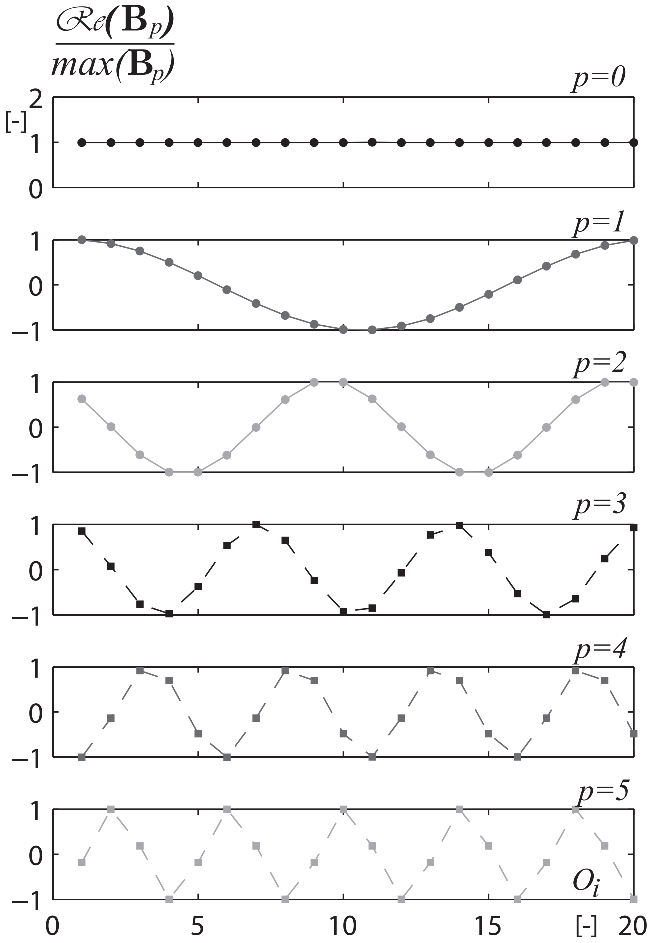

Figure 12.4: Real part of the first six torsion angle eigenvectors for $0 \leq p \leq 5$ normalized with their maximum value.

According to eq. 3.40, each p value features a particular phase shift $\Delta\phi = \frac{2\pi}{z_o} \cdot p$ between two adjacent guide vanes of the cascade. Assuming a permanent response, one may compute the resulting torsion angle as follows:

$$\hat{\mathbf{y}}\left(45n\right) = \left[-\omega_{45n}^2\left[I\right] + \left[K\right] + \imath \cdot \omega_{45n}\left[C\right]\right]^{-1} \hat{\mathbf{F}}^{RSI}\left(45n\right) \tag{12.4}$$

In Figure 12.5, the eigenfrequency of the torsion eigenmodes $0 \leq p \leq 5$ at the RSI 5^{th} harmonic frequency $f = 45n$ are plotted against the corresponding frequency.

In Figure 12.6, the real part of the eigenvalues corresponding to the torsion eigenmodes $0 \leq p \leq 5$ at the RSI 5^{th} harmonic frequency $f = 45n$ are plotted against the corresponding frequency.

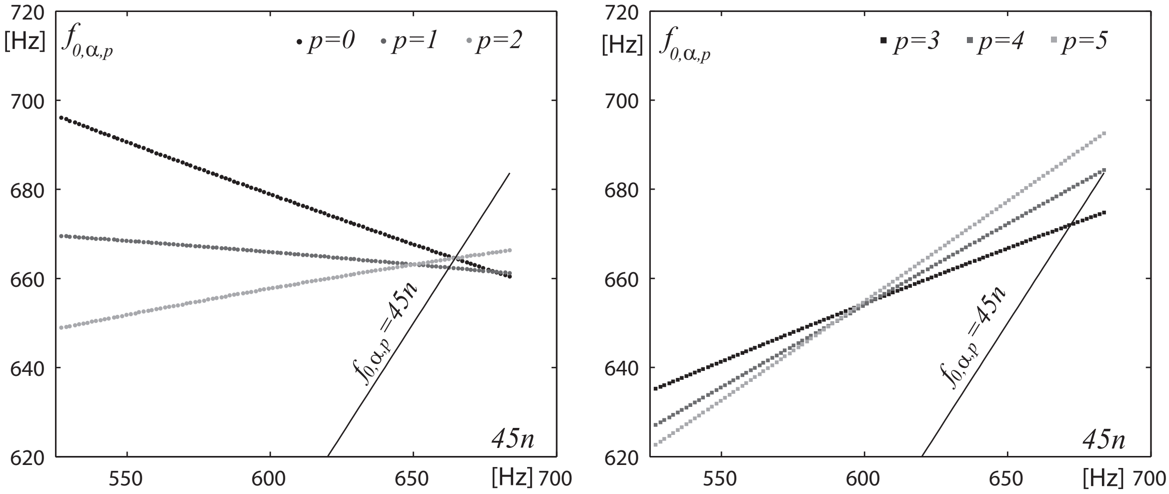

Figure 12.5: Eigenfrequency of the guide vane cascade, corresponding to the modes $0 \leq p \leq 2$ (left) and the modes $3 \leq p \leq 5$ (right) against the excitation frequency corresponding to the RSI 5^{th} harmonic frequency $f = 45n$.

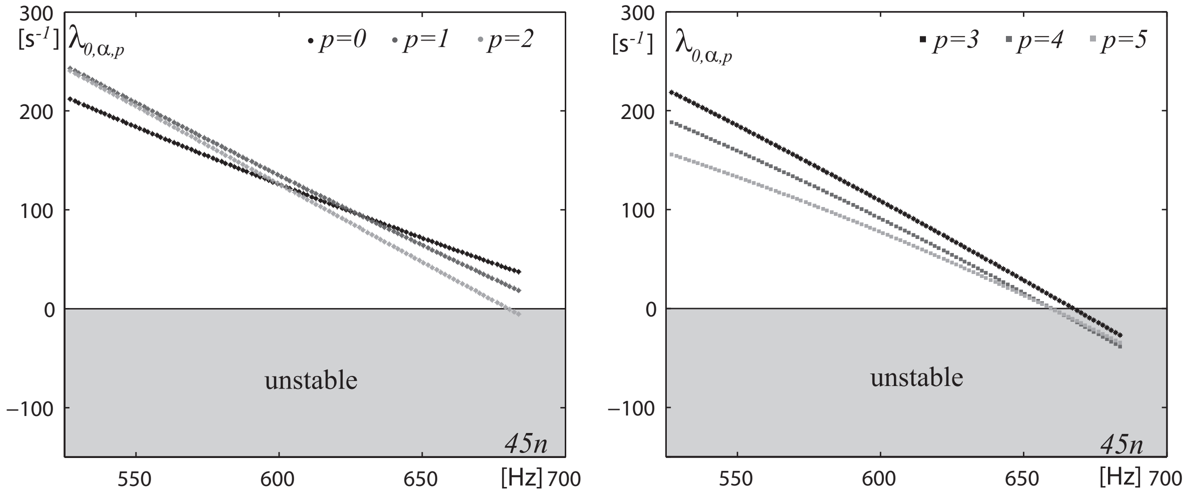

Figure 12.6: Eigenvalue real part of the guide vane cascade, corresponding to the modes $0 \leq p \leq 2$ (left) and the modes $3 \leq p \leq 5$ (right) against the excitation frequency corresponding to the RSI 5^{th} harmonic frequency $f = 45n$.

The frequency at which the guide vanes respond preferably varies between 650 Hz and 695 Hz, see Figure 12.5, which is slightly different from the frequency at which the guide vanes respond preferably in the experiments: up to 8% frequency shift. The real part of the eigenvalues is strongly varying depending on the mode p. Since the RSI pressure mode at this frequency features a phase shift $\Delta\phi_{p=2} = \frac{2\pi}{20} \cdot 5$, all the evidence suggests that the eigenmode $p = 5$ is most likely. Above 660 Hz, the real eigenvalue of this mode becomes negative, that is the mechanical system is unstable. If all the guide vanes feature flexible stem, premature failures of the guide vanes are expected if the pump-turbine is operated at BEP above $n = 14.6$ Hz.

In the following lines, we propose two different ways to prevent damage to the guide vanes. On the one hand, by multiplying the structural damping constant by a factor of 2, the mechanical system becomes stable. In Figure 12.7, the real part of the modified guide vane cascade eigenvalues is plotted for the eigenmode $p = 5$. It may be seen that the eigenfrequencies are not shifted due to the higher damping. Moreover, the real part remains positive in the whole impeller frequency range, which means that the mechanical system is stable.

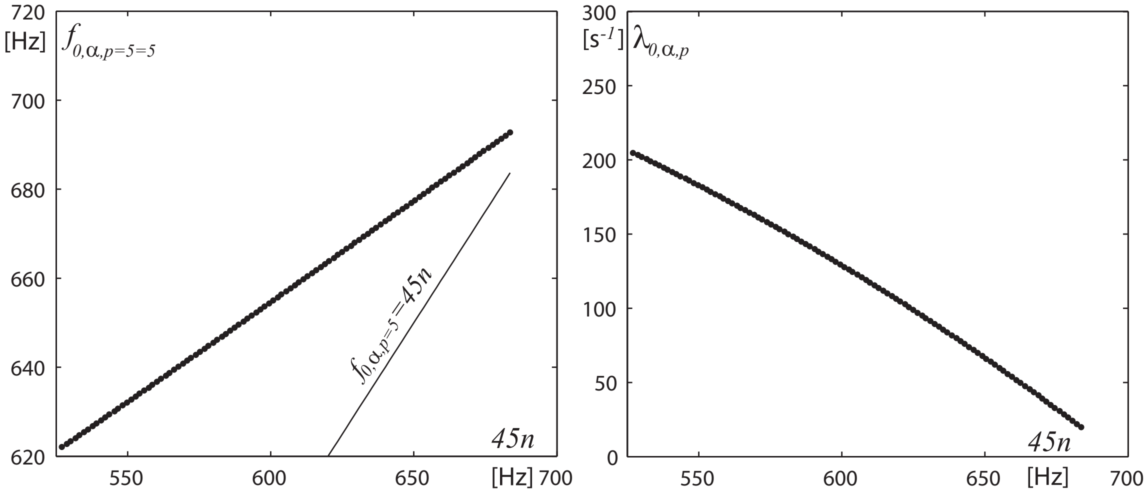

Figure 12.7: Eigenfrequencies (left) and eigenvalue real part (right) of the eigenmode $p = 5$, against the excitation frequency corresponding to the RSI 5^{th} harmonic frequency $f = 45n$. The guide vanes feature a structural damping constant twice higher than the initial one.

On the other hand, the instability leads to high vibration amplitude when the shape of the excitation, that is the RSI pressure mode, is similar to the eigenmode of the cascade. If all the guide vanes feature similar structural parameters, the shape of the RSI pressure mode is identical to the shape of the cascade eigenmode. By multiplying by a factor 0.8 the inertia of 10 guide vanes and placing them alternately between the guide vanes featuring the initial inertia, the mechanical system is mistuned. In such a case, the phase shift between the vibrations of the guide vanes O_i and O_{i+1} is different from the one between the vibrations of the guide vanes O_{i+1} and O_{i+2}. The shape of the structural eigenmode is thereby changed, both in terms of amplitude and phase, and does not match anymore the shape of the pressure mode.

Considering the eigenmode presenting 5 diametrical nodes, the phase shifts between the eigenvector components corresponding to the guide vanes O_i and O_{i+1} as well as between the eigenvector components corresponding to the guide vanes O_{i+1} and O_{i+2} for the mistuned cascade are plotted against the RSI 5^{th} harmonic frequency $f = 45n$ in Figure 12.8.

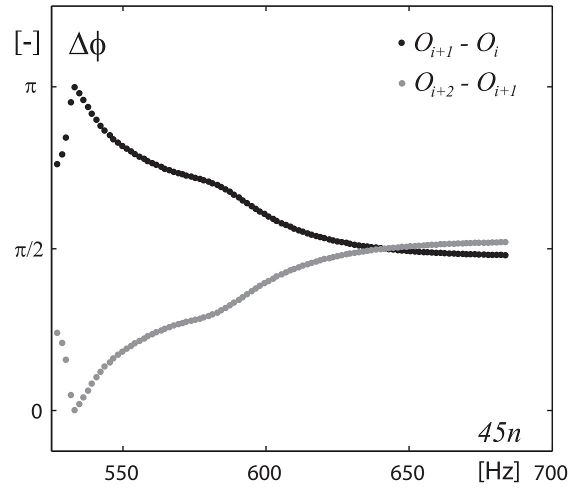

Figure 12.8: Phase shifts between the eigenvector components corresponding to the guide vanes O_i and O_{i+1} as well as between the eigenvector components corresponding to the guide vanes O_{i+1} and O_{i+2}, against the excitation frequency corresponding to the RSI 5^{th} harmonic frequency $f = 45n$.

In Figure 12.9, the complex visualization of the eigenvectors components associated to the guide vanes O_i, O_{i+1} and O_{i+2} corresponding to the tuned cascade and the mistuned cascade is plotted for the BEP at $n = 13.3$ Hz. As it may clearly be seen, the eigenvectors phase are shifted.

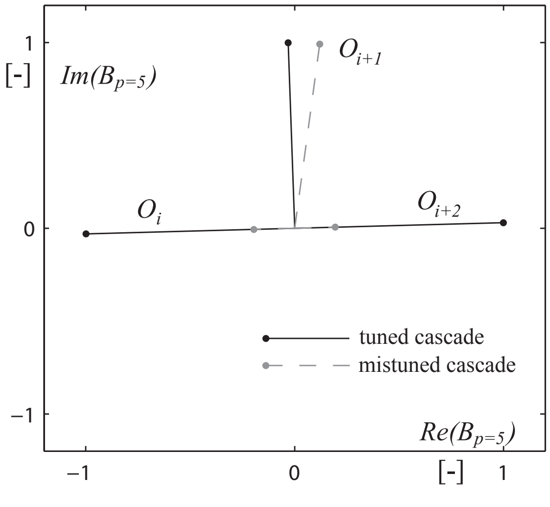

Figure 12.9: Complex visualization of the eigenvectors components associated to the guide vanes O_i, O_{i+1} and O_{i+2} corresponding to the tuned cascade and the mistuned cascade.

In Figure 12.10, the eigenfrequencies and the real part of the mistuned guide vane cascade eigenvalues are plotted for the eigenmode with 5 diametrical nodes. By mistuning the cascade, the eigenvalues are increased and the range of negative eigenvalue real part is shifted to slightly higher excitation frequencies compared to the tuned cascade.

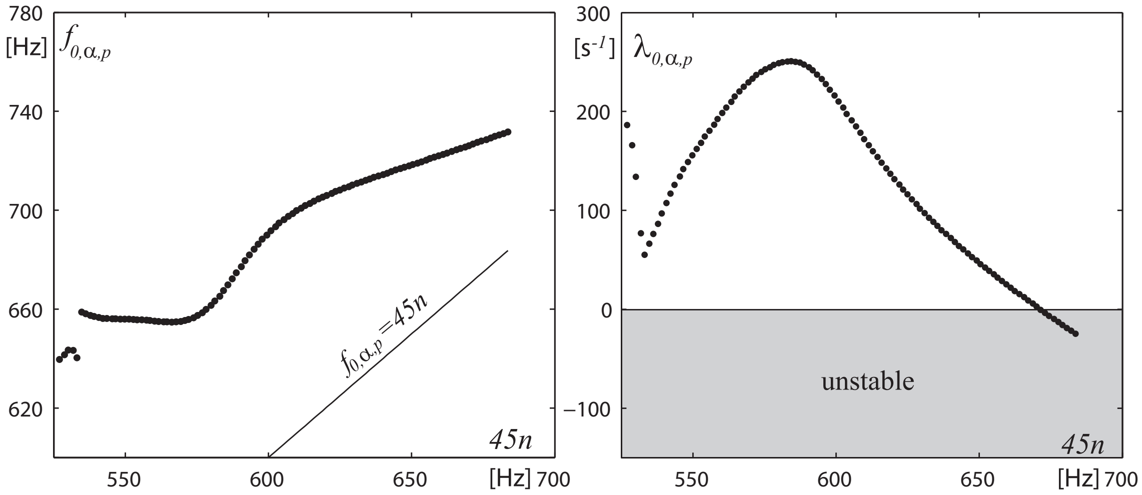

Figure 12.10: Eigenfrequencies and real part of the mistuned guide vane cascade eigenvalues for the eigenmode with 5 diametrical nodes, against the excitation frequency corresponding to the RSI 5^{th} harmonic frequency $f = 45n$.

Part IV

Conclusions and Perspectives

Chapter 13

Conclusions

Experimental investigations of the guide vane cascade dynamic response to the excitation due to the Rotor-Stator Interaction in a low specific speed pump-turbine reduced scale model are reported. The investigated pump-turbine features 9 impeller blades and 20 guide vanes and is operated at the Best Efficiency operating Point at 18° opening angle. The bending and torsion vibrations of the guide vanes are studied. The influence of the adjacent guide vane vibrations are pointed out. A methodology is given to reliably identify the hydrodynamic parameters of the mechanical system, which is shown to be of the 2nd order. The entire guide vane cascade dynamic response is studied based on the measurements on two guide vanes equipped with strain gages and three pressure sensors adequately placed in the stator.

The impulse response of immersed guide vanes is obtained using a spark plug flush mounted on the bottom flange in a guide vane channel. This type of measurements are successfully undertaken in water, model at rest, and model in operation.

Keeping the operating conditions of the Best Efficiency Point constant, the impeller rotation frequency is swept and the guide vanes are therefore excited by the Rotor-Stator Interaction, RSI, over a wide frequency range. The combination of z_b impeller blades with z_o guide vanes makes apparent many different spinning diametrical pressure modes. Nevertheless, the guide vanes are mainly excited at the frequencies $f = z_b n$ and $f = 2 z_b n$, but also respond up to the RSI 5^{th} harmonic.

The amplitude of the fluctuating bending displacement and torsion angle of the guide vanes is strongly varying across the impeller frequency range. The ranges of the 2^{nd} and the 5^{th} RSI harmonic frequency contain the frequency of the 1^{st} bending eigenmode and the 1^{st} torsion eigenmode, respectively. The pressure fluctuations close to the vibrating guide vanes are strongly varying and may even decrease by 50% at resonance. Therefore, a transfer of energy between the vibrating structure and the flow pressure should occur.

The influence of an adjacent guide vane on the vibrations of a guide vane is found to vary significantly between its position on the pressure side and suction side of the latter. Regarding the guide vane bending vibrations, the hydrodynamic force acting on a guide vane induced by its neighboring guide vane on the pressure side is up to 10 times higher than the force induced by its suction side neighbor. As for the guide vane torsion vibrations, the hydrodynamic torque acting on a guide vane induced by its neighboring guide vane on the pressure side is up to 5 times higher than the force induced by its suction side neighbor.

The hydrodynamic damping coefficient and the added mass corresponding to the vibrations of the adjacent guide vanes are successfully identified and an influence matrix is built. These two terms are shown to depend strongly on the relative amplitude of their vibrations, the absolute flow velocity and the phase shift between their vibration signals.

Taking into account the periodic condition, the influence matrix is built in order to predict the dynamics of the entire guide vane cascade. Four and six different eigenmodes are investigated for the case of bending and torsion motions, respectively. On the one hand, the bending modes feature eigenfrequencies varying from 221 Hz to 222 Hz, which is between 2% and 3% lower than the frequency at which the guide vanes respond preferably in the tests made with two adjacent flexible guide vanes. The eigenvalue real part of each eigenmode remains positive on the investigated impeller frequency range, that is the mechanical system is stable. On the other hand, the torsion modes feature eigenfrequencies varying from 650 Hz to 695 Hz. Above 660 Hz, the eigenvalue real part of the mode which is the most likely to be excited by the RSI becomes negative. This means that the mechanical system is unstable and premature failures of the guide vanes are expected if the pump-turbine is operated at BEP above $n = 14.6$ Hz.

Finally, two different ways to prevent damage to the guide vanes excited at the RSI 5^{th} harmonic frequency are proposed. On the one hand, it is shown that by increasing the structural damping constant by a factor 2, the mechanical system becomes stable. On the other hand, the modification of the shape of the cascade eigenmode is achieved by mistuning the cascade, such that its shape does no longer match the shape of the RSI pressure mode. This way, even if the mechanical system remains unstable, the risk of damaging the guide vanes is reduced.

Chapter 14

Perspectives

The present document does not pretend to clarify all the pending issues of fluid-structure coupling occurring in hydraulic machines. Incidentally, it gives rise to several questions whose answer would contribute greatly to the further development of these machines. In addition to opening the way for further experiments, the present study proposes complete results of a case study which may constitute a benchmark for the validation of numerical tools.

Entire guide vane cascade

The study intends to predict the vibrating behavior of the entire cascade featuring similar flexible guide vanes from the local measurements on two isolated flexible guide vanes. It would be interesting to place flexible guide vanes in the entire cascade to validate the forecasted results. Nonetheless, the difficulty lies in manufacturing guide vanes featuring exactly similar structural properties.

Mistuned guide vane cascade

At the end of the present document, two solutions to prevent guide vane damage are shortly investigated. Mistuning the cascade is one of the solutions, and we show that this way, we are able to shift the shape of the structural eigenmode and, thus to reduce the risk of damaging the guide vanes. This technique is already used in gas turbine, [45] and [10]. It needs further attention: by optimizing the type of mistuning, a reduction of the guide vane vibration amplitude should be possible.

Parameters influencing the coupling

After having shown the relevance of the vibration phase, amplitude and the flow velocity on the coupling terms, it is necessary to investigate all these parameters in a simpler case. For instance, two vibrating plates immersed in a uniform flow would allow a deeper investigation of the mentioned parameters. Moreover, the dependence of the distance between the vibrating structures could easily be analyzed.

Pressure fluctuations

At guide vane resonance, a transfer of energy occurs from the flow to the vibrating structure. Therefore, the pressure fluctuations in the rotor-stator gap decrease. By reaching the resonance of the guide vanes, the periodic loading due to the RSI acting on the impeller blades might be minimized and, as a consequence, the risk of crack appearance on the impeller might be lowered. A more detailed study of the relation between the vibrations of the guide vanes and the decrease of the pressure fluctuations might be undertaken.

Validation of numerical tools

As already mentioned, the case study of the present work may constitute a benchmark for the validation of numerical tools. Following the procedures used by Munch [56], one might successively study the forced motion of a single guide vane in the cascade and its free motion, by neglecting the RSI excitation. The effect of its vibrations on the neighboring guide vane may be quantified by an influence matrix. Then, the forced response due to the RSI excitation might be studied and the results might be compared to experimental data.

Recommendations for hydraulic machine design

This chapter is not concluded without proposing recommendations for the assessment of hydraulic machine dynamics. Assessments tend to occur at the early stage of the product development. Manufacturers are often compelled to verify the vibrating behavior by using numerical tools. Modal analyzes of machine components both in air and in still water are usually made. The present study highlights the dependence of the phase shift and the relative amplitudes of the vibrations on the influence matrix. These parameters have to be considered in the assessment of components that might be influenced by others: guide vanes, impeller blades, stay vanes, etc.

The relevance of the hydrodynamic damping on the vibration amplitude highlighted in the present experimental work should urge the researchers to develop reliable numerical tools for dealing with fluid-structure coupling. Highly dissipative numerical codes might be a source of wrong dynamic behavior assessment.

Finally, as already mentioned above, mistuning techniques to minimize the risk of guide vane damage should be taken into account in the design process. Nevertheless further studies are needed to optimize the type of mistuning.

Appendices

Appendix A

Signal processing

A.1 Random data spectral analysis

Let q simultaneously recorded discrete signals, featuring M samples, be given by [52]:

$$x_k\left(m\right),\ 1 < k < q\ \&\ 1 < m < M. \tag{A.1}$$

The values of the signals $\{x_{k,i}\}$ are associated with equally spaced time $t_m = m\Delta t$ in such a way that

$$x_k\left(m\right) = x_k\left(t_m\right) \tag{A.2}$$

According to the Shannon theorem, the sampling frequency $f_s = 1/\Delta t$ is assumed superior to the double of the highest frequency contained in the signal. Let the signals $x_k\left(t\right)$ also be divided into n_d segments, each of length M_j, which may overlap. $x_{k,j}\left(t\right)$ denotes the function $x_k\left(t\right)$ being restricted to the j^{th} segment.

The discrete frequency at which the Fourier components may be computed is defined as:

$$f_i = \frac{i}{T} \tag{A.3}$$

The discrete Fourier transform components related to the j^{th} segment are expressed as:

$$\hat{x}_k\left(f_i\right) = \Delta t \cdot \sum_{m_j=0}^{M_j-1} \left(x_{k,j}\left(m_j\right) - \overline{x_{k,j}}\right) W_h\left(m_j\right) e^{-\mathrm{i}2\pi f_i m_j} \tag{A.4}$$

with $W_h\left(m_j\right)$, the Hamming windowing function, being defined as:

$$W_h\left(m_j\right) = 0.54 - 0.46 \cdot cos\left(2\pi \frac{m_j}{M_j - 1}\right),\ 0 < m_j < M_j - 1 \tag{A.5}$$

and $\overline{x_{k,j}}\left(m_j\right)$, the signal time average, computed as:

$$\overline{x_{k,j}} = \frac{1}{M_j} \sum_{m_j=0}^{M_j-1} x_{k,j}\left(m_j\right) \tag{A.6}$$

The averaged magnitude of the discrete Fourier transform of the signal $x_k(t)$ is expressed as:

$$\overline{|\hat{x}_k(f_i)|} = \frac{1}{n_d}\sum_{j=1}^{n_d}|\hat{x}_{k,j}(f_i)| \tag{A.7}$$

The power spectral density estimate of the signal $x_k(t)$ is defined as follows:

$$\overline{|\hat{x}_k|}^2(f_i) = \frac{1}{n_d}\sum_{j=1}^{n_d}|\hat{x}_{k,j}(f_i)|^2 \tag{A.8}$$

The cross power spectral density estimate between the signals $x_k(t)$ and $x_l(t)$ is defined as:

$$\overline{|\hat{x}_k\hat{x}_l|}^2(f_i) = \frac{1}{n_d}\sum_{j=1}^{n_d}\hat{x}^*_{k,j}(f_i)\cdot\hat{x}_{l,j}(f_i) \tag{A.9}$$

The coherence function between the signals $x_k(t)$ and $x_l(t)$ is defined as follows [9]:

$$\Gamma^2_{x_k x_l}(f_i) = \frac{|\hat{x}_k\hat{x}_l|^2(f_i)}{|\hat{x}_k|^2(f_i)\cdot|\hat{x}_l|^2(f_i)} \tag{A.10}$$

In the present document, for readability reason, the $^-$ sign for averaged magnitude of Fourier Transform, power spectral density and cross power spectral denstity is omitted.

Appendix B

Analytical identification of the guide vane dynamics

B.1 Deflection and rotation of a beam due to simple bending

According to the simple bending theory [27], an embedded beam, subject to a concentrated force F at its free end, see Figure B.1, features the following elastic line equation:

$$y_F(x) = \frac{F}{6\mathrm{E}I_z}(3lx^2 - x^3) \tag{B.1}$$

E being Young's modulus, I_z, the moment of inertia and l, the lever arm length.

The rotation β_F of the free extremity is obtained as follows:

$$\beta_F = \frac{Fl^2}{2\mathrm{E}I_z} \tag{B.2}$$

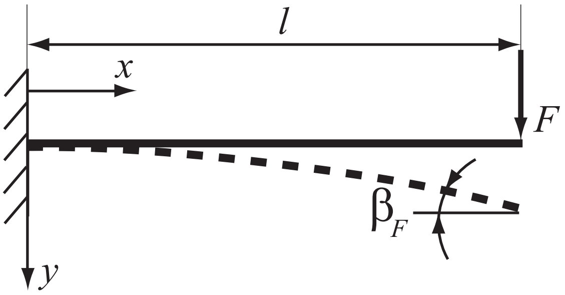

Figure B.1: Embedded beam deflection y_F and rotation β_F due to a concentrated force F at its free end.

The effect of a concentrated torque T applied at its free end, see Figure B.2, provides the following elastic line equation:

$$y_T(x) = \frac{T}{2\mathrm{E}I_z}x^2 \tag{B.3}$$

The rotation β_T of the extremity is obtained as follows:

$$\beta_T = \frac{Tl}{\mathrm{E}I_z} \tag{B.4}$$

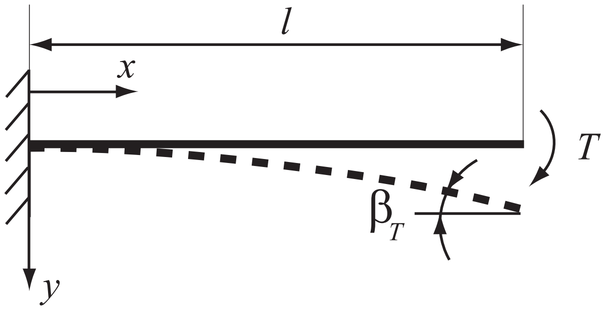

Figure B.2: Embedded beam deflection y_T and rotation β_T due to a concentrated torque T at its free end.

B.2 Angular deflection of a beam due to simple torsion

An embedded circular beam, subject to a concentrated torque T around its neutral axis, see Figure B.3, features the following angular deflection α [27]:

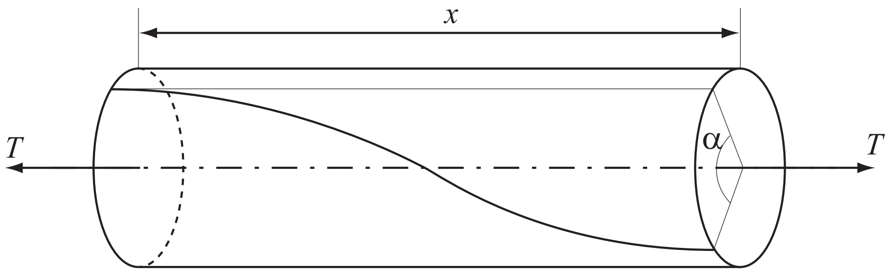

Figure B.3: Embedded beam deflection due to concentrated torque around the neutral axis.

$$\alpha\left(x\right) = \frac{T}{\mathrm{G}I_p}x \tag{B.5}$$

G being the shear modulus and I_p the polar moment of inertia

B.3 Guide vane stiffness identification

B.3.1 Modified guide vanes

The stem of the modified guide vane is simplified and partitioned into four different segments, see Figure B.4, featuring the dimensions, the moment of inertia and the mass per unit length μ given in Table B.1. The guide vane is assumed to be ideally embedded at the beginning of the segment 1. The hydrofoil inertia $J_m = 2.3$ kg·m^2 and its mass $m = 0.4$ kg are concentrated at the end of segment 4. The moment of inertia in the direction normal to the stem axis I_z and the polar moment of inertia I_p for circular segment are obtained as follows:

$$I_z = \frac{\pi\,(D_{ext}^4 - D_{int}^4)}{64} \tag{B.6}$$

$$I_p = \frac{\pi\,(D_{ext}^4 - D_{int}^4)}{32} \tag{B.7}$$

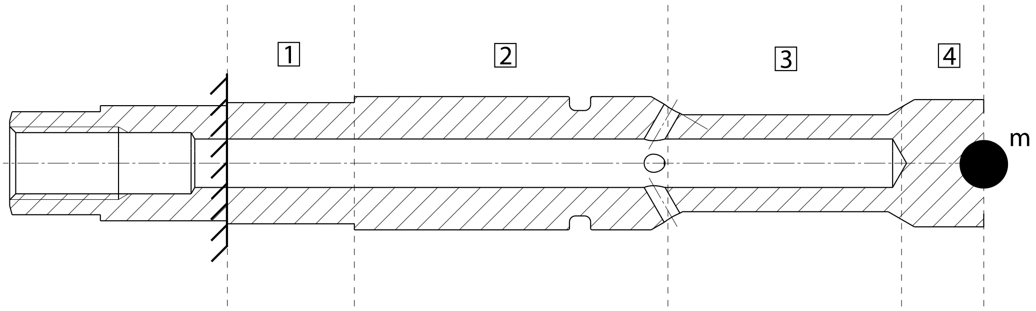

Figure B.4: Guide vane partitioning, hydrofoil concentrated mass and embedding location.

Table B.1: Guide vane dimensions, D_{ext}, D_{int} and l, moment of inertia, I_z and I_p, and mass per unit length μ.

	Units	**Segment 1**	**Segment 2**	**Segment 3**	**Segment 4**
D_{ext}	[m]	0.020	0.022	0.016	0.021
D_{int}	[m]	0.008	0.008	0.008	-
l	[m]	0.021	0.052	0.039	0.014
I_z	[m^4]	$7.65 \cdot 10^{-9}$	$1.13 \cdot 10^{-8}$	$3.02 \cdot 10^{-9}$	$9.55 \cdot 10^{-9}$
I_p	[m^4]	$1.53 \cdot 10^{-8}$	$2.26 \cdot 10^{-8}$	$6.03 \cdot 10^{-9}$	$1.91 \cdot 10^{-8}$
μ	[kg · m]	2.27	2.84	1.30	2.98

Denoting the segment number by i and considering small rotations at extremities, the total deflection y obtained when applying a concentrated force F at the free extremity of the guide vane, may be expressed as follows:

$$\begin{aligned} y &= \sum_{i=1}^{4}\left(y_{F,i}+y_{T,i}\right)+\sum_{i=1}^{3}\left(sin\left(\beta_i\right)\cdot\sum_{j=i+1}^{4}L_j\right) \\ &\approx \sum_{i=1}^{4}\left(y_{F,i}+y_{T,i}\right)+\sum_{i=1}^{3}\left(\beta_i\cdot\sum_{j=i+1}^{4}L_j\right) \end{aligned} \tag{B.8}$$

Using eqs. B.1 to B.4, the guide vane bending stiffness K^s is finally recovered by dividing the force F by the deflection y as follows:

$$K^s = \frac{F}{y} = 1.28\cdot 10^6 \text{ N·m}^{\text{-1}} \tag{B.9}$$

The total angular deflection α due to a torque T around the neutral axis may be expressed as the sum of the angular deflection α_i of each of the four segments as follows:

$$\alpha = \sum_{i=1}^{4}\alpha_i \tag{B.10}$$

Using eq. B.5, the torsion stiffness L^s is then obtained as follows:

$$L^s = \frac{T}{\alpha} = 3610 \text{ N·m·rad}^{\text{-1}} \tag{B.11}$$

B.3.2 Usual guide vanes

The usual guide vane stem is simplified and partitioned into three different segments, see Figure B.5, featuring the dimensions, the moment of inertia and the mass per unit length μ given in Table B.2. The guide vane is assumed to be ideally embedded at the beginning of the segment 1. Similarly to the modified guide vanes, the hydrofoil inertia $J_m = 2.3kg\cdot m^2$ and its mass $m = 0.4$ kg are concentrated at the end of segment 4.

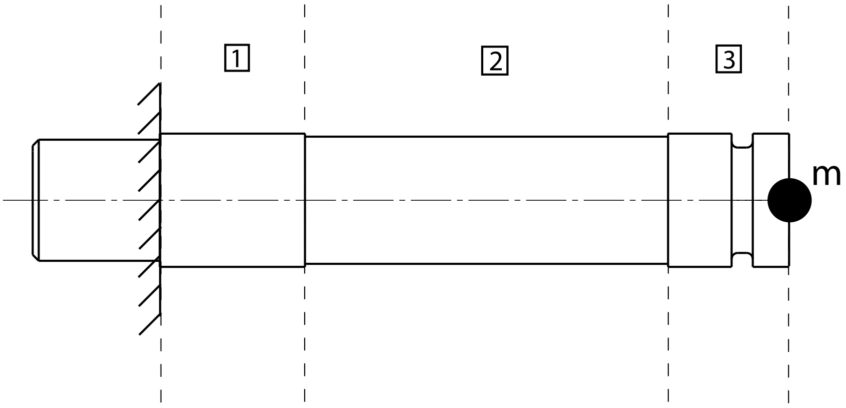

Figure B.5: Usual guide vane stem partitioning, hydrofoil lumped mass and embedding location.

Table B.2: Usual guide vane dimensions, D_{ext}, D_{int} and l, moment of inertia, I_z and I_p, and mass per unit length μ.

	Units	**Segment 1**	**Segment 2**	**Segment 3**
D_{ext}	[m]	0.022	0.021	0.022
D_{int}	[m]	0	0	0
l	[m]	0.024	0.060	0.020
I_z	[m^4]	$1.15 \cdot 10^{-8}$	$9.55 \cdot 10^{-9}$	$1.15 \cdot 10^{-8}$
I_p	[m^4]	$2.30 \cdot 10^{-8}$	$1.91 \cdot 10^{-8}$	$2.30 \cdot 10^{-8}$
μ	[kg · m]	3.27	2.98	3.27

In the same manner as for the modified guide vanes, the bending K^s_{usual} and torsion L^s_{usual} stiffness yields:

$$K^s_{usual} = 2.94 \cdot 10^6 \text{ N·m}^{-1} \tag{B.12}$$

$$L^s_{usual} = 7749 \text{ N·m·rad}^{-1} \tag{B.13}$$

The bending stiffness of the usual guide vanes is 2.3 higher than the one of the modified guide vanes and the torsion stiffness of the usual guide vanes is 2.15 higher than the one of the modified guide vanes.

B.4 Identification of the guide vane bending and torsion eigenfrequencies

B.4.1 Modified guide vanes

The Rayleigh-Ritz method [80] is used to estimate the first bending and torsion eigenfrequencies of the guide vane. The dynamic motion of the guide vane is supposed to be similar to the static motion. This assumption is valid for the study of the 1st bending and torsion modes. The system is assumed to be conservative and, thus, the maximal energy of deformation must equal the maximal kinetic energy. Therefore, the first bending eigenfrequency $f^{R-R}_{0,y}$ is approximated as:

$$f^{R-R}_{0,y} = \frac{1}{2\pi}\sqrt{\frac{\sum_{i=1}^{4} \frac{EI_{x,i}}{2} \cdot \int_0^{L_i} \left(\frac{d^2}{dx^2} y_{F,i}(x)\right)^2 + \left(\frac{d^2}{dx^2} y_{T,i}(x)\right)^2 dx}{\frac{1}{2}\sum_{i=1}^{4} \int_0^{L_i} \mu_i \cdot y_{i,tot}(x)^2\, dx + \frac{1}{2} \cdot m \cdot \left(y_{4,tot}(L_4)\right)^2}} = 306 Hz \tag{B.14}$$

with

$$\begin{aligned} y_{i,tot}(x) \;&=\; \sum_{j=1}^{i-1} \left(y_{F,j}(L_j) + y_{T,j}(L_j) + (\beta_{F,j-1} + \beta_{T,j-1}) \cdot L_j\right) \\ &+\; (\beta_{F,i-1} + \beta_{T,i-1}) \cdot x + y_{F,i}(x) + y_{T,i}(x) \end{aligned} \tag{B.15}$$

The first torsion eigenfrequency $f_{0,\alpha}^{R-R}$ is evaluated as follows:

$$f_{0,\alpha}^{R-R} = \frac{1}{2\pi}\sqrt{\frac{\frac{1}{2}T\sum_{i=1}^{4}\alpha_i}{\frac{1}{2}\cdot J^*}} = 645Hz \tag{B.16}$$

with

$$\begin{aligned} J^* &= \sum_{i=1}^{4}\int_0^{L_i}\left[\rho\left(\alpha_i(x)+\sum_{j=1}^{i-1}\alpha_j(L_j)\right)^2\int_{D_{1,int}}^{D_{1,ext}}\pi\frac{D^4}{16}dD\right]dx \\ &+ \left(\sum_{i=1}^{4}\alpha_i(L_i)\right)^2\cdot J_m \end{aligned} \tag{B.17}$$

B.4.2 Usual guide vanes

Using the same approach as for the modified guide vanes, the bending $f_{0,y,usual}^{R-R}$ and torsion $f_{0,\alpha,usual}^{R-R}$ eigenfrequencies of the usual guide vanes yields:

$$f_{0,y,usual}^{R-R} = 411Hz \tag{B.18}$$

$$f_{0,\alpha,usual}^{R-R} = 945Hz \tag{B.19}$$

The bending eigenfrequency of the usual guide vanes is 1.34 higher than those of the modified guide vanes and the torsion eigenfrequency of the usual guide vanes is 1.47 higher than those of the modified guide vanes.

B.5 Identification of the guide vane mass and inertia

B.5.1 Modified guide vanes

The modified guide vane bending and torsion inertia are analytically found as follows:

$$I^s = \frac{K^s}{\left(2\pi f_{0,y}^{R-R}\right)^2} = 0.47 \text{ kg} \tag{B.20}$$

$$J^s = \frac{L^s}{\left(2\pi f_{0,\alpha}^{R-R}\right)^2} = 2.20\cdot 10^{-4} \text{ kg}\cdot\text{m}^2 \tag{B.21}$$

B.5.2 Usual guide vanes

The usual guide vane bending and torsion inertia are analytically found as follows:

$$I_{usual}^s = \frac{K_{usual}^s}{\left(2\pi f_{0,y,usual}^{R-R}\right)^2} = 0.44 \text{ kg} \tag{B.22}$$

$$J^s_{usual} = \frac{L^s_{usual}}{\left(2\pi f^{R-R}_{0,\alpha,usual}\right)^2} = 2.20 \cdot 10^{-4}\ \mathrm{kg} \cdot \mathrm{m}^2 \tag{B.23}$$

On the one hand, the structural mass of the usual guide vanes I^s_{usual} is 6.4% lower than the one of the modified guide vanes. On the other hand, the structural inertia of the usual guide vanes J^s_{usual} is similar as the one of the modified guide vanes.

Appendix C

Green functions for solving potential flow

C.1 Potential flow

One is interested in solving the potential flow Φ in the fluid volume V bounded by the surface A. The approach is treated for a simply-connected domain, which drastically simplifies the problem without loss of generality. The potential flow problem is expressed by the following Laplace equation [26]:

$$\triangle\Phi = 0 \text{ , in } V \tag{C.1}$$

A Neumann condition is imposed on the boundary A:

$$\frac{\partial\Phi}{\partial n} = \mathrm{g} \text{ , on } A \tag{C.2}$$

g being a function defined on the boundary A

C.2 Green functions

To solve the potential flow problem, an auxiliary function is defined, a Green function Θ of the Laplace operator. By definition, the function Θ is the solution of:

$$\triangle\Theta\left(\mathbf{x}-\mathbf{x}'\right) = \delta\left(\mathbf{x}-\mathbf{x}'\right) \tag{C.3}$$

$\delta\left(\mathbf{x}-\mathbf{x}'\right)$ being the Dirac delta function centered at $\mathbf{x}'$ It may easily be demonstrated that in 2D:

$$\Theta\left(\mathbf{x}-\mathbf{x}'\right) = \frac{1}{2\pi}\ln r \tag{C.4}$$

with $r = \left|\mathbf{x}-\mathbf{x}'\right|$

The Green's second identity is expressed as follows:

$$\int_V \Phi\triangle\Theta - \Theta\triangle\Phi dV = \int_A \Phi\frac{\partial\Theta}{\partial n} - \Theta\frac{\partial\Phi}{\partial n}dA \tag{C.5}$$

According to the Green's function properties, one may express the potential at any position in V as a function of the conditions imposed on the boundary A from eq. C.5:

$$\Phi(\mathbf{x}) = \frac{1}{2\pi}\left(\int_A \Phi(\mathbf{x}')\frac{\partial \ln r}{\partial n}dA - \int_A \ln r \frac{\partial \Phi(\mathbf{x}')}{\partial n}dA\right) \text{ , if } \mathbf{x} \in V \text{ and } \mathbf{x}' \in A \quad \text{(C.6)}$$

When $\mathbf{x} \in A$, one has [50]:

$$\frac{\Phi(\mathbf{x})}{2} = \frac{1}{2\pi}\left(\int_A \Phi(\mathbf{x}')\frac{\partial \ln r}{\partial n}dA - \int_A \ln r \frac{\partial \Phi(\mathbf{x}')}{\partial n}dA\right) \text{ , if } \mathbf{x},\, \mathbf{x}' \in A \quad \text{(C.7)}$$

We use the notation of the boundary elements method to express the relation between the potential and the boundary conditions, in which the Einstein summation convention is used. In this method, the boundary A is first discretized and then a collocation method is applied, see Figure C.1.

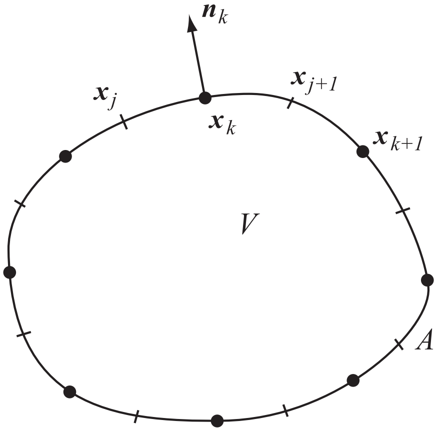

Figure C.1: Boundary discretization according to the boundary elements method.

Using this notation, the eq. C.7 is expressed as follows:

$$\Theta_{kj}\left(\frac{\partial \Phi}{\partial n}\right)_j = \Upsilon'_{kj}\Phi_j \quad \text{(C.8)}$$

with

$$\Upsilon'_{kj} = \Upsilon_{kj} - \frac{1}{2}\delta_{kj} \quad \text{(C.9)}$$

and where Θ_{ij} and Υ_{ij} are defined as:

$$\Theta_{kj} = \frac{1}{2\pi}\int_{\mathbf{x}_j}^{\mathbf{x}_{j+1}} \ln r dx \quad \text{(C.10)}$$

$$\Upsilon_{kj} = \frac{1}{2\pi}\int_{\mathbf{x}_j}^{\mathbf{x}_{j+1}} \nabla_x \ln r \cdot \mathbf{n} dx \text{ , with } r = |\mathbf{x}_k - \mathbf{x}| \quad \text{(C.11)}$$

From eq. C.8, the potential at each position x_j of the boundary A may be found as follows:

$$\Phi_j = \Upsilon'^{-1}_{kj}\Theta_{kj}\left(\frac{\partial\Phi}{\partial n}\right)_j \tag{C.12}$$

Writing the eq. C.6 in a discretized formulation, the potential in the whole domain V is expressed:

$$\Phi_i = \Xi_{ij}\Phi_j - \Pi_{ij}\left(\frac{\partial\Phi}{\partial n}\right)_j \tag{C.13}$$

where

$$\Xi_{ij} = \frac{1}{2\pi}\int_{\partial\Omega}\ln r dx \tag{C.14}$$

and

$$\Pi_{ij} = \frac{1}{2\pi}\int_{\partial\Omega}\nabla_x \ln r \cdot \mathbf{n} dx \text{ , with } r = |\mathbf{x}_i - \mathbf{x}| \tag{C.15}$$

Finally, one may express the potential Φ at any position in V by replacing eq. C.12 in eq. C.13:

$$\Phi_i = \left(\Xi_{ij}\Upsilon'^{-1}_{kj}\Theta_{kj} - \Pi_{ij}\right)\left(\frac{\partial\Phi}{\partial n}\right)_j = \Lambda_{ij}\cdot\left(\frac{\partial\Phi}{\partial n}\right)_j \tag{C.16}$$

C.3 Application to the guide vane cascade

In this section, the influence level undergone by a guide vane due to the vibrations of its neighbors is considered. For that matter, the problem is simplified in such a way that the cascade is represented linearly. Each guide vane is simplified by a linear segment discretized by three points x_j, x_{j+1}, x_{j+2}. The midpoint rule method is used to approximate the integrals in eq. C.16. Two intermediate points x_k, x_{k+1} are used to take into account the term $\Upsilon'^{-1}_{kj}\Theta_{kj}$.

Assuming that all the guide vanes exhibit a bending motion whose rate $\dot{y}$ is the same for each guide vane and according to eq. C.16, one defines the influence coefficient $\Lambda_{i,i-J}$ of the guide vane O_{i-J} vibrations on the potential flow Φ_i at the position x_i as follows:

$$\Phi_i = \Lambda_{i,i-J}\cdot\dot{y} = \sum_j \Lambda_{ij}\cdot\dot{y} \tag{C.17}$$

This coefficient finally indicates the influence of the guide vane O_{i-J} on the guide vane O_i, since the potential flow Φ_i at the position x_i is directly related to the pressure at the wall of the guide vane O_i, see eq. 3.18 and, consequently, to the force applied on the guide vane O_i.

In Figure C.3, the influence coefficient $\Lambda_{i,i-J}$ of the guide vane O_{i-J} vibrations on the potential flow Φ_i at the position x_i is plotted for the first five neighboring guide vanes.

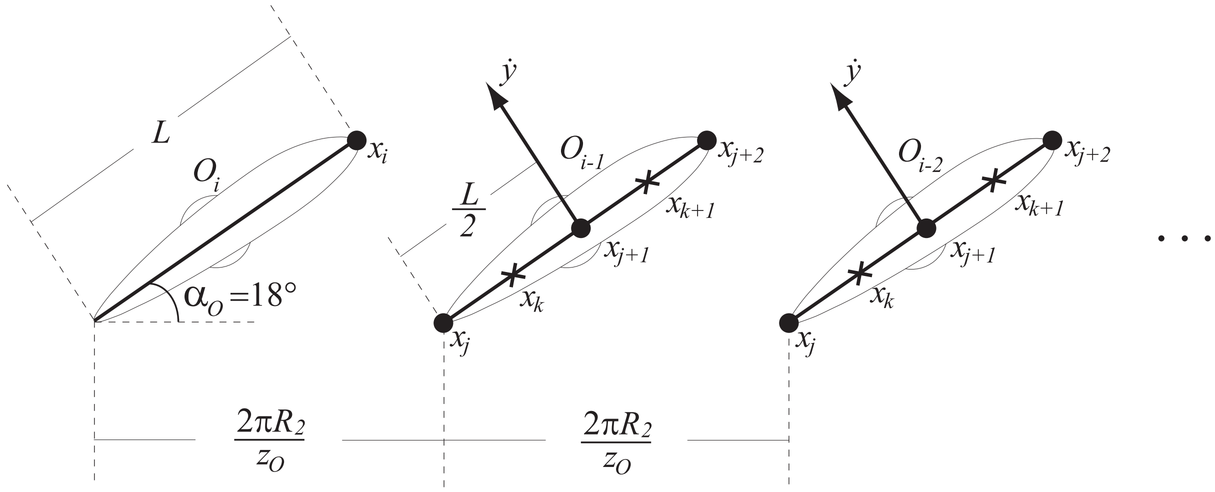
L
O_i
x_i
α_O=18°
$\dot{y}$
O_{i-1}
x_{j+2}
$\frac{L}{2}$
x_{k+1}
x_{j+1}
x_k
x_j
$\dot{y}$
O_{i-2}
x_{j+2}
x_{k+1}
x_{j+1}
x_k
x_j
. . .
$\frac{2\pi R_2}{z_O}$
$\frac{2\pi R_2}{z_O}$

Figure C.2: Simplified guide vane cascade represented linearly.

The influence of the guide vanes O_{i-2} and O_{i-5} on the guide vane O_i is found to be 3.7 and 12.3 times lower than the influence of the guide vane O_{i-1}. In the reality, one certainly observe a lower influence of the guide vanes O_{i-J} $(J \geq 2)$, because of the intermediate guide vanes. In this approach, the intermediate guide vanes are neglected for the sake of simplicity.

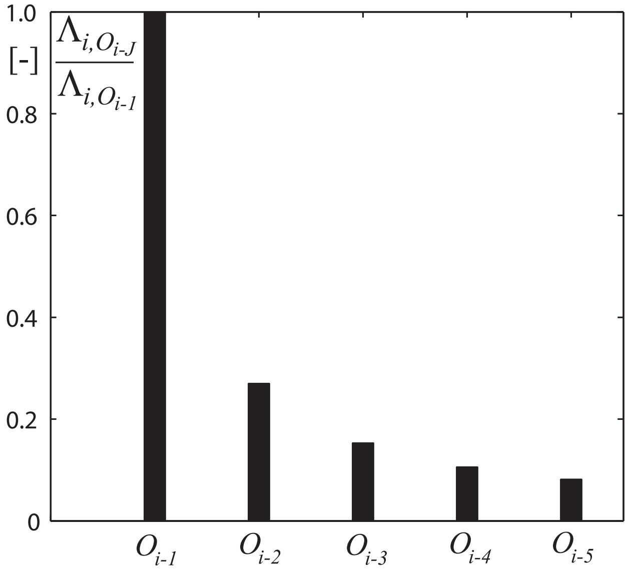

Figure C.3: Influence coefficient $\Lambda_{i,i-J}$ of the guide vane O_{i-J} vibrations on the potential flow Φ_i at the position x_i, normalized by $\Lambda_{i,i-1}$ for the first five neighboring guide vanes.

Appendix D

Procedure for hydrodynamic parameter identification

1) Newton's law governing the guide vane cascade $[I]\,\ddot{\mathbf{y}} + [C]\,\dot{\mathbf{y}} + [K]\,\mathbf{y} = \mathbf{F}$

with $\mathbf{y} = \left(y_1 \; y_2 \; ... \; y_{z_o} \; \alpha_1 \; \alpha_2 \; ... \; \alpha_{z_o}\right)^T$

$\mathbf{F} = \left(F_1 \; F_2 \; ... \; F_{z_o} \; T_1 \; T_2 \; ... \; T_{z_o}\right)^T$

and the matrices whose components are built from the potential flow theory

$$[K] = \begin{bmatrix} K_1^S & 0 & \dots & 0 & K_1^{f,\alpha} & \dots & \dots & 0 \\ 0 & K_2^S & \dots & 0 & 0 & K_2^{f,\alpha} & \dots & 0 \\ \vdots & \vdots & \ddots & \vdots & \vdots & \vdots & \ddots & \vdots \\ 0 & \dots & \dots & K_{z_o}^S & 0 & \dots & \dots & K_{z_o}^{f,\alpha} \\ 0 & \dots & \dots & 0 & L_1^S + L_1^{f,\alpha} & \dots & \dots & 0 \\ 0 & 0 & \dots & 0 & 0 & L_2^S + L_2^{f,\alpha} & \dots & 0 \\ \vdots & \vdots & \ddots & \vdots & \vdots & \vdots & \ddots & \vdots \\ 0 & \dots & \dots & 0 & 0 & \dots & \dots & L_{z_o}^S + L_{z_o}^f \end{bmatrix}$$

$$[I] = \begin{bmatrix} I_1^S + I_{1,1}^f & I_{1,2}^f & \dots & I_{1,z_o}^f & I_{1,1}^{f,\alpha} & I_{1,2}^{f,\alpha} & \dots & I_{1,z_o}^{f,\alpha} \\ I_{2,1}^f & I_2^S + I_{2,2}^f & \dots & I_{2,z_o}^f & I_{2,1}^{f,\alpha} & I_{2,2}^{f,\alpha} & \dots & I_{2,z_o}^{f,\alpha} \\ \vdots & \vdots & \ddots & \vdots & \vdots & \vdots & \ddots & \vdots \\ I_{z_o,1}^f & I_{z_o,2}^f & \dots & I_{z_o}^S + I_{z_o,z_o}^f & I_{z_o,1}^{f,\alpha} & I_{z_o,2}^{f,\alpha} & \dots & I_{z_o,z_o}^{f,\alpha} \\ J_{1,1}^f & J_{1,2}^f & \dots & J_{1,z_o}^f & J_1^S + J_{1,1}^{f,\alpha} & J_{1,2}^{f,\alpha} & \dots & J_{1,z_o}^{f,\alpha} \\ J_{2,1}^f & J_{2,2}^f & \dots & J_{2,z_o} & J_{2,1}^{f,\alpha} & J_2^S + J_{2,2}^{f,\alpha} & & J_{2,z_o}^{f,\alpha} \\ \vdots & \vdots & \ddots & \vdots & \vdots & \vdots & \ddots & \vdots \\ J_{z_o,1}^f & J_{z_o,2}^f & \dots & J_{z_o,z_o}^f & J_{z_o,1}^{f,\alpha} & J_{z_o,2}^{f,\alpha} & \dots & J_{z_o}^S + J_{z_o,z_o}^{f,\alpha} \end{bmatrix}$$

$$[C] = \begin{bmatrix} C_1^S + C_{1,1}^f & C_{1,2}^f & \dots & C_{1,z_o}^f & C_{1,1}^{f,\alpha} & C_{1,2}^{f,\alpha} & \dots & C_{1,z_o}^{f,\alpha} \\ C_{2,1}^f & C_2^S + C_{2,2}^f & \dots & C_{2,z_o}^f & C_{2,1}^{f,\alpha} & C_{2,2}^{f,\alpha} & \dots & C_{2,z_o}^{f,\alpha} \\ \vdots & \vdots & \ddots & \vdots & \vdots & \vdots & \ddots & \vdots \\ C_{z_o,1}^f & C_{z_o,2}^f & \dots & C_{z_o}^S + C_{z_o,z_o}^f & C_{z_o,1}^{f,\alpha} & C_{z_o,2}^{f,\alpha} & \dots & C_{z_o,z_o}^{f,\alpha} \\ D_{1,1}^f & D_{1,2}^f & \dots & D_{1,z_o}^f & D_1^S + D_{1,1}^{f,\alpha} & D_{1,2}^{f,\alpha} & \dots & D_{1,z_o}^{f,\alpha} \\ D_{2,1}^f & D_{2,2}^f & \dots & D_{2,z_o}^f & D_{2,1}^{f,\alpha} & D_2^S + D_{2,2}^{f,\alpha} & & D_{2,z_o}^{f,\alpha} \\ \vdots & \vdots & \ddots & \vdots & \vdots & \vdots & \ddots & \vdots \\ D_{z_o,1}^f & D_{z_o,2}^f & \dots & D_{z_o,z_o}^f & D_{z_o,1}^{f,\alpha} & D_{z_o,2}^{f,\alpha} & \dots & D_{z_o}^S + D_{z_o,z_o}^{f,\alpha} \end{bmatrix}$$

2) The guide vanes O_{10} and O_{11} having a flexible stem, the others being stiff, the system is reduced to:

$$\begin{cases} \left(-\omega^2\,[I^s] + [K^s] + i\omega\,[C^s]\right)\hat{\mathbf{y}}(\omega) = \hat{\mathbf{F}}(\omega) & \text{①} \\ \hat{\mathbf{F}}(\omega) = \bar{\hat{\mathbf{F}}}_i + \hat{\mathbf{F}}_i^{RSI}(\omega) - \left(-\omega^2\left[I^f\right] + i\omega\left[C^f\right] + \left[K^f\right]\right)\hat{\mathbf{y}}(\omega) & \text{②} \end{cases}$$

with $\hat{\mathbf{y}} = \left(\hat{y}_{10} \;\; \hat{y}_{11} \;\; \hat{\alpha}_{10} \;\; \hat{\alpha}_{11}\right)^T$ is known from the measurements
and $\hat{\mathbf{F}} = \left(\hat{F}_{10} \;\; \hat{F}_{11} \;\; \hat{T}_{10} \;\; \hat{T}_{11}\right)^T$ is unknown.

3) $[K^s]$ is analytically estimated from the simple bending and torsion theory
4) $[I^s]$ is experimentally estimated from the modal analysis in air and from $[K^s]$
5) $[C^s]$ is experimentally identified from the impulse response in air
6) Knowing these matrices, the vector $\hat{\boldsymbol{F}}$ may be computed with ①
7) The matrices $[I^f]$,$[C^f]$and $[K^f]$ are expressed as follows:

$$[I^f] = \begin{bmatrix} \boxed{I_{10,10}^f} & I_{10,11}^f & I_{10,10}^{f,\alpha} & I_{10,11}^{f,\alpha} \\ I_{11,10}^f & \boxed{I_{11,11}^f} & I_{11,10}^{f,\alpha} & I_{11,11}^{f,\alpha} \\ J_{10,10}^f & J_{10,11}^f & \boxed{J_{10,10}^{f,\alpha}} & J_{10,11}^{f,\alpha} \\ J_{11,10}^f & J_{11,11}^f & J_{11,10}^{f,\alpha} & \boxed{J_{11,11}^{f,\alpha}} \end{bmatrix} \quad [C^f] = \begin{bmatrix} \boxed{C_{10,10}^f} & C_{10,11}^f & C_{10,10}^{f,\alpha} & C_{10,11}^{f,\alpha} \\ C_{11,10}^f & \boxed{C_{11,11}^f} & C_{11,10}^{f,\alpha} & C_{11,11}^{f,\alpha} \\ D_{10,10}^f & D_{10,11}^f & \boxed{D_{10,10}^{f,\alpha}} & D_{10,11}^{f,\alpha} \\ D_{11,10}^f & D_{11,11}^f & D_{11,10}^{f,\alpha} & \boxed{D_{11,11}^{f,\alpha}} \end{bmatrix} \quad [K^f] = \begin{bmatrix} K_{10,10}^f & 0 & K_{10,10}^{f,\alpha} & 0 \\ 0 & K_{11,11}^f & 0 & K_{11,11}^{f,\alpha} \\ L_{10,10}^f & 0 & L_{10,10}^{f,\alpha} & 0 \\ 0 & L_{11,11}^f & 0 & L_{11,11}^{f,\alpha} \end{bmatrix}$$

8) The outlined diagonal terms are known from the modal analyzes in water, model at rest.

9) Focus on the response to the frequency *f=18n* at which the torsion response is negligible compared to the bending:

$$\begin{cases} \left(-\omega^2\left[I^s\right]+\left[K^s\right]+i\omega\left[C^s\right]\right)\left(\hat{y}_{10}\left(\omega\right) \quad \hat{y}_{11}\left(\omega\right)\right)^T = \left(\hat{F}_{10}\left(\omega\right) \quad \hat{F}_{11}\left(\omega\right)\right)^T \\ \left(\hat{F}_{10}\left(\omega\right) \quad \hat{F}_{11}\left(\omega\right)\right)^T = \bar{\hat{\mathbf{F}}}_i + \hat{\mathbf{F}}_i^{RSI}\left(\omega\right) - \left[\hat{H}^f\right]\left(\hat{y}_{10}\left(\omega\right) \quad \hat{y}_{11}\left(\omega\right)\right)^T \quad ② \end{cases}$$

where $\omega = 2\pi \cdot 18n$ and $\left[\hat{H}^f\right] = \begin{bmatrix}\hat{H}^f_{10,10} & \hat{H}^f_{10,11} \\ \hat{H}^f_{11,10} & \hat{H}^f_{11,11}\end{bmatrix} = \begin{bmatrix}-\omega^2 I^f_{10,10}+i\omega C^f_{10,10}+K^f_{10,10} & -\omega^2 I^f_{10,11}+i\omega C^f_{10,11} \\ -\omega^2 I^f_{11,10}+i\omega C^f_{11,10} & -\omega^2 I^f_{11,11}+i\omega C^f_{11,11}+K^f_{11,11}\end{bmatrix}$

10) $\hat{y}_{11}$ is assumed not strong enough to have any influence at the lowest value of the impeller frequency shift, and, therefore, the force due to RSI acting on O_{10} may be known:

$$\hat{F}^{RSI}_{10}\left(f_{min}\right) = \hat{F}_{10}\left(f_{min}\right) + \left(-\left(\omega_{min}\right)^2 I^f_{10,10} + i\left(\omega_{min}\right) C^f_{10,10}\right) \cdot \hat{y}_{10}\left(f_{min}\right)$$

11) The force due to RSI acting on O_{11} is known by taking into account the phase shift of pressure mode *k*=2:

$$\hat{F}^{RSI}_{11}\left(f_{min}\right) = \hat{F}^{RSI}_{10}\left(f_{min}\right) \cdot e^{i\Delta\phi_{k=-2}}$$

12) The force due to RSI on the entire impeller frequency range investigated is known by solving:

$$\begin{cases} \hat{F}^{RSI}_{10}\left(f=18n\right) = \hat{L}_{s,10} \cdot \hat{p}^{RSI}_{s_{10}}\left(f=18n\right) \\ \hat{F}^{RSI}_{11}\left(f=18n\right) = \hat{L}_{s,11} \cdot \hat{p}^{RSI}_{s_{11}}\left(f=18n\right) \end{cases}$$

where $\hat{L}_{s,10}$ and $\hat{L}_{s,11}$ are assumed constant over the frequency range. The pressure terms are then linearly linked to the pressure monitored by the sensor g_{15} which is not influenced by the guide vanes vibrations.

13) The non diagonal components of the influence matrix $\left[\hat{H}^f\right]$ are known by using ②:

$$\hat{H}^f_{10,11} = \frac{\left(\hat{F}_{10} - \overline{\hat{F}}_{10} - \hat{F}^{RSI}_{10}\right)}{\hat{y}_{11}} \qquad \hat{H}^f_{11,10} = \frac{\left(\hat{F}_{11} - \overline{\hat{F}}_{11} - \hat{F}^{RSI}_{11}\right)}{\hat{y}_{10}}$$

14) The hydrodynamic parameters are finally known as follows:

$$I^f_{10,11}\left(f=18n\right) = -\frac{\Re\left(\hat{H}^f_{10,11}\right)}{\omega^2_{18n}} \qquad I^f_{11,10}\left(f=18n\right) = -\frac{\Re\left(\hat{H}^f_{11,10}\right)}{\omega^2_{18n}}$$

$$C^f_{10,11}\left(f=18n\right) = \frac{\Im\left(\hat{H}^f_{10,11}\right)}{\omega_{18n}} \qquad C^f_{11,10}\left(f=18n\right) = \frac{\Im\left(\hat{H}^f_{11,10}\right)}{\omega_{18n}}$$

15) Focusing on the response to the frequency *f=45n* at which the bending response is negligible compared to the torsion, and repeating the steps from 10) to 13) accordingly, the corresponding hydrodynamic parameters are known as follows:

$$J^{f,\alpha}_{10,11}\left(f=45n\right) = -\frac{\Re\left(\hat{G}^f_{10,11}\right)}{\omega^2_{45n}} \qquad J^{f,\alpha}_{11,10}\left(f=45n\right) = -\frac{\Re\left(\hat{G}^f_{11,10}\right)}{\omega^2_{45n}}$$

$$D^{f,\alpha}_{10,11}\left(f=45n\right) = \frac{\Im\left(\hat{G}^f_{10,11}\right)}{\omega_{45n}} \qquad D^{f,\alpha}_{11,10}\left(f=45n\right) = \frac{\Im\left(\hat{G}^f_{11,10}\right)}{\omega_{45n}}$$

Appendix E

Rotating pressure modes due to the RSI - an acoustic approach

The spinning pressure modes resulting from RSI have been theoretically approached in axial gas turbomachines. Blake [12] summarizes the different studies on spinning pressure modes made in the past. Basically, the fluid in the stator is considered as an acoustic medium. The rotating and fluctuating forces exerted on rotor blades due to RSI induce pressure fluctuations in the stator. The combination of the stator and rotor blade numbers makes apparent different pressure modes. Lowson [51] theoretically analyzes the noise of an axial compressor and preliminary agreements with experiments are demonstrated. Kaji and Okazaki [46] investigate the effects of the Mach number, the rotor-stator axial clearance, the blade spacing ratio and the drag coefficient of upstream airfoils on the sound generated by RSI.

The theoretical approach applied to axial gas turbomachines is adapted here to the case of a radial hydraulic pump-turbine. The water is taken as a compressible fluid. Recently, Yan et al. [89], [88], have launched both compressible and incompressible simulations for understanding the RSI phenomenon in hydraulic machines. The results of the compressible simulation corroborate the experimental results. The effect of compressibility has thereby a significant influence on the RSI. The influence level is strongly linked to the length scale. The higher the length scale, the stronger the influence. The incompressibility assumption often made in hydraulic machines means that the acoustic waves travel at an infinite speed. The pressure fluctuations in the rotor-stator gap may also be instantaneously observed in the spiral casing.

The Figure E.1 shows the rotating impeller where each blade consists of a source S of acoustic wave, which is assumed to be located at the blade leading edge. The stay- and guide vanes are removed and, therefore, the sound is assumed to propagate rectilinearly from the rotating source of sound positioned at $\mathbf{x}(t)$ to an observer placed in the acoustic medium at the fixed location $\boldsymbol{x}$. The waves are propagating in the plane (x_1, x_2) normal to the impeller rotation axis. According to Blake [12], the pressure $p(\boldsymbol{x}, t)$ coming from the source S is expressed as a function of the force F_i exerted by the blades on the fluid in the direction i:

$$[p'(\boldsymbol{x}, t)]_S = -\frac{1}{4\pi}\frac{\partial}{\partial x_i}\left(\frac{F_i\left(t - r_S/c_o\right)_S}{r_S}\right) \tag{E.1}$$

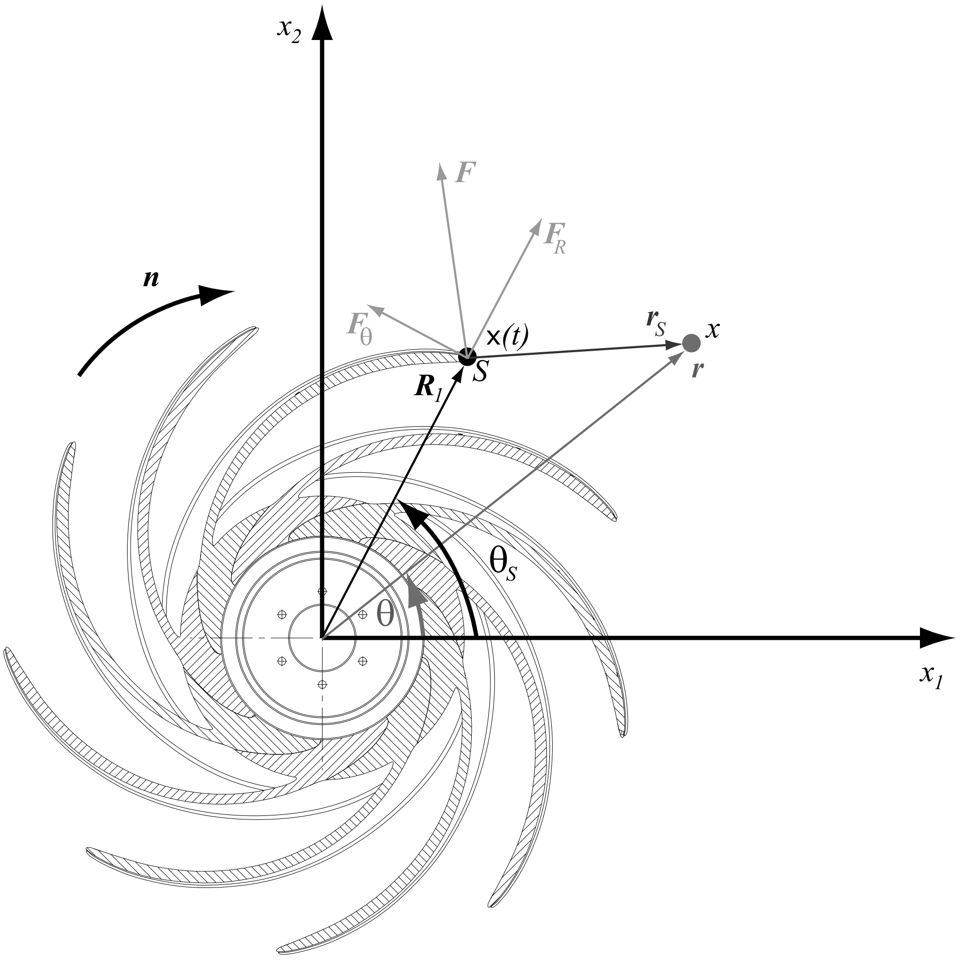

Figure E.1: Rotating acoustic source of pressure.

where the Einstein summation convention is used and c_o denotes the speed of sound and r_S, the source-observer vector which may be approximated as follows:

$$\begin{aligned} r_S(t) &= \sqrt{r^2 + R_1^2 - 2R_1 r cos(\theta - \theta_S(t))} \\ &\approx r - R_1 cos(\theta - \theta_S(t)) \end{aligned} \tag{E.2}$$

where $\theta_S(t)$ denotes the angular position of the sound source S and is expressed as follows:

$$\theta_S(t) = \theta_0 + S\frac{2\pi}{z_b} - 2\pi n \cdot t \tag{E.3}$$

z_b being the number of impeller blades and n the impeller rotation frequency.

From eq. E.1, the following approximation may be established:

$$\begin{aligned}
\left[p'\left(\mathbf{x},t\right)\right] &= \sum_{s=0}^{z_b-1} -\frac{1}{4\pi}\left(\frac{1}{r_S}\frac{\partial\left(F_i\left(t-r_S/c_o\right)\right)_S}{\partial x_i} + F_i\left(t-r_S/c_o\right)\cdot\frac{\partial\left(\frac{1}{r_S}\right)}{\partial x_i}\right) \\
&= \sum_{s=0}^{z_b-1} -\frac{1}{4\pi}\left(\frac{1}{r_S}\frac{\left(\partial F_i\left(t-r_S/c_o\right)\right)_S}{\partial t}\frac{\partial t}{\partial r_S}\frac{\partial r_S}{\partial x_i} - \frac{1}{r_S^2}F_i\left(t-r_S/c_o\right)\frac{\partial r_S}{\partial x_i}\right) \\
&\approx \sum_{s=0}^{z_b-1} \frac{1}{4\pi\cdot c_o\cdot r_S}\frac{\left(\partial F_i\left(t-r_S/c_o\right)\right)_S}{\partial t}\frac{\partial r_S}{\partial x_i} \\
&\approx \sum_{s=0}^{z_b-1} \frac{1}{4\pi\cdot c_o\cdot r_S}\frac{\left(\partial F_i\left(t-r_S/c_o\right)\right)_S}{\partial t}\frac{\partial\left(r-R_1 cos\left(\theta-\theta_S\right)\right)}{\partial x_i} \\
&= \sum_{s=0}^{z_b-1} \frac{1}{4\pi\cdot c_o\cdot r_S}\frac{\left(\partial F_i\left(t-r_S/c_o\right)\right)_S}{\partial t}\cdot\frac{r_i}{r}
\end{aligned} \tag{E.4}$$

The fluctuating force is dependent on the impeller inflow velocity field. Respecting the spatial periodicity condition and taking into account the number of guide vanes z_o in the cascade causing the impeller inflow velocity field to periodically present defects in the wake of the guide vanes, the fluctuating force may be written as follows:

$$\left(F_i\left(t-r_S/c_o\right)\right)\cdot\frac{r_i}{r} = \sum_{s=0}^{z_b-1}\sum_{m=-\infty}^{\infty}\left(|\hat{F}_i|_{s,m}\cdot\frac{r_i}{r}\right)e^{i\left(mz_o\theta_S(t)+k_o r_S\right)} \tag{E.5}$$

Taking eqs. E.2 and E.5, one can write:

$$\begin{aligned}
\left(\frac{F_i\left(t-r_S/c_o\right)}{r_S}\right)\cdot\frac{r_i}{r} &= \sum_{s=0}^{z_b-1}\sum_{m=-\infty}^{\infty}\frac{|\hat{F}_i|_{s,m}\cdot\frac{r_i}{r}}{r_S}e^{i\left(mz_o\left(\theta_0+s\frac{2\pi}{z_b}-2\pi n\cdot t\right)\right)}\cdot e^{ik_0 r} \\
&\cdot\quad e^{-ik_0 R_1 cos\left(\theta_S-\theta\right)} \\
&= \sum_{s=0}^{z_b-1}\sum_{m=-\infty}^{\infty}\sum_{q=-\infty}^{\infty}\frac{|\hat{F}_i|_{s,m}\cdot\frac{r_i}{r}}{r_S}e^{i\left(mz_o\left(\theta_0+s\frac{2\pi}{z_b}-2\pi n\cdot t\right)\right)}\cdot e^{ik_0 r} \\
&\cdot\quad\left(-i\right)^q e^{iq\left(\theta_0-\theta+s\frac{2\pi}{z_b}-2\pi n\cdot t\right)}\cdot J_q\left(k_o R_1\right)
\end{aligned} \tag{E.6}$$

where $J_q\left(k_o R_1\right)$ is the q^{th} order Bessel function evaluated at $k_o R_1$.

From Figure E.1, one may write the components of the vectors $\boldsymbol{r}$ and $\boldsymbol{F}$ on the two axis x_1 and x_2:

$$\begin{aligned}
r_1 &= r\cdot cos\left(\theta\right) \\
r_2 &= r\cdot sin\left(\theta\right) \\
F_1 &= F\cdot cos\left(\theta_S+\gamma\right) \\
F_2 &= F\cdot sin\left(\theta_S+\gamma\right)
\end{aligned} \tag{E.7}$$

where γ refers to the mean impeller blade inflow incidence angle.

Therefore, one has:

$$\begin{aligned}|\hat{F}_i|_{s,m}\cdot\frac{r_i}{r} &= |\hat{F}_1|_{s,m}\cdot cos\left(\theta\right)+|\hat{F}_2|_{s,m}\cdot sin\left(\theta\right)\\ &= |\hat{F}|_{s,m}\cdot\left(cos\left(\theta_S+\gamma\right)cos\left(\theta\right)+sin\left(\theta_S+\gamma\right)sin\left(\theta\right)\right)\\ &= |\hat{F}|_{s,m}\cdot cos\left(\theta_S+\gamma-\theta\right)\end{aligned}\tag{E.8}$$

The rather complex summation in eq. E.6 is simplified using the following relation:

$$\begin{aligned}\sum_{s=0}^{z_b-1}e^{i(mz_0+q)\frac{2\pi}{z_b}\cdot s}|\hat{F}_i|_{s,m}\cdot\frac{r_i}{r} &= \sum_{s=0}^{z_b-1}e^{i(mz_0+q)\frac{2\pi}{z_b}\cdot s}|\hat{F}|_{s,m}\cdot cos\left(\theta_S+\gamma-\theta\right)\\ &= z_b\cdot|\hat{F}|_m\cdot\sum_{m'=-\infty}^{\infty}\delta\left(mz_0+q-m'z_b\right)\end{aligned}\tag{E.9}$$

assuming that the amplitude of the unsteady loading on each blade is the same $|F|_{s,m}=|F|_m$.

Moreover, in the following lines, the problem is restricted to the case where $r>R_1$ leading to the simplification in the denominator $r_S\approx r$.

$$\begin{aligned}\left(\frac{F\left(t-r_S/c_o\right)}{r_S}\right)\cdot\frac{r_i}{r} \approx & \sum_{m=-\infty}^{\infty}\sum_{m'=-\infty}^{\infty}\left(-i\right)^{m'z_b-mz_o}\frac{|\hat{F}|_m\cdot z_b}{r}e^{-im'z_b2\pi nt}e^{im'z_b\theta_0}\\ & \cdot\ e^{i(mz_o-m'z_b)\theta}e^{ik_or}J_{m'z_b-mz_o}\left(k_oR_1\right)\end{aligned}\tag{E.10}$$

On the one hand, according to eq. E.4, the pressure due to the RSI is written:

$$\begin{aligned}p'\left(\mathbf{x},t\right) \approx & \frac{1}{4\pi}\sum_{m=-\infty}^{\infty}\sum_{m'=-\infty}^{\infty}\left(-i\right)^{m'z_b-mz_o+1}\frac{|\hat{F}|_m\cdot z_b}{r}\frac{m'z_b2\pi n}{c_o}e^{-im'z_b2\pi nt}e^{im'z_b\theta_0}\\ & \cdot\ e^{i(mz_0-m'z_b)\theta}e^{ik_or}J_{m'z_b-mz_o}\left(k_oR_1\right)\end{aligned}\tag{E.11}$$

On the other hand, from eq. E.1 and using eq. E.10, one may write the pressure due to the RSI as:

$$\begin{aligned}p'\left(\mathbf{x},t\right) &= \sum_{s=0}^{z_b-1}-\frac{1}{4\pi}\frac{\partial}{\partial x_i}\left(\frac{F_i\left(t-r_S/c_o\right)_S}{r_S}\right)\\ &= \sum_{s=0}^{z_b-1}-\frac{1}{4\pi}\frac{\partial}{\partial r}\left(\frac{F_i\left(t-r_S/c_o\right)_S}{r_S}\right)\cdot\frac{\partial r}{\partial x_i}\\ &= \sum_{s=0}^{z_b-1}-\frac{1}{4\pi}\left(\frac{1}{r_S}\frac{\partial F_i\left(t-r_S/c_o\right)_S}{\partial r}-\frac{1}{r_S^2}\frac{\partial r_i}{\partial r}\right)\frac{\partial r}{\partial x_i}\\ &\approx -\frac{1}{4\pi}\frac{1}{r_S}\frac{\partial F_i\left(t-r_S/c_o\right)}{\partial r}\frac{r_i}{r}\\ &\approx \frac{1}{4\pi}\sum_{m=-\infty}^{\infty}\sum_{m'=-\infty}^{\infty}\left(-i\right)^{m'z_b-mz_o+1}\frac{|\hat{F}|_m\cdot z_b}{r}k_oe^{-im'z_b2\pi nt}e^{im'z_b\theta_0}\\ &\quad\cdot\ e^{i(mz_0-m'z_b)\theta}e^{ik_or}J_{m'z_b-mz_o}\left(k_oR_1\right)\end{aligned}\tag{E.12}$$

Comparing eqs. E.11 and E.12, one finds:

$$k_o = \frac{m' z_b 2\pi n}{c_o} \tag{E.13}$$

Moreover, the Bessel function features the following property:

$$\sum_{m'=-\infty}^{\infty} J_{m'z_b - mz_o}\left(k_o R_1\right) = 2 \cdot \sum_{m'=1}^{\infty} J_{m'z_b - mz_o}\left(k_o R_1\right) \tag{E.14}$$

Therefore, the pressure fluctuations due to the RSI may be written as follows:

$$\begin{aligned} p'\left(\mathbf{x}, t\right) \quad &\approx \quad \sum_{m=0}^{\infty} \sum_{m'=1}^{\infty} \left(-i\right)^{m'z_b - mz_o + 1} \frac{|\hat{F}|_m \cdot z_b}{r} \frac{m' z_b 2\pi n}{c_o} e^{-im' z_b 2\pi n t} e^{\pm i m' z_b \theta_0} \\ &\cdot \quad e^{i(mz_0 \pm m' z_b)\theta} e^{i k_o r} J_{m' z_b \pm m z_o}\left(\frac{m' z_b 2\pi n}{c_o} R_1\right) \end{aligned} \tag{E.15}$$

The pressure fluctuations may then be expressed as the summation of the m and m' harmonics:

$$p'\left(\mathbf{x}, t\right) \approx \sum_{m=0}^{\infty} \sum_{m'=1}^{\infty} \left(p'\left(\mathbf{x}, t\right)\right)_{m,m'} \tag{E.16}$$

where

$$\begin{aligned} \left(p'\left(\mathbf{x}, t\right)\right)_{m,m'} \quad &= \quad \left(\frac{|\hat{F}|_m \cdot z_b}{r} \frac{2 m' z_b 2\pi n}{c_o}\right) \cdot \\ &\quad\; \left(J_{k_+}\left(\frac{m' z_b 2\pi n}{c_o} R_1\right) \cdot cos\left(k_+ \cdot \theta - m' z_b 2\pi n \cdot t + \phi_{k_+}\right)\right. \\ &+ \quad \left. J_{k_-}\left(\frac{m' z_b 2\pi n}{c_o} R_1\right) \cdot cos\left(k_- \cdot \theta - m' z_b 2\pi n \cdot t + \phi_{k_-}\right)\right) \end{aligned} \tag{E.17}$$

with $k_+ = m'z_b + mz_o$ and $k_- = m'z_b - mz_o$ being the number of diametrical nodes of the spinning modes.

The pressure fluctuations monitored at the angular positions corresponding to two adjacent guide vanes are phase shifted by an angle $\Delta\phi_k$ expressed as follows:

$$\Delta\phi_k = 2\pi \frac{k}{z_o} \ , \tag{E.18}$$

where k refers either to k_- or k_+.

References

References

[1] Abu-Zeid, M. World water: challenges and vision for the twenty first century. *La Houille Blanche*, 2 (1998), 7–10.

[2] Arndt, N., Acosta, A. J., Brennen, C. E., and Caughey, T. K. Rotor-stator interaction in a diffuser pump. *Journal of Turbomachinery 111* (1989), 213–221.

[3] Arndt, N., Acosta, A. J., Brennen, C. E., and Caughey, T. K. Experimental investigation of rotor-stator interaction in a centrifugal pump with several vaned diffuser. *Journal of Turbomachinery 112* (January 1990), 98–108.

[4] Ausoni, Ph. *Turbulent vortex shedding from a blunt trailing edge hydrofoil.* PhD thesis, Ecole Polytechnique Fédérale de Lausanne, 2009.

[5] Avellan, F. l'Agefi magazine, January 2008.

[6] Avellan, F. Evolution des groupes de pumpage-turbinage. *Bulletin SEV/AES 2* (2012), 37–40.

[7] Basak, S., and Raman, R. Hydrodynamic coupling between micromechanical beams oscillating in viscous fluids. *Physics of Fluids 19* (2007).

[8] Batchelor, G. *An Introduction to Fluid Dynamics.* Cambridge University Press, 1967.

[9] Bendat, J. S., and Piersol, A. G. *Random Data, Analysis and Measurement Procedures*, 3$^{\text{rd}}$ ed. John Wiley & Sons, 2000.

[10] Beretta, A. *Influence of Mechanical Mistuning on the Forced Response of a Turbine Cascade.* PhD thesis, Ecole Polytechnique Fédérale de Lausanne, 2006.

[11] Beretta, A., Rottmeier, F., and Ott, P. Combined/simultaneous gust and oscillating turbine row unsteady aerodynamics in subsonic flow. *Experimental Thermal and Fluid Science 30* (2006), 393–401.

[12] Blake, W. *Mechanics of Flow-Induced Sound and Vibration*, vol. I & II. Academic Press, 1986.

[13] Blanc-Coquand, R., and Lavigne, S. Etude numérique et expérimentale des fluctuations de pression dans l'entrefer d'une turbine pompe. *La Houille Blanche*, 3-4 (2001), 46–50.

[14] Bogenrieder, W., and Groschke, L. Design and construction of germany's goldisthal pumped-storage scheme. *The International Journal on Hydropower & Dams*, 1 (2000), 29–31.

[15] Bregar, Z. The role of Slovenia' hydro plants in 2005. *The International Journal on Hydropower & Dams*, 5 (2005), 100–105.

[16] Brennen, C. *Hydrodynamics of Pumps.* Concepts ETI, Inc. and Oxford University Press, 1994.

[17] Brennen, C. E. A review of added mass and fluid inertial forces. Naval Civil Engineering Laboratory, 1982.

[18] Carlier, M. *Machines Hydrauliques.* Ecole National du Génie Rural des Eaux et des Forêts, 1968.

[19] Chatelain, J., Jufer, M., and Périllard, A. *Groupes de pompage.* Atelier de Sécheron, 1968.

[20] Cizmas, P. G. A., and Palacios, A. Proper orthogonal decomposition of turbine rotor-stator interaction. *Journal of Propulsion and Power 19*, 2 (March-April 2003), 268–281.

[21] Collard, J. E., and Cizmas, P. G. A. The effects of vibrating blades on turbomachinery rotor-stator interaction. *International Journal of Turbo and Jet Engines 20* (2003), 17–39.

[22] Conca, C., Osses, A., and Planchard, J. Added mass and damping in fluid-structure interaction. *Computational Methods Applied Mechanical Engineering 146* (1997), 387–405.

[23] Coutu, A., Aunemo, H., Badding, B., and Velagandula, O. Mechanical behavior of high-head Francis turbines. *The International Journal on Hydropower & Dams*, 1 (2006), 108–111.

[24] Coutu, A., Roy, M., Monette, C., and Nennemann, B. Experiments with rotor-stator interaction in high head Francis turbine. In *Proceeding of the IAHR 24th Symposium on Hydraulic Machinery and Systems* (Foz do Iguassu, Brazil, 2008).

[25] Dan Ciocan, G., Kueny, J., Combes, J.-F., and Parkinson, E. Analyse expérimentale de l'interaction roue-distributeur dans une pompe-turbine. *La Houille Blanche*, 3-4 (1998), 55–60.

[26] Darrozes, J., and François, C. *Mécanique des fluides incompressibles.* 1982.

[27] Del Pedro, M., Gmür, T., and Botsis, J. *Introduction à la mécanique des solides et des structures.* Presses Polytechniques et Universitaires de Lausanne, 2010.

[28] Del Pedro, M., and Pahud, P. *Mécanique vibratoire, systèmes discrets linéaires.* Presses Polytechniques et Universitaires de Lausanne, 2003.

[29] Dring, R. P., Joslyn, H. D., W., H. L., and Wagner, J. H. Turbine rotor-stator interaction. *Journal of Engineering for Power 104* (1982), 729–742.

[30] Dubas, M. Über die erregung infolge der periodizität von turbomachinen. *Ingenieur-Archiv 54* (1984), 413–426.

[31] Ducheney, P. Sticky wickets: Replacing a sheared wicket gate. *Hydro review 28*, 6 (2009).

[32] Finnegan, P., Bartkowiak, J. A., and Deslandes, L. Repairing a failed turbine: The story of returning G.M. shrum unit 3 to service. *Renewable Energy World North America Magazine March* (March 2010).

[33] Fisher, R., Powell, C., Franke, G., Seidel, U., and Koutnik, J. Contributions to the improved understanding of the dynamic behavior of pump turbines and use thereof in dynamic design. In *Proceedings of the 22nd IAHR Symposium on Hydraulic Machinery and Systems* (2004).

[34] Franke, G., Fisher, R., Powell, C., Seidel, U., and Koutnik, J. On pressure mode shapes arising from rotor/stator interactions. *Sound and Vibrations March* (2005).

[35] Giesing, J. P. Two dimensional potential flow theory for multiple bodies in small amplitude motion. *AIAA Journal 8*, 11 (1970), 1944–1953.

[36] Gmür, T. *Dynamique des structures, Analyse modale numérique*. Presses Polytechniques et Universitaires de Lausanne, 1997.

[37] Graeser, J.-E. *Installations de pompage-turbinage dans le monde: Réalisations et perspectives de dévelopement.* Ecole Polytechnique Fédérale de Lausanne, 1979.

[38] Guo, S., and Okamoto, H. An experimental study on the fluid forces induced by rotor-stator interaction in a centrifugal pump. *International Journal of Rotating Machinery 9*, 2 (2003), 135–144.

[39] Guérassimoff, G., and Maïzi, N. *Eau et Energie: destins croisés.* Presses des Mines, 2011.

[40] Henscheid, P. Sticky wickets: In-place replacement of a wicket gate. *Hydro review 28*, 7 (2009).

[41] Hydropower & Dams, Ed. *The International Journal of Hydropower & Dams*, vol. 18. ICOLD, IAHR, ICID, 2011.

[42] International Electrotechnic Commission. Hydraulic Turbines, Storage Pumps and Pump-Turbines - Model Acceptance Tests, International Standard IEC 60193, 1999, 2$^{\text{nd}}$ Edition.

[43] International Energy Agency. *Key World Energy Statistics.* 2011.

[44] International Hydropower Association. Activity report, 2011.

[45] Kahl, G. *Aeroelastic effects of Mistuning and Coupling in Turbomachinery Bladings.* Thesis no 2629, Ecole Polytechnique Fédérale de Lausanne, 2002.

[46] Kaji, S., and Okazaki, T. Generation of sound by rotor-stator interaction. *Journal of Sound and Vibration 13*, 3 (1970), 281–307.

[47] Kemp, N. H., and Sears, W. R. Aerodynamic interference between moving blade rows. *Journal of the Aeronautical Sciences 20*, 9 (September 1953), 585–597.

[48] Kemp, N. H., and Sears, W. R. The unsteady forces due to viscous wakes in turbomachines. *Journal of the Aeronautical Sciences 22*, 1 (1955), 478–483.

[49] Kimber, M., Lonergan, R., and Garimella, S. Experimental study of aerodynamic damping in arrays of vibrating cantilever. *Journal of Fluids and Structures 25* (2009), 1334–1347.

[50] Le Niliot, C. *La méthode des Eléments de Frontière pour la Résolution de Problèmes Inverses en Conduction de la Chaleur : Applications numériques et Expérimentales.* PhD thesis, Université de Provence - Aix-Marseille I, 2002.

[51] Lowson, M. V. Theoretical analysis of compressor noise. *The Journal of the Acoustical Society of America 47*, 1 (1968), 371–385.

[52] Max, J. *Méthodes et techniques de traitement du signal et applications aux mesures physiques, Tome 1 & 2.* Masson, 1985.

[53] Mei, Z.-Y. *Mechanical Design and Manufacturing of Hydraulic Machinery.* Avebury Technical, 1991.

[54] Meier, W., and Jaquet, M. Single and multi-stage pump-turbines for high head storage plants. In *ASME-CSME Pump-Turbine Schemes: Planning, Design and Operation* (Niagara Falls, June 1979).

[55] Mount, A., and Stipanovic, A. Development of improved francis pump-turbine runner for existing installations. In *ASME-CSME Pump-Turbine Schemes: Planning, Design and Operation* (Niagara Falls, June 1979).

[56] Muench, C., Ausoni, P., Braun, O., Farhat, M., and Avellan, F. Fluid-structure coupling for an oscillating hydrofoil. *Journal of Fluids and Structures 26* (2010), 1018–1033.

[57] Naudascher, E., and Rockwell, D. *Flow-Induced Vibrations.* Dover Publications, Inc, 2005.

[58] Nennemann, B., and Parkinson, E. Yixing pump turbine guide vane vibrations: problem resolution with advanced cfd analysis. In *Proceedings of the 25th IAHR Symposium on Hydraulic Machinery and Systems* (2010).

[59] Nowicki, P., Sallaberger, M., and Bachmann, P. Modern design of pump-turbines. In *Proceedings of the IEEE Electrical Power & Energy Conference* (2009).

[60] Nüssli, W., and Engel, A. Design considerations of pump/turbine installations with regard to reliability and availability. In *ASME-CSME Pump-Turbine Schemes: Planning, Design and Operation* (Niagara Falls, June 1979).

[61] Office Fédéral de l'Energie. *Graphiques de la statistique suisse de l'électricité 2010.*

[62] Office Fédéral de l'Energie. *Statistique suisse de l'électricité.* 2010.

[63] Office Fédéral de l'Energie. *Perspectives Energétiques 2050.* May 2011.

[64] Palffy, S., and Netsch, H. Pump turbines: Present state and future developments. In *Proceedings of the International Symposium on Pumps in Power Stations* (Brunswick, September 1966).

[65] PennWell Global Energy Group, Ed. *Hydro Review*, vol. 29. January 2010.

[66] PennWell Global Energy Group, Ed. *Hydro Review Worldwide*, vol. 18. September 2010.

[67] Pereira, F., Farhat, M., and Avellan, F. Dynamic calibration of transient sensors by spark generated cavity. In *Proceedings of IUTAM Symposium on Bubble Dynamics and Interface Phenomena* (1993).

[68] Randall, R. B. *Frequency analysis*, 3^{rd} ed. Brüel & Kjaer, 1987.

[69] Rodriguez, C. G., Egusquiza, E., and F., S. I. Frequencies in the vibration induced by the rotor-stator interaction in a centrifugal pump turbine. *Journal of Fluids Engineering 129* (2007), 1428–1435.

[70] Rodrique, P. The selection of high-head pump-turbine equipment for underground pumped hydro energy storage application. In *ASME-CSME Pump-Turbine Schemes: Planning, Design and Operation* (Niagara Falls, June 1979).

[71] Roth, S., Calmon, M., Farhat, M., Muench, C., Huebner, B., and Avellan, F. Hydrodynamic damping identification from an impulse response of a vibrating blade. In *Proceedings of the 3rd IAHR International Meeting of the Workgroup on Cavitation and Dynamic Problems in Hydraulic Machinery and Systems.* (Brno, Czech Republic, 2009), vol. 1, pp. 253–270.

[72] Rottmeier, F. *Experimental Investigation of a Vibrating Axial Turbine Cascade in Presence of Upstream Generated Aerodynamic Gusts.* Thesis no. 2758, Ecole Polytechnique Fédérale de Lausanne, 2003.

[73] Ruchonnet, N., Nicolet, C., and Avellan, F. Hydroacoustic modeling of rotor-stator interaction in francis pump-turbine. In *Proceedings of the IAHR International Meeting on Cavitation and Dynamic Problems in Hydraulic Machinery and Systems* (Barcelona, June 2006).

[74] Ryhming, I. *Dynamique des fluides.* Presses Polytechniques et Universitaires de Lausanne, 2004.

[75] Sabonnadière, J.-C. *Nouvelles technologies de l'énergie*, vol. 2. Hermes Science Publications, 2007.

[76] Schleiss, A. J. The importance of hydraulic schemes for sustainable development in the 21st century. *The International Journal on Hydropower & Dams*, 1 (2000), 19–24.

[77] Tanaka, H. Vibration behavior and dynamic stress of runner of very high head reversible pump-turbine. In *Proceeding of the 15th IAHR Symposium on Hydraulic Machinery and Systems* (1990).

[78] Tanaka, H. Special design considerations for ultra high head pump-turbines. *The International Journal on Hydropower & Dams* (November 1994), 107–112.

[79] Tanaka, H. The role of pumped-storage in the 21st century. *The International Journal on Hydropower & Dams*, 1 (2000), 27.

[80] Ugural, A. C., and Fenster, S. K. *Advanced Mechanics of Materials and Applied Elasticity*, 5th ed. Prentice Hall, 2011.

[81] U.S. Energy Information Administration. *International Energy Outlook.* 2010.

[82] Špidla, J., and Čepa, Z. Upgrading of a pump-turbine at dalešice. *The International Journal on Hydropower & Dams*, 5 (2005), 106–108.

[83] VaTech Hydro / ANDRITZ. Hydro news, October 2008.

[84] Wallis, S. Pumped-storage contributes to China's peak energy requirements. *The International Journal on Hydropower & Dams* (2004), 74–76.

[85] Wilkins, G. *Technology Transfer for Renewable Energy, Overcoming Barriers in Developing Countries.* Earthscan, 2002.

[86] Williams, L. O. *An End to Global Warming.* Elsevier Science, 2002.

[87] World Energy Council. *Survey of Energy Resources.* 2010.

[88] Yan, J., Koutnik, J., Seidel, U., and Huebner, B. Compressible simulation of rotor-stator interaction in pump-turbines. In *Proceedings of the 25th IAHR Symposium on Hydraulic Machinery and Systems* (Timisoara, 2010).

[89] Yan, J., Koutnik, J., Seidel, U., Huebner, B., and Scherer, T. Compressible simulation of rotor-stator interaction in a pump-turbine. In *Proceedings of the 3rd IAHR International Meeting of the Workgroup on Cavitation and Dynamic Problems in Hydraulic Machinery and Systems,* (Brno, 2009).

[90] Zobeiri, A. *Investigations of Time Dependent Flow Phenomena in a Turbine and a Pump-Turbine of Francis Type: Rotor-Stator Interactions and Precessing Vortex Rope.* PhD thesis, EPFL, 2009.

[91] Zobeiri, A. *Effect of Hydrofoil Trailing Edge Geometry on the Wake Dynamics.* PhD thesis, Ecole Polytechnique Fédérale de Lausanne, 2012.

[92] Zobeiri, A., Kueny, J.-L., Farhat, M., and Avellan, F. Pump-turbine rotor-stator interactions in generating mode: Pressure fluctuation in distributor channel. In *Proceedings of the 23*rd *IAHR Symposium on Hydraulic machinery and systems* (Yokohama, October 2006).

Curriculum Vitae

Steven Roth

Avenue de Montoie 37
1007 Lausanne
Suisse

+41 76 421 88 74
steven.roth13@gmail.com

Suisse et Anglais
Né le 13 janvier 1984

FORMATION

2008-2012	**Doctorat ès sciences techniques** Ecole Polytechnique Fédérale de Lausanne (EPFL), Suisse
2003-2008	**Etudes universitaires en Génie Mécanique, EPF** 2008: Prix Rhyming pour le projet de Master 2008: Master avec spécialisation en mécanique des structures et des fluides 2006: Bachelor en Génie Mécanique
1999-2003	**Maturité fédérale** Collège Claparède (GE)

EXPERIENCES PROFESSIONNELLES

2005-2009	**Ecole Polytechnique Fédérale de Lausanne (EPFL), Suisse** **Laboratoire de Machines Hydrauliques (LMH)** **Activités de recherche:** Thèse de Doctorat: Etude expérimentale du couplage fluide-structure dans la grille d'aubes directrices d'un modèle réduit de pompe-turbine • Mesures de pressions pariétales • Mesures des vibrations Rédaction de publications scientifiques et participation à diverses conférences **Activités d'enseignement:** • Encadrement de projets de Masters • Préparation de séances d'exercices et d'examens
2008	**Voith Siemens, Heidenheim, Allemagne** Stage de six mois dans le département R&D Identification de l'amortissement hydrodynamique d'une aube de roue Francis à l'aide d'outils numériques
2006-2007	**EPFL, Lausanne, Suisse** En parallèle des études Evaluation de divers accidents d'équipements de construction
2006	**SebSchmidt, Genève, Suisse** Conception d'une aile rigide d'un char à voile dans l'optique de battre le record du monde de vitesse

2006	**Méca-Test Giannino Scampa SA, Genève** Stage d'usinage d'un mois
2001-2005	**Pronaval SA, Genève** Durant les vacances scolaires En charge de la maintenance des bateaux et de la gestion d'une Marina.

COMPETENCES INFORMATIQUES ET TECHNIQUES

Outils num.	Ansys, CFX, ICEM, Fluent
CAO.	Catia V5
Equipement exp.:	Capteurs de pression, jauges de contraintes, conditionnement et acquisition.
Programmation:	C++, Matlab
Multimédia:	Adobe Suite

LANGUES

Français	Langue maternelle
Anglais	Avancé
Allemand	Avancé

List of Publications

Journal papers

1. Roth S., Hasmatuchi V., Botero F., Dreyer M., Farhat M. and Avellan F. Fluid-Structure Coupling Effects on the Dynamic Response of Pump-Turbine Guide Vanes. *Journal of Fluids and Structures, Submitted for publication*

2. Hasmatuchi V., Farhat M., Roth S., Botero F. and Avellan F. Experimental Evidence of Rotating Stall in a Pump-Turbine at Off-Design Conditions in Generating Mode. *Transactions- American Society of Mechanical Engineers Journal of Fluids Engineering, Vol. 133, num. 5, 2011.*

Conference papers

1. Hasmatuchi V., Roth S., Botero F., Farhat M. and Avellan F. Hydrodynamics of a Pump-Turbine Operation at Off-Design Conditions in Generating Mode. *Simhydro, Nice, France, 2012.*

2. Müller A., Bullani A., Dreyer M., Roth S., Favrel A., Landry C. and Avellan F. Interaction of a pulsating vortex rope with the local velocity field in a Francis turbine draft tube. *26th IAHR Symposium on Hydraulic Machinery and Systems, Beijing, China, 2012.*

3. Hasmatuchi V., Farhat M., Roth S., Botero F. and Avellan F. Hydrodynamics of a Pump-Turbine Operating at Off-Design Conditions in Generating Mode: Experimental Investigation. *SHF Conference on Cavitation and Hydraulic Machines, Lausanne, Switzerland, 2011.*

4. Landry C., Alligné S., Hasmatuchi V., Roth S., Müller A. and Avellan F. Non-Linear Stability Analysis of a Reduced Scale Model Pump-Turbine at Off-Design Operation. *4th IAHR International Meeting on Cavitation and Dynamic Problems in Hydraulic Machinery and Systems, Belgrade, Serbia, 2011.*

5. Roth S., Hasmatuchi V., Botero F., Farhat M. and Avellan F. Influence of the Pump-Turbine Guide Vanes Vibrations on the Pressure Fluctuations in the Rotor-Stator Vaneless Gap. *4th IAHR International Meeting on Cavitation and Dynamic Problems in Hydraulic Machinery and Systems, Belgrade, Serbia, 2011.*

6. Hasmatuchi V., Roth S., Botero F., Farhat M. and Avellan F. Hydrodynamics of a Pump-Turbine at Off-Design Operating Conditions: Numerical Simulation. *ASME-JSME-KSME Joint Fluids Engineering Conference 2011 - 7th International Symposium on Pumping Machinery, Hamamatsu, Japan, 2011.*

7. Hübner B., Seidel U. and Roth S. Application of Fluid-Structure Coupling to Predict the Dynamic Behavior of Turbine Components. *25th IAHR Symposium on Hydraulic Machinery and Systems, Timisoara, Romania, 2010.*

8. Roth S., Hasmatuchi V., Botero F., Farhat M. and Avellan F. Fluid-Structure Coupling in the Guide Vanes Cascade of a Pump-Turbine Scale Model. *25th IAHR Symposium on Hydraulic Machinery and Systems, Timisoara, Roumania, 2010.*

9. Hasmatuchi V., Roth S., Botero F., Avellan F. and Farhat M. High-speed flow visualization in a pump-turbine under off-design operating conditions. *25th IAHR Symposium on Hydraulic Machinery and Systems, Timisoara, Romania, 2010.*

10. Roth S., Hasmatuchi V., Botero F., Farhat M. and Avellan F. Advanced Instrumentation for Measuring Fluid-Structure Coupling Phenomena in the Guide Vanes Cascade of a Pump-Turbine Scale Model. *ASME 2010* 7^{th} *International Symposium on Fluid-Structure Interactions, Flow-Sound Interactions, and Flow-Induced Vibration & Noise, Montreal, Québec, Canada, 2010.*

11. Roth S., Calmon M., Farhat M., Münch C. and Hübner B. and Avellan F. Hydrodynamic Damping Identification from an Impulse Response of a Vibrating Blade. 3^{rd} *IAHR International Meeting of the Workgroup on Cavitation and Dynamic Problems in Hydraulic Machinery and Systems, Brno, 2009.*